UNIVERSITÉ DE MONTRÉAL

"STUDY OF THE FRACTOGRAPHY AND MICROMECHANISMS OF NEAR-THRESHOLD FATIGUE CRACKING AND TRANSGRANULAR STRESS-CORROSION CRACKING"

par

Li SHIQIONG

DÉPARTEMENT DE MÉTALLURGIE ET DE GÉNIE DES MATÉRIAUX

ÉCOLE POLYTECHNIQUE

THÈSE PRÉSENTÉE EN VUE DE L'OBTENTION
DU GRADE DE PHILOSOPHIAE DOCTOR (Ph.D.)
(GÉNIE MÉTALLURGIQUE)

Octobre 1991

© droits réservés de Li SHIQIONG 1991.

onal Library
Canada

adian Theses Service

va, Canada
0N4

Bibliothèque nationale
du Canada

Service des thèses canadiennes

e author has granted an irrevocable non-
clusive licence allowing the National Library
Canada to reproduce, loan, distribute or sell
pies of his/her thesis by any means and in
y form or format, making this thesis available
interested persons.

e author retains ownership of the copyright
his/her thesis. Neither the thesis nor
ostantial extracts from it may be printed or
erwise reproduced without his/her per-
ssion.

L'auteur a accordé une licence irrévocable et non exclusive permettant à la Bibliothèque nationale du Canada de reproduire, prêter, distribuer ou vendre des copies de sa thèse de quelque manière et sous quelque forme que ce soit pour mettre des exemplaires de cette thèse à la disposition des personnes intéressées.

L'auteur conserve la propriété du droit d'auteur qui protège sa thèse. Ni la thèse ni des extraits substantiels de celle-ci ne doivent être imprimés ou autrement reproduits sans son autorisation.

ISBN 0-315-72729-2

anada

UNIVERSITÉ DE MONTRÉAL

ÉCOLE POLYTECHNIQUE

Cette thèse intitulée:

"STUDY OF THE FRACTOGRAPHY AND MICROMECHANISMS OF NEAR-THRESHOLD FATIGUE CRACKING AND TRANSGRANULAR STRESS-CORROSION CRACKING"

présentée par: Li Shiqiong

en vue de l'obtention du grade de: Philosophiae Doctor (Ph.D.)

a été dûment acceptée par le jury d'examen constitué de:

M. Jean-Paul Baïlon, D.Sc.A., président

J. Ivan Dickson, Ph.D., Directeur de recherche

M. Thierry Magnin, Docteur d'état, membre

M. Yves Verreman, Ph.D., membre

To my husband,

Mr. Mu Chengxiong

SOMMAIRE

La fractographie et la cristallographie de la corrosion sous contrainte transgranulaire (CSCT) dans les métaux c.f.c. constituent le thème central de cette étude. Plusieurs études préalables avaient déterminé les orientations cristallographiques des détails microfractographiques produits par la CSCT dans le but d'identifier les mécanismes actifs de fissuration. Cependant, à cause de la complexité de ces détails fractographiques et des limites des techniques de détermination de l'orientation de très petites facettes de fissuration, plusieurs des fins détails fractographiques de la CSCT n'ont pas été identifiés, ni expliqués de façon appropriée. Or, ces détails devraient fournir des informations importantes sur les mécanismes de fissuration. Une théorie d'ensemble de la CSCT devrait expliquer tous les détails morphologiques de la fissuration alors que les mécanismes actuellement proposés pour la CSCT sont souvent incompatibles avec les caractéristiques fractographiques observées.

Ces dernières années, des progrès considérables ont été réalisés dans la compréhension du comportement en fatigue près du seuil et au seuil. Mais, une attention moins grande avait été apportée aux mécanismes de fissuration dans cette région du seuil. De plus, il existe une ressemblance importante entre les aspects microfractographiques présents en fissuration transgranulaire en fatigue à des

vitesses de propagation très faibles et ceux observés sur les surfaces de rupture en CSCT des métaux cubiques à faces centrées (c.f.c.). Ceci indique que la compréhension des mécanismes de fissuration impliqués dans la fatigue près du seuil devrait être utile à la compréhension des mécanismes actifs dans la CSCT et vice-versa.

L'objectif principal de ce travail était donc d'identifier clairement et de façon détaillée les traits cristallographiques et fractographiques associés à la CSCT des métaux c.f.c. et à la fissuration près du seuil en fatigue-propagation dans les métaux c.f.c. et c.c. Nous avons entrepris cette étude dans le but de comparer les détails fractographiques typiques observés aux mécanismes de rupture proposés de façon à mieux identifier les mécanismes responsables de ces deux importants phénomènes de rupture.

Le rôle joué par l'environnement dans des mécanismes de fissuration a été étudié pour le cuivre, le laiton 70-30 et l'aluminium 2024-T351 grâce à des essais de fatigue réalisés à l'air et sous vide et, dans des bronzes au Mn-Al-Ni, grâce à des essais de fatigue réalisés à l'air ou dans une solution à 3,5% NaCl.

Après avoir établi une synthèse bibliographique des travaux publiés relatifs à la fractographie et aux mécanismes de fissuration par fatigue ou par fissuration

assistée par l'environnement, nous présentons les techniques expérimentales que nous avons employées. Les études relatives à la fatigue-propagation au voisinage du seuil ont porté sur plusieurs métaux c.f.c. (acier inoxydable 316, laiton 70-30, cuivre, alliage d'aluminium 2024-T351) et certains métaux ou phases c.c. (acier doux, alliage Fe-3% Si, phase β des bronzes au Mn-Al-Ni). Les échantillons utilisés étaient des éprouvettes de tension compactes (éprouvettes CT) caractérisées par une largeur W = 50.8 mm et ayant une épaisseur B = 12.7 mm.

Pour la fissuration près du seuil en fatigue, ces essais ont été effectués avec des rapports R de 0.1 et 0.5 et à des fréquences de 20 Hz dans l'air, l'argon sec et le vide en réduisant de façon contrôlée la vitesse de propagation da/dN jusqu'à 10^{-7} - 10^{-8} mm/cycle.

Les essais de fissuration en corrosion sous contrainte de l'acier inoxydable 316, dans une solution de $MgCl_2$ portée à ébullition, ont été effectués dans des conditions de potentiel libre à 154°C en utilisant une éprouvette d'épaisseur B = 3.2 mm et présentant une entaille en T.

Pour le laiton-α 70Cu-30Zn, les essais de fissuration en corrosion sous contrainte ont été faits à déplacement constant (donc en réduisant l'intensité de contrainte), grâce à des éprouvettes en double poutre encastrée ayant des

dimensions de 19 x 14 x 127 mm. Le milieu corrosif pour ces essais était une solution d'ammoniaque 15M à laquelle 6 g/l de cuivre étaient ajoutés sous forme de $Cu(NO_3)_2$ ou de poudre de Cu pur et les essais étaient réalisés en corrosion libre. Nous avons également entrepris une étude fractographique sur des rubans de laiton-α, ayant une épaisseur de 20 μm, rompus après immersion dans une solution d'ammoniaque dans le but de vérifier de façon plus approfondie la validité des différents modèles proposés pour la CSCT.

Pour les essais en fatigue-corrosion des bronzes 8-14% Mn-Al-Ni, des éprouvettes CT, d'épaisseur B = 22.3 mm et de largeur W = 101 mm, ont été utilisés. Les essais en fatigue étaient effectués à température ambiante sous chargement sinusoïdal, à fréquence de cyclage de 20 ou 1 Hz et généralement sous un rapport R de 0.1. Les essais de fatigue-corrosion dans la solution bien aérée de NaCl 3.5% étaient effectués dans des conditions de corrosion libre. Les techniques expérimentales utilisées pour les observations fractographiques détaillées réalisés dans cette étude comprennent l'étude macroscopique de la surface de rupture à faible grossissement par microscopie stéréo, l'étude métallographique par microscopie optique et par microscopie électronique à balayage (MEB) des éprouvettes, l'observation microfractographique à fort grossissement en MEB (en particulier de régions se correspondant sur les deux faces opposée de la rupture), des observations stéréofractographiques en MEB ainsi que des observations, par

microscopie électronique en transmission (MET), de repliques secondaires au carbone des surfaces de rupture. La technique des figures d'attaque a aussi été utilisée fréquemment dans le but de déterminer la cristallographie des facettes de rupture de la corrosion sous contrainte transgranulaire, de la fatigue-corrosion et de la fissuration près du seuil en fatigue. Nous avons également employé des mesures d'angles entre facettes à l'intérieur d'un même grain dans le but de déterminer les orientations probables et possibles des facettes.

Pour la fissuration près du seuil en fatigue, les facettes de rupture primaire rencontrées avaient des orientations {100}, {110} et {111}. Cependant, nous avons démontré que, généralement, à une échelle très microscopique, cette fissuration suit des plans de glissement dans les métaux avec structure c.f.c. et c.c. Dans l'acier inoxydable austenitique 316, le laiton-α 70Cu-30Zn et la phase c.f.c. des bronzes 8-10% Mn-Al-Ni lorsque fissurés à l'air, la fissuration près du seuil de fatigue se produit le plus souvent selon des plans {100} et dans des directions <110>. Une fraction relativement plus importante de facettes primaires {110} avec des directions de fissuration <100> ou voisines de <100> a été décelée pour dans les métaux c.f.c. à base de cuivre (cuivre, laiton-α et phase c.f.c. des bronzes). Pour les métaux c.c. (Fe-3% Si et l'acier 1008 AISI testé à l'air), les facettes étaient fréquemment des plans {100} et {110}. Nous avons remarqué que ces facettes primaires {100} et {110} présentaient, à une échelle plus fine, deux ensembles de microfacettes

alternant selon des plans de glissement. Pour les métaux c.f.c. et c.c. étudiés, la présence de ces microfacettes alternées provoquait fréquemment des facettes primaires {100} ou {110} présentant des stries ou des ondulations. L'absence de tout indice de clivage sur ces facettes primaires observées dans les métaux c.c. indique clairement que la fissuration près du seuil en fatigue est principalement due à du glissement.

Dans la fissuration en fatigue au voisinage du seuil, le degré de complexité de la fractographie observée dans une région dépend du nombre de plans de glissement localement actifs et sur lesquels la décohésion se produit et de l'importance relative de la décohésion sur chacun de ces plans de glissement. Ces deux aspects dépendent principalement de l'orientation de la région (grain) par rapport à l'axe de traction, des effets de contraintes locales associés au fait que les segments des fissures orientés différemment doivent nécessairement se joindre pour produire un front de fissure macroscopique, du type du matériau (surtout la facilité de glissement planaire) et finalement de l'effet de l'environnement sur le degré de planéité du glissement.

Pour le laiton 70-30 testé à l'air et qui présente parfois des régions ayant des aspects fractographiques complexes, nous avons montré qu'une cristallographie de fissuration {100} <100> se produit par glissement et décohésion, à une échelle

microscopique sur quatre plans de glissement {111} différents. Nous pouvons interpréter l'observation plus fréquente d'une rupture selon {100} <100>, dans l'alliage d'aluminium 2024-T351 en propagation près du seuil comme étant la conséquence de la formation d'oxydes en fond de fissure qui peuvent réduire la réversibilité du glissement et ainsi favoriser le glissement multiple.

Dans les métaux c.f.c. et c.c. étudiés, la fissuration transgranulaire au voisinage du seuil de propagation peut donc s'interpréter grâce à une décohésion à une échelle très fine, le long des plans de glissement actifs en tête de la fissure. La décohésion se fait généralement de façon alternée sur deux plans de glissement.

Pour le cuivre, le laiton-α 70Cu-30Zn et l'alliage d'Al 2024-T351, nous avons comparé les fractographies obtenues au seuil de propagation, soit dans l'air du laboratoire, soit dans le vide. Dans le cas du cuivre et du laiton-α, les résultats obtenus montrent une différence frappante entre la morphologie microfractographique produite sous vide et celle obtenue à l'air. Pour le cuivre, en particulier, plusieurs détails fractographiques produits sous vide, incluent des grands cupules, ressemblent à ceux produits par une rupture ductile. Ces observations indiquent clairement que, pour ces deux matériaux, la fissuration en fatigue sous vide provoque moins de glissement localisé, conduisant ainsi à moins de fissuration cristallographique. Par contre, la fissuration très cristallographique obtenue au seuil

dans l'air et qui inclut de larges facettes {111} à des valeurs de da/dN suffisamment faibles (~ 10^{-7} mm/cycle) est attribuable à un effet de l'environnement par lequel est intensifiée la localisation de la déformation plastique en fond de fissure. Cet effet permet un glissement plus planaire et provoque donc des grandes facettes de décohésion qui suivent des plans de glissement favorablement orientés. Cette différence dans les faciès fractographiques produits à l'air et sous vide est aussi cohérente avec les résultats obtenus par d'autres chercheurs qui ont étudié les structures de dislocations localisées près de la surface de rupture et à des faibles valeurs de da/dN. Ces auteurs ont montré le rôle important de l'environnement dans la variation des caractéristiques de la déformation plastique en tête de fissure, ce qui modifie aussi les aspects microfractographiques.

De très faibles vitesses de propagation favorisent la formation de facettes {111}. L'observation fréquente de ce type de facette dans l'alliage Al 2024-T351 testé sous vide suggère que la présence de ces facettes {111} est principalement attribuable à la vitesse de propagation extrêmement faible, pour laquelle correspond une forte tendance à obtenir du glissement localisé sur un seul plan en fond de fissure. Pour cet alliage, la possibilité d'effets d'adsorption ne peut pas être entièrement rejettée même dans les essais sous vide.

Nous avons observé une fissuration intergranulaire pour une gamme de

valeurs relativement faibles de da/dN dans le cuivre et le 70Cu-30Zn testés dans l'air, alors que cette fissuration intergranulaire était absente dans les essais sous vide. Ce comportement indique que, pour ces deux métaux, la fissuration intergranulaire est clairement un effet de l'environnement qui implique probablement de l'hydrogène, produit sur les surfaces fraîches de rupture par dissociation de l'eau et transporté aux joints de grain par les dislocations mobiles. Ce mécanisme conduit soit à une fragilisation des joints de grain facilitant une fissuration purement intergranulaire, soit à une plasticité localisée au voisinage des joints des grains favorisant la production de facettes quasi-intergranulaires. Cependant, dans le vide, la concentration résiduelle en vapeur d'eau est trop faible pour que ce mécanisme ait lieu dans ces deux métaux. Une autre interprétation possible de cette rupture intergranulaire suggèrerait que le glissement plus diffus produit lors des essais sous vide cause moins d'incompatibilité de déformation et de concentration locale de contrainte aux joints de grain.

L'étude fractographique détaillée de la fissuration en corrosion sous contrainte transgranulaire (CSCT) d'éprouvettes d'acier inoxydable 316 recuit et testé dans une solution de $MgCl_2$ portée à l'ébullition (154°C) indique que la fissuration survient, de façon prédominante, sur des plans ayant une orientation moyenne {100} et dans une direction de propagation <110>, alors que, dans le laiton-α testé dans une solution d'ammoniaque, la fissuration a lieu selon des plans

ayant une orientation moyenne {100}, et dans des directions de propagation <100> ou <112>. Cependant, nous avons trouvé que les facettes primaires {100} ou {110} de la CSCT étaient souvent composées de deux séries alternées de microfacettes {111}. Ceci indique une similarité importante avec les facettes identifiées dans les surfaces de rupture près du seuil en fatigue pour les mêmes matériaux. Ces résultats montrent que la CSCT dans les deux métaux étudiés se produit par une fissuration due à une décohésion alternée le long des plans sur lequel le glissement a lieu. Nous avons observé que la complexité des aspects microfractographiques croît quand le facteur d'intensité de contrainte K augmente. Nous avons montré que cette variation était associée au plus grand nombre de plans de glissements impliqués dans la propagation de la fissure ainsi qu'à l'augmentation des longueurs de décohésion sur les plans individuels de glissement. A K élevé, la présence de microfacettes {111} devient l'aspect microfractographique prédominant. Ces variations montrent qu'une déformation plastique localisée en fond de fissure joue un rôle important dans la formation de la CSCT.

Pour l'acier inoxydable 316, l'observation, en MET, de répliques des surfaces de rupture obtenues par fissuration près du seuil en fatigue ou par CSCT indique que les micro-facettes {111}, présentes sur les facettes primaires, sont plus visibles en MET qu'en MEB. Ces observations sur répliques indiquent que, lors de l'observation en MEB, l'absence apparente de microfacettes, sur des facettes

primaires {100} relativement lisses, était due à la finesse des microfacettes {111}, qui n'étaient pas résolues en MEB. Cette variation des faciès cristallographiques quand K croît permet aussi d'expliquer, du moins en partie, les différences fréquemment rencontrées dans la description des faciès cristallographiques que font plusieurs auteurs, qui ne précisent toutefois pas à quelle valeur de K leur observations sont faites. D'autre part, sur les répliques des surfaces de rupture de l'inox 316 obtenues par CSCT, nous avons observé certains détails très fins qui pourraient correspondre à des microcupules. Cependant, nous avons aussi observé de tels détails sur des répliques au carbone du film d'acétate primaire. Ce résultat indique donc que ces détails fins sont des artéfacts de la méthode des répliques. Nous avons donc montré que les observations en MET des répliques secondaires en carbone permettent de résoudre des détails plus fins que ceux observés en MEB, bien que certains artéfacts soient observés sur ces répliques. L'interprétation des observations de répliques au MET nécessite donc un soin particulier.

L'étude des rubans de laiton-α 70Cu-30Zn, rompus après immersion dans une solution d'ammoniaque, a montré que, dans certaines régions, une fissuration cristallographique, s'est amorcée à partir de fentes ou de piqûres de corrosion et s'est propagée initialement sur des facettes {111} relativement grandes ($\approx$ 5 à 10 μm) et approximativement perpendiculaires à l'axe de traction.

Cette observation suggère que ces facettes sont probablement produites par un mécanisme de clivage. La fissuration cristallographique des rubans de laiton se poursuit ensuite en alternance sur deux ou plusieurs jeux de microfacettes {111} et la fin de la rupture, au travers de l'épaisseur de l'échantillon, se produit souvent par striction ductile. Ces observations indiquent que la plasticité augmente de façon continue quand la fissure progresse dans le matériau. Cette augmentation de plasticité a souvent comme conséquence une rupture finale ductile.

De ces observations, on peut déduire que le mécanisme de fissuration cristallographique du laiton-α en CSCT est partiellement en accord avec certains arguments proposés par les théories basées sur une plasticité locale activée par l'environnement, mais aussi que ce mécanisme possède certaines caractéristiques qui sont en accord avec les théories invoquant une fragilisation, par l'environnement, d'une petite région du matériau au voisinage du fond de fissure.

Nous n'avons observé aucune trace de fissuration cristallographique sur les rubans de laiton-α, préalablement immergés et qui ne présentaient pas de fentes ou piqûres de corrosion plus grandes que $\approx$ 0,1 μm. Ces observations indiquent qu'une dissolution est nécessaire pour initier la fissuration cristallographique le long des plans {111} dans le laiton-α. Cependant, le rôle possible de la dissolution dans la poursuite de cette propagation cristallographique semble être moins important

à cause des grandes vitesses de propagation, ce qui exclut un effet de dissolution chimique. Par ailleurs, le fait qu'il n'a pas été possible d'obtenir des ruptures cristallographiques dans des rubans de laiton-α superficiellement désallié et en l'absence de dissolution microscopique détectable nous pousse à douter de la validité du modèle de film superficiel ou de couche désalliée fragile qui initierait un clivage se poursuivant sur une certaine distance dans le substrat ductile. Ce résultat indique aussi que la dissolution est nécessaire dans l'initiation de la CSCT dans le laiton-α.

Pour l'acier inoxydable 316 et le laiton-α soumis à la corrosion sous contrainte ainsi que pour les rubans de laiton-α préimergés, le mécanisme de CSCT qui nous paraît le plus compatible avec l'ensemble de nos observations fractographiques est une fissuration impliquant au tout début une plasticité localisée en fond de fissure, suivie d'un clivage - ou une décohésion similaire à un clivage - le long des plans de glissement. Nous suggérons que la plasticité localisée et la décohésion par clivage sont probablement associées à une adsorption en fond de fissure. La très grande similitude dans les aspects fractographiques et cristallographiques obtenus dans la CSCT et dans la fissuration près du seuil en fatigue dans les métaux c.f.e. peut être attribuée au rôle important et similaire du glissement localisé présent dans ces deux modes de rupture, pour lesquels le fond de fissure demeure relativement aigu et très peu émoussé. Le rôle de

l'environnement est particulièrement important dans la CSCT mais les observations comparant la microfractographie de la fatigue près du seuil dans le cuivre et dans le laiton-α, soit dans l'air, soit dans le vide, suggèrent un rôle similaire de l'environnement, les essais à l'air permettant un effet d'adsorption.

Tout mécanisme de rupture proposé doit être donc totalement compatible avec les aspects détaillés de la fractographie. Cependant, aucune des théories de la CSCT proposées jusqu'à maintenant n'est entièrement en accord avec les résultats actuels, car aucune de ces théories (à l'exception d'une étude très récente de Magnin et Lépinoux) ne prévoît un chemin de fissuration qui suit microscopiquement les plans de glissement. Il est donc proposé que les mécanismes de CSCT dans les aciers inoxydables austenitiques et dans le laiton-α impliquent une plasticité localisée suivie d'un clivage (ou d'une décohésion semblable au clivage) le long des plans sur lesquels un glissement localisé est survenu. Nous suggérons que ce glissement localisé et que la décohésion semblable au clivage sont associés à des effets d'adsorption en fond de fissure. La fissuration cristallographique près du seuil en fatigue implique aussi du glissement localisé et probablement du clivage ou une décohésion similaire au clivage sur les plans de glissement. En s'appuyant sur la comparaison de la fractographie obtenue par fatigue près du seuil dans l'air et dans le vide pour le cuivre et le laiton-α, nous proposons que l'adsorption joue aussi un rôle dans le mécanisme de fissuration près

du seuil en fatigue.

Dans les bronzes à 8-10% de Mn-Al-Ni et à des valeurs relativement élevées de ΔK, nous avons observé des stries de fatigue moins cristallographiques et un franchissement plus aisé des joints de grain et des interfaces lorsque les essais de fatigue sont réalisés dans une solution à 3.5% NaCl et à 1 Hz, en comparaison aux faciès cristallographiques obtenus au cours d'une fissuration à l'air.

Ces résultats sont en accord avec une plasticité en fond de fissure plus intense sous environnement corrosif. Le fait que ceci se produise à des valeurs élevées de da/dN suggère un effet d'adsorption. Dans le cas d'un fond de fissure relativement émoussée, l'effet de l'environnement dans l'intensification de la plasticité en fond de fissure provoque une plasticité plus généralisée. Cependant, les effets de fatigue-corrosion à des faibles valeurs de da/dN dans les bronzes 8-10% Mn sont associés à une fissuration le long des interfaces α-β où des observations révèlent une dissolution préférentielle de la phase β. Aucun effet de fatigue-corrosion n'était cependant remarqué à des fréquences de 20 Hz, résultat qui est cohérent avec l'influence de la fréquence de cyclage sur la propagation en fatigue-corrosion, puisqu'il existe une fréquence critique en dessous de laquelle les effets de corrosion commencent à se manifester.

Nous avons trouvé que l'augmentation remarquable de la résistance à la propagation de la fissure en fatigue, qui manifestent les alliages 12-14% Mn ayant subi un traitement thermique approprié (HT2) en comparaison aux alliages 8-10% Mn, semble être du à un effet de la fraction volumique et de la distribution de la phase β dans leur microstructure, ce qui conduit à une fraction plus importante de la propagation de la fissure en fatigue dans cette phase β plus dure. De plus, la forte tendance à la fissuration cristallographique dans la phase β et la grande taille de grain de cette phase β conduisent à une surface microscopiquement très tourmentée, avec pour conséquence d'importants effets de fermeture induite par la rugosité ainsi que des effets importants de déviation de fissure. Dans les deux cas, ces effets entraînent des valeurs de ΔK_{eff} (amplitude efficace du facteur d'intensité de contrainte en fond de fissure) significativement plus faibles que les valeurs nominales de ΔK.

Pour les essais dans la solution de NaCl, les surfaces de rupture des alliages à plus haute teneur en Mn et à l'état HT2 étaient moins rugueuses mais cependant recouvertes de quantités importantes de produits de corrosion, produisant des effets marqués de fermeture.

Il semble aussi que la microstructure complexe obtenue après traitement thermique HT2 et pour laquelle la fissure semble passer avec difficulté de la phase

β à la phase α primaire ou secondaire, contribue considérablement à l'augmentation de la résistance à la propagation de la fissure. Cet effet serait dû aux nombreux obstacles présents dans la microstructure complexe dans l'alliage HT2 et qui dévient ou arrêtent la fissure, particulièrement dans les essais dans l'air. Cependant, à des faibles vitesses de propagation dans une solution de NaCl, les effets de dissolution, se produisant à proximité de l'interface α-β et des interfaces des précipités ainsi que la tendance à favoriser une plasticité accrue sur des surfaces en contact avec un environnement agressif, suggèrent que des effets semblables peuvent être à l'origine d'une initiation de fissure plus facile en fatigue-corrosion.

ABSTRACT

After a literature review of the micromechanisms and fractography of fatigue cracking and of environment-assisted cracking, a detailed microfractographic study was carried out of near-threshold fatigue cracking in f.c.c. 316 stainless steel, 70Cu-30Zn α-brass, copper and 2024-T351 Al alloy and in b.c.c. mild steel and Fe-3% Si, of transgranular stress-corrosion cracking in f.c.c. 316 stainless steel and 70Cu-30Zn, as well as of corrosion-fatigue cracking of Mn-Al-Ni bronzes, which are primarily dual phase alloys. Particular attention was paid in these studies to the determination of the cracking crystallography, and to the examination of factors which affect the fractographic features and which can provide information on the cracking mechanisms.

For near-threshold fatigue cracking, the primary facets were identified to have {100}, {110} and {111} orientations. The microscopic crack path however was generally demonstrated to follow slip planes for the f.c.c. and b.c.c. metals studied. The detailed microfractography was determined by the number and orientations of slip planes involved and the relative amounts of cracking on each. The {100} <110> cracking crystallography was found to occur predominantly for 316 austenitic stainless steel, 70Cu-30Zn α-brass, copper and the f.c.c. phase of 8-10% Mn-Al-Ni bronzes tested in air. A relatively larger number of {110} primary

facets with a <100> or near-<100> cracking direction, however, were observed for copper, α-brass and the f.c.c. phase of the bronzes. For both the b.c.c. Fe-3% Si and the AISI 1008 steel tested in air, the different orientations of cracking facets were most often identified to correspond to {100} and {110}. It was generally noticed that these {100} or {110} primary facets on a more microscopic scale presented two alternating sets of microfacets following slip planes. For the f.c.c. as well as for the b.c.c. metals studied, the presence of alternating sets of microfacets frequently resulted in primary facets with a {100} or {110} orientation and with a striated or wavy microfractographic aspect. The absence of any cleavage aspects on these primary facets observed for both the b.c.c. metals strongly indicates that the near-threshold fatigue cracking is at least primarily produced by slip.

Comparison of the fractography of near-threshold fatigue cracking produced in laboratory air and in vacuum was carried out for copper, 70Cu-30Zn α-brass and 2024-T351 Al alloy. The results obtained clearly showed the occurrence of highly crystallographic facets, including the relatively large {111} facets observed at sufficiently low da/dN values for the copper and the α-brass tested in air but not for the tests in vacuum. These observations suggested that the crystallographic cracking was associated with environment-enhanced localized plasticity in the crack tip region which gave rise to slip plane decohesion. Extremely low cracking rates were found to favour larger {111} facets. Their frequent observation for 2024-T351

Al alloy tested in vacuum suggested that their occurrence was mainly attributed to the effect of the ultra-low crack propagation rates at which there is a strong tendency to get planar slip in this alloy for which adsorption may not be completely ruled out even for the tests in vacuum. The intergranular cracking was found to occur for a range of relatively low da/dN values for copper and 70Cu-30Zn tested in air but disappeared in the tests in vacuum, which indicates that for both metals this intergranular cracking is an environmental effect. The different observations for this intergranular cracking are compatible with a hydrogen-assisted cracking mechanism.

The detailed fractographic studies of transgranular stress-corrosion cracking (TSCC) on bulk specimens of annealed 316 stainless steel (s.s.) tested in boiling (154°C) $MgCl_2$ solution and of 70Cu-30Zn α-brass tested in ammoniacal solutions performed indicated that cracking occurred predominantly on {100} planes with <110> crack propagation directions for 316 s.s., and on {110} planes with <100> or <112> propagation directions for the α-brass. However, it was clearly found that the {100} or {110} primary cracking facets of TSCC were also often made up of two sets of alternating {111} microfacets, which showed considerable similarity to those identified on the near-threshold fatigue fracture surfaces in the same materials. These results indicate that TSCC in both metals studied is consistent with this cracking being produced by decohesion on planes on which slip has

occurred and often on alternating slip planes. The degree of complexity of the fractographic features was observed to increase strongly with increasing K. This variation was shown to result from an increasing number of sets of slip planes involved in the crack propagation as well as increasing decohesion lengths on the individual slip planes with increasing K. These observations demonstrate that plastic deformation should play an important role during TSCC crack propagation.

The fractographic study was also performed on 70Cu-30Zn α-brass ribbon specimens fractured after immersion in ammoniacal solutions in order to further verify the applicability of the different TSCC models proposed. The observations in this study showed that initiation occurred on relatively large {111} facets approximately perpendicular to the tensile axis, which suggests that these facets were probably produced by a cleavage mechanism. This suggests that their formation and therefore the TSCC mechanism for α-brass may incorporate aspects of the theories based on the environment enhancing localized plasticity and those on the environment embrittling a small zone of material in the vicinity of the crack tip. Then, the continuation of cracking in the brass ribbon specimens was observed to alternate between two or more sets of {111} microfacets with the final portion of the fracture across the specimen thickness often occurring by ductile necking. These observations indicate that the plasticity increased continuously as the crack propagated in the ductile material, with this increased plasticity often resulting in

the final fracture being ductile. No trace of crystallographic cracking was obtained on pre-immersed ribbon specimens of α-brass in the absence of crystallographic corrosion slots or etch pits larger than ≈ 0.1 μm. This indicates that dissolution was necessary for the initiation of such crystallographic cracking along slip planes in α-brass. However, the possible role of dissolution in promoting crystallographic crack propagation was suggested to be less important, owing to the crack growth rates for the ribbon specimens being generally sufficiently rapid to preclude a chemical dissolution reaction. On the other hand, the lack of success in obtaining crystallographic fractures on superficially de-alloyed 70Cu-30Zn α-brass ribbons in the absence of microscopically visible dissolution raises serious questions concerning the applicability of a surface film or de-alloyed layer in initiating cleavage which then continues in the ductile substrate. This result also indicates that dissolution is required to at least initiate TSCC in α-brass.

The mechanism of TSCC which appears to be most compatible with the microfractographic observations on the stress corroded bulk specimens of 316 s.s. and of α-brass as well as on the brass ribbon specimens studied is that the fractography of TSCC in both metals simultaneously involves localized crack tip plasticity, followed by cleavage or cleavage-like decohesion on slip planes, with both the localized plasticity and the cleavage-like decohesion being associated with crack tip adsorption effects. The very strong similarity in the fractographic and

crystallographic aspects obtained for TSCC and for near-threshold fatigue cracking in f.c.c. metals can be attributed to the similar important role of localized slip involved in both fracture processes for which the crack tips remain relatively sharp. The role of the environment is particularly important in TSCC, but the observations on near-threshold fatigue cracking of copper and 70Cu-30Zn in air also suggest a similar role of the environment compatible with an adsorption effect.

For given ΔK values, less crystallographic striations and easier propagation across grain boundaries and interfaces were observed at high da/dN values for the 8-10% Mn-Al-Ni bronzes tested in 3.5% NaCl solution, compared to those tested in air. These results are also consistent with an environment-enhanced crack tip plasticity effect. In this case of a more blunted crack tip, the environment effect, which is again suggested to be an adsorption effect, resulted in more generalized plasticity.

Any proposed fracture mechanism must be fully compatible with the detailed aspects of the fracture surface. It is therefore proposed that the mechanism of TSCC in austenitic stainless steels and in 70Cu-30Zn α-brass involves localized plasticity, as well as cleavage or cleavage-like decohesion on the planes on which localized slip has occurred, with both the localized slip and the cleavage-like decohesion being associated with crack tip adsorption effects. Crystallographic near-

threshold fatigue cracking also involves localized slip and probably "cleavage" or cleavage-like decohesion on slip planes. Based on the comparison of the fractography for near-threshold fatigue tests in air and in vacuum on copper and 70Cu-30Zn, it is proposed that adsorption is also at times involved in the near-threshold fatigue cracking mechanism.

ACKNOWLEDGEMENTS

This work could not be completed without recognizing the contributions of many people whose names do not appear on the title page.

First of all, I am in particular indebted to professors J. Ivan Dickson and Jean-Paul Baïlon for the frequent discussions as well as for their esthusiasm, generosity, keen interest, excellent advice and constant encouragement throughout the research program and the thesis writing process.

As well, I am grateful for Dr. D. Tromans for his helpful suggestions. I express my sincere gratitude to the Drs. J. Petit and N. Ranaganathan of École Nationale Supérieure de Mécanique et d'Aérotechnique, Poitiers, France, who supplied some of fracture surfaces of the 2024-T351 Al alloy tested in air and in vacuum and who performed the tests in vacuum on both Cu and 70Cu-30Zn α-brass. I also gratefully acknowledge the Department of Metallurgy of McGill University for supplying the Fe-3% Si plate.

I express my sincere gratitude to professors Dominique Piron, Gilles L'Espérance and Normand Marchand for their advice and encouragement. Helpful discussions with professor Yves Verreman are also acknowledged.

The contribution of Dr. Louis Handfield to the fatigue and corrosion-fatigue testing portion of this study is gratefully acknowledged. I am also sincerely grateful for his advice and assistance in carrying out fatigue tests and in analyzing fatigue data.

I gratefully acknowledge all the technicians and secretaries of the Département de métallurgie et de génie des matériaux for their assistance and encouragement. In particular, I thank Mme Céline Labelle for her help in preparing a number of posters which have received awards in the International Metallography Exhibitions, Mr. Gérard Guérin for preparing excellent TEM replicas, Mr. Jean-Philippe Bouchard for his help in performing heat treatments, Mr. André Desilets for his help in setting up the experiments on the brass ribbon specimens, as well as with Mr. Lucien Gosselin, in setting up experiments on liquid metal embrittlement, which because of space and time limitations, are not described in this thesis.

A very large number of micrographs were taken in the course of the different phases of this work, I express my sincere thanks to Miss Josée Laviolette, Mr. André Riel and Mr. Jean Claudinon for the quality of the photographs and slides which they prepared.

The $(CM)^2$ laboratory has been my frequent work site, where all of the staff and technicians gave me very important help concerning electron microscopy techniques. Their contribution to this study is also acknowledged. In particular, I wish to express my sincere gratitude to Mario Caron, Rafik Allem, René Veillette, Jean Claudinon, Gérard Guérin, Sophie Boisvert as well as Jacques Desrochers, for his help in preparing a number of drawings which have been published.

I also wish to express my sincere gratitude to Serge Lalonde, Gianluigi Botton, Jacques Boutin, Daniel Larouche, Jean-Gabriel Legoux, José Hallen-Lopez, Sylvain St-Laurent, Salvator Nigarura, Pierre Leblanc, Claude Armand, Driss Berechid, Marc Sider, Hui-Jun Miao, Jin Xia, Changzun Zhou, Bin Hong, Beigang Nie, Weimin Zhong, Wenyue Zheng, and Zhaoxiong Tong as well as all of my colleagues in the department for their assistance in carrying out different portions of their work as well as for useful discussions.

Last but not least, I wish to thank Danièle Dagenais and Julie Chamberlain for the very professional typing of this thesis.

TABLE OF CONTENTS

PAGE

DEDICATION iv

SOMMAIRE v

ABSTRACT xxii

ACKNOWLEDGEMENTS xxix

TABLE OF CONTENTS xxxii

LIST OF FIGURES xlvii

LIST OF TABLES lxx

INTRODUCTION 1

CHAPTER 1 - LITTERATURE SURVEY 3

1.1 Micromechanisms and Fractography of Fatigue Cracking 3

1.1.1 Fatigue Crack Initiation 4

1.1.2 Fatigue Crack Growth Curve (FCG) 8

1.1.3 The Infuence of Mean Stress on Fatigue Propagation . 10

1.1.3.1 High Growth Rate Regime 10

1.1.3.2 At Near-Threshold Regime 12

1.1.4 The Influence of Gaseous Environment on Fatigue Cracking 13

1.1.4.1 The Effects of Gaseous Environments on Fatigue Crack Initiation 14

1.1.4.2 Role of Gaseous Environment on Fatigue Crack Growth 17

1.1.5 Crack Closure Mechanisms 19

1.1.5.1 Plasticity-Induced Crack Closure 20

1.1.5.2 Oxide-Induced Crack Closure 21

1.1.5.3 Roughness-Induced Crack Closure 21

1.1.6 The Influence of Temperature 22

1.1.7 The Influence of the Microstructure on Fatigue Crack Propagation 24

1.1.7.1 The Effect of Atomic Bond Strength and Modulus of Elasticity 24

1.1.7.2 The Effect of Stacking Fault Energy 25

1.1.7.3 The Effect of Grain Size on Fatigue Threshold and Low Propagation Rates 26

1.1.7.4 The Effect of Precipitates 29

1.1.7.5 Microstructural Effects in Two Phase Alloys . 30

1.1.7.6 The Effect of Inclusions 31

1.1.7.7 The Effect of Strength Level 32

1.1.8 Fatigue Striations 34

1.1.8.1 Non-Crystallographic Fatigue Striations 36

1.1.8.2 Crystallographic Fatigue Striations 38

1.1.9 Crystallographic Orientation of Fatigue Striations and of the Crack Propagation Plane 41

1.1.9.1 In f.c.c Metals 41

1.1.9.2 In b.c.c Metals 43

1.1.9.3 In h.c.p. Metals 45

1.1.10 Fatigue Striation Spacing 48

1.1.11 "Tire tracks" 50

1.1.12 Cyclic Cleavage Striations 50

1.1.13 General Fractographic Features of Transgranular Facets Near the Threshold 52

1.1.14 Crystallographic Fracture Facets Identified at Low Crack Growth Rates 52

1.1.15 Mechanisms Proposed for Explaining Crystallographically Faceted Fatigue Propagation at Low Crack Growth Rates 59

1.1.15.1 Discontinuous Cleavage Model 59

1.1.15.2 Glide Plane Decohesion Model 60

1.1.15.3 Alternating Slip Models 61

1.1.15.4 Fine Scale Decohesion Along Slip Planes . . . 62

1.1.16 Intergranular Cracking at Low Propagation Rates . . . 62

1.2 Fractography and Mechanisms of Environment-Assisted Cracking 66

1.2.1 Fractography and Mechanisms of Stress-Corrosion Cracking 67

1.2.1.1 Crack Growth Response in SCC and HE Cracking 68

1.2.1.2 Macroscopic Aspects of Environmentally Assisted Cracking 69

1.2.1.3 Microfractography of SCC 71

1.2.1.3.1 Intergranular Stress-Corrosion Cracking (ISCC) Aspects 72

1.2.1.3.2 Transgranular Stress-Corrosion Cracking (TSCC) Aspects 73

1.2.1.4 Crystallography of TSCC 74

1.2.1.4.1 Crystallography in b.c.c. Metals . . . 75

1.2.1.4.2 Crystallography in h.c.p. Metals . . . 75

1.2.1.4.3 Crystallography in f.c.c. Metals . . . 77

1.2.1.5 Mechanisms of Intergranular Stress-Corrosion Cracking (ISCC) 81

1.2.1.6 Mechanisms of Transgranular Stress-Corrosion Cracking (TSCC) 82

1.2.1.6.1 Film Rupture Model (Slip-Dissolution) 82

1.2.1.6.2 Film-Induced Cleavage 86

1.2.1.6.3 Dissolution-Induced Lowering of K_{IC} for Cleavage 88

1.2.1.6.4 Dissolution-Enhanced Dislocation Mobility Leading to Pile-Ups at Lomer-Cottrell Barries for Microcleavage 90

1.2.1.6.5 Dissolution-Enhanced Atomic Mobility (Surface Diffusion) 93

1.2.1.6.6 Models Based on Adsorption 94

1.2.1.6.7 Hydrogen Contribution to SCC . . . 97

1.2.2 The Mechanisms and Fractography of Hydrogen-Assisted Cracking 99

1.2.2.1 Internal Pressure Theory 100

1.2.2.2 Hydrogen Transport by Dislocations 101

1.2.2.3 Decrease of Surface Energy 101

1.2.2.4 Hydride Formation Mechanism 102

1.2.2.5 The Decohesion Model 104

1.2.2.6 Hydrogen Enhanced Local Plasticity (HELP) Mechanism 107

1.2.2.7 Fractographic Features of HAC 113

1.2.3 Fractography and Mechanisms of Crack Growth in Liquid Metal Environments 121

1.2.3.1 Cracking Characteristics of LME 121

1.2.3.2 Fractography of LME 123

1.2.3.3 Mechanisms Proposed for LME 124

1.2.4 Fractography and Mechanism of Corrosion-Fatigue Cracking 128

1.2.4.1 Aqueous Environmental Effects on Fatigue Crack Initiation 128

1.2.4.1.1 Strain Enhanced Dissolution of Slip Steps for Crack Initiation 129

1.2.4.1.2 Surface Film Rupture and Electrochemical Attack at the Rupture Sites 131

1.2.4.1.3 Formation of Corrosion Pits and Stress Concentration at the Base of the Pit 132

1.2.4.1.4 Surface Adsorption of a Specific Species from the Environment for Crack Initiation 133

1.2.4.2 Aqueous Environmental Effects on Fatigue Crack Propagation 134

1.2.4.3 Effects of Corrosion-Fatigue on the Fatigue Propagation Curve 136

1.2.4.4 The Major Variables Affecting Corrosion-Fatigue Crack Propagation Response of a Material Subjected to an

Aggressive Environment 138
1.2.4.4.1 The Effect of Testing Frequency . . 138
1.2.4.4.2 The Effect of Load Profile 138
1.2.4.4.3 The Effect of Load Ratio R 139
1.2.4.4.4 The Effect of Test Temperature . . 140
1.2.4.5 Corrosion Fatigue Superposition Model 140
1.2.4.6 Fractographic Aspects of Corrosion Fatigue . . 142
1.2.4.6.1 Brittle Striations 143
1.2.4.6.2 Some of Fractographic Features of Corrosion-Fatigue in Multiphase Alloys 147
1.2.4.6.3 Intergranular Corrosion-Fatigue Cracking 151

CHAPTER 2 - BASIC TECHNIQUES FOR STUDYING THE FRACTOGRAPHY AND CRYSTALLOGRAPHY OF CRACKING 166

2.1 Macrofractographic Observations 166

2.2 Metallographic Observations Related to Fractography 167

2.2.1 Introduction 167

2.2.2 Metallographic Sectioning Techniques and Observation Procedures 169

2.3 Microfractographic Observations 172

2.3.1 General Observation with SEM 172

2.3.2 Observation of Stereofractographs 173

2.3.3 Observation of Fractographs on Matching Microregions 174

2.3.4 Replication TEM 176

2.3.4.1 Details of Replica Preparation 177

2.3.4.2 Operation of the TEM 179

2.4 Techniques for Determination of the Crystallography of Fracture Facets 181

2.4.1 Introduction 181

2.4.2 Etchpit Technique 182

2.4.3 Measuring Angles Between Fractographic Details 185

2.4.4 Selected Area Channelling Patterns 187

2.4.5 SEM Photogrammetric Technique 188

CHAPTER 3 - THE FRACTOGRAPHY OF NEAR-THRESHOLD FATIGUE CRACKING IN F.C.C. AND B.C.C. METALS 190

3.1 Introduction 190

3.2 Summary of Materials and Experimental Procedures 192

3.2.1 Materials 192

3.2.2 Fatigue Tests 194

3.2.3 Etch Pitting Procedures 195

3.2.3.1 Etching AISI 316 Stainless Steel 196

3.2.3.2 Etching Copper 196

3.2.3.3 Etching 70 Cu-30 Zn α-brass 197

3.2.3.4 Etching 2024-T 351Al Alloy 197

3.2.3.5 Etching Bronzes 197

3.2.3.6 Etching Fe-3% Si 198

3.2.3.7 Etching Mild Steel 198

3.3 Observations and Discussion of the Microfractography of Fatigue Cracking Near-Threshold for FCC Metals 199

3.3.1 316 Stainless Steel 199

3.3.2 70 Cu - 30 Zn (α-brass) 202

3.3.3 α-phase in 8-14%Mn-8%Al-2%Ni Bronzes 205

3.3.4 Copper 207

3.3.5 2024-T 351 Al Alloy 210

3.3.6 Microfractography of Fatigue Cracking in Vacuum for Copper and α-brass at Threshold 213

3.3.7 Summary of the Crystallography Identified and the Cracking Mechanisms for f.c.c. Metals Near the Threshold 216

3.3.8 Fractography of Intergranular Cracking Near the Threshold 222

3.4 The Microfractography in b.c.c. Metals 226

3.4.1 The Objective of This Study 226

3.4.2 Observations and Results 227

3.4.2.1 Observations on Fe-3% Si 227

3.4.2.2 Observations on Mild Steel 230

3.4.2.3 Observations for the b.c.c. β-phase of Mn-Al-Ni bronzes 232

3.4.3 Discussion 233

CHAPTER 4 - FRACTOGRAPHY OF STRESS CORROSION CRACKING OF ANNEALED 316 STAINLESS STEEL 257

4.1 Introduction 257

4.2 Experimental Procedure 259

4.2.1 Material 260

4.2.2 Specimen Geometry and Stress Corrosion Testing 261

4.2.3 SEM Fractographic Study 262

4.3 Aspects of Fractography and Crystallography 262

4.3.1 Terminology 262

4.3.2 The Influence of the Stress Intensity Factor on the Fractography 263

4.3.2.1 Microfractography at Low K Region 264

4.3.2.2 Microfractography Associated with Intermediate K 265

4.3.2.2.1 Occurrence of Sheet-Like Microfacets 265

4.3.2.2.2 Fan-Shaped Facets 266

4.3.2.3 Microfractography at High K Region 268

4.3.2.3.1 Feather-Like and Sheet-Like Micro-

fractographic Features 268

4.3.2.3.2 Herring-Bone Patterns of River Lines 270

4.3.2.4 Observations Near the Lateral Edges of the Specimen 272

4.3.3 Observations on Opposite Fracture Surfaces 272

4.3.4 Stereographic Observations at Low and Intermediate Magnifications 273

4.3.5 TEM Observations of Secondary-Carbon Replicas of Fracture Surfaces 275

4.4 Discussion 277

4.4.1 Summary of Microfractographic Observations and Results 277

4.4.2 Discussion of the Fractographic Features 279

4.4.2.1 The Microscopic Crack Path 279

4.4.2.2 Complete or Incomplete Linkage Processes of River Lines During TSCC 282

CHAPTER 5 - FRACTOGRAPHY AND CRYSTALLOGRAPHY OF STRESS CORROSION CRACKING OF 70Cu-30Zn α-BRASS IN AMMONIACAL SOLUTIONS 296

5.1 DCB Specimen Experiments 296

5.1.1 Introduction 296

5.1.2 Experimental Methods 297

5.1.2.1 Material 297

5.1.2.2 Specimen Geometry 298

5.1.2.3 Preparation of the Specimens 299

5.1.2.4 Composition of the Testing Solutions 300

5.1.2.5 Experimental Procedures 301

5.1.3 Results and Discussion 302

5.1.3.1 The Plot of log V vs. K 302

5.1.3.2 Intergranular and Transgranular Cracking 303

5.1.3.3 Fractography of ISCC of α-Brass 305

5.1.3.4 Fractography of TSCC of α-Brass 306

5.1.3.5 Crystallography at High K (K ~ 20 MPa $m^{1/2}$) . 308

5.1.3.6 Crystallography At Low K (≈ 15-10 MPa $m^{1/2}$) 311

5.1.3.6.1 {110} <100> and {110} <112> cracking crytallography 311

5.1.3.6.2 Nature of the Wavy Aspect on the Primary {110} Facets 312

5.1.3.6.3 Matching of {111} microfacets and striations 314

5.1.3.7 Comparison of the Relative Ease of Cracking for the Different Crystallography Identified of TSCC Facets 315

5.2 Superficially Dealloyed Cu-30Zn Ribbon Experiments 320

5.2.1 Experimental Ojbectives 320

5.2.2 Experiments 323

5.2.2.1 Material Condition 323

5.2.2.2 Preparation of the Specimens 324

5.2.2.3 Composition of the Test Solution 325

5.2.2.4 Test Procedure 325

5.2.3 Observations and Discussion 332

5.2.3.1 Results of the First Series of Tests 332

5.2.3.1.1 General Observations of Fractographic Aspects 332

5.2.3.1.2 Crystallography Near the Initial Cracking Site 334

5.2.3.1.3 Crystallography of Subsequent Crack Propagation 336

5.2.3.1.4 Occurrence of the Etch Pits 338

5.2.3.2 Results of the Second Series of Tests 340

5.2.3.3 Intergranular Fracture on Ribbon Specimens . . 342

5.2.3.4 Summary of the Results 343

CHAPTER 6 - FRACTOGRAPHY OF CORROSION - FATIGUE CRACK PROPAGATION OF 8-14%Mn-8%Al-2%Ni BRONZES 359

6.1 Introduction 359

6.2 Experimental Procedures 360

6.3 Results and Discussion 362

6.3.1 Fatigue Propagation 362

6.3.2 Macrofractography 366

6.3.3 Microfractography 367

6.3.3.1 Intergranular Cracking 368

6.3.3.2 Influence of the Environment on Striations . . . 370

6.3.3.3 Microfractography of the As-Received (AR) Propeller Specimens 372

6.3.3.4 Microfractography of the HT2 Propeller Specimens 374

6.3.3.5 Microfractographic Evidence Related to the Influence of Precipitates 377

6.4 Conclusions 380

CHAPTER 7 - GENERAL DISCUSSION 396

7.1 Microfractographic Similarities Between TSCC and Near-Threshold Fatigue Cracking 396

7.2 Mechanisms of Transgranular Near-Threshold Fatigue Cracking 400

7.3 The TSCC Mechanisms Indicated by the Fractographic Observations 404

CONCLUSION 414

RECOMMENDATIONS 423

REFERENCES 425

LIST OF FIGURES

PAGE

Fig. 1.1: Schematic variation of fatigue crack growth rate as function of stress intensity range (7). 153

Fig. 1.2: Crack surface interference results in crack opening K_{op} to be above zero, ΔK_{eff} defined as K_{max}-K_{op}. 153

Fig. 1.3: Variation with the R ratio of the f(R) function in equation [1-3] (14). 153

Fig. 1.4: Schematic illustration of mechanisms of fatigue crack closure (40). 154

Fig. 1.5: Schematic of the plastic blunting process of fatigue crack propagation during a loading cycle (79). 154

Fig. 1.6: Model of Tomkins and Biggs (80). 154

Fig. 1.7: Schematic of order of the localized slip which produces crystallographic striations (307). 155

Fig. 1.8: Model of Pelloux (81). 155

Fig. 1.9: Schematic of the alternate slip plane model showing the slip processes during a loading cycle (82). 155

Fig. 1.10: Model of Bowles and Broek (83). 156

Fig. 1.11: Models of Beevers and Ward-Close (97, 102). 157

Fig. 1.12: Schematic diagram of typical three stages curve of crack propagation rate, log da/dt vs. crack tip stress intensity, K, in SCC and HE cracking. 157

Fig. 1.13: Schematic diagram summarizing the model of SCC and corrosion-fatigue cracking proposed by Jones (199). 158

Fig. 1.14: Schematic diagram illustrating a film-induced cleavage model proposed for TSCC in copper and α-brass by Newman et al. (202). . . 158

Fig. 1.15: Schematic drawing of a dog-leg crack, formed by corrosion along a slip plane, approaching a Lomer-Cottrell lock (model of Lichter et al. (175)). 159

Fig. 1.16: Schematic of the dislocation behavior at the crack tip and of the crack growth when dislocations of type B are activated and induce crack blunting (from 194). 159

Fig. 1.17: Schematic of the effect of the localized anodic dissolution on the plasticity at the crack tip. (a) Dislocation in a slip band and formation of a step just at the crack tip. (b) formation of dislocation pile-ups (from 194). 159

Fig. 1.18: Crystal geometry of the slip planes, the Cottrell-Lomer dislocation barrier and their relation to the cracking plane (163). 160

Fig. 1.19: Generalized model for crack initiation and propagation in SCC (the details here are for austenitic stainless steel in a chloride environment) (264). 160

Fig. 1.20: Schematic illustrating a hydride-induced cleavage fracture processes. 161

Fig. 1.21: Schematic illustration of the adsorption-induced localized-slip process for environmentally assisted cracking (168). 161

Fig. 1.22: Diagram illustrating the formation of herringbone patterns on fracture surfaces of f.c.c. and b.c.c. materials (168). 161

Fig. 1.23: Summary of hydrogen processes: sources leading to hydrogen in solution, transport leading to accumulation at microstructural locations, and finally fracture. Dashed line refers to cleavage of hydrides. From Thompson and Bernstein (264). 162

Fig. 1.24a: Combined tearing and shearing during the formation of dimples, which results in short shear dimples at top and long shear dimples at the bottom. Material at B continues to be stretched after stretching has stopped at A (356). 163

Fig. 1.24b: The unit process of elastic-plastic fracturing which best fits the observations. Four stages of continuous cracking by a blending of Modes I and II are shown, (b) up, (c) across, (d) down, and (e) across. The process is restarted in (f) (356). 163

Fig. 1.25: Mechanism of surface film rupture for environmentally enhanced crack initiation. 163

Fig. 1.26: Schematic of correspondence between regions of a polarization curve and corrosion fatigue mechanisms. 164

Fig. 1.27: Illustration of the four types of corrosion fatigue crack propagation curves (152). 165

Fig. 1.28: Illustration of typical effect of testing frequency on corrosion-fatigue crack propagation (152). 164

Fig. 3.1: Microstructure of Fe-3% Si 236

Fig. 3.2: Microstructure of the mild steel 236

Fig. 3.3: Geometry of CT specimen 236

Fig. 3.4: log da/dN - log ΔK crack growth curve for the 316L stainless steel tested in air. 237

Fig. 3.5: log da/dN - log ΔK (and ΔK_{eff}) crack growth curve for 316L stainless steel tested in "dry argon". 237

Fig. 3.6: A typical log da/dN - log ΔK (and ΔK_{eff}) plot of Fe-3% Si tested in air. - da/dN - ΔK; Δ - da/dN - ΔK_{eff}. 237

Fig. 3.7: A typical log da/dN - log ΔK crack growth curve for the mild steel tested in air. 237

Fig. 3.8: (a) Schematic of typical etch pits produced in 316 s.s. (b) schematic of the correspondence between the orientations of fracture facets and the shapes of the etch pits. 238

Fig. 3.9: Schematic of the correspondence between the orientations of fracture facets and the shapes of the etch pits produced in the bronzes studied. 238

Fig. 3.10: Schematic of etch pits bounded by {100} and {110} planes in Fe-3% Si. 238

Fig. 3.11: Large {100} facets produced in near-threshold fatigue test in air on 316 s.s. 239

Fig. 3.12: Complex near-threshold facets for 316 s.s. tested in air. (a) stereographs pair (b) the matching aspect on the opposite fracture surface of the same region of (a). 239

Fig. 3.13: Serrated river lines, 316 s.s. tested in dry argon, da/dN ≈ 10^{-7} mm/cycle. 240

Fig. 3.14: Small tetrahedra-like facets occurred near grain boundaries for 316 s.s. tested in air. 240

Fig. 3.15: Fractographic details on the near-threshold {100} average facets observed on TEM replicas. 240

Fig. 3.16: Striated near-threshold facet. 70-30 α-brass tested in air. Arrows indicate small etch pits. 241

Fig. 3.17: Near-threshold facet for 70-30 α-brass tested in air, with two regions (A and B) of striations separated by a more complex region. 241

Fig. 3.18: Striated facets of {110} average orientation are made up of two sets of alternating {111} microfacets for α-brass near-threshold fatigue cracking in air. 241

Fig. 3.19: Large {100} and {111} facets, 70 Cu-30 Zn α-brass, tested in air, da/dN ≈ 10^{-7} mm/cycle. 241

Fig. 3.20: {100} <110> cracking crystallography observed for da/dN ≈ 10^{-6} mm/cycle in 8% Mn-8% Al-2% Ni (AC condition) bronze tested in air. 242

Fig. 3.21: Herringbone pattern of river lines observed at ~ 10^{-6} mm/cycle in 8% Mn-8% Al-2% Ni (AC condition) bronze tested in air. . . . 242

Fig. 3.22: Stair-like facets observed for ultra-low crack growth rates (da/dN ≈ 10^{-8} mm/cycle) in 8% Mn-8% Al-2% Ni bronze tested in air (HT_1 condition). 242

Fig. 3.23: Two relatively large {111} facets observed for ultra-low crack growth rates (da/dN ≈ 10^{-8} mm/cycle) in 8% Mn-8% Al-2% Ni bronze (HT_1 condition tested in air). 243

Fig. 3.24: Complex pattern of very fine facets present near the threshold for copper tested in air. (~10^{-7} mm/cycle). 243

Fig. 3.25: Sheet-like facets observed for copper at da/dN values of ~

10^{-7} mm/cycle. 243

Fig. 3.26: Sheet-like {111} facets observed for copper at da/dN values of ~ 10^{-7} mm/cycle. 244

Fig. 3.27: Striated near-threshold facets observed for copper tested in air. The arrows indicate etchpits produced on the small microfacets. 244

Fig. 3.28: Wavy primary facets made up of two sets of microfacets observed for copper tested near the threshold in air. 244

Fig. 3.29: Pyramid-shape facets observed near a grain boundary in copper tested near the fatigue threshold in air. 244

Fig. 3.30: Well-defined etchpits indicative of a {110} orientation observed on large and relatively flat intergranular-like facets for copper tested in air (~ 10^{-6} mm/cycle). 245

Fig. 3.31: Striated transgranular facets of average {110} orientation observed near the threshold for copper tested in air. 245

Fig. 3.32: Typical aspects of {100} sheet facets presented near-threshold for 2024-T351 Al alloy tested in air observed a) before and b) after etching. 245

Fig. 3.33: Primary {100} near-threshold facets, with secondary {111} facets corresponding to serrated river lines in 2024-T351 Al alloy tested in air. 246

Fig. 3.34: {111} facets seen in region A of this micrograph of a near-threshold

fracture surface of 2024-T351 Al alloy tested in air. 246

Fig. 3.35: Pyramid-like large {111} facets presented on an unetched fracture surface at ultra-low crack rates in the test in vacuum (a) aspects at low magnification; (b) details of facets A, showing rubbing appearance at region R; (c) details at region D of facet A. 247

Fig. 3.36: General fractographic aspects for copper tested in vacuum (da/dN ≈ 10^{-8} mm/cycle). 248

Fig. 3.37: General fractographic aspects for α-brass tested in vacuum (da/dN ≈ 10^{-8} mm/cycle). 248

Fig. 3.38: Dimpled aspect of the fracture surface of copper tested in vacuum at the threshold. 248

Fig. 3.39: Striation-like aspects observed for ~-brass tested in vacuum (da/dN ≈ 10^{-8} mm/cycle). 248

Fig. 3.40: Microfractographic aspects of copper tested in vacuum (da/dN ≈ 10^{-8} mm/cycle). 249

Fig. 3.41: Crystallographic facets observed for α-brass tested in vacuum (da/dN ≤ 10^{-8} mm/cycle). 249

Fig. 3.42: Model for cracking along {100} or {110} by decohesion along two alternating {111} slip planes. 249

Fig. 3.43: Transition in fracture surface morphology in copper, associated with change in atmosphere from vacuum to lab. air. 250

Fig. 3.44: Transition in fracture surface morphology in α-brass, associated with change in atmosphere from vacuum to lab air. 250

Fig. 3.45: Features resembling intrusions and extrusions observed on the intergranular facets for copper tested in air (da/dN ≈ 10^{-6} mm/cycle). 250

Fig. 3.46: Matching triangular pits and protrusions on opposite fracture surfaces of unetched intergranular facets for α-brass tested in air (da/dN ≈ 10^{-6} mm/cycle). 251

Fig. 3.47: Tetrahedra-like small facets present on the intergranular facets for 316 stainless steel tested in air at low da/dN values (~ 10^{-6} mm/cycle). Very fine river lines can also be clearly seen on the intergranular facets. 251

Fig. 3.48: Striation-like markings, on an unetched fracture surface of Fe-3% Si, da/dN ≈ 10^{-7} mm/cycle. 252

Fig. 3.49: Primary {100} facet with fine striation observed in Fe-3% Si for da/dN ≈ 10^{-7} mm/cycle. 252

Fig. 3.50: Different alternate slip cracking combinations which are consistent with the experimental observations obtained on the b.c.c. metals studied. 252

Fig. 3.51: Striated {100} facet on Fe-3% Si for da/dN ≈ 10^{-7} mm/cycle. The cracking in regions A and B is consistent with models a and b

schematized in Fig. 3.50, respectively. 253

Fig. 3.52: {110} striated primary facets with <111> striations and near-<112> river lines observed in Fe-3%Si for da/dN ≈ 10^{-7} mm/cycle. . 253

Fig. 3.53: Two different sets of {110} primary facets with <111> or <113> striations observed in Fe-3%Si for da/dN ≈ 10^{-7} mm/cycle. . 253

Fig. 3.54: Herringbone river lines patterns, Fe-3%Si, da/dN ≈ 10^{-7} mm/cycle. 254

Fig. 3.55: Unetched matching surface of region "M" in figure 3.54. . . 254

Fig. 3.56: Typical {100} cleavage facets in Fe-3%Si with <110> and <100> river lines determined by comparison with the etch pits. . . . 254

Fig. 3.57: Near-{110} facet observed on mild steel tested in air for da/dN ≈ 10^{-7} mm/cycle. (a) etched fracture surface, (b) matching region on the unetched fracture surface. 255

Fig. 3.58: Sheet-like fine facets observed on the mild steel at R = 0.5 for da/dN ≈ 10^{-6} mm/cycle. 255

Fig. 3.59: Primary wavy facets with {100} average orientation consistent with model a of Fig. 3.50, (mild steel, R = 0.5, da/dN ≈ 10^{-6} mm/cycle). 255

Fig. 3.60: Large flat facets in the β-phase of 13.5% Mn-Al-Ni bronze, da/dN ≈ 10^{-5} mm/cycle, in air. 256

Fig. 3.61: Path of secondary crack along slip traces in the β-phase of 13.5% Mn-

Al-Ni bronze, in 3.5% NaClk solution da/dN ≈ 10^{-5} mm/cycle. 256

Fig. 3.62: Relationship between microfractography and microstructure of the β-phase on 13.5% Mn-Al-Ni bronze tested in air, da/dN ≈ 10^{-6} mm/cycle. 256

Fig. 3.63: {110} facets present in the β-phase of 13.5% Mn-Al-Ni bronze (HT_2), in air, R = 0.1, da/dN ≈ 10^{-5} mm/cycle. 256

Fig. 4.1: Dimensions and geometry of TN-DCB specimen. 287

Fig. 4.2: Previously obtained curves of crack velocity vs. K for annealed 316 and 310 stainless steels (112). 287

Fig. 4.3: Schematic diagram defining the fractograpic features associated with TSCC: LAFP, local average fracture plane; LCD, local crack propagation; MF, microfacet; PF, primary facet; RL, river line; S, striations; SF, serration facets; SMF, sheet-like microfacets; SRL, serrated river line, UC, undercutting (415). 287

Fig. 4.4: Aspect of the fracture surface produced near the SCC threshold. The etch pits indicate a {100} orientation of the primary facets. Fine horizontal striation-like features can be seen parallel to the <110> direction which is perpendicular to the main direction of river lines. 288

Fig. 4.5: Stereographic pair of micrographs showing fine striations which, in region "A" can be seen to result from the presence of sets of {111}

microfacets parallel to sides 1 and 2 of the etch pits. 288

Fig. 4.6: In this micrograph, the striations and the waviness of fracture surface can be seen to result from the presence of sets of {111} microfacets parallel to sides 1 and 2 of the etch pits. 288

Fig. 4.7: Serration facets A and B on a prominent river line correspond to faces 1 and 2 of the etch pits. Sheet-like microfacets C on another river line correspond to face 2 of the etch pits. 289

Fig. 4.8: More complex fractographic aspect observed at intermediate K, presenting numerous microfacets not parallel to the average orientation of the fracture plane. 289

Fig. 4.9: Stereographic pair of micrographs from the region below the annealing twin in Fig. 4.8, allowing one to observe the microfractographic aspects at higher magnification. The presence of different sets of {111} microfacets can be identified. Fig. 4.9 is rotated almost 90° with respect to Fig. 4.8. 289

Fig. 4.10: Fan-shaped pattern of river lines observed for an intermediate value of K. River lines are parallel to the two <110> directions as well as to one of the <100> directions contained in the average {100} fracture plane. 290

Fig. 4.11: The more complex aspect of the SCC fracture surface observed for 316 s.s. at high K. The presence of many sheet-like microfacets results

in feather-like microfractographic features. 290

Fig. 4.12: The presence of an etchpit on this stereographic pair of micrographs permits one to identify the {111} orientations of the sheet-like microfacets. For example, the microfacets indicated A, B and C can be seen to be parallel to faces 1, 2 and 3 respectively of the etchpit. 290

Fig. 4.13: Another etch-pitted region of SCC fracture surface produced at high K for which the {111} orientation of the sheet-like microfacets a and b were identified as parallel to sides 1 and 2 respectively of the etchpit. 291

Fig. 4.14: Unetched region of SCC fracture surface produced at high K, with feather-like features which result from the presence of numerous sheet-like microfacets. The crystallography of these features can be identified by comparison with Fig. 3.12(a) (see section 3). . 291

Fig. 4.15: Herring-bone patterns of river lines observed at quite low K. The {100} primary facet presents two sets of {100} river lines and a <110> central spine. 291

Fig. 4.16: Fractographic features produced in the high K portion of stage II of the log da/dN-log K curve. Secondary cracks permit one to identify intermediate positions of the crack front. 292

Fig. 4.17: Herring-bone pattern of river lines observed at high K. . . . 292

Fig. 4.18: Region of fracture surface produced at low K at a lateral specimen edge and presenting fractographic features more typical of those observed away from the lateral edges at higher K. 292

Fig. 4.19: Low K region of fracture surface near a lateral edge, presenting two sets of <110> and a set of <100> river lines. 292

Fig. 4.20: The same site of the fracture surface observed on opposite fracture. The microfractographic features match in an interlocking manner.293

Fig. 4.21: Stereofractographic pairs of a relatively low magnification
(a) at low and intermediate K values region,
(b) at high K values region. 293

Fig. 4.22: Stereographic pair of TEM fractographs observed for a flat facet produced at low K. 294

Fig. 4.23: Photograph of carbon film made from acetate film which was not replicated on any surface. 294

Fig. 4.24: Schematic representation of crack growth which occurs solely by alternate slip at the crack tip in the absence of reversed slip. 294

Fig. 4.25: Schematic representation of the incomplete linkage of primary facets which extend into the metals as parallel tongues separated by uncracked ligaments. If the stress intensity factor acting on the ligaments is not sufficiently high, the discontinuous fracture of the ligaments can be expected not to extend the river lines all the way to

the tips of the tongues. 295

Fig. 4.26: Schematic representation of the linkage process which can be expected at high K. The discontinuous fracture of the ligaments causes linkage to occur all the way to the tips of the tongues and is generally accompanied by the formation of a step along the crack front, effectively blunting the crack tip. 295

Fig. 5.1: Microstructure of α-brass employed. 346

Fig. 5.2: Dimensions and geometry of DCB specimen. 346

Fig. 5.3: Schematic of test cell. 347

Fig. 5.4: The plot of log V vs K for tests performed in the non-tarnishing solution on three specimens. 347

Fig. 5.5: Aspect of SCC of α-brass viewed at low magnification 347

Fig. 5.6: Typical intergranular facets observed for α-brass tested in the non-tarnishing ammoniacal solution. 348

Fig. 5.7: Slip traces observed on some of intergranular facets for α-brass tested in the non-tarnishing ammoniacal solution. 348

Fig. 5.8: Complicated fractographic aspect observed in higher K region (~ 20 MPa $m^{1/2}$) 348

Fig. 5.9: Stereo pairs shows complex aspect with presence of four sets of {111} microfacets observed on TSCC of α-brass (K ≈ 20 MPa $m^{1/2}$). 349

Fig. 5.10: (a) {110} <110> crystallography of the primary facets and of the

{100} <110> average secondary facets identified on the TSCC fracture surface produced at K ~ 20 MPa $m^{1/2}$.

(b) Schematic of the cracking crystallography observed in (a). 349

Fig. 5.11: The presence of numerous river lines with relatively important step heights observed on TSCC fracture surface produced at relatively high K values. 350

Fig. 5.12: Stereo pairs shows {110} <100> cracking crystallography identified on TSCC facets produced in the region corresponding K ≈ 15 MPa $m^{1/2}$. 350

Fig. 5.13: Small size {111} microfacets observed in the low K region (K ≥ 10 MPa $m^{1/2}$). 351

Fig. 5.14: Relatively flat facets observed at low K. Some very fine striation-like markings can be seen in the region as indicated by the arrow. 351

Fig. 5.15: The {111} microfacets can be seen to match in an interlocking manner. For example the facet indicated A_1 matches to that indicated A_2 on the mating fracture surfaces. 351

Fig. 5.16: Fan-shaped {110} primary facets with two <112> orientations of river lines and an average <110> orientation of serrated river lines observed at relatively low K values. 350

Fig. 5.17: Microstructure of α-brass foil after annealing (etching conditions: 30 ml of HCl + 10 gm of $FeCl_3$ + 120 ml of methanol, at 24 °C for

1 minute) 354

Fig. 5.18: Schematic of the geometries of ribbon specimens employed for the first series of tests. Only the geometry shown in (b) was employed for the second series of tests. 354

Fig. 5.19: Test arrangement 354

Fig. 5.20: Schematic of the experimental arrangement for test 20 in table 5.4 354

Fig. 5.21: Fracture surface produced in air without any exposure to the test solution. 355

Fig. 5.22: General aspect of crystallographic fracture surfaces fractured in air after 100 minutes of immersion then rinsing with deionized water and methanol and air-drying. 355

Fig. 5.23: A small crystallographic region present near ductile fracture surface produced after 100 minutes of immersion, rinsed, dried and then kept 25 hours in the vacuum chamber of the SEM. 355

Fig. 5.24: Crystallographic cracking initiated following the relatively large {111} facets with subsequent propagation on two or more sets of alternating {111} microfacets observed on rinsed specimens (100 minutes of immersion). 355

Fig. 5.25: Stereomicrofractographs show that crystallographic cracking initiated following the relatively large flat {111} facets which are almost

perpendicular to the tensile axis (fractured in air after 100 minutes of immersion). 356

Fig. 5.26: Matching fracture surfaces for crystallographic cracking observed after fracture of a ribbon specimen, rinsed and dried after immersion and then fractured. Initiation occurred along a dissolution slot; cracking then followed large {111} facets and then two alternating sets of {111} microfacets. 356

Fig. 5.27: Crystallographic cracking initiated at lines of the etch pits and propagated on two or more sets of {111} facets decohesion observed on the specimens rinsed after 100 minutes of immersion and then fractured in air. 357

Fig. 5.28: Dissolution slots and etch pits on ribbon surface not fractured after 100 minutes of immersion. 357

Fig. 5.29: Crystallographic cracking observed after fracture of a ribbon, rinsed and dried after immersion and then fractured. Average primary facets with {100} <110> cracking crystallography resulted from two alternating sets of {111} microfacets. 357

Fig. 5.30: Crystallographic cracking on a ribbon ultrasonically rinsed before fracture, with presence of dissolution slots near initiation site, and with increasing plasticity accompanying the crack propagation. . . 358

Fig. 5.31: Intergranular cracking occurred on the upper portion of the ribbon

specimen immersed in the solution (first series of tests) for 100 minutes. 358

Fig. 5.32: Metallographic observations of the (a) upper part, and (b) lower part of the surfaces on the same ribbon specimen immersed for 100 minutes in the solution of the first series of tests. 358

Fig. 6.1: Comparison of the crack growth curves for the 8% Mn Ac alloys. 385

Fig. 6.2: Examples of log da/dN-log ΔK_{eff} crack growth curves for the 8% Mn AC alloy. 385

Fig. 6.3: Comparison of different crack propagation curves for the 8 and 10% Mn HT1 alloys. 385

Fig. 6.4: Comparison on a ΔK_{eff} basis of the high da/dN portion of crack growth curves for the 8% Mn HT1 alloy. 385

Fig. 6.5: Comparison of different crack propagation curves for the 8 and 10% Mn HT2 alloys. 386

Fig. 6.6: Comparison of the crack growth curves in air and in the NaCl solution for the propeller specimens in the as-received and HT2 conditions. 386

Fig. 6.7: Macroscopic aspect of fracture surfaces of the 8% Mn AC specimens tested in air at 20 Hz (a) and in 3.5% NaCl solution at 1 (b) and 20 (c) Hz. 387

Fig. 6.8: Macroscopic aspect of fracture surfaces of the as-received (A) and HT2 (H) propeller specimens tested in air (a) and in NaCl solution (s). 387

Fig. 6.9: Small precipitates and dimples on the intergranular-like facets produced in air for 8% Mn AC bronze at da/dN ≈ 10^{-6} mm/cycle. 388

Fig. 6.10: Path of secondary crack observed on the metallographic section of the 8 % Mn AC specimen tested in air, showing that the intergranular-like cracks are situated in the α-phase in the immediate vicinity of the α-β interface (da/dN ~ 10^{-6} mm/cycle). 388

Fig. 6.11: Microstructure of the 8% Mn AC bronze specimen tested in air, showing the presence of fine κ_{II} precipitates in and near the regions of the β phase. 388

Fig. 6.12: Intergranular facets in 8% Mn AC alloy tested in NaCl solution, 1Hz ≈ 10^{-6} mm/cycle. 389

Fig. 6.13: Dissolution of β-phase in 10% Mn HT1 alloy, tested in NaCl solution at 1 Hz. 389

Fig. 6.14: Curved aspects of striations for the 8% Mn AC alloy tested in air, indicating that the cracks encounter some difficulty to cross boundaries between α grains, da/dN ≈ 10^{-3} mm/cycle. 389

Fig. 6.15: Striations which cross boundaries between α grains with no apparent

difficulty, 8% Mn AC alloy tested at 1 Hz in the NaCl solution, da/dN ≈ 10^{-3} mm/cycle. 390

Fig. 6.16: Aspect of striations in 8% AC alloy, NaCl solution at 20 Hz, da/dN ≈ 10^{-3} mm/cycle. 390

Fig. 6.17: Aspect of striations in 10% Mn HT2 alloy, NaCl solution, 1Hz, da/dN ≈ 10^{-3} mm/cycle. 390

Fig. 6.18: Profile of the fracture surface and secondary crack observed for the AR propeller specimen tested in air, da/dN ≈ 10^{-5} mm/cycle. 391

Fig. 6.19: Curved striations near a site at which the fatigue crack crossed a β - α interface, AR propeller, tested in air, da/dN ≈ 7 x 10^{-4} mm/cycle. 391

Fig. 6.20: Fracture facets showing the cracking leading in the β phase, AR propeller tested in air, da/dN ≈ 10^{-5} mm cycle. 391

Fig. 6.21: Striations which continue across α-β interfaces, AR propeller, da/dN ≈ 10^{-3} mm/cycle. 391

Fig. 6.22: Secondary crack in the immediate vicinity of the fracture surface, showing β phase dissolution near an α-β interface, AR propeller, da/dN ≈ 5 x 10^{-5} mm/cycle. 392

Fig. 6.23: Dimples in β phase of HT2 propeller, tested in air, da/dN ≈ 2 x 10^{-4} mm/cycle. 392

Fig. 6.24: Crack path in the α and β phases, HT2 propeller tested in air, da/dN ≈ 10^{-5} mm/cycle. 392

Fig. 6.25: β fracture facet presenting ridges corresponding to secondary α grains arranged in Widmanstatten patterns, HT2 propeller, tested in air, da/dN $\approx 10^{-5}$ mm/cycle. 392

Fig. 6.26: Profile of the fracture surface of the HT2 propeller specimen tested in the NaCl solution, showing the crack path in the β phase tended to be crystallographic with the crack orientation deviating on crossing α - β interfaces, da/dN $\approx 1 \times 10^{-5}$ mm/cycle. 393

Fig. 6.27: Profile of the fracture surface of the HT2 propeller specimen tested in the NaCl solution, showing a tendency for cracking to follow a path near α - β interfaces, da/dN $\approx 10^{-4}$ mm/cycle. 393

Fig. 6.28: Dissolution in the vicinity of the interfaces of κ_I precipitates, HT2 propeller specimen tested in the NaCl solution, da/dN $\approx 10^{-4}$ mm/cycle. 393

Fig. 6.29: Striation on β facets at da/dN $\approx 9 \times 10^{-4}$ mm/cycle for 14% Mn HT2 specimen tested at 1 Hz in the NaCl solution. 393

Fig. 6.30: Influence of fine κ precipitates on the microfractographic features in the α phase, 10% Mn HT2 alloy tested in air, da/dN $\approx 2 \times 10^{-5}$ mm/cycle. 394

Fig. 6.31: Semi-elliptical dimples formed in the β phase of the HT2 propeller specimen tested in air, da/dN $\approx 10^{-5}$ mm/cycle. 394

Fig. 6.32: (Left) Dimples in the β phase of the 10 % Mn HT2 alloy tested in air,

da/dN ≈ 10^{-5} mm/cycle. (observed after etch-pitting).

(Right) Precipitates present on the β phase of the 10% Mn HT2 alloy tested in air, da/dN ≈ 10^{-4} mm/cycle. (observed on a surface not etched). 394

Fig. 6.33: Interaction of medium-size κ precipitates with fatigue striations in the α phase, 8% Mn AC bronze tested in air, da/dN ≈ 10^{-3} mm/cycle. 395

Fig. 6.34: Presence of dissolved medium-size κ precipitates on the fatigue fracture surface of the 8% HT1 specimen tested at 1 Hz in the NaCl solution, da/dN ≈ 10^{-3} mm/cycle. 395

LIST OF TABLES

PAGE

Table (1.1)a: Crystallographic facets of fatigue cracking in some f.c.c. metals 54

Table (1.1)b: Crystallographic facets of fatigue cracking in some b.c.c. metals 56

Table (1.1)c: Crystallographic facets of fatigue cracking in some h.c.p. metals 58

Table (1.2): Crystallography of TSCC in some f.c.c. metals 78

Table 3.1: The composition of Fe-3% Si plate 193

Table 4.1: The composition of 316 s.s. and 310 s.s. (wt.%) (371) . . 260

Table 4.2: The yield stress of 316 s.s. and 310 s.s. (371) 261

Table 5.1: The composition of 70Cu-30Zn (wt%) (376) 297

Table 5.2: Crystallography identified for TSCC facets of α-brass in bulk DCB specimens. 318

Table 5.3: The primary data recording of EDS analysis of the α-brass ribbon specimens 352

Table 5.4: Summary of the procedure employed in the first series of tests 329

Table 5.5: Summary of the procedure employed in the second series tests 331

Table 6.1: Fatigue propagation tests performed on the Mn-Al-Ni bronzes 383

Table 6.2: Chemical analysis (wt%) Mn-Al-Ni bronzes 384

INTRODUCTION

The fractography and crystallography of transgranular stress-corrosion cracking (TSCC) in f.c.c. metals has been the subject of considerable interest. A number of previous studies have focused on the crystallographic orientations of the microfractographic features produced by TSCC, in order to identify the operative cracking mechanisms. However, because of the complexity of the fractographic features of TSCC, and of the limitation of the techniques in determining the orientations of fine cracking facets and of the local crack propagation direction, many detailed fractographic aspects of TSCC, which should provide important information on the fracture mechanisms, have not yet been adequately identified and explained. A comprehensive theory of TSCC must be able to explain all details of the observed crack morphology, however, the mechanisms proposed for TSCC are often incompatible with the fractographic characteristics observed.

There has been considerable progress in understanding metal fatigue behavior near and at the threshold. Less attention, however, has been paid to the active cracking mechanisms in this threshold region. On the other hand, a very strong similarity of the microfractographic aspects presented between the transgranular fatigue cracking at very low propagation rates and TSCC in f.c.c. metals has been noted, indicating that understanding the cracking mechanisms

associated with near-threshold fatigue should assist in understanding those which operate during transgranular stress-corrosion cracking and vice-versa.

The main objective of the present study was to clearly identify the detailed fractographic and crystallographic features associated with TSCC for f.c.c. metals and with near-threshold fatigue cracking for both f.c.c. and b.c.c. metals, in order to compare the typical fractographic features observed with the fracture mechanisms proposed so as to better understand the possible mechanisms associated with these two important fracture phenomena.

Moreover, the studies of the influence of environment on fatigue cracking should also be beneficial for understanding the role of the environment on cracking, therefore, a study was also carried out of the details fracture surfaces produced by fatigue testing in vacuum and in aqueous solutions for some relevant materials.

CHAPTER 1

LITTERATURE SURVEY

1.1 MICROMECHANISMS AND FRACTOGRAPHY OF FATIGUE CRACKING

A fracture that is the result of repetitive or cyclic loading is known as fatigue fracture.

A fatigue fracture generally occurs in three stages. It initiates during stage I, propagates for most of its length during stage II, and proceeds to catastrophic fracture during stage III.

Stage I of fatigue-fracture progress is characterized by the initiation of cracks and their propagation by slip-plane fracture, extending inward from the surface at approximately 45° to the normal stress axis for an unnotched smooth specimen. Stage I cracking generally extends over more than a few grains (e.g. 2 to 10 grains) around the origin. In each grain, the fracture surface is along a well-defined crystallographic plane. There are usually no fatigue striations associated with a stage I fracture surface, although some fine striations by chance are present, which could be observed by means of TEM replicas.

The transition from stage I to stage II of fatigue fracture process is characterized by the change of orientation of the main fracture plane in each grain from one to two shear planes to many parallel plateaus separated by longitudinal ridges. The plateaus are usually normal to the direction of maximum tensile stress. A stage II fracture generally presents striations which differ in appearance, depending on environmental effects, the relative ductility of the metal, the stress intensity level propagating the crack, and the stress state. The mechanism of formation of striations is described in section 1.1.8.2.

The fatigue fracture associated with stage III is generally combines striations with some static fracture features, such as cleavage, intergranular or fibrous fractographic characteristics.

In order to narrow the focus, this section will be restricted to the discussion of the micromechanisms and fractography associated with fatigue crack propagation. Fatigue crack initiation behaviour is described only very briefly.

1.1.1 Fatigue Crack Initiation

Most investigators generally agree that fatigue crack nucleation occurs at external surfaces of engineering structures, although subsurface nucleation has been observed in metals covered with a strong adherent surface oxide (1).

Surface flaws and defects can introduce severe stress concentrations which promote crack initiation. Even when the surface of the sample is initially smooth, the cyclic straining process itself can cause the surface topography to roughen. The development of this roughness is associated with near-surface dislocation motion, and consequently, depends on the local strain. Therefore, initiation processes are influenced by the cyclic hardening or softening characteristics of the material.

Various dislocation models have been proposed to explain the fatigue crack nucleation process (2,3). It is now generally believed that repeated strain cycling produces a surface layer which is atypical of the bulk material. The dislocation density in this layer is higher than in the bulk and these high dislocation density regions can play a crucial role in the fatigue fracture process. In many materials, this role involves the development of sites of strain localization.

The morphology of the strain localization developed during plastic deformation of a metal depends on the stress state and the stacking fault energy (SFE) of metals or tendency to develop planar slip. For instance, in copper, wavy slip (high SFE) causes the formation of dislocation clusters or groups during fatigue deformation at low to moderate stress. For copper, during the saturation stage of cyclic deformation, slip becomes concentrated along narrow bands (referred to as PSB's) and these bands become softer. Intensive slip at PSB's can give rise to the

formation of intrusions and the extrusions. After the intrusion is initially formed it acts as a stress raiser and facilitates further slip only at the notch root from which microcracks may grow. However, the dislocations in planar slip or low SFE materials, such as 70-30 α-brass, undergo planar slip thus, only a few slip planes are active. Sharply defined crevices (valleys) and ridges (hills) of morphology on the surfaces are more often observed at high strain amplitude. The role of the crevices is similar to that of the intrusions in assisting the nucleation of microcracks.

Generally, cracks tend to nucleate wherever inhomogeneous slip is concentrated including at interfaces with the surface. A microcrack grows inward along a slip plane on which the resolved cyclic shear stress is large. It grows by to-and-fro shear on the slip plane. Once a small macroscopic crack, formed by coalescence of certain individual microcracks, reaches a critical length and depth, it turns and grows in a direction normal to the maximum tensile stress and enters the stage II macrocrack propagation stage.

The process of nucleation and coalescence of fatigue microcracks is strongly influenced by the state of stress, microstructure of material and environment. For instance, at low strain amplitudes, it was shown that cracks were nucleated at PSB's (2). In high strain fatigue, however, the cracks usually develop at grain boundaries (4). If a microcrack initiated at a low stress level does not reach a critical length

and depth for change over to a stage II macrocrack, it will not propagate as a macroscopic crack.

A small grain size is favorable to large resistance to the formation of a fatigue macrocrack formation since grain boundaries may retard the coalescence of the crystallographic microcracks in different grains. Therefore, the grain size can have a considerable effect on fatigue endurance limit (5) which corresponds to the horizontal portion of an S-N curve representing the maximum stress that the metal can withstand for an infinitely large number of cycles with 50% probability of failure.

Fatigue crack initiation process is further complicated by the addition of an aggressive environment. For example, an aggressive gaseous environment in facilitating oxidation or adsorption on an active fresh surface corresponding to portion of a new slip step may either decrease the reversibility of plastic deformation or reduce the surface energy and therefore accelerate the fatigue crack initiation process. The influence of environment on fatigue cracking is described further in the other sections.

1.1.2 Fatigue Crack Growth Curve (fcg)

In recent years, the primary approach to fatigue propagation studies has been based on fracture mechanics. The application of linear-elastic fracture mechanics and related to small-scale crack tip plasticity has provided a semi-empirical basis for describing the phenomenon of fatigue crack propagation.

It has been well established that fatigue crack propagation rates (da/dN) in metals generally vary with the range of stress intensity factor ΔK ($=K_{max}-K_{min}$). A typical fatigue crack growth curve (fcg), log da/dN vs. log ΔK, can be represented by the three-regime curve schematized in Fig. 1.1. In most metals, crack growth rates vary over a wide range, typically between 10^{-8} and 10^{-2} mm/cycle.

At crack growth rates between 10^{-6} and 10^{-3} mm/cycle, namely regime B in the fcg curve, cracking generally proceeds by a transgranular ductile striation mechanism (or continuum mechanism) and the crack growth rates are weakly sensitive to microstructure and mean stress (characterized by load ratio $R = K_{min}/K_{max}$). This regime is denoted the Paris law regime where da/dN is related to ΔK by

$$da/dN = C\Delta K^m \qquad [1\text{-}1]$$

where C and m are experimentally-determined scaling constants (6).

At growth rates above 10^{-3} mm/cycle, namely regime c in the fcg curve, instability is approached before final failure and the crack growth rate is much faster than that predicted by the Paris equation [1-1]. When K_{max} approaches K_{IC} (fracture toughness), static fracture mechanisms, such as cleavage, intergranular and fibrous fracture occur in addition to striation growth, resulting in a marked sensitivity of propagation rates to microstructure, mean stress as well as component thickness.

At low crack growth rates, typically below 10^{-6} mm/cycle, namely regime A in the fcg curve, the Paris equation [1-1] is violated again and the fatigue crack growth rates diminishes rapidly as ΔK approaches ΔK_{th}, the threshold stress intensity factor below which no crack propagation can be detected. In this regime, fatigue crack growth rates are strongly sensitive to microstructure, mean stress and environment. The measured propagation rate can correspond to values less than an interatomic spacing per cycle. The detailed mechanism in this regime has not been known well, although it has been characterized as "discontinuous" mechanisms. Fracture morphology in this regime generally presents very crystallographic facets. A certain amount of intergranular cracking can occur for some metals at some values of low crack growth rates (7-10).

1.1.3 The Influence of Mean Stress on Fatigue Propagation

As mentioned, in fatigue studies, the influence of mean stress is often expressed in terms of the stress or the stress or load ratio R ($=K_{min}/K_{max}$). Little influence of R ratio has been demonstrated experimentally for the mid-range of growth rates. For high growth rates and the near-threshold regimes of fcg curve, however, the crack propagation is generally extremely sensitive to the load ratio.

1.1.3.1 High Growth Rate Regime

In the high growth rate regime, the ΔK dependence of crack growth rate increases markedly. A main factor to be considered for this deviation to Paris equation [1-1] is that as K_{max} approaches K_c, local crack instabilities occur as evidenced by increasing amounts of microvoid coalescence and/or cleavage on the fracture surface. This effect is expected to become more important with increasing mean stress, so that crack growth rates at high ΔK values increase with increasing mean stress.

One relationship expressing crack growth rates in terms of ΔK, K_c and a measure of K_{mean} was proposed by Forman et al. (11) in the form

$$\frac{da}{dN} = \frac{C\,\Delta K^n}{(1-R)K_c - \Delta K} \qquad [1\text{-}2]$$

where: C and n are material constants

K_c is the fracture toughness

Equation [1-2] shows that the simple power relationship equation [1-1] has been modified by the term [(1-R) K_c-ΔK], which decreases with increasing load ratio R and decreasing fracture toughness, both of which lead to higher crack growth rates at a given ΔK level. Other relationships describing mean stress effects on fatigue crack propagation response have taken account of the plastic zones at the crack tip and the plastic deformation process itself.

Elber (12) proposed that the crack might be partially closed during part of the loading cycle, even when $R > 0$. He argued that residual tensile displacements, resulting from the plastic damage of fatigue crack extension, would interfere along the crack surface in the wake of the advancing crack front and cause the crack to close above the minimum applied load level. This hypothesis was verified with compliance measurements taken from fatigue test panels that showed that an effective change in crack length occurred prior to any actual change in crack length. In other words, the crack was partially closed for a portion of the loading cycle and did not open fully until a certain opening K level, K_{op}, was applied. Since the crack is unable to propagate while it remains closed, the net effect of closure is to reduce the applied ΔK ($=K_{max}$-K_{min}) value to some lower effective value, ΔK_{eff} ($=K_{max}$-K_{op})

actually experienced at the crack tip, as shown in Fig. 1.2. Thus, fatigue crack propagation should be affected by changes in mean load level, which has been verified by a number of experimental results. Since the work of Elber who employed on thin samples, it has been shown that crack closure effects are particularly important at low ΔK.

1.1.3.2 At Near-Threshold Regime

The R ratio strongly influences ΔK_{th} and the very low propagation rates. Studies in a wide range of steels and non-ferrous alloys, tested in ambient-temperature (e.g. 8, 15, 16) indicate that the value of ΔK_{th} is markedly decreased, and that propagation rate is increased, as the R ratio is raised within a range of 0 to 0.9.

The influence of R ratio on ΔK_{th} can be described by a general equation (14):

$$\Delta K_{th} = \Delta K_0 \cdot f(R) \qquad [1\text{-}3]$$

where ΔK_{th} is the threshold for a given R ratio and ΔK_0 is the threshold for $R = 0$.

Several empirical or theoretical forms have been proposed. One of such correlation proposed by Klesnil and Lukas (17) from a study of the propagation threshold in carbon steels is given by:

$$\Delta K_{th} = (1\text{-}R)^{\gamma} \Delta K_0 \qquad [1\text{-}4]$$

Values of γ, material parameter, in several materials and uncontrolled environment have usually fallen in the range between 0.25 and 1.0 (18).

Fig. 1.3 presents the variation of several different correlation f(R) proposed with R ratio and indicates that when γ approaches a value of 1.0 (curve a of this figure) the ΔK_{th} varies greatly with R. In this case, equation [1-4] changes to the form

$$\Delta K_{th} = (1\text{-}R) \Delta K_0 \qquad [1\text{-}5]$$

which gives the most conservative predication.

Many experimental results suggest that the influence of the R ratio on ΔK_{th} and low crack growth rates is strongly dependent on the mechanical properties and on the microstructure of the material as well as on the testing environment.

1.1.4 The Influence of Gaseous Environment on Fatigue Cracking

The resistance of most metals and alloys to failure is generally reduced when fatigue tests are conducted in the presence of an aggressive environment. These environments can be either gaseous or aqueous solution and the reductions in fatigue resistance occur because of environmental effects on mechanical and/or chemical processes. The effects of aqueous environments on fatigue cracking are

presented in section 1.2.4. This section describes briefly some gaseous environment effects on fatigue processes in metals and alloys.

1.1.4.1 The Effects of Gaseous Environments on Fatigue Crack Initiation

The near-surface regions of specimens tested in fatigue undergo pronounced deformation and the characteristics of this deformation can be significantly altered by external environment. Several mechanisms (19-22) have been proposed to explain the effects of gaseous environments on crack initiation. These mechanisms include:

i) Obstruction of reversible slip (19).

ii) Inhibition of crack rewelding in slip bands (20).

iii) Reduction of surface energy at the crack tip (21).

iv) Formation of bulk oxide (22).

Early investigations (19) suggested that the slip bands produced during cyclic deformation in oxygen-rich environments became regions of high oxygen concentrations. These high concentrations were developed because of the oxygen diffusion into these regions of strain induced high vacancy concentrations. Because of the localized strain and hence localized vacancy development, oxygen was assumed to segregate at these sites. Such segregation was also thought to influence

the formation of surface cracks. The dissolved oxygen in the slip bands could retard the rewelding of incipient cracks, thereby promoting microcrack formation. This model assumes that the interaction between the metal and oxygen occurs before crack initiation and that this interaction plays a major role in crack development. Metals such as gold do not necessarily react chemically with oxygen (23), hence this model for environmental effects cannot be a general one and thus is not applicable to all metals.

Some observations (24) coupled with the lack of any major environmental effects of different inert gases, such as helium or nitrogen, on aluminum and copper, suggest that a variety of gases were as effective as vacuum in increasing crack growth resistance. If rewelding were important, adsorption of helium and/or nitrogen should retard the process and thus fatigue in helium should be different from fatigue in vacuum. This effect is not observed; thus these results imply that neither interference with a rewelding mechanism nor gas adsorption can explain satisfactorily the environmental effects on crack initiation processes.

Sudarshan and Louthan (25) argued that the most promising mechanism proposed to explain environmental effects on crack initiation appears to be the formation of bulk oxides during deformation. These bulk oxides can interact with slip processes and thus influence the fatigue process. Support for this proposal has

been drawn from experiments on single crystals of aluminum tested in both air and vacuum environments (26). The prime near-surface deformation characteristic of samples tested in vacuum was dislocation pileups while numerous dislocation dipoles were observed in samples tested in air. Such oxidation would promote local hardening and decrease the tendency for slip reversibility. The lack of reversibility would promote the operation of parallel slip systems and the formation of dislocation dipoles.

Fatigue tests on 1100 aluminium alloys showed that the number of cycles to failure was independent of the partial pressure of oxygen above 40 kPa and below 1.3 Pa (22). This observation led to the suggestion that the strength of an oxide film was dependent on the oxygen partial pressure at intermediate pressure ranges and that this strength determined the behaviour of the near-surface deformation regions. The formation of thick oxide during air exposure inhibits the egress of dislocations and results in the accumulation of large amount of debris in the near-surface regions. The presence of this debris could promote the formation of cavities and voids (27) and result in accelerated initiation.

Reduction in surface energy by gas adsorption should increase the fatigue crack growth rates because the surface energy can be related to the fracture stress by the expression:

$$\sigma_F = (2E\gamma_S/\pi a)^{1/2} \qquad [1\text{-}6]$$

where a is the crack length, E is the Young's modulus, and γ_S is the surface energy. Although, the Griffith expression is for brittle behavior, modifications of this equation always show that the ease of fracture increases as surface energy is reduced. Furthermore, some investigations (28) have even associated this reduction in surface energy with the easy of formation of slip bands.

One major objection to the surface energy model for environmental effects is that oxygen adsorbs more strongly than hydrogen, yet its potency as an embritting agent is not as severe as hydrogen.

1.1.4.2 Role of Gaseous Environment on Fatigue Crack Growth

As mentioned, because fatigue is basically a slip process, any environment that affects slip also affects the rate at which a fatigue crack propagates. In general, conditions that promote easy slip, such as elevated temperature, or interfere with slip reversal (oxidation), enhance fatigue crack propagation and increase the fatigue striation spacing. However, in some embrittling or corrosive environments, the fatigue crack propagation rate can be affected not only by interfering with the basic slip process but also by affecting the material ahead of the crack front. This can result in the formation of brittle striations and the introduction of quasi-cleavage or cleavage and intergranular decohesion fracture

models (see section 1.2.4.6).

Several fatigue studies on samples tested in laboratory air have shown that crack growth rates can be significantly increased in the presence of moisture (29-31). The effects of humidity on fatigue crack growth have been observed in aluminium alloys, steels and in titanium alloys, as well as in copper alloys, especially at low fatigue crack growth rates when the environment has the greatest opportunity to exert its influence. One possible mechanism that has been suggested for the increased growth rates observed in aluminium alloys tested in the presence of water vapour is the liberation of hydrogen. The reaction responsible for that liberation (25) is:

$$2Al + 3H_2O = Al_2O_3 + 6H^+$$

The hydrogen liberated by such reaction can be adsorbed by the metal and can accelerate crack propagation. Such increases in propagation rate are attributed to the embrittling effects associated with hydrogen accumulation at grain boundaries and at other microstructural interfaces. These embrittled regions provide easy fracture paths. The mechanisms of hydrogen embrittlement are presented more in detail in section 1.2.3.

Humidity has also been shown to affect the deformation processes at the crack tip in low-carbon steels. Investigators (32) found that in dry nitrogen an

abundance of dislocation subcells were formed in regions ahead of the crack tip, but such formation was significantly reduced when tests were conducted in humid environment. This change in dislocation substructure resulted in differences in the local residual crack tip strain and therefore in the crack tip opening displacement (32). The humidity level also influenced the fracture mode and fracture topography of 4140 steel. Flat, intergranular fracture were observed on samples tested in high humidity, while slant transgranular fractures were observed on samples tested in low humidity (33).

Even though in most studies, there is an increasing trend to invoke a role for hydrogen in fatigue process in humid air, some investigators indicate that an oxide induced closure argument must also be included particularly in the near-threshold region (25), because of the tendency of many metals to form oxides during fatigue, especially for alloys which contain precipitates or particles that have a high affinity for oxygen.

1.1.5 Crack Closure Mechanisms

In general, environmentally-influenced crack propagation at near-threshold levels has been considered in terms of a mutual competition between two basic mechanisms, namely corrosion-fatigue processes, such as hydrogen embrittlement in both gaseous and aqueous environments or active path corrosion produced in

aggressive aqueous solutions, which can accelerate growth rates, and the resultant closure mechanisms which decelerate growth rates. This section considers some of the crack closure phenomena which can occur near the near-threshold.

1.1.5.1 Plasticity-Induced Crack Closure

As mentioned in section 1.1.3, this phenomenon proposed by Elber (12), has proved useful in relationalizing the influence of the R ratio on the fcg curve.

In the low ΔK regime, since the crack propagation rates are very low that the kinetics of the reaction between the environment and the freshly produced fracture surfaces can become very important and could in turn influence the amount of plasticity of the crack tip, so that could alter the plasticity-induced crack closure.

Baïlon et al. (34) reported that testing at low R ratio in an inert environment resulted in a significant increase of ΔK_{th} and K_{op} for 70-30 Zn α-brass compared to air. They argued that for this material, plasticity-induced crack closure can have a strong influence on ΔK_{th} and on the near-threshold fatigue propagation behaviour. Bouchet et al. (35) also observed that the size of the plastic zone ahead of the crack tip was larger in vacuum than in air.

1.1.5.2 Oxide-Induced Crack Closure

Oxide-induced crack closure arises from the fact that when oxide deposits, formed on freshly exposed surfaces at the crack tip in moist environments, reach a thickness comparable to crack tip opening displacement (CTOD), the crack can become effectively wedged-closed at stress intensity above K_{min}, which tends to increase the value of K_{op}, as well as the measured value of ΔK_{th}. Stewart and Ritchie (36, 37) as well as Skelton and Haigh (38) all observed a higher ΔK_{th} in air than in both vacuum and dry hydrogen. They suggested that their results can be rationalized in terms of the mechanism of oxide-induced crack closure.

1.1.5.3 Roughness-Induced Crack Closure

Roughness-induced crack closure arises in situations where the size-scale of the fracture surface roughness is comparable to crack tip opening displacement. The roughness-induced closure is most prevalent at near-threshold levels where maximum plastic zone sizes are typically less than the grain size. In such instances, the low restraint on cyclic slip will primarily promote crystallographic crack propagation, resulting in serrated or zig-zag fracture paths (16, 39, 40). Such faceted fracture morphologies have been shown to be microstructurally-sensitive. The deviation of individual crystallographic facets from the macroscopic crack plane can make a significant contribution to crack closure behavior in the near-threshold regime.

Fig. 1.4 gives the schematic illustration of the three types of crack closure mechanisms. They cannot be considered as truly independent (34). For instance, the marked microscopic roughness of the fracture surfaces produced in the near-threshold regime may (36) assist the formation of oxide debris which can then act as a wedge giving rise to oxide-induced crack closure. The wedging effect caused by corrosion product debris can be expected to become more important as the R ratio decreases. The crystallographic morphology of the fracture surfaces produced in the near threshold regime can also be modified by different environments (141,145).

1.1.6 The Influence of Temperature

Yuen and Roy (41) studied the effect of temperature on the near-threshold fatigue crack growth behavior of a nickel base precipitation hardenable superalloy 718 tested in air from room temperature up to 649°C, over the range of growth rates from 10^{-8} to 10^{-4} mm/cycle. They found both accelerating and decelerating crack growth mechanisms. At intermediate growth rates (~ above 10^{-5} mm/cycle), accelerating mechanisms dominated and at near-threshold growth rates (below 10^{-5} mm/cycle), decelerating mechanisms were found to be operating. The room temperature ΔK_{th} values was higher than the elevated temperature ΔK_{th} values. In considering only the elevated temperature ΔK_{th} values, the values increased with increasing temperature. These results were explained with a mechanism that

involves the accumulation of oxidation products within the crack enhancing crack closure. At room temperature, however, the fracture appearance consisted of fatigue striations in the intermediate growth regime and became crystallographic in nature in the near threshold growth regime. The fracture morphology at elevated temperature was similar. They measured the thickness of oxides with a SIMS technique, indicating that the maximum oxide thickness formed at 24°C and hence concluded that the oxide-induced crack closure effect was more important at room temperature than in the elevated temperature.

However, corresponding studies on the role of closure at low temperatures were complicated by the intrinsic effects of low temperature deformation characteristics on the crack extension mechanisms (395).

For example, Vincent and Rémy (42) found that the occurrence of {111} faceted planes in the threshold regime for a cast nickel base superalloy MAR M004 at 20°C, and {100} facets at 600°C. These results were attributed shorter slip distances at 600°C compared to 20°C due to the ease of cross slip of dislocations at higher temperatures. This resulted in a lower ΔK_{th} value and higher growth rates compared to those at 20°C for a given ΔK value.

1.1.7 The Influence of the Microstructure on Fatigue Crack Propagation

It is generally accepted that plastic deformation in the surface grains plays an important role in crack initiation, thus microstructure will play a very important role at this stage. In general, for crack propagation, microstructure has little influence on the fatigue striation regime but a large influence on the fatigue threshold and at low crack propagation rates.

To try to understand the effects of the microstructure of materials on the fatigue propagation resistance, it is important to consider the size of the plastic zone with respect to that of the characteristic microstructure parameters, such as the grain size, and the distance between inclusions. In the fatigue striation regime, the lack of sensitivity of fatigue propagation to the microstructure is expected to be related to a large plastic zone at the tip of the crack.

In addition, the effects of microstructure on fatigue resistance can also be related to the interatomic bonding, to the stacking fault energy and to various microstructure parameters: different phase, precipitates, inclusions and so on.

1.1.7.1 The Effect of Atomic Bond Strength and Modulus of Elasticity

The interatomic bond strength is expected to influence the fatigue resistance of a material in two ways. Firstly, it prevents the opening of cracks and is directly

connected to the surface energy. Secondly, once a crack is created, the energy release rate G and the crack tip opening displacement CTOD are inversely proportional to the Young's modulus E. If the crack propagation per cycle da/dN is proportional to the CTOD it should vary as 1/E. This relation is indeed well observed by Hickerson and Hertzberg (43). However, Kumble et al. (44) found that da/dN was proportional to $1/E^2$ rather than to 1/E. Tomkins (45) studying the relation between crack advance Δa and the CTOD in the midrange of the propagation rates, where growth occurs by a striation mechanism, proposed an expression to justify a crack propagation rate which was also proportional to $1/E^2$.

1.1.7.2 The Effect of Stacking Fault Energy

When the stacking fault energy is low, dislocation cross slip becomes difficult resulting in slip being very planar which was a strong influence on the fatigue properties. Laird (2,46) observed that a low stacking fault energy reduced the cyclic strain hardening rate for f.c.c. metals at low strain amplitudes. Abel et al. (47) who studied Cu-Al alloys showed that the saturation stress increased with decreasing stacking fault energy.

As mentioned in section (1.1.1), the slip character has also a marked influence on fatigue crack nucleation. When the slip is planar the initiation of crack takes place along the slip bands (2). Mughrabi et al. (48) also noted that a low

stacking fault energy favored fatigue crack initiation. On the other hand, for wavy slip alloys, fatigue crack initiation often occurs at grain boundaries (49).

Nevertheless, for the same plastic strain range, planar slip was observed to enhance fatigue life as compared to wavy slip for both low cycle (46) and in high cycle fatigue (50) of copper base alloys. Chaland and Remy (51) also found that the fatigue life increased as the stacking fault energy decreased in Co-Ni alloys, and they assumed that the stage I crack propagation rate was lower when it was transgranular, which was the case for the lower stacking fault energy alloys in their studies. They suggested that this could be due to a higher reversibility of the plastic deformation at the tip of the stage I transgranular cracks.

1.1.7.3 The Effect of Grain Size on Fatigue Threshold and Low Propagation Rates

The fatigue threshold has been found to be grain size dependent (16, 52-55). In materials having a well-defined grain structure, an increase in grain size can result in a significant increase in ΔK_{th}. There is generally a marked effect in mild and low alloy steels (5, 16, 54, 55), a moderate effect in 70-30 α-brass (56), 316 stainless steel (53) and Ti-6Al-4V (57) and little or very little effect for aluminium alloys (58).

For two mild steels considered to be 100% ferritic (59), the following empirical relationship was obtained for a R = 0 load ratio.

$$\Delta K_{th} = \Delta K_0 + K_f \, d^{1/2} \qquad [1\text{-}7]$$

with $\Delta K_0 = 0$ and $K_f = 1580$ MPa.

Similar equations were also reported for a low carbon steel (5) and for an austenitic stainless steel (60).

This influence of grain size on ΔK_{th} is the opposite of that on the yield stress as given by the Hall-Petch relationship,

$$\sigma_y = \sigma_c + K_y(d)^{-1/2} \qquad [1\text{-}8]$$

and on the endurance limit.

Grain size refinement is beneficial for the yield stress and the endurance limit but detrimental for ΔK_{th}. This completely reversed situation underlines the fundamental difference in the physical significance of ΔK_{th} and of the endurance limit (14). The latter is related to the probability of crack nucleation followed by crack growth to complete fracture, while ΔK_{th} relates to the arrest of a pre-existing macrocrack in the absence of over loading effects and does not concern crack nucleation.

The large influence of grain size on ΔK_{th} have been attributed to following aspects:

The first approach proposed by Masounave and Baïlon (16), based on zig-zag crystallographic path for the propagation direction and on the effective crack length. Since fracture should occur first in the most favourably oriented grains, the size of uncracked microligaments between crack segments should increase as the grain size increases. The increased size of uncracked ligaments can give rise to an increasing of ΔK_{th}, which can be treated by a modified Dugdale-Barenblatt model as shown by Gerberich and Moody (61) to take into account the semi-cohesive or partially cracked zones.

Priddle (53) previously suggested that the local deviation in the crack plane due to the crystallographic cracking leads to mixed mode propagation, to a loca decrease in ΔK_{thI} and to a local increase in ΔK_{thII}. This suggestion is based on the work of Kitagawa et al. (62) who showed that, for a crack with bent tip, the true K_I value is less than that for a straight crack. Priddle (53) also showed that the increase in real crack surface area over that suggested from macroscopic crack length and specimen thickness measurements could account for a further reduction in the true K_I value at the crack tip on increasing the grain size.

Benson (55), however, pointed that these two approach of above are not sufficient to explain the large changes in the threshold with grain size experimentally found in some steels. It has been noted (14) that the uncracked ligaments along the crack front will be subjected to mixed ΔK modes since neighbouring leading crack segments will not be in the same plane, however, as the grain size increases, the distance parallel to the applied stress direction between neighbouring leading crack segments should only increase in proportion to the increase in the width of the uncracked ligaments. The concluded that this implied the need for further ΔK_{th} measurements in mode II and III and in combined modes.

In addition, it has been suggested (10, 55) that the influence of the grain size on ΔK_{th} is also a function of the environment or that the influence of the environment is a function of the grain size, since the threshold is often changed by testing in vacuum or in some inert environments compared to in air.

1.1.7.4 The Effect of Precipitates

The effect of precipitates on fatigue is very different according to whether or not they are shearable by dislocations. In the first case slip remains very planar and strain softening is often observed. On the contrary, dislocation tangles are formed around non-shearable precipitates, cyclic strain hardening increases and slip is homogenized (63).

This influence of the precipitates on the slip character plays a particularly important role in fatigue crack propagation near threshold. The shearable precipitates which produce very planar slip, give long crystallographic cracks near the threshold with strong deviations, resulting in a large closure effect and thus a high ΔK_{th} value. This phenomenon was clearly demonstrated in a number of studies on aluminium alloys (e.g., 64, 65) and Ni base superalloys (e.g., 66). For instance, Lafarie-Frenot and Gasc (64) measured fatigue crack propagation near the threshold in a 7075 alloy and showed that the crack closure was the strongest and the ΔK_{th} value was the highest for the underaged alloy where the slip is very planar. Similar effects were reported in a nickel base superalloy (66) where the shearable γ' precipitates induced planar slip near the threshold and a high ΔK_{th} value.

1.1.7.5 Microstructural Effects in Two Phase Alloys

The effects of microstructure in alloys containing two phases present in various proportions have not been documented as well as the effects of grain size or of the precipitates on the fatigue behavior. The microstructure in two phase alloys involves the proportion of one phase with respect to the other, their mean size and also their morphologies and their plastic deformation behavior. The different parameters to consider make the problem complicated.

In general, more homogeneous slip is beneficial for fatigue crack initiation resistance but not for fatigue propagation. Mediratta et al. (67) showed that in dual phase steels, structures in which either the ferrite or the matensite was encapsulated by the second phase displayed more localized slip than a structure where the martensite was finely dispersed within the ferrite. In the latter case the initiation resistance was better at least for the lower strain amplitudes.

The martensite distribution was reported to have an influence on the fatigue crack propagation threshold. One example was given by Suzuki and McEvily (68) who found that a microstructure in which a continuous martensite phase encapsulated islands of ferrite possessed a much higher threshold than microstructures in which a continuous ferrite matrix encapsulated islands of matensite.

1.1.7.6 The Effect of Inclusions

Many studies have shown that inclusions can play a very important role in fatigue crack initiation. However, it seems little influence has been observed on the fatigue propagation except that they can induce anisotropy (69) with preferential directions for growth and also that they can favour ductile cracking mechanisms which add to the striation mechanisms at high ΔK values. This is often the case for Al alloys.

Fine (70) described the different ways in which inclusions could affect fatigue crack nucleation. Firstly, arge non-shearable precipitates can have a beneficial effect by homogenizing the slip. Secondly, inclusions are very potent sites for the nucleation of crack, because they act as obstacles to slip and large stress concentrations are built up at the tip of dislocation pile-ups on the interface. This can lead either to cracking of the matrix, to decohesion at the interface, or to cracking of the inclusion itself. As a general rule, the removal of inclusions improves the fatigue limit of steels (70).

It can be summarized that in general all phenomena which localize slip such as a low stacking fault energy, large grains, shearable precipitates are detrimental for fatigue crack initiation but tend to improve the fatigue crack propagation threshold.

1.1.7.7 The Effect of Strength Level

Early studies of near-threshold fatigue behaviour in ferrous alloys (16, 71, 72) indicated a large influence of strength in increasing ultra-low growth rates and decreasing ΔK_{th}. This effect, however, is less prominent at high load ratios (71), as well as for small cracks (73) and for non-ferrous alloys (74).

The major role of yield strength is influencing near-threshold fatigue crack growth in ferrous alloys is consistent with an important role of crack closure. The studies (40) in steels over a very wide range of strength levels (i.e., 290 to 1740 MPa) have confirmed that the extent of crack surface corrosion debris and hence oxide-induced closure was sharply decreased with increasing strength at R = 0.05. This was attributed to a reduced role of plasticity-induced closure (which promotes crack surface contact and therefore enhances fretting oxidation) in higher strength steels (75). Furthermore, it has been pointed out that the microstructures typically utilized for highest strength levels, i.e. tempered martensites, are generally considerably finer scale than for lower strength structures, leading to a smoother fracture path and thus reducing roughness-induced crack closure.

The effect of strength level on near-threshold crack growth in non-ferrous alloys, however, is somewhat more complex. Although the behavior in copper alloys (76) is similar to steels, there is no marked trend of increasing or decreasing ΔK_{th} values with a change in strength level in precipitation hardened systems (74), which has been interpreted as in a view of the different hardening mechanisms responsible for a given yield strength. Some investigators (75), therefore, argued that is is inappropriate to identify a direct correlation of yield strength and near-threshold behavior in non-ferrous alloys.

1.1.8 Fatigue Striations

Although microvoid coalescence usually occurs at high ΔK levels, and a cleavage-like faceted appearance dominates in many materials at very low ΔK levels, the most important microfractographic characteristic of a fatigue fracture surface are probably the fatigue striations which generally occur at an intermediate propagation rates, e.g. typically 2×10^{-5} to 2×10^{-3} mm/cycle for 2024-T3 aluminium alloy (77).

A high-magnification examination of the clam sheel markings observed on service failure fracture surfaces as well as the growth bands developed in laboratory samples subjected to block loading conditions reveals the presence of many smaller parallel lines, referred to a fatigue striations. The following important aspects are known about these markings:

- They appear on fatigue fracture surfaces in many materials, such as b.c.c, h.c.p, and f.c.c metals, and many engineering polymers.
- In a quantitative sense and for metals, each striation generally represents the incremental advance of the crack front resulting from one loading cycle (78).
- The extent of this advance which corresponds to the interspacing of the striations, varies with the stress range.
- They are most clearly observed on flat surfaces associated with plane strain conditions ($R>0$).

- The relative striation density at intermediate ΔK values varies with stress state and alloy composition.
- In terms of metallurgical factors, it is much easier to find fatigue striations surfaces on aluminum alloys than on high-strength steels.
- Fatigue striations can have many forms, such as highly three-dimensional or flat aspects. Generally striations tend to appear more ductile when formed in air or in an inert environment, but are relatively flat and tend to take on a cleavage-like appearance when formed in an aggressive environment.

From metallographic sections and electron fractographic examination, three basic interpretations of the morphology of fatigue striations have evolved. The striations are considered to be undulation on the fracture surface with (i) peak-to-peak, and valley-to-valley matching of the two mating surfaces, (ii) matching crevices separating flat facets, or (iii) peak-to-valley matching. Based on these interpretations of striation morphology, different mechanisms have been proposed for striation formation. One type of mechanism involves plastic blunting processes at the crack tip (79), which occurs regardless of the microscopic slip character of the material; the other type of mechanism takes account of crystallographic considerations; wherein, striations are thought to form by sliding off on preferred slip planes (79-84). These two types of models have been employed to explain the formation of non-crystallographic and crystallographic fatigue striations, respectively.

1.1.8.1 Non-Crystallographic Fatigue Striations

Laird and Smith (79) proposed that the formation of non-crystallographic fatigue striations can be explained by crack blunting in the stress increasing portion of the load cycle and by crack resharpening and advance in the stress decreasing portion. A schematic of the plastic blunting process of fatigue crack propagation during a loading cycle is illustrated in Fig. 1.5. Fig. 1.5a exhibits striations on the fracture surface. As a small tensile load is applied (Fig. 1.5b), the metal begins to plastically yield. This deformation occurs mainly along slip planes at 45° from the major stress axis. As the maximum tensile load is reached (Fig. 1.5c), the crack tip radius increases and the crack tip blunts to a semi-circular configuration. As the compressive load is applied (Fig. 1.5d), the direction of the slip in the slip zone reverses and the distance between the mating surfaces decreases. However, the new surface created in the tensile loading cannot be completely removed by rejoining of atomic bonds. This new surface is partially folded by bucking into a double notch at the tip. The final configuration at the maximum compressive load (Fig. 1.5e) is once again a sharp crack tip; however, the crack length has been increased by a length equal to the spacing between the previous and the new striations. This process repeats itself with continued application of tensile load (Fig. 1.5f).

This mechanism could operate when the form of the plastic zone of the crack tip is determined by the maximum shear planes rather than by the orientation of the slip planes in front of the crack tip. This is just the case when the size of the plastic zone is larger than the grain size, which explains that non-crystallographic striations are usually obtained at the regime corresponding to relatively high propagation rates.

The plastic blunting model is widely accepted among researchers as a general description of fatigue crack propagation. However, there is some disagreement on the mechanism by which this plastic blunting actually occurs. Furthermore, this model cannot account for the absence of striations when a metal is fatigue tested in vacuum and it does not adequately predict the peak-to-peak and valley-to-valley as well as peak-to-valley notching morphologies on mating halves of the fracture (81-84).

Tomkins and Biggs (80) proposed another mechanism for explaining the formation of non-crystallographic fatigue striations. This model involves a combination of both tensile tearing and shear slip. Detailed fractographic studies of fatigued samples of annealed aluminium revealed that a large striation was succeeded by a number finer ripples at high strain levels (85). This tearing-shearing model is illustrated in Fig. 1.6. At the minimum loading, the crack tip is sharp. As

a tensile load is applied, plastic flow occurs along well defined slip bands. A new crack surface is formed and a blunted crack tip is produced. Under continued tensile loading, this shear deformation is stopped on the original slip planes because of considerable strain hardening. Fracture by tensile tearing then occurs at the center of the blunted crack tip which then allows further blunting on new slip planes. This process continues until the maximum tensile stress is reached. When the reversing load is applied, the slip direction reverses on the slip planes resulting in striations.

1.1.8.2 Crystallographic Fatigue Striations

The main difference in morphologies of the crystallographic fatigue striations compared to the non-crystallographic striations are as follows:

- They are generally straight, following a crystallographic direction and have a well defined sawtooth morphology.
- They generally change orientation at grain boundaries, while the non-crystallograpic striations do not change orientation at grain boundaries.
- Occurrence of the crystallographic striations is strongly dependent upon the orientation of each grain with respect to the tensile stress axis. Unfavourable crystallographic orientations can give rise to the formation of poorly defined striations or, perhaps, even to none at all (86, 87).

Mechanisms which give rise to crystallographic striations have been proposed and identified by several investigators (81-84, 88, 89). All of these models are based on an alternating slip behaviour at the crack tip. During fatigue propagation, if plastic deformation is limited to a small region near the tip of the crack and the remainder of the structure is elastic, the crack tip deformation can proceed either alternately on one slip band and then on the other or simultaneously on both. A general pattern of this process of deformation by alternating slip resulting in an extension of the crack can explain the formation of crystallographic fatigue striations, as shown schematically in Fig. 1.7. The crack opens on the increasing tension portion of the load cycle by slip on two alternating slip planes. During the decreasing load portion of the fatigue cycle, reverse slip will occur along opposite direction to produce crack closure. This process is repeated, which then results in the formation of saw-tooth like striations with a peak-to-valley matching morphology on the opposite halves of the fracture.

Pelloux (81) and Neumann (82) presented their experimental observations to demonstrate the alternate slip mechanism. They explained that the activation of two slip systems alternates, because the currently active slip plane work hardens and the crack tip moves away from the previously activated and work-hardened slip plane.

Based on the absence of striations observed on the fatigue fracture surface of 2024-T3 aluminium alloys tested in a vacuum of 5 x 10^{-6}. Torr, Pelloux (81) assumed that oxidation reduces slip reversal during crack closure, which results in the formation of striations, and proposed the model shown in Fig. 1.8. Other experimental results (90, 91) also suggested that the lack of oxidation in high vacuum promotes more complete reversal slip, which results in a smooth and relatively featureless fatigue fracture surface.

Neumann (82, 92) confirmed the alternating slip mechanism by observations performed at the crack tips of copper and silicon-iron single crystal specimens loaded cyclically inside a scanning electron microscope. Based on the observations, he proposed the model shown in Fig. 1.9, which presents a peak-to-valley matching pattern of mating fracture surfaces. He suggested that the formation of striations is due to partial of irreversibility of alternating slip process and that the size of slip steps is determined by the stacking fault energy of the material.

In contrast to the non-crystallographic striations, the crystallographic striations are more often observed at low growth rates. The crack growth rate at which the transition in striation type occurs increases with decreasing stacking fault energy (SFE). It can be expected that for small plastic zone size in low SFE metals, the inhomogeneous deformation can be confined to the limited number of available slip

systems within one or two grains at the crack tip, resulting in relatively large slip steps.

1.1.9 Crystallographic Orientation of Fatigue Striations and of the Crack Propagation Plane

1.1.9.1 In f.c.c Metals

In terms of the alternating slip model, the crack front should be always parallel to the intersecting line of two {111} slip planes in f.c.c metals, which are <011> directions and the crack plane should be the plane bisecting the two operating {111} planes. Pelloux (81) pointed out that there are basically two crystallographic orientations which can satisfy the requirements of the alternating slip model.

(a) (001) crack plane, $[\bar{1}10]$ crack tip direction, (111) and $(\overline{111})$ slip planes. The slip planes make an angle of 54°44' with the crack plane.

(b) (011) crack plane, $[0\bar{1}1]$ crack tip direction, (111) and $(\bar{1}11)$ slip planes. The slip planes make an angle of 36°16' with the crack plane.

The combinations of crack and slip planes for these two crystallographic orientations are shown in Fig. 1.10 schematically.

Pelloux (81) found that the (001) [$\bar{1}$10] crystallographic orientation is favoured over the (011) [0$\bar{1}$1], although they both have the same Schmid factor. He explained this by the slip planes in orientation (a) being closer to the planes of maximum elastic shear stresses than in orientation (b). The planes of maximum elastic shear stress make an angle of approximately 70° with the crack plane in crack opening mode I. Many experimental findings (82, 84, 89), also showed a strong tendency for the macroscopic fracture plane to lie parallel to {100} planes more often than to {110} planes. However, Newmann (82) based on his observations of the macroscopic crack front usually being bent, argued that a plane which macroscopically is suitable for crack propagation must at least contain two different <011> directions, since two sets of <011> segments are necessary to make up a macroscopically curved crack front. Therefore, he concluded that the {100} planes are the only ones suitable for macroscopic crack propagation.

Bowles and Broek (83) pointed out that the {100} and {110} propagation planes considered by Pelloux (81) is the ideal symetrical case where the amount of slip on two alternating {111} planes is almost equal. They considered an asymetrical case where the slip amount on the two active sets of slip planes is unequal, and proposed a model (Fig. 1.10) to indicate that the average crack plane will vary, but that the fracture surface itself will primary consist of {111} fragments. This model was supported by the observation of small triangular etch pits on one

striation flank and some irregular pits were observed on fatigue fracture surfaces of Al 7075-76 specimens. These authors suggested that a striation may be the result of slip occurring on several parallel pairs of alternating slip planes other than only on one pair during a fatigue cycle.

1.1.9.2 In b.c.c Metals

Compared to f.c.c metals, fewer studies were carried out to investigate the crystallography associated with fatigue crack propagation in b.c.c metals.

As mentioned previously, the direct observation of alternating slip of Fe-2.5% Si single crystal during cycling inside a scanning electron microscope was carried out by Neumann et al. (93, 94) who demonstrated the operation of the same mechanism for explaining ductile fatigue striations as in f.c.c. metals, namely alternating slip model. The orientation for the notched specimen tested was chosen as a <110> tensile axis, <111> notch root and <112> crack propagation direction. The authors observed that the displacement of the crack tip was clearly due to sliding off on two alternate slip planes.

Another systematic study on the crystallographic orientation during fatigue crack propagation in b.c.c metals was performed by Rieux (95). Notched single crystal specimens of ferritic stainless steels (Fe-26Cr-1Mo) were fatigued in air and

in different orientations of crack planes and crack propagation directions for da/dN from 10^{-6} to 10^{-4} mm/cycle. The correlations between the macroscopic appearance of the fracture surfaces and the resistance to crack propagation were observed. It was found that the orientations which developed macroscopic plane fracture surfaces in this alloy, with correspondingly high propagation rates, were those which contain a pair of <111> slip direction symetrically located about the crack plane and normal to the crack front, such as {110} <011> and {100} <011> orientations. However, the authors noted that for the orientations, such as {111} <110> and {110} <111>, the fracture planes became progressively distorted resulting in low propagation rates. Therefore, they argued that for the former case the crack propagation is accordance with the alternating slip model, while, for the latter case, the crack propagates by multiple slip, which implies that slip on planes which do not intersect along the crack front must be accommodated by some additional localized slip and/or tearing processes at the crack tip. The authors particularly noted that two orientations, namely {112} <110> and {110} <112>, for which pairs of {110} and {112} slip planes are symetrically inclined to the crack plane and intersect along the crack front, do not develop plane fracture surfaces under the test conditions employed, since these two orientations do not contain a pair of <111> slip directions symetrically located about the crack plane and normal to the crack front (95). These observations, therefore, also clearly show that in b.c.c metals, which have a large number of possible slip planes, the orientation

requirements for crystallographic fatigue crack growth are less stringent, as well as that the appearance of fatigue fracture surfaces depends on the crystal orientation, and thus the crack growth resistance depends on the average fracture plane, as also found by Richards (96).

Other results reported in different studies concerning the crystallography of near-threshold fatigue in b.c.c metals are described further in section 1.1.14.

1.1.9.3 In h.c.p. Metals

The fatigue propagation behaviour is affected strongly by the anisotropic nature of plastic flow in h.c.p metals. Many studies reported in literatures (97-102) have shown that the morphologies of fracture surfaces are influenced by the orientation of the grain with respect to the principal stress axis and by the crack growth rates as well as by the testing environment (97). For high cycle fatigue failures of titanium and α/β titanium, the fracture surfaces are frequently highly irregular in appearance. A variety of fractographic features have been reported for this type of fracture surface. These include cleavage-like facets (97-102), areas of regular fatigue striations sometimes showing a one to one correspondence with the load cycles, or under other conditions each striation corresponding to many load cycles (100), irregular striations with secondary cracks (103) as well as parallel, furrow-like markings (98). For the cleavage-like facets the fracture plane has been

established using Laue X-ray techniques as being within 15 degrees of a (0001). And, in one instance, {1120} cracking was also reported for flat features formed in Ti-8Al-1Mo-1V fatigued in vacuum (99). Fatigue tests on textured Ti-6Al-4V (100, 101) revealed that grain orientation can affect both of the fatigue fracture morphology and the fatigue crack growth rates.

Beevers et al. (97, 102) established 3 modes for explaining the morphologies observed from their studies on α-titanium alloy fatigued in laboratory air at a frequency of ~ 100 Hz over a ΔK range of ~ 6-20 MPa $m^{1/2}$. Firstly, they observed striations on fracture surface where the orientation of the grain with respect to the principal stress axis and the crack growth direction was that illustrated in Fig. 1.11a which indicated that the grain orientation in this case would permit slip activity on two sets of $\{10\bar{1}0\}$ type planes. In grains where the slip planes were not symetrical about the crack growth plane, "fissure" striations were observed. The authors thus, argued that these observations indicated an alternating slip mechanism for the formation of striations at the intermediate ΔK level employed. A second distinctive mode of crack growth observed was that of the formation of "furrow"-like markings, as shown in Fig. 1.11b. The furrows were always observed to run in the c direction. This mode of growth was suggested as resulting from asymetrical slip on two pyramidal slip planes forming striations parallel to a $<11\bar{2}3>$ direction, which makes an angle of 32.2 degrees with the

[0001] direction. This asymetrical slip on two $\{10\bar{1}1\}$ type planes would form a series of tongue-like cracks which subsequently join together by a ductile tearing process. The third mode of fatigue crack growth for h.c.p metals was assumed to occur in grains with orientations similar to those illustrated in Fig. 1.11c. The facets were identified to form on planes within $\pm$ 1 degree of the (0001) plane. This type of flat facets formed over the whole ΔK range investigated. Finally, at low growth rates approaching threshold ΔK levels, the authors observed that striation formation was replaced by a "ripple" mode of growth for grains with the orientations shown in Fig. 1.11a, and that the furrow mode was replaced by a mixed mode of growth, involving facet formation and ductile tearing.

A recent study of near-threshold fatigue cracking in α-Ti (104) has shown observations consistent with the findings of Beevers et al. (97), particularly for those aspects observed at the higher da/dN values studied. At ultra-low da/dN, however, the sets of very small facets in the shapes of tetrahedra or pyramid, which were similar to those observed by Beevers et al. (102), were present primarily in grain boundary regions, where their occurrence permitted an average local crack plane orientation which was neither parallel nor perpendicular to the c-axis and which allowed the crack planes on opposite sides of the grain boundaries to join up reasonably well. The orientations of this type of tetrahedral-like small facet were identified to correspond to the (0001) and to {1010} or {1210} planes from their

aspects (104). Furthermore some relatively large secondary facets on the serrated river lines were identified to correspond to (0001) a orientation. These authors thus argued that a few facets, apparently with a (0001) orientation, had a cleavage-like aspect; however, their aspect was not completely incompatible with that which could be produced by basal slip (104).

1.1.10 Fatigue Striation Spacing

More quantitative information can be obtained from the measurement of the spacing between fatigue striations when these are produced in each loading cycle, in which case the striation spacing indicates the local microscopic crack propagation rate da/dN. However, it has been shown repeatedly that in laboratory experiments, for constant stress intensity conditions, striation spacings in a local region may vary locally. This is because the formation of striation is a highly localized event and is dependent on the stress state and metallurgical conditions as well as the testing environmental conditions. Therefore, perfect agreement between macroscopic and microscopic crack growth rates should not be expected in the majority of instances.

For example, under normal conditions, each striation is the result of one load cycle, however, when there is a sudden decrease in the applied load, the crack can temporarily stop propagating, and no striations are formed. The crack resumes propagation only after a certain number of cycles are applied at the lower stress

(89). This phenomenon of crack arrest is due to the presence of a residual compressive stress field within the crack tip plastic zone produced after the last high-stress fatigue cycle and/or to crack closure effects (12).

Moreover, large second-phase particles and inclusions in metal can change the local crack growth rate and thus the local fatigue striation spacing. When a fatigue crack approaches such a particle, it is briefly retarded if the particle remains intact or is accelerated if the particle cleaves (108). In both cases, however, the crack growth rate is changed only in the immediate vicinity of the particle and therefore does not significantly affect the total crack growth rate. Nevertheless, for low-cycle (high-stress) fatigue, the relatively large plastic zone at the crack tip can cause cleavage and matrix separation at the particles at a significant distance ahead of the advancing fatigue crack. The cleaved or matrix-separated particles will behave as cracks or voids that promote a tear or shear fracture between themselves and the fatigue crack thus significantly advancing the crack front (105, 106).

Environments can modify the morphology and the spacing of the fatigue striations. This effect is described in the section of corrosion fatigue (1.2.4).

1.1.11 "Tire tracks"

Another type of distinct, periodic markings occasionally observed on fatigue fracture surfaces are known as tire tracks, because they often resemble the tracks left by the tread pattern of a tire. These rows of parallel markings are either the result of a particle or protrusion on one fatigue fracture surface being successively impressed into the surface of the mating half of the fracture during the closing portion of the fatigue cycle (84, 106, 107) or are associated with the strong rubbing together of the fracture surfaces, which is favoured by the important shear stress component acting along some pronounced ridges (108). These ridge lines can protect the tire marks which correspond to remains of striations from the surface rubbing effects. The tire tracks are frequently found on steeply inclined regions of the fracture surface and in grooves where striations or possibly stretch marks were protected from fracture surface rubbing effects. Tire tracks are more common for the tension-compression than the tension-tension type of fatigue loading (84). The direction of the tire tracks and the change in spacing of the indentations within the track can indicate the type of displacement that occurred during the fracturing process, such as lateral movement from shear or torsional loading.

1.1.12 Cyclic Cleavage Striations

In the case of fatigue cracking under conditions which favour cleavage, cyclic cleavage can occur. Such facets will present fatigue striations when sufficient

plasticity occurs to mark the crack arrest site in each cycle. The fact that the cyclic cleavage striations correspond to true crack-arrest sites has been verified from the interactions between the striations and the river lines (109). These striations correspond to sites at which the arrested crack has blunted. The cleavage crack can then initiate on any plane parallel to the original cleavage plane and which intersects the blunted crack tip. In other words, on reinitiation, the height of the cleavage plane tends to change. The height at which neighbouring portions of the cleavage crack reinitiate with respect to each other is thus responsible for the interactions of river lines and striations. The types of interaction which have been observed for cyclic cleavage (109) include river lines terminating at or starting at striations, river lines becoming either more pronounded or less pronounced on crossing striations and river lines changing direction to follow striations for a short distance.

For the lowest crack growth rates, the cyclic cleavage striations will be very faint and finely-spaced and very difficult to recognize. At sufficiently high propagation rates the cleavage will have a tendency to proceed by jumps within clusters of grains, resulting in the cyclic cleavage striations being best visible at the end of such clusters, when the cyclic cleavage has slowed down (108).

1.1.13 General Fractographic Features of Transgranular Facets Near the Threshold

Numerous investigators have shown that the fracture surface at very low crack growth rates usually takes on a strongly crystallographic aspect. Most of the crystallographic facets present cleavage-like appearance. Crystallographic striations which are generally perpendicular to the river lines or tear ridges can at times be observed on certain relatively flat facets in the region of the threshold (9, 77, 110). Careful measurements (77) confirmed that the interspacing of the striations were much too large to correspond to the average advance of the crack during each cycle (77). Fan-shaped or herring-bone patterns of river lines can frequently be seen for some f.c.c. and b.c.c. metals (110, and sections 3.3.2, 3.4.2.1), which are similar to those observed in transgranular stress corrosion cracking (TSCC) at intermediate K values (112). Serrated river lines have often been observed, such as in Al-2024, α-brass and 316 stainless steels (110, 111) and serrated secondary facets on the river lines generally are highly crystallographic and appear to be normal to the primary crack flat facets which are also strongly similar to those observed on TSCC for some f.c.c. metals especially at relatively low K values (112).

1.1.14 Crystallographic Fracture Facets Identified at Low Crack Growth Rates

The crystallographic facets at low crack growth rates are generally identified as low index planes. Beevers (9) has compiled a list of fractographic results obtained in several metals and alloys. In this section, more recent results reported

in the literature and some new results obtained in the present study are further collected for f.c.c, b.c.c. and h.c.p. metals, as presented in Table (1.1) a, b, and c respectively.

Table (1.1)a: Crystallographic facets of fatigue cracking in some f.c.c. metals

Ref.	Material	Environ-ment	Experimental condition	Facets plane and cracking direction	Identifica-tion technique
(113)	Al-Zn-Mg	Lab. air		{001}	Laué x-ray
(114)	Al-Zn-Mg	3% NaCl solution	$N_f = 10^3$	{001}	Laué x-ray
(80)	Al-2024	Lab. air	$\Delta K = 5.5 \rightarrow 16.5$	3° to 20° from {100}	Laué x-ray
(90)	Al-2024	Vacuum (3 x 10^{-3} torr)	$\Delta K = 5.5 \rightarrow 16.5$	{001} $\pm$ 5° {111}	Laué x-ray
(115)	Al 2219-T6	Lab. air		{111} $\pm$ 5°	Laué x-ray
(74)	Al-3% Cu	Lab. air	$\Delta K = 7 \rightarrow 30$	{001} $\pm$ 5-10°	Laué x-ray
(110)	Al 2024-351	Lab. air	ΔK = 2.7 MPa $\sqrt{m}$ ΔK = 4.7 MPa $\sqrt{m}$	{100} <110> {100} <100>	Etch-pitting
(116)	Al (single crystals)	Lab. air	K_{II} (ΔK_{th})	{111}	Laué x-ray
(117)	Al-Li alloy 20%-T8E41	Lab. air	ΔK = 11 MPa $\sqrt{m}$	{111}	Angle measure-ments
(118)	Al-Li-Cu-Zr (2029-T8)	Lab. air	$\Delta K = 2 \rightarrow 5$ MPa $\sqrt{m}$	{111}	Angle measure-ments
(119)	Nickel superalloy	Lab. air	$N_f = 10^4 \rightarrow 10^7$	{111}	Laué x-ray
(120)	Nickel-base superalloy (single crystal)	Lab. air	$\Delta K = 1 \rightarrow 3$ MPa $\sqrt{m}$ da/dN = 10^{-8} mm/cycle	{111} in zig-zag manner	SEM

Table (1.1)a (Cont'd)

Ref.	Material	Environment	Experimental condition	Facets plane and cracking direction	Identification technique
(42)	Nickel-base superalloy (MAR M004)	Lab. air, 20 °C 600 °C	da/dN = 10^{-3}→10^{-7} mm/cycle	{111} {100}	Laué x-ray
(121)	Nickel-base superalloy (API. IN718 N901)	Lab. air 20 °C, vacuum	ΔK = 10→12 MPa √m	{111}, {100} more {111} in vacuum	
(53)	316 stainless steel	Lab. air	ΔK = 5.5→30.0 MPa √m	{111}	Laué x-ray
(123)	Copper (single crystal)	Lab. air	near threshold	{111}	trace analysis
(111)	316 stainless steel	Lab. air	da/dN = 10^{-6}~10^{-7}	{100} <110> more often {110} <100> less	etch-pitting
(111) and section (3.3.2)	α-brass (70-30)	Lab. air	da/dN = 10^{-6}~10^{-8} mm/cycle	{100} <110> often {100} <100> less often {110} <100> some {111} micro facets macro facets	etch-pitting
(111) and section (3.3.4)	Copper	Lab. air	da/dN = 10^{-6}~10^{-8}	{100} <110> some {110} <100> some {111} micro sheet facets often	etch-pitting
(124)	Copper	Lab. air	da/dN = 10^{-5}~10^{-7} mm/cycle	{110} often {100} less	TEM
(122)	Nickel-base (Inconel 706)	297 K and 4.2 K	da/dN = 10^{-6}→10^{-8} mm/cycle	Large facets less often observed at 4.2 K; fracture surface smoother at 4.2 K than at 297K	SEM

Table (1.1)b: Crystallographic facets of fatigue cracking in some b.c.c. metals

Ref.	Material	Environ-ment	Experimental condition	Facets plane and cracking direction	Identifica-tion technique
(96)	Fe-3 Si (single crystal)	Lab. air	ΔK = 10-30 MPa $m^{1/2}$	{100}	Laué x-ray
(125)	Duplex (α-γ) s.s. (KCR-171)	Lab. air	ΔK = 10 MPa $m^{1/2}$ da/dN = $5x10^{-7}$ mm/cycle	{100}	etch-pitting
(126)	β-phase of Ti-40V (single and poly-crystals)	Lab. air, dry argon	$\Delta K \approx 11$ MPa $m^{1/2}$ da/dN = 10^{-4}~10^{-5} mm/cycle	{100} with <110> or <012> striations {110} with <110> striations {111} with <113> striations	trace analysis
(127)	S38C steel	Lab. air	$\sigma_a \simeq$ 9.4 Kg/mm^2 N_f = 7.9 x 10^6	{112} <110> {112} <111> {110} <110> {100} <110>	etch-pitting
(128)	mild-steel (annealed)	Lab. air	da/dN = 10^{-6}~10^{-8} mm/cycle	{110} <111>	etch-pitting

Table (1.1)b (Cont'd)

Ref.	Material	Environ-ment	Experimental condition	Facets plane and cracking direction	Identifica-tion technique
(129)	Pure iron	Lab. air	low $\Delta\epsilon$	{110} <111> {112} <111>	selection area diffraction analysis
(130)	Low carbon steels	Lab. air	stage I	{110} <111>	etch-pitting
(131)	Pure iron	Lab. air	plane bending fatigue	along the slip plane and in the slip direction of one of the dominating slip systems of the grain	
(95)	Fe-26% Cr - 1% Mo (single)	Lab. air	$\Delta K \approx 10$ MPa $m^{1/2}$ $da/dN = 10^{-6}$ mm/cycle	(001) [110] (001) [100] (110) [001]	trace analysis; SEM
(94)	Fe-3 Si (single)	Lab. air	stage II	{110} <112> (average direction)	trace analysis; SEM
(132)	Cu-47.6% Zn	Lab. air	$N_f = 10^5 \rightarrow 10^7$	{110} $\pm$ 10°	Laué x-ray

Table (1.1)c: Crystallographic facets of fatigue cracking in some h.c.p. metals

Ref.	Material	Environment	Experimental condition	Facets plane and cracking direction	Identification technique
(97)	α-titanium 155	Lab. air	ΔK = 5→14 MPa $m^{1/2}$	(0001) ± 5°	SACP
(99)	Ti-8Al-1Mo-1V	Vacuum ($2x10^{-7}$ torr)	ΔK = 1.1→100	two {1120} examples	Laué x-ray
(99)	Ti-8Al-1Mo-1V	3.5% NaCl solution	ΔK = 1.1→100	{0001} and 15° from {0001} at low ΔK	Laué x-ray
(133)	Ti-6Al-4V Ti-4Al-4Mo 2Sn-0.5Si	Dry air Moist air	$N_f = 10^7$	15° from (0001), {10$\bar{1}$7}	Laué x-ray
(102)	α-titanium	Lab. air	ΔK = 6~20 MPa $m^{1/2}$	{10$\bar{1}$0} <11$\bar{2}$0> {11$\bar{2}$0} <0001> (0001)	SACP
(104)	α-titanium	Lab. air	da/dN = 10^{-7} mm/cycle	macro and micro facets with {1010} {1120} and (0001) orientations	SEM + stereo-photographic observations
(134)	α-titanium (commercial pure)	Lab. air	$\Delta\epsilon$ = ± 0.008 $\Delta\epsilon$ = ± 0.003	(000$\underline{1}$) {1$\bar{1}$00} {1120} (000$\underline{1}$) {1$\bar{1}$0$\underline{0}$} {1011} {1120} {11$\underline{0}$2} {1123}	Laué x-ray

1.1.15 Mechanisms Proposed for Explaining Crystallographically Faceted Fatigue Propagation at Low Crack Growth Rates

1.1.15.1 Discontinuous Cleavage Model

The mechanism of fatigue crack growth by discontinuous cleavage was first proposed by Forsyth (135), based on the finding of the brittle striations observed on {100} crystallograpic facets of high strength aluminium alloys. This mechanism envisages the crack propagating on the favoured cleavage plane during the tensile cycle until it is blunted by plastic flow. Work-hardening promotes the resharpening of the crack tip in the compressive cycle, which permits cleavage to occur on the next tensile portion of the load cycle.

In addition, Thompson and Craig (115), from a case study of a commercial 2219 aluminium alloy, identified {111} as the plane of fracture and concluded that discontinuous cleavage along these planes led to brittle striation formation.

The infrequent occurrence of true cleavage fracture in aluminium alloys led to uncertainty concerning the most likely plane across which cleavage could occur. Moreover, the evidence of extensive slip associated with fracture paths were observed frequently, a number of investigators (e.g., 74) hence, expressed doubt to the operation of a true cleavage mechanism, particularly for f.c.c. metals fatigued in the low crack growth regime.

1.1.15.2 Glide Plane Decohesion Model

Primarily, the term glide plane decohesion is used to describe that single crystals of pure metal may, when plastically deformed, glide apart along slip planes. If this process continued on the same plane, it leads eventually to the specimen parting along a glide plane. Beachem (136) pointed out that this mode of separation, whether on a macroscopic or microscopic scale, and whether or not it continued to completion, should be appropriately called glide plane decohesion when the glide surfaces can be identified.

Stage I fracture is usually considered to be shear-induced because it either occurs on a crystallographic slip plane or on surfaces of maximum resolved shear stress. This viewpoint was supported by the relatively featureless stage I fracture surfaces and by the evidence for rubbing. However, Gell and Leverant (119), from a case of study of a high-strength nickel alloy tested in pulsating tension at room temperature, found that stage I fatigue crack propagation occurred on {111} planes and preferentially in <110> directions, and that the fracture facets were highly reflective and exhibited many features similar to tensile cleavage in b.c.c. and h.c.p. materials. They therefore suggested that local normal stresses, as well as shear stresses, control the growth of this stage I faceted cracking. They further explained that the faceted appearance results from a glide plane decohesion mechanism in which reverse slip on a limited number of slip planes ahead of the advancing crack

front weakens the cohesive strength of atomic bonds in this small region (119). When the slip planes have been weakened sufficiently, low tensile stresses initiate local separation thereby resulting in a crystallographic appearance (119).

1.1.15.3 Alternating Slip Models

Models for explaining the formation of facets, such as those proposed by Pelloux (81) and Neumann (82), involves alternating slip activity, i.e. {111} slip leading to a {100} plane of separation in aluminium and copper. The details of these models have been described in section 1.1.9. From their observations of near-threshold cracking in several alloys, Baïlon et al. (110) concluded that the crystallography of crack propagation identified often agrees with a model of crack propagation by alternating slip at the crack tip. However, they also pointed out that such models have been employed primarily to explain the formation of the crystallographic striations in stage II and their applicability to the discontinuous crack growth which occurs in the near-threshold region can be questioned. Baïlon et al. (110) noted that near-threshold fractographic aspects were particularly similar to those produced by transgranular stress-corrosion cracking, while certain aspects of the surface were more consistent with a cleavage-type fracture. Therefore, they suggested that more detailed confirmation of this alternating slip mechanism appeared highly desirable.

1.1.15.4 Fine Scale Decohesion Along Slip Planes

The studies of detailed microfractography and crystallography of near-threshold fatigue for f.c.c. (111) and b.c.c. (145, 360) metals and for α-Ti (104, 145), performed at Ecole Polytechnique have clearly confirmed that near-threshold fatigue cracking in metals usually occurs by fine scale decohesion along slip planes. Decohesion on alternating slip planes is often favoured, while larger decohesion steps on individual slip planes occurs in some metals for extremely low crack growth rates. The experimental results performed as part of the present study and further discussion associated with this mechanism will be presented in chapter 3.

1.1.16 Intergranular Cracking at Low Propagation Rates

For fatigue tests in laboratory air, some intergranular cracking has been observed in the near threshold region corresponding to the knee of the log da/dN-log ΔK curve. The occurrence of intergranular cracking has been observed in different metals including in some carbon and alloy steels (19, 137, 138), copper (10, 139), α-brass (10, 140), 316 stainless steels (110, 141) and α-Ti (104, 142). Two possible mechanisms for this intergranular cracking have been proposed.

One is that intergranular cracking results from grain boundary embrittlement by an enviromental effect (10, 138, 139), such as atomic hydrogen, produced by the dissociation of water vapour in contact with the fresh fracture surfaces and

transported to grain boundaries by dislocations.

Usually the intergranular facets disappear above or below a certain da/dN value (10, 137, 143) which is consistent with these facets being produced by an hydrogen-embrittlement effect involving hydrogen swept to grain boundaries by dislocations (143, 144). For tests in vacuum on both copper (141) and 70 Cu-30 Zn (145), the intergranular cracking has been found to completely disappear, clearly indicating that for these two f.c.c. metals the intergranular cracking is indeed an environmental effect.

Tests in vacuum reported by other researchers (146), however, indicate that the amount of intergranular cracking can be as high as approximately 30% when at the cyclic plastic zone size is equal to the grain size in the absence of an environmental influence in a commercially pure steel. Moreover, no intergranular cracking was observed for a microstructure containing highly dislocated lath martensite of a quench-and-tempered high strength steel tempered at 300°C fatigued in laboratory air (143). Therefore, it has been suggested that the cyclic crack tip plasticity and its relationship to the microstructure can also be important in promoting the occurrence of intergranular cracking in fatigue tests.

The second mechanism proposed is that intergranular cracking occurs when the cyclic plastic zone size d_{cpz} is comparable to the grain size d (or the prior austenitic grain size for quenched and tempered steels) as a result of strain incompatibilities or dislocation pile-ups in the grain boundary regions.

The results on steels reported by some investigators (137, 146, 147) indicate that good correlation exists between the occurrence of a maximum in the amount of intergranular fracture and d_{cpz}=d. Cooke et al. (137) observed a maximum in the percentage of intergranular fracture (approximately 60%) at d_{cpz}=d in a quenched-tempered medium carbon steel, and it was attributed to the consequence of reverse crack tip plasticity rather than a tensile tearing fracture mode. Several later studies (e.g. 10, 138, 148), however, found no correlation between grain size and plastic zone size and the occurrence of intergranular cracking.

The observations of Congleton et al. (140) showed the presence of matching "extrusions and intrusions" as well as one-to-one matching of slip lines on the intergranular facets of α-brass tested in air for da/dN values of 10^{-5} to 10^{-6} mm/cycle. The occurrence of the intergranular cracking in this case was attributed by these authors to the inability of the grain boundary region to accommodate the imposed shape changes caused by plastic deformation.

The investigations of Ravichandran et al. (143) showed that the microstructure of a quenched-and-tempered high strength steel tempered at 550°C exhibited a partially transgranular faceted cracking and partially intergranular cracking at d_{cpz}=d, and suggested a mechanism involving transgranular planar slip leading to intergranular fracture in the next grain in microstructures exhibiting a low strain-hardening behavior and a relatively low strength. These authors further argued that the process of nucleation of intergranular fracture at d_{cpz}=d necessitates transgranular crystallographic slip either to promote a local hydrogen concentration or to cause a stress concentration by dislocation pile-ups at the grain boundary. They explained their observations of the absence of intergranular fracture at d_{cpz}=d in the microstructure tempered at 300°C as a consequence of the difficulty in promoting transgranular crystallographic slip for the high strain hardening behavior, resulting in both dislocation transport of hydrogen and dislocation pile-up being difficult. They hence concluded that transgranular planar slip leading to slip localization is essential in promoting intergranular fracture when the cyclic plastic zone size becomes equal to the prior austenite grain size.

1.2 FRACTOGRAPHY AND MECHANISMS OF ENVIRONMENT-ASSISTED CRACKING

Environment-assisted cracking refers to the cracking of materials under the combined action of stress and of a specific environment. The stress can be either the applied operation stress or the residual stress in the structure, and can be either static or cyclic. The environment, in which cracking occurs, can be liquid, including aqueous, non-aqueous and metallic liquids, or gaseous e.g. moist air, dry hydrogen, hydrogen sulphide, chlorine, etc. Environment-assisted cracking mechanisms involving a cooperative interaction between a static stress and the environment include stress corrosion cracking (SCC), hydrogen embrittlement (HE) and liquid metal embrittlement (LME). If the stress is cyclic or fluctuating, then the term corrosion fatigue is employed.

Since the discovery of "season cracking" of cartridge brass in ammoniacal environments in the early 1920's (149), numerous alloys have been found to suffer premature fracture in various environments. The long history of the study of environment-assisted cracking of metals and alloys has resulted in many proposed mechanisms for explaining this cracking phenomena. It is not within the scope of this section to cover all of these materials. The objective of this section is to focus on some of the environment-assisted cracking mechanisms which can produce

crystallographic cracking characteristics.

1.2.1 Fractography and Mechanisms of Stress-Corrosion Cracking

Stress-corrosion cracking (SCC) is a failure phenomenon that occurs because of the simultaneous presence of tensile stress, an environment, and a susceptible material. The susceptibility of a material to SCC depends on many variables, such as strength, microstructure, magnitude of the applied stress, the nature of the corrosive environment and grain orientation (longitudinal or short transverse) with respect to the principal applied stress.

Stress-corrosion cracks normally initiate and propagate by tensile stress, however, compressive-stress corrosion cracking has been observed in a 7075-T6 aluminium alloy and a type of 304 stainless steel (150). As well, SCC has also been produced in torsion (shear) testing (144). Stress-corrosion cracking is a complex phenomenon. Despite the intensive investigative effort since 1940, the basic fracture mechanisms are still not completely understood. Indeed, as Staehle (151) has pointed out, "A general mechanism for stress-corrosion cracking seems to be an unreasonable and unattainable goal, specific processes appear to operate under specific sets of metallurgical and environmental conditions". It is generally accepted that SCC may involve both hydrogen assisted cracking and electrochemical processes that operate in parallel.

1.2.1.1 Crack Growth Response in SCC and HE Cracking

Many published data showed that SCC and HE cracking kinetics generally follow a characteristic pattern, namely the three stage curve of crack propagation rate, log da/dt, versus crack tip stress intensity factor K, as illustrated schematized in Fig. 1.12. These three stages are indicated in this figure and consist of two strongly K-dependent stages (stage I and III) joined by a K-independent stage II (152).

In stage I, crack growth begins from an apparent threshold K_{ISCC}, and the crack growth rate subsequently increases rapidly with increasing K. The threshold level K is dependent on environmental, compositional and microstructural factors. In this stage, the environmentally active processes are thought to be sufficiently fast to supply the embrittling species to the crack tip region, and the rate is determined by the mechanical process, e.g., by plastic deformation at the crack tip.

Stage III crack growth rates again increase rapidly with increasing K. This region of growth corresponds to the onset of crack instability (i.e., K approaching K_C), where the rate of crack growth "oustrips" the transport of the environment to the crack tip, and is thereby completely controlled by the purely mechanical process of fracture.

The K-independent stage II is the most useful stage for identifying the rate limiting chemical process(es). The usefulness of this stage is based on the fact that the crack growth rate becomes independent of the mechanical driving force, which indicates that the crack growth rate within this stage is controlled by some appropriate chemical process(es). It is therefore possible to study the variation of velocity da/dt in stage II with temperature, pressure and other environmental variables, in order to reveal the controlling kinetic process(es) such as the phenomena of transport or diffusion of H or the adsorption of ions at the crack tip (153).

The case of a K-dependent stage II crack growth response is also possible, and appears to be associated with the alloy conditions and to reflect a rapid transition from stage I to stage III.

1.2.1.2 Macroscopic Aspects of Environmentally Assisted Cracking

Macroscopically, fractures produced by environmentally assisted cracking always appear brittle, exhibiting little or no ductility even in very tough materials. It is generally difficult to identify cracking produced by SCC, HE, LME or corrosion fatigue only by macrofractography.

The area of slow crack growth often contains corrosion products or deposits or is stained or otherwise discolored with respect to the area of final fast fracture. However, some environmentally assisted cracking fractures are not stained or discolored, especially in materials with good corrosion resistance.

For many cases of stress-corrosion cracking and for some cases of other types of environmentally assisted cracking, considerable crack branching can occur, which can often be observed macrofractographically. Such crack branching is a strong indicator of environmentally-assisted cracking, although its absence cannot be taken as proof that the cracking was not environmentally-assisted.

Macroscopic crack branching is related to the occurrence of a plateau (i.e., stage II) in the curve of crack velocity versus stress intensity factor, which permits cracks of different lengths to propagate at the same velocity, as well as to a sufficiently high K value so that sufficient elastic strain energy can be released to permit the simultaneous propagation of more than one crack (152, 154).

Macroscopically visible hill-and-valley lines which are perpendicular to the crack propagation direction and appear to correspond to previous crack front positions can also be observed on the fracture surfaces of some hydrogen embrittlement failures of high-strength steels (108); however, such lines are also

found in the case of ductile fractures of such materials.

More crack branching and a more irregular aspect of the crack front usually occur in stress corrosion cracking in comparison with corrosion fatigue cracking. Stress-corrosion fractures that result from hydrogen embrittlement closely resemble SCC fractures macroscopically, however, stress-corrosion cracks usually exhibit more secondary cracking, pitting and corrosion products. It must also be noted that pitting and corrosion products can be present on a clean hydrogen embrittlement fracture exposed to a corrosive environment (108).

1.2.1.3 Microfractography of SCC

The typical microfractography of stress-corrosion cracking is either intergranular facets or transgranular highly crystallographic facets having an aspect suggesting a cleavage-like propagation.

The factors controlling the transition from one fracture mode to the other can be relatively complicated. In general, which of these two types of fracture modes is produced can depend on the material, the environment, the degree of cold work, the stress intensity factor, the applied electrochemical potential, the testing temperature and so forth. Some of the factors which influence the fracture path will be described in the next sections.

1.2.1.3.1 Intergranular Stress-Corrosion Cracking (ISCC) Aspects

The intergranular facets produced in SCC are generally smooth and relatively featureless, however, different types of line markings (155) have been found on some intergranular fracture facets.

In a small number of cases, striations which are consistent with crack arrest markings have been reported for aluminium alloys (156).

Slip traces and shear bands at times were found on intergranular facets produced by stress-corrosion cracking (156). The presence of the lines of crystallographic protrusions along slip traces as well as the nucleation of transgranular cracking along some slip traces has also been observed (156). These features on intergranular facets in SCC are similar to those observed frequently for near-theshold fatigue cracking.

On the other hand, based on the examination of opposite fracture facets of intergranular stress-corrosion cracking of 70Cu-30Zn α-brass tested in the ammoniacal solutions, Pugh et al. (157) found no matching aspect of the parallel markings commonly observed on the intergranular facets. They suggested that such markings could be slip steps produced after the SCC process.

1.2.1.3.2 Transgranular Stress-Corrosion Cracking (TSCC) Aspects

More studies have shown that the transgranular stress-corrosion cracks follow definite crystallographic planes, and most fracture surfaces are cleavage-like in appearance. They are characterized by a series of flat, parallel facets separated by crystallographic steps which are frequently serrated. These steps can multiply on crossing twin or grain boundaries and generally change directions. By delineating the crack front with the application of stress pulses it has been shown that the steps are approximately perpendicular to the crack front (157). Examination of SEM stereo pairs shows the occurrence of undercutting of the steps (158), and the steps on opposite fracture surfaces generally match apparently perfectly in an interlocking manner (158). These steps at times form "herring-bone" river line patterns which are commonly found for conventional cleavage of brittle solid (158). Fan-shaped patterns of river lines spreading out from a point or small region at the grain boundary can also be observed in a range of stress intensity K_I, indicating that the crack propagates more rapidly within a grain than across a grain boundary (112).

Another important fractographic feature reported on the transgranular facets is crystallographic striation markings which are often present, some of which have been found to strongly resemble the aspect of cyclic cleavage features (112, 159), suggesting that transgranular stress-corrosion cracking propagates by small discontinuous cleavage-like jumps. That these striations correspond to crack arrest

sites has been verified from the interaction of the river lines with the striations (112). Also, acoustic-emission (157, 202), electrochemical transient (202) and load pulsing experiments (157) have indicated that the TSCC is discontinuous in nature.

Although some fractographic features indicate that TSCC occurs by a discontinuous cleavage-like process, other features reported are not completely consistent with the characteristics of a real cleavage fracture surface in a brittle crystals. For instance, Kaufman and Fink (160, 161) noticed that the primary cleavage facets are much rougher than those which comprise the fracture surfaces of brittle solids, and that a significant number of cleavage steps appear to originate from and/or disappear into the cleavage facets at least in copper-base alloys, which is not observed for truly brittle fractures.

1.2.1.4 Crystallography of TSCC

Since the transgranular stress-corrosion fracture surfaces generally consist of flat parallel facets separated by steps, much attention has been paid to the crystallography of TSCC in order to shed further light on probable TSCC mechanisms. Meletis and Hochman (162, 163) as well as Dickson et al. (112) have reviewed this aspect.

1.2.1.4.1 Crystallography in b.c.c. Metals

The TSCC fracture plane identified in b.c.c. metals is generally {100}, e.g., for β-brass tested in distilled water (164), the β-Ti-13V-11Cr-3Al alloy in the NaCl solution (165), and in CH_3OH/HCl solution (166). Many SCC failures in steels occur by means of intergranular separation, and therefore limited information exists concerning the TSCC mode. Transgranular cracking observed in steels has often been reported as "cleavage-like" or "quasi-cleavage", but we know of no studies performed to identify the cracking crystallography (162). It is well known, of course, that b.c.c. metals exhibit {100} cleavage. It also was reported, however, that the path of HE facture for pure iron was on {110} slip planes (167), while for Fe-2.6% Si it was on a {100} plane in a <110> direction (168).

1.2.1.4.2 Crystallography in h.c.p. Metals

The fracture path of SCC in hexagonal close-packed (h.c.p.) metals and alloys is usually transgranular. The orientation of the stress corrosion fracture plane, however, has been determined only for a few h.c.p. alloys.

Beck and Blackburn [ref. 73 in (162)], using standard back reflection x-ray techniques, determined the cracking plane in coarse-grained specimens of a Ti-8Al alloy fractured in air and by SCC. In both cases, the cracking plane was described by a 12°-14° rotation from the base plane about $[1\bar{2}10]$, and therefore was a plane

of the $\{10\bar{1}7\}$ or $\{10\bar{1}8\}$ type. The results reported in other studies on Ti-5Al (169) and Ti-7Al-2Nb-1Ta (162) appear to be consistent with the failure of the α-Ti alloys tested either in air or under SCC or HE conditions occurring by cleavage on $\{10\bar{1}7\}$ or $\{10\bar{1}8\}$ plane. This plane is a hydride habit-plane in Ti-Al alloys, and therefore indicates that stress corrosion cracking occurs through the thin plates of the hydride phase.

Transgranular cracking of pure Zr and Zircaloy-2 and -4 in several environments has been reported by Cox (170). The cracking plane was not identified, but the geometry of the fracture suggested that cleavage was taking place on or near the basal plane. The metallurgical similarities between Zr and Ti suggest that Zirconium-base alloys may also exhibit $\{10\bar{1}7\}$ cleavage, therefore, the formation of hydrides is also considered to be the cause of transgranular cleavage in these alloys (171). However, Beavers et al. (172) investigated SCC of pure Zr and Zircoloy-2 and -4 in HNO_3 by slow strain rate and constant strain techniques and reported that fracture occurred on the basal plane or in one of the planes having a $<10\bar{1}0>$ zone axis. These authors argued that since the electrochemical potential range in which cracking was observed was considerably more noble than the hydrogen reversible potential in this environment, their results did not support a hydrogen model for cracking.

1.2.1.4.3 Crystallography in f.c.c. Metals

There is a particular interest in face-centred cubic (f.c.c) metals and alloys since they have multiple slip systems and do not readily cleave. However, many f.c.c alloys exhibit cleavage-like mode of cracking under SCC conditions. Therefore, a number of attempts have been made to determine the crystallographic character of the cleavage-like facts and steps in these metals in an effort to relate them to the underlying SCC mechanism(s). Some of the principal results on the crystallography of TSCC in f.c.c metals which have been published are given in Table (1.2).

Table (1.2): Crystallography of TSCC in some f.c.c. metals

Ref.	Alloy	Environment	Cracking planes and cracking directions	Identification technique
(173)	Cu_3Au (single crystals)	$FeCl_3$ sol.	{110} fracture facets {111} serrated steps	Laué x-ray
(174)	Cu-15% Au Cu-25% Au (ordered and disordered)	1. 0.13M $FeCl_3$ sol. 2. 0.6M NaCl sol. 3. IN Na_2SO_4 - 0.01 **N** H_2SO_4 sol.	{110} fracture facets {111} serrated steps	measurement of angle and single-surface trace analysis
(175)	Cu-25% Au (single crystals)	0.6M NaCl sol. E=300-430 mV (SCE) (precludes HE)	{110} <100> {110} <110> {110} <112>	electron channeling patterns and trace analysis
(176)	Cu-1Be (single crystals)	Ammoniacal aqueous solution	{123} crack plane for [111] axial orientation {110} crack plane for [110] axial orientation	trace analysis
(177)	Cu-1.8Be	Ammoniacal aqueous solution	{112} for aged to peak harden {111} for the overaged	measurement of facets angles
(172)	Admiralty brass	Ammoniacal aqueous solution	{110} primary facets {111} step facets	two-surface trace, photogrammetric techn.
(163)	Cu-30 Zn pure Cu	14N NH_3 sol. 1M $NaNO_2$ sol.	{111} crack initiation {110} facets (propagation) {111} step facets (propagation)	electron channeling patterns
(178)	Copper (single crystals)	IM $NaNO_2$ sol. E = 0V (SCE)	near {110}	trace analysis
(179) (180)	Cu-30 Zn	both neutral and 15N ammonia solutions	{100} low K_I {111} high K_I {110} high K_I	measurement of facets angles
(181)	Al-5.5 Zn - 2.5 Mg	NaCl aqueous solution	{110} primary facets {111} step facets <112> direction	two surface trace analysis photogrammetric techn.

Table (1.2) (Cont'd)

Ref.	Alloy	Environment	Cracking planes and cracking directions	Identification technique
(168) (182)	Al-6 Zn-3 Mg (single)	liquid metals, distilled water, saturated KI aqueous sol. moist air	{100} <110>	Laué x-ray
(168)	Ni (single)	H_2 (gaseous)	{100} <110>	Laué x-ray
(183)	Al-4 Cu single	NaCl solution	{100}	trace analysis
(184)	Fe-20 Cr-20 Ni (single) Fe-20 Cr-12 Ni 304 S.S.	$MgCl_2$ (154 °C) solution "	large {100} facets small facets (less than 1 μm)	two-surfaces trace analysis
(185)	310 S.S. 304 S.S.	$MgCl_2$ (154 °) solution	{100} in 310 S.S. small and complicated facets near {211} or {110} orientations in 304 S.S.	photogrammetry and ECP
(186)	310 S.S. 316 S.S. (single)	$MgCl_2$ (154 °C) solution	{100} in 310 S.S. more irregular fracture surfaces in 316 S.S.	trace analysis
(187)	304 S.S.	$MgCl_2$ (154 °C) solution	{100} <110>	etch-pitting
(162) (163)	304L S.S. (single)	$MgCl_2$ (154 °C) solution	{100} primary facets, some secondary cracking on {110}	etch-pitting two surfaces trace ECP
(188)	304 S.S.	$MgCl_2$ (154 °C) solution	{110}	measuring angles between facets in SEM
(189)	304 S.S.	$MgCl_2$ (154 °C) solution	{100} {111}	etch-pitting HVTEM
(190)	316 S.S. (single)	$MgCl_2$ (154 °C) solution	{210}	trace analysis
(191)	Fe-25 Cr-20 Ni (single)	$MgCl_2$ (154 °C) solution	near {100}	two surfaces trace analysis

Table (1.2) (Cont'd)

Ref.	Alloy	Environment	Cracking planes and cracking directions	Identification technique
(192)	Austenitic S.S.	hot chloride environment	{111} initiation	TEM
(193)	304 S.S.	$MgCl_2$ (boiling aqueous sol.)	{111} initiation	TEM
(112)	310 S.S.	$MgCl_2$ (154 °C) solution	{100} <110> predominant {100} <100> less often {110} occasionally	etch-pitting and measurement of facets angles
(194)	316 S.S.	$MgCl_2$ (153 °C) solution	more {100}, less {110} in the directions of <100> or <110>. {111} micro shear facets	etch-pitting

From Table (1.2), it can be seen that there seems to be some agreement concerning the crystallography of stress corrosion cracks in f.c.c. metals, e.g.:

- Stress corrosion cracks in f.c.c. metals initiate along or at {111} slip planes, as a result of dissolution;
- In copper-base alloys, cracking on {110} is favoured;
- The fracture facets in austenitic stainless steels appear to be principally on {100} planes. However, in steels with lower Ni content, the fracture surfaces morphology becomes more complicated and the cracking facets are generally very fine complicating their identification;
- The crystallographic steps are usually of {111} orientations.

Nevertheless, it also can be seen that some results are contradictory. Furthermore, because of the limitations of the identification techniques, there is considerable difficulty in the determination of orientations for very fine fracture facets. In addition, the detailed information of the crystallography of stress-corrosion cracking should include at least the fracture planes and crack-growth directions, as well as the orientation of the fracture facets with respect to the stress axis. More information on these aspects is desirable for establishing the cracking mechanisms.

1.2.1.5 Mechanisms of Intergranular Stress-Corrosion Cracking (ISCC)

Many models have been proposed to explain the mechanisms of ISCC. For the SCC of mild steels in carbonates (as well as in other environments), the models have been summarized by Duquette (195) as involving preferential dissolution of grain boundary material; preferential adsorption of selected anionic species at the grain boundaries resulting in a reduction of cohesive energy; hydrogen-assisted cracking; stress-assisted intergranular corrosion and preferential film rupture at grain boundaries. Based on the recent investigation in his laboratory on ISCC of mild steels in carbonate solutions (195), he emphasized that, for most metals and alloys, the stress (and strain) distributions are most severe at grain boundaries rather than in individual slip bands and accordingly, dislocation densities are higher at grain boundaries. Since the dislocation cores are in a higher energy state than the

surrounding structure, hence, preferential corrosion should occur at dislocation accumulations, and therefore at grain boundaries.

1.2.1.6 Mechanisms of Transgranular Stress-Corrosion Cracking (TSCC)

A number of investigators have considered fracture mechanism which can explain apparently brittle transgranular stress-corrosion cracking in f.c.c. metals and alloys. An attempt is made here to describe some of the mechanisms proposed recently to account for the fracture features of TSCC in f.c.c. metals and alloys. These models include those based on the effects of anodic dissolution, the effects of hydrogen and the effect of adsorption of other species.

For materials in which SCC via hydrogen absorption appears implausible (e.g., Cu and Cu-Zn alloy and certain austenitic stainless steels), there is considerable evidence suggesting that anodic dissolution is crucial to SCC crack propagation.

1.2.1.6.1 Film Rupture Model (Slip-Dissolution)

This model was widely accepted in the past. It was initially developed by Champion (196) and Logan (197) and has been extensively modified by other researchers. The central idea in this model is that a passive film forms on the crack walls and/or at the crack tip. The application of stress ruptures the film at

the crack tip and the crack propagates by a process of localized dissolution. As a result of an electrochemical potential difference between the new exposed metal surface and the passive film, a small electrical current is generated between the anodic metal and the cathodic film. The relatively small area of the new metal surface compared to the large surface area of the surrounding passive film results in an unfavorable anode-to-cathode ratio. This causes a high local current density and induces high metal dissolution at the anodes as the new metal protects the adjacent film from corrosion. If the exposed metal surface can form a new passive film (repassivate) faster than bare metal surface is created by film rupture, the corrosion attack will stop. However, if the repassivation process is suppressed, as in the presence of chlorides, or if the repassivated film is continuously ruptured by strain, the localized corrosion attack proceeds (198-200). The kinetics of repassivation, hence, determines the SCC susceptibility of a metal in a specific environment (200).

In terms of the principle of this dissolution model the maximum crack growth rate (v) can be related to the Faraday's law to a crack tip anodic current density (i_a):

$$v = \frac{i_a . m}{Z . F . \rho} \qquad [1\text{-}9]$$

where m = the atomic weight of the metal,

F = the Faraday constant,

Z = the number of electrons involved in the dissolution of metal,

ρ = the density of the metal dissolving.

This equation has been verified for cases usually of intergranular SCC in some metal and alloy/environment systems, e.g., by Ford (198) and Parkins (201). However, some investigators (202, 203) pointed out that for transgranular stress corrosion cracking of certain f.c.c. metal and alloys, e.g. α-brass in ammonia, copper and copper-gold alloys in nitrate solutions, the calculated crack growth rates according to Faraday's law are considerably lower than those found from experiments.

Flanagan et al. (204) recently reported that in the passive domain, transient currents resulting from crack advance during TSCC of Cu-25 at% Au in 0.6M NaCl aqueous solution were analagous to transients observed during surface scratching in the same corrosive environment hence they argued that crack-related deformation could lead to enhanced dissolution in the newly-formed crack portion.

Duquette (195) also postulated that the synergism between corrosion-enhanced deformation and deformation-enhanced corrosion may be the reason for

the generally poor correlation that is generally reported between calculated corrosion rates at crack tips and measured crack advance rates.

Some new evidence and considerations supporting a TSCC mechanism based on the effect of anodic dissolution on the slip process at the crack tip have also been published. Studies (160, 161) on Cu-30 Zn α-brass have indicated that no TSCC occurred in the absence of anodic dissolution. Jones (199) also showed the strong correlation between the amount of dissolution and the crack velocity, then proposed the SCC mechanism schematized in Fig. 1.13, emphasizing that relief of strain hardening at the crack tip surface by anodic dissolution reduces the fracture stress and facilitates nucleation of brittle cracks. However, it has been argued (175, 194) that the transition from the anodic dissolution to macroscopically brittle fracture is not obvious. As well, the formation of vacancies due to the anodic dissolution and the migration of divacancies on {100} or {110} planes has been postulated in this model, but there is no direct experimental evidence confirming the generation of the divacancies.

The major objection to a slip-dissolution mechanism of TSCC is that the interlocking fracture surfaces, cleavage-like morphology and crack arrest markings found in TSCC are difficult to explain by such a mechanism. Pickering and Swann (205) suggested that selective dissolution leads to the corrosion tunnel formation in

some systems and that cracking results from mechanical tearing of slots weakened by the tunnels. However, the fractographic features which should result are not compatible with those generally observed of cleavage-like facets (205).

In recent years, a number of new physical models (194, 202, 206, 207) have been proposed to explain brittle cleavage-like discontinuous cracking suggested by the fractography of TSCC in f.c.c. copper-base alloys and in austenitic stainless steels. All of these new models are also associated with the effects of dissolution at the crack tip enhancing cleavage cracking.

1.2.1.6.2 Film-Induced Cleavage

In the film-induced cleavage model (202, 203, 208), a thin layer of corrosion product (either a dealloyed layer or another passive film such as an oxide) forms at the crack tip. Such a film can be either brittle or ductile in nature, with lattice parameters different from those of the matrix metals. With a suitable combination of the lattice misfit and an appropriate coherency between the film and the matrix, a brittle crack developed in the thin film can run across the film/metal interface and penetrate into the matrix for a distance of the order of microns. The crack then arrests due either to plastic blunting or exhaustion of the driving energy. Consequently, a corrosion reaction takes place at the crack tip (Fig. 1.14). In TSCC of an alloy, such a reaction is the selective dissolution of the less noble

component, i.e. dealloying. In the case of a pure metal, this reaction can be active dissolution and the consequent repassivation. Once a film of a suitable thickness has been formed, the subsequent micro-cleavage event is imminent. Two assumptions have been proposed in this model: i) cracks attain a high velocity in the film and continue into the matrix at sufficiently high velocities that the generation of dislocations does not have time to blunt crack tips, and ii) the interface between the film and the matrix is sufficiently strong and coherent that cracks are not arrested at this interface.

This mechanism is supported by observations that pre-exposure of foils (~ 12.5 μm thick) of α-brass to an ammoniacal solution to produce a dealloyed film, and then immediately fracturing the foils at ~ 77 K (to freeze the solution and thereby remove any environmental effect during testing) resulted in cleavage-like fractures, foils which were not pre-exposured or not immediately tested after pre-exposure) were ductile at 77°K (208). Similar results were also obtained for fractures produced at room temperature.

Cassagne et al. (209) also obtained interesting observation on Cu_3Au single crystals tested in aqueous ferric chloride. This alloy undergoes TSCC on {110} planes in this environment, and the fracture surfaces resemble those produced in Cu-30 Zn. The work of Cassagne et al. has demonstrated that stressing the

exposed samples at room temperature, after the solution has been removed, causes fracture of the brittle dealloyed sponge produced at the external surface and its continuation with the ductile substrate. Therefore, these authors assumed that sponge formation assisted in nucleating TSCC cracks at a free surface.

The most troublesome feature of the film-induced cleavage model is, however, that up to now there has been no direct experimental evidence presented which shows that cleavage of the ductile matrix can start from the film, although this is suggested in one set of micrographs published by Cassagne et al. (386). In addition, since copper alloys do not cleave at high strain rates, and generally cleavage cracks in a brittle phase do not continue into an adjacent matrix when fracture of the matrix is not very sensitive to strain rate (210), therefore, the validity of a film being able to induce a ductile matrix to cleave is questionable.

1.2.1.6.3 Dissolution-Induced Lowering of K_{IC} for Cleavage

Very recently, Lichter et al. (175, 207) proposed a model for explaining the fractographic features observed and crystallography identified on TSCC fracture surfaces of Cu-25 Au single crystals tested in 0.6M NaCl solution at potentials between 300-430 mV (SCE) which preclude hydrogen embrittlement. This model employed fracture mechanics approach incorporating Stroh's pileup mechanism (211) for opening up a Lomer-Cottrell lock, but under conditions where the stress

state at the lock is modified by corrosion processes occurring at the main crack tip. Detailed calculations (175) indicate that if the corrosion action is concentrated along the active slip plane, forming a dog-leg crack which begins to grow towards a Lomer-Cottrell lock as shown in Fig. 1.15, the normal stress acting to open up the lock will increase while the shear stress acting to dissociate the lock is relatively unaffected. Moreover, the ratio of the normal stress to the effective shear stress at the lock increases with increasing length of dog-leg crack. These authors, therefore suggested that such a modification of stress state at crack tips by dissolution could have the effect of lowering the value of K_{IC} for cleavage cracking in f.c.c. ductile materials. The nucleated crack grows as a result of a "burst" of piled-up dislocation moving into the fractured lock. This model also postulated that continued growth is controlled by selective dissolution at the crack tip through its effect on K_{IC} and is not simply due to Faradic dissolution.

This model can explain the cracking crystallography identified on TSCC for Cu-25% Au (175) in that the crack propagation is anisotropic, with {110} <001> cracking being continuous and relatively rapid. It was also emphasized by these authors that because of the anisotropic behaviour of crack propagation, the average crack propagation rate is highly dependent on the crystallographic direction; however, the instantaneous crack velocity is essentially independent of growth direction, and is dependent on the electrode potential at the crack tip through its

effect on the rate of selective dissolution.

1.2.1.6.4 Dissolution-Enhanced Dislocation Mobility Leading to Pile-Ups at Lomer-Cottrell Barries for Microcleavage

Magnin (194) noticed that there are two different situations of TSCC in Cu-Au alloys and in austenitic stainless steels. One of these is that cleavage on {110} facets is favoured (175, 202) during TSCC in Cu-Au alloys, however, that fracture by cleavage on {100} facets and shearing on {111} facets is predominant in the stainless steels. Another difference is related to the important role of the selective dissolution in Cu-Au alloys (i) for the formation of a brittle de-alloyed layer which has been proposed to initiate the TSCC (202) and (ii) on the formation of the cleavage microcrack by a lowering of K_{IC} value (175). However, the case is different for passive alloys such as the austenitic stainless steels tested in Cl^- solution. Therefore, he pointed out the fact that the brittle transgranular stress-corrosion cracking of f.c.c. alloys cannot be explained by only one mechanism, and then he proposed a new physical modelization for explaining TSCC of 316 s.s. His model is based on the influence of the localized anodic dissolution on the enhancement of the plasticity at the crack tip. The formation of dislocation pile-ups and the conditions of restricted slip induce a brittle microcrack. The crack propagation is then limited and arrested by the strong effect of relaxation in the ductile alloy. Some details of considerations of this model is summarized in the

following.

The dislocation arrangements at the crack tip of ductile f.c.c. alloy without any corrosion was assumed as shown in Fig. 1.16. During SCC of this alloy in the $MgCl_2$ solution at the free corrosion potential, the following sequence of events was proposed by Magnin (194).

(i) Local breakdown of the passive film by slip emergence at the crack-tip.

(ii) Localized anodic dissolution of the bare alloy by an electrochemical coupling effect between the bare and the passive alloy. Moreover, the presence of Cl^- ions can delay the repassivation, which increases the amount of dissolution.

(iii) Preferential dissolution of the more stressed atoms just at the tip of the crack. This localized dissolution (which can be associated with adsorption) favours the formation of slip steps just at the crack tip, which induces a new stress concentration (Fig. 1.17a).

(iv) Activation of the dislocations emitted by the sources A because of the preferential dissolution of the atoms of the crack tip. Thus, the main role of the dissolution is to enhance the local plasticity by emission of more mobile type A dislocation.

(v) The formation of dislocation pile-ups due to the interaction between

the more mobile dislocations of source A and the dislocation bundles initially formed to accommodate the plastic zone at the crack tip and related to sources B and C (Fig. 1.16).

(vi) The local stress can increase markedly if the pile-ups are strong enough. The local stress σ_p can be expressed as (194):

$$\sigma_p = n\sigma = \left(\frac{2L\sigma}{\mu b}\right)\sigma \qquad [1\text{-}10]$$

where L is the length of the pile-up, μ the shear modulus, b the Burger's vector and σ the applied stress.

Magnin (194) pointed out that further slip can become restricted in the slip band where the pile-ups are formed because of the triaxial stress state and the previous hardening by sources B and C, and that this restriction will be particularly pronounced for materials with a low ability to cross slip.

(vii) Formation of a brittle microcrack, either by cleavage or by shearing. Cleavage on {100} facets can occur when σ_p reaches the critical stress $\sigma_c = 2\gamma/b$, where γ is the interfacial energy. Nevertheless, cleavage is not the only way to relax the stress, brittle shear can also be promoted before or during cleavage if the dissolution of the slip bands emanating from the crack tip is large enough (Fig. 1.17b).

Magnin also emphasized that the role of the anodic dissolution on the SCC is essential but indirect, and is related to the local enhancement of the plasticity and not directly to the initiation of a crack by corrosion. This proposition means that the rate of SCC is not only related to an electromechanical effect, which is consistent with the crack growth rate being often greater than that calculated from the anodic current density (212).

Lichter et al. (175) recently argued that the model presented by Magnin allows the possibility of microcleavage by dissolution-enhanced dislocation mobility leading to pile-ups at Lomer-Cottrell barriers, however, the model does not explain some of the morphological details, nor does it explain away Stroh's prediction of ductility.

1.2.1.6.5 Dissolution-Enhanced Atomic Mobility (Surface Diffusion)

A mechanism involving enhanced mobility of the atoms at the free surface of the cracks has also been recently proposed by Galvele (213). Since the difficulties of predicting the crack velocities quantitatively only by anodic dissolution mechanisms proposed in the literature are frequently experienced, Galvele invoked a mechanism whereby anodic dissolution was necessary for SCC but where the actual cracking process involved enhanced atomic mobility (surface diffusion) which occurred at the crack tip and relieved the stresses by producing trenches and

fissures perpendicular to the local tensile axis. The crack velocity is in this case a function of the surface mobility, which is related to the nature of the adsorbed layer and to the stress concentration at the crack tip.

The main merit of this model is that it retains the correlation between crack velocity and increased anodic dissolution during straining. However, the mechanism does not predict the crystallographic features of the TSCC fracture surfaces and is mainly related to a bidimensional surface film (194).

1.2.1.6.6 Models Based on Adsorption

Adsorption mechanisms are also referred to as stress-sorption which was extended by Uhlig (214, 215) to stress-corrosion cracking from the adsorption-based theory proposed by Petch and Stables (406) for hydrogen cracking of steels. This model explains brittle failure in SCC not by chemical or electrochemical dissolution of metal at the tip of a crack but by weakening of already strained metal atom bonds through adsorption of the environment or its constituents. The surface energy of the metal thus is considered to be reduced, encouraging the metal to part under tensile stress. This mechanism is related to the simplified Griffith criterion of crack formation which equates strain energy in the metal to the surface energy of the incipient crack area. Langmuir (407) showed that only a monolayer of adsorbate (e.g. oxygen atoms) is necessary to decrease affinities of surface atoms

for themselves or for their environment, specifically adsorbed species chemically bonded (chemisorbed) to the surface being especially effective in this regard. It is such adsorbed films which prevent cold welding of solids, including metals, placed in contact with each other.

Support of the view that stress sorption cracking is the prevailing mechanism in SCC of metals comes from the observations, such as specificity of environments causing cracking. For example, the addition of 5% $NaNO_3$ to a $MgCl_2$ test solution at 130°C extended the cracking time of cold rolled 18-8 stainless steel from 0.3 to 200 hours (215).

Meletis and Hochmann (163) presented a modified stress sorption model for explaining the crystallographic results identified in TSCC of three f.c.c. materials (copper, α-brass and type 304L stainless steel).

Firstly, they modified the explanation of Robertson and Tetelman (408) based on Cottrell-Lomer locks, and suggested that dislocations moving on two intersecting {111} slip planes can combine to produce <110> sessile Cottrell-Lomer dislocations, as shown in Fig. 1.18a, and that these sessile dislocations impede further dislocation motion and create dislocation pile-ups. Then, they suggested that selective dissolution at the sessile dislocation sites results in formation of a crevice

as shown in Fig. 1.18b. The combined result of the above processes is a high stress concentration at the crevice and especially on the {110} and {100} planes which bisect angles between slip planes.

Secondly, they took into account the possibility of adsorption at the crack tip on the highly stressed {100} and {110} planes with a subsequent reduction of the surface energy on these two planes followed by cleavage on the plane of lowest surface energy. They postulated that the different tendencies for cracking on {110}, {100} and {111} planes in different f.c.c. metals would be related to the surface energies of these planes. For austenitic steels, {100} plane, while for the copper-base alloys, {110} plane were postulated as those with the lowest surface energies by these authors.

It has been noted (112), however, that this explanation involving cleavage and Lomer-Cottrell locks is inconsistent with some crystallographic features identified by these authors themselves, such as a tendency for a preferred <110> crack propagation direction on a {110} plane for copper and 70-30 Zn α-brass alloy.

Moreover, it also has been argued that although some fractographic aspects of TSCC (e.g., the cleavage-like appearance, the evidence for discontinuous crack propagation), are reconciliable with the mechanism based upon the effect of

adsorption, this mechanism lacks credibility for SCC of copper alloys because the embrittling species has not been identified (409).

The adsorption-induced embrittlement model has been widely accepted for explaining the cracking of metals embrittled by liquid metals in that only specific solid metal-liquid metal couples are damaging, and also a tensile stress is essential. Since adsorption at room temperature is a relatively fast process, such a model can account for high crack propagation rates, which is the case for liquid metal embrittlement cracking.

Lynch (168) has proposed that stress-corrosion cracking, as well as hydrogen and liquid metal embrittlement, is due to the adsorption of an aggressive species at the crack tip which weakens the interatomic bonds, but results in highly localized easy slip. This model is described in section 1.2.2.6 in more detail.

1.2.1.6.7 Hydrogen Contribution to SCC

The hydrogen ions can result from the electrochemical reaction between the exposed metal and the solution at the crack tip, and the subsequent reduction of the hydrogen ions by the acquisition of electrons from environment can result in the formation either of atomic hydrogen or of hydrogen gas. Hydrogen protons can also enter into and diffuse in the metal. This absorption or adsorption of hydrogen

can produce localized cracking due to hydrogen assisted cracking mechanisms. As a general position, SCC should be viewed as comprising two parallel processes, one example of which is shown in Fig. 1.19. As mentioned formerly, at one extreme, anodic dissolution by film rupture by a stress-assisted process, or by some other localized process, and repassivation can certainly produce SCC phenomena. On the other hand, cracking due to hydrogen processes can be produced under suitable environmental conditions in some alloys.

It has been widely accepted that for example, the stress-corrosion fractures of most high strength steels in aqueous environments, and of aluminum alloys especially the 7000 series, in the high-strength T6 or underaged tempers in environments such as moist air, water and solution containing chlorides, are often thought to involve a hydrogen contribution (410, 411). Since the pH of the crack tips of SCC has been analysed in accordance with Pourbaix's potential-pH diagram (412) and have been measured (413) to be in the range of 3.5 to 3.9 in steels while the bulk solution varied between 2 and 10, and to be 3.5 for 7075 aluminium alloy. Such electrochemical parameters at the advancing crack front are such that water is thermodynamically unstable and hydrogen can be liberated. These acid conditions thus would easily drive hydrogen in critical crack tip volumes to induce HAC. But in most cases, SCC involves both anodic dissolution and hydrogen cracking. This has been suggested for austenitic stainless steels in hot chloride solutions as a

summary illustration in Fig. 1.19.

A number of hydrogen-assisted cracking mechanisms have been proposed. The application of these models is dependent on the material-environmental system as well as the testing conditions. These are described in the next section.

1.2.2 The Mechanisms and Fractography of Hydrogen-Assisted Cracking

The term "hydrogen-assisted cracking" (HAC) introduced by Beachem in 1972 (216), has been considered to be more descriptive than the term "hydrogen embrittlement" (HE) in concerning the variety of the effect of hydrogen on fracture phenomena. HAC is defined as the hydrogen-caused reduction of the load-bearing and/or the mechanical energy absorption ability of a metallic alloy.

The effect of hydrogen on the mechanical properties of metals and alloys has long been recognized (217). Much work has been expended on this very important technique problem to understand the role of hydrogen on fracture behavior, and hence resulted in various mechanisms proposed to date. These mainly include 1) the internal pressure theory; 2) hydrogen transport by dislocations; 3) decrease of surface energy by hydrogen; 4) hydride formation mechanism; 5) decohesion model and 6) hydrogen enhanced local plasticity (HELP) mechanism.

Even though there is still incomplete understanding of the basic mechanisms by which hydrogen related failures occur, there has been considerable progress achieved particularly in recent years. It has been generally accepted that there are several hydrogen-assisted cracking mechanisms rather than a single dominent mechanism, and that even within one material system, several of these mechanisms may be operative. An attempt in this section is to review briefly the first four models, and then to describe the last two mechanisms in more detail. Some fractographic features associated with these mechanisms of HAC in steels and in some other alloys are also presented in this section.

1.2.2.1 Internal Pressure Theory

This model was originally proposed by Zapffe and Sims (218) and later modified by a number of investigators including Telelman and his co-workers (219, 220). They assumed that the accumulation of molecular hydrogen in internal voids and cracks would exert a pressure which lowers the apparent fracture stress. It was estimated (220) that such internal hydrogen pressure can be as high as 10^5 atmospheres. Blister formation in steels under pressurized gaseous hydrogen is a typical example of this model (221). However, the pressure model is believed not to be generally representative of hydrogen embrittlement associated with corrosion.

1.2.2.2 Hydrogen Transport by Dislocations

Hydrogen transport by dislocations was first proposed by Azou and Bastien (222) and then developed by Tien et al. (223, 224). These authors assumed that hydrogen carried by moving dislocations would be stripped from the dislocations and deposited in other traps such as second-phase particle interfaces and grain boundaries, and there contribute to decohesion and embrittlement. They specifically suggested that for steel large supersaturations could develop, such that substantial pressures could arise in voids, promoting failure by a pressure mechanism. Observations of dislocation transport have been reported in terms of tritium release measurements performed during deformation and by autoradiographic techniques (225, 226). It has been evident that in plastically deformed nickel dislocation transport of hydrogen is the predominant mechanism and that the transport rates are several orders of magnitude higher than in unstrained nickel where lattice diffusion is the predominant mechanism. Therefore, the mechanism of hydrogen transport by dislocations could influence on the kinetic process controlling the rate of embrittlement, however, the dislocation transport or any other rapid transport process does not directly relate to the nature of the effects of hydrogen on fracture.

1.2.2.3 Decrease of Surface Energy

This model was proposed by Petch and Stables (216, 227) and was based on Griffith's thermodynamic criterion for the fracture of brittle materials. As

mentioned in Griffith's theory, the work done to cause a sharp crack equals the sum of the surface energy of the two sides of the resultant crack. It follows that the fracture stress will be proportional to the square root of the surface energy [1-6]. Petch and Stables (216) claimed that the embrittling effect of hydrogen was a result of the reduction in surface energy, which resulted from adsorption of hydrogen on crack surfaces.

This model is subject to many criticisms. For example, it greatly underestimates the work of fracture (210, 228) (plasticity effects are not addressed) and it cannot account for discontinuous cracking, as well as it cannot explain why oxygen, which has a greater heat of adsorption, not only fails to promote cracking but stops the hydrogen effect, to mention but a few criticisms.

1.2.2.4 Hydride Formation Mechanism

Westlake (229) first proposed that cracking could proceed by the formation and cracking of a hydride near the crack tip. Gahr et al. (230) elucidated this model, showed that the hydrostatic stress field ahead of a stressed crack tip could stabilize hydrides even when it is unstable in the absence of stress, and demonstrated embrittlement by hydride cracking in niobium. For iron, Baranowski (231) found that no hydride is stable up to a hydrogen pressure of 2 GPa, so this model is generally not considered for iron and steel.

This model has been further developed and established by Birnbaum et al. (230, 232). It has been found that brittle fracture contributes to hydrogen embrittlement in metals in which hydrides form, including the group V metals Nb, V, and Ta, alloys of Mg, Ti and Zr, and Pd (233). High-voltage TEM studies of crack growth in hydrogen-charged foils of vanadium (231) and zirconium (235) showed directly that fracture involved repeated formation and fracture of hydrides at crack tips. There is also evidence, such as striations on fracture surfaces indicating that crack growth is discontinuous (236). Thus, there is little doubt that brittle fracture of hydrogen-charged specimens involved repeated sequences of (i) hydrogen diffusion to crack tips under the influence of a stress gradient, (ii) nucleation and growth of hydride near the crack tip, (iii) cleavage of the hydride when it reaches a critical size, and (iv) crack-arrest at the hydride matrix interface (Fig. 1.20).

It has been shown that for niobium, bulk specimens of the hydride cleave along {110} planes, the same fracture plane as observed for specimens initially containing solute hydrogen (210). Furthermore, cleavage of hydrogen-charged niobium only occurs in strain-rate regimes where hydrogen has time to diffuse to crack tip regions, and at temperatures where the hydride is stable. This indicates that hydrogen embrittlement by stress induced formation of hydrides is restricted under conditions where the hydrides can form at a rate sufficient to preclude other

forms of failure (237). It is generally accepted that hydrides do not form during HAC in iron alloys, nickel (for low hydrogen fugacities) and aluminium alloys, and that hydrides can occur for titanium alloys and magnesium in some circumstances. Hence, the application of this model is limited.

1.2.2.5 The Decohesion Model

This model is one of the oldest and most commonly referred to mechanism of hydrogen embrittlement. This mechanism originated with Pfeil in 1926 (238) and was substantially extended by Troiano (239, 240) and later by Oriani (241, 242).

Troiano's theory of hydrogen embrittlement was that the "true fracture strength of the lattice was lowered, causing a loss in lattice cohesion (i.e. "perfect cleavage" was made easier) (243). In this theory, Troiano suggested that the electrons from the hydrogen ions would enter the d bands of the metallic cores, and that "the increase of the electron concentration of these bands produces an increase in repulsive forces between metallic cores, or, in other words, a decrease in the cohesive strength of the lattice". He also postulated that the accumulation of hydrogen at regions of positive triaxial stress ahead of the crack tip permits the attainment of sufficiently large local hydrogen concentration so as to reduce bond strength and facilitate the nucleation of microcracks within these regions.

Then, Oriani further modified the lattice decohesion concept and developed it into a semi-quantitative model (241, 242). He suggested that hydrogen-induced crack propagation can occur when the local tensile stress, σ_z (in mode I loading) just equals the local maximum cohesive force, F_m, per unit area, as reduced by the local hydrogen concentration. That is:

$$\sigma_z = nF_m\,(C_H) \qquad [1\text{-}11]$$

where n is the number of metal atoms per unit area of crack plane. Since the local stress at the crack tip, (σ_z), is related to the measurable macroscopic parameters, for example, expressed by:

$$\sigma_z = k'\,K/(\rho)^{1/2} \qquad [1\text{-}12]$$

where K is the stress intensity factor at crack tip, ρ is the macroscopic radius of the curvature of the crack, k' is a numerical parameter. Thus, the effect of hydrogen can be expressed using measurable parameters, such as:

$$k'.\,K/(\rho)^{1/2} = nF_m\,(C_H) \qquad [1\text{-}13]\ (242)$$

These theoretical considerations have been reported to be correlated experimentally in some tests where the decrease in critical stress intensity for crack growth with increasing hydrogen pressure was found to follow the calculated curve (244).

In recent years, atomistic calculations of crack growth in nickel using an "embedded-atom method" (245) indicate that adsorbed hydrogen can weaken interatomic bonds in hydrogen environment. Cluster calculations have also shown that the presence of impurity atoms can decrease the electron density between metal atoms thereby possibly reducing their interatomic bond strength (246, 247).

The most direct investigation of the validity of the decohesion model is that of Vehoff and Rothe (248). It showed that Fe-2.6% Si single crystals, underwent crack propagation on a (100) plane in a purely ductile, wedge-opening manner by the alternate activation of two {112} slip planes that intersect along the crack front in vacuum environment, and that if such crystals were exposed to hydrogen, the wedge angle decreased with increasing hydrogen chemical potential and the density of accomodation dislocations decreased. This experimental observation indicated that hydrogen has a greater influence on the occurrence of cleavage, thus is qualitatively consistent with theories for the competition between cleavage and blunting (249).

Also, there is strong evidence for a decohesion-type hydrogen-induced fracture at grain boundaries. McMahon and co-workers (250) have studied extensively the deleterious effect of hydrogen superposed on that of temper embrittling elements in quench and tempered alloy steels. They presented an

extraction replica transmission electron micrograph of a boundary embrittled by tellurium, sulphur and hydrogen that show no evidence for any local plastic deformation.

Nevertheless, there exists other evidence which is not in agreement with the decohesion model. Beachem, Lynch and Birnbaum claimed that a considerable amount of plasticity has been found on fracture surfaces produced by HAC. Accordingly, they proposed models based on hydrogen enhanced local plasticity (HELP) mechanisms.

1.2.2.6 Hydrogen Enhanced Local Plasticity (HELP) Mechanism

It was Beachem (243) who first suggested, on the basis of careful fractographic examination, that hydrogen embrittlement of steels was in fact associated with localized plastic deformation at the crack tip rather than the classical concept of co-linear parting of the lattice. This idea was resisted for a long time until revived by Lynch and by Birnbaum. In recent years, it has become evident that hydrogen "embrittlement" by means of locally enhanced plasticity is at least a viable mechanism of hydrogen assisted cracking.

Lynch (168, 182, 210) in his detailed metallographic and fractographic studies of crack growth in aluminium alloys nickel, iron-silicon, high-strength steels,

magnesium and titanium alloys in liquid-metal, aqueous and hydrogen environments found remarkable similarities between hydrogen-assisted cracking, stress-corrosion cracking and adsorption-induced liquid metal embrittlement. Usually, he observed dimples occurred on the fracture surfaces that failed in the liquid-metals and hydrogen environments. Even on the microscopically cleavage-like facets, very fine dimple-like features, less than 0.1 μm in size, were detected using replication TEM. Based on these findings, Lynch suggested that adsorption weakened the interatomic bonds at crack tips, thereby facilitating the generation of dislocations on a pair of slip planes symmetrically situated with respect to the crack plane and intersecting this plane parallel to the crack front, and that the coalescence of the growing cracks with voids formed just ahead of the crack front essentially re-sharpens the crack tip so that macroscopically brittle (transgranular cleavage-like) fractures are produced along a low-index crystallographic plane bisecting the two active slip planes. The schematic diagrams illustrating the adsorption induced localized-slip process proposed by Lynch is shown in Fig. 1.21. In terms of this model, if crack growth occurs in two <110> directions in f.c.c. and b.c.c. metals, steps (or river lines) parallel to these directions form herringbone patterns, as shown in Fig. 1.2.2, and which have been observed frequently by Lynch. Even though the microvoids are not always experimentally observed on fracture surfaces produced by environmentally-assisted fracture surfaces, the occurrence of locally enhanced plasticity due to the effect of environment could affect the fracture process.

The studies of Birnbaum and his co-workers showed that hydrogen, at least, can significantly alter the rate of dislocation generation in a variety of metals including Ni, Fe, Al and Ti alloys (251, 254) and lent further support to the HELP mechanism (237). These studies suggest that the distribution of hydrogen can be highly non-uniform under an applied stress. Moreover, the flow stress can be locally reduced, resulting in localized deformation which leads to highly localized failure by ductile processes, while the total macroscopic deformation remains small. At low resolution, the fracture surfaces will appear as "brittle" because of the highly localized nature of the ductile failure.

One consequence of the HELP mechanism is that the fracture surface is predicted to be that along which the shear localization occurs. In general, this is the slip plane, which has become evident. In-situ TEM observations for iron in the presence of hydrogen shown a flat fracture parallel to the primary {110} slip plane (233). Robertson and Birnbaum (252) observed crack propagation along active {111} slip planes for nickel in the presence of hydrogen by in-situ high voltage TEM, with the edges of the fracture ligaments parallel to either a <110> or a <112> direction.

The dynamic events occurred at the crack tip were recorded by video during in-situ TEM (252), which showed that crack advance was confined to the

deformation zone and occurred either by the direct emission of dislocations from the crack tip or by the nucleation, growth and coalescence of holes. The resulting fracture surface was a "zig-zag" interface composed of mating crystallographic ligaments of thinned material which were backed by a dense tangle of dislocations and thick material.

Birnbaum et al. (253) also observed by in-situ TEM that gaseous injection of hydrogen into iron foils increased the velocity of screw dislocations. The work of Kimura and co-workers (255) also clearly showed that hydrogen lowered the flow stress required to produce low strains in very pure iron at temperatures from about 200 K to room temperature but raised the flow stress at large strains or below 200 K.

The details of the dislocation morphologies in iron single crystals (256) during stage I plastic straining in the presence and in the absence of a concurrent supply of hydrogen showed that hydrogen can greatly enhance the tendency of strain localization (i.e., cause slip to become more coplanar). Near spherical inclusions around which hydrogen had accumulated, the dislocation arrays changed from multiple-slip, three-dimentional tangles to planar arrays of dislocations with one predominant slip system in the presence of hydrogen. From these observations, Bernstein et al. (256) suggested that hydrogen not only enhances the mobility of

primary screw dislocations, but also affects the local stress and strain associated with second phase particles. They also found that hydrogen-induced microcracks had an orientation similar to that of the strain localization bands, suggesting that a direct correspondence exists between the presence of hydrogen-induced strain localization bands and the initiation of hydrogen-induced cracks.

For the studies performed by in-situ TEM, it has been argued (257) that the observed effects of hydrogen may be due to the large fugacity of hydrogen produced by the electron beam dissociating and ionizing the hydrogen, which can generate large mechanical stresses and hence, large dislocation densities.

However, a number of investigators also have observed HAC to be connected with the process of plastic deformation on a more macroscopic scale. For example, Chu et al. (258) reported delayed plasticity for the high strength steel tested in water or in hydrogen gaseous environment at a mode I crack tip under a constant displacement and decreasing stress intensity during crack propagation, in which plastic flow spreaded from the crack tip until a microcrack was nucleated ahead of the main crack, the cracks then joined, and the process repeated, suggesting the incompatibility stresses associated with the plastic deformation was related to the microcrack nucleation. It has been argued (414), however, that the plastic deformation observed on the specimen surfaces may have been produced by

a crack tunneling effect. In another study (259), it was observed that strain-controlled, plasticity-related cracking in the presence of hydrogen occurred along surfaces of maximum shear stress within the prior austenite grains for a vacuum-melted laboratory heat of quenched-and-tempered steel which was relatively free of non-metallic inclusions. In this case, two types of fracture observed were glide-plane decohesion in martensitic laths and interface decohesion between lath colonies. Hirth et al. (260) also observed that the presence of plastic deformation occurred followed the macroscopic slip-line field in notched specimens of quenched and tempered steel.

Moreover, based on the atomic calculations of Daw and Baskes (261, 262), showing that the same phenomena that decrease the resistive force for the co-linear separation of metal atoms also decrease the resistive force for the shear separation, there is no reason why the shear fracture aspect cannot be simultaneously affected by the presence of hydrogen.

It has been noted that there is subtle difference between the proposals of Lynch and of Birnbaum et al., in that Lynch believes the effects of hydrogen are caused by surface effects due to adsorption while Birnbaum et al. consider the hydrogen effect to occur in the volume of the material as well as near the surface. However, both agree that the presence of hydrogen increases the localized plasticity

at the crack tip and leads to fracture (237).

An autocatalytic model for shear instability has been proposed by Hirth (263) based on observations of hydrogen-precharged specimens of higher carbon spheroidized steels under plane strain loading. In terms of this model, hydrogen enhances the onset of shear instability. In turn, the shear instability augments void formation by the plastic incompatibility effect. The voids further enhance the shear localization tendency (as observed by Bernstein et al.), and the process proceeds autocatalytically, lowering the strain to fracture, which occurs in a mixed mode I-mode II manner.

Essentially, we are faced with two apparently different models as far as the mechanism itself of HAC, i.e. the decohesion model and the hydrogen enhanced localized plastic deformation. A number of studies of detailed fractography of hydrogen assisted fracture have shown that these two models can occur. However, the question, such as what factors determine which mode of cracking will occur, is not yet well understood.

1.2.2.7 Fractographic Features of HAC

Hydrogen-induced fracture is usually thought of as brittle, and intergranular fractures are in fact common, but many materials exhibit ductile fracture (with

reduced ductility) in the presence of hydrogen. Transgranular fracture modes like cleavage or quasi-cleavage, can also occur in the matrix or through a precipitated hydride phase. The fractographic features of intergranular or transgranular facets produced in HAC generally are very similar to those produced by SCC, hence, in many cases, the mechanism of SCC is considered to correspond to HAC.

Thompson and Bernstein (264) have presented a "road map" of the fracture paths in HAC as shown in Fig. 1.23, which provides a useful summary of hydrogen sources, transport paths, destinations, and induced fracture micromechanisms, i.e. the physical fracture processes. Hydrogen tends to accumulate at grain boundaries, inclusions, voids, dislocation arrays, and solute atoms, and thus, HAC is controlled by those hydrogen accumulation sites that are able to act as favoured nuclei and/or propagation paths, facilitating hydrogen fracture and giving rise to the different fracture modes. Consequently, there is no single fracture micromechanism that is characteristic of HAC.

The effect of hydrogen on fracture of high strength steels at room temperature is very typical and important. It has long been recognized (216) that the fracture mode in the presence of hydrogen often depends on the stress intensity factor, K. There is a transition of fractography from intergranular to quasi-cleavage to ductile tearing with increasing stress intensity, although in some steels or for

certain conditions, the quasi-cleavage fracture can be at times absent (159). A decrease in the strength of the steel or a decrease in the test or service temperature tends to favour the occurrence of quasi-cleavage at the expense of intergranular cracking (265). An increase in amount of hydrogen adsorbed at crack tip region tends to favour the occurrence of intergranular cracking (266). In the presence of hydrogen, low K values favour intergranular cracking, because as K decreases, the associated local plasticity at the crack tip decreases, possibly inducing hydrogen to be able to diffuse fastest along grain boundaries which can act as effective traps for hydrogen in the hydrostatic stress zone ahead of crack tip. At intermediate K values, the quasi-cleavage fracture occurs possibly because hydrogen is distributed more uniformly in the hydrostatic stress zone and can effectively reduce the necessary fracture stress for cleavage by weakening atomic bonds or can effectively enhance localized plasticity giving rise to crystallographic transgranular cracking (or slip plane-decohesion) under a certain amount of restricted local plasticity (e.g., the transport of hydrogen possibly can be affected by planar dislocation arrangements). At high K values, because of more important plastic deformation occurring at the crack tip, possibly multiple-slip, three-dimensional tangles (256) of the dislocation arrays can force hydrogen to be trapped at the interfaces of second phase particles within grains, facilitating nucleation and growth of microvoids and resulting in a dimple ductile fracture surface appearance.

Beachem and Yoder (356) studied that the mating fracture surfaces developed by slow cracking in salt water as well as by rapid overload fractures in high strength steels in which the fracture occurs by microvoid coalescence. They observed that the major portion of the fracture surfaces in both the 13Cr-18Ni-2Mo steel and the maraging steel which they studied consisted of series of alternating ridges and valleys, which were perpendicular to the direction of local crack propagation. The ridges on one surface mated with the valleys on the other. They proposed a model involving tearing along alternating shear planes to explain the mechanisms of formation of the periodic ridges and valleys ("zig-zag" fracture) from their examinations of the size and shape of the mating dimples. They suggested that the crack advances along the first plane inclined to the macroscopic model I fracture plane (Fig. 1.24b), is then interrupted by a forward stretching step, which is followed by cracking along the second inclined plane, in terms of a sample tension-compression model within a constrained plastic zone, based on that dimples on one surface are stretched more than their mates as shown in Fig. 1.24a. According to this model, the zig-zag form of fracture is basically a continuous process in that a moving crack front is maintained, even though the plane of the crack changes orientation with crack length.

In the case of hydrogen giving rise to cleavage-like or quasi-cleavage in ferrite or in tempered martensite, the aspects of the facets observed generally are

similar to those observed for cyclic cleavage (109), with crack arrest markings and slip steps indicating a discontinuous propagation process. Moreover, crack reinitiation sites produced ahead of the macroscopic crack tip can at times be observed. This aspect can be the other indicator of the discontinuous crack propagation involved in HAC. For lower strength steels, embrittled by hydrogen charging (267), the brittled flat zone ($\approx$ 100 μm x 50 μm) was observed to have quasi-cleavage aspects typically containing ridges or river lines radiating from an inclusion, and to be surrounded and separated from each other by steeply inclined ductile tearing zones presenting some dimples.

The microfractographic aspects observed on the cleavage-type fracture surface of a mild galvanized bar (268) showed that frequent reinitiation of cracking occurred at grain boundaries and inclusions, both of which present interfaces which are traps for hydrogen, and that the presence of deformation markings were observed about the newly reinitiated crack portions, which indicates that considerable localized plasticity accompanied the reinitiation and propagation processes in HAC. These aspects appeared to be particularly interesting in light of the suggested role of such plasticity in hydrogen-assisted and other environmentally-assisted cracking (182). This study also indicated that the microfractographic aspects can help identify the physical fracture process, i.e., the micromechanisms of fracture.

Microscopic and macroscopic crack deviations following aligned inclusions, carbide particles or pearlite, secondary cracks which initiate at such particles, as well as pronounced decohesions at inclusions are also fractographic features of HAC in high strength steels.

In the case of the austenitic stainless steels, several modes of HAC fracture have been reported, such as microvoid formation producing dimples (269), quasi-cleavage (270), intergranular fracture (270) and faceted fracture (271). The cleavage-like fracture surface morphology of HAC reported for austenitic stainless steels generally appeared to be very similar to that observed in SCC (272). In a number of cases, HAC of metastable stainless steels (e.g., type 304) has been associated with hydrogen-enhanced transformation of the γ f.c.c. phase to the α' b.c.c. and ϵ h.c.p. martensites (273-275). In-situ TEM studies (274), have shown that these martensitic phases are formed in front of the crack tip and along the crack sides, favouring fracture by cleavage. However, this matter is still uncertain, because the cleavage-like facets (e.g., 276) showed that fracture was along {111} planes for type 304L stainless steel supersaturated with hydrogen gas and fractured in tension at 200 to 250K by brittle fracture. On this evidence, the author (276) concluded that the mode of formation of the facets was parting along coherent twin boundaries.

There is conclusive evidence (e.g., 277, 278) that some aluminium alloys, such as 2124, 7050, 7075, are embrittled by hydrogen, and that the embrittlement is apparently due to mechanisms, such as enhanced slip and trapping of hydrogen at precipitates within grain boundaries. The embrittlement in aluminum alloys depends on such variables as the microstructure, strain rate, and temperature. In general, underaged microstructures are more susceptible to hydrogen embrittlement than the peak and overaged structures.

The effect of hydrogen on the fracture appearance in aluminum alloys can vary from no significant change to a dramatic change from the normal dimple fracture to a combination of intergranular and cleavage-like transgranular fracture in high-strength 7075 and 7050 aluminum alloys (278).

Albrecht et al. (277) investigated the role of microstructure during HAC of 7075 aluminum and found that the ductility loss was a function of the microstructure. This effect was largest for the underaged microstructure and smallest for the overaged. They suggested that the degree of susceptibility to hydrogen embrittlement is strongly correlated to slip planarity. In the underaged condition, the coherent GP zones present in the matrix could be cut by passing dislocations, leading to a local softening of the slip plane and thus to the formation of concentrated slip bands. In the T73 temper, the matrix precipitates were

semicoherent, resulting in quite homogeneous slip of dislocations. The T6 temper represents a transition state; the matrix contains a mixture of GP zones and semicoherent z′ precipitates. In this condition, the slip distribution is inhomogeneous at low plastic strain, but with increasing strain becomes more and more homogeneous (277). The correlation between slip distribution and hydrogen sensitivity indicates the possibility that hydrogen transport in this material is influenced by mobile dislocation in an important manner. These authors (277) argued that a certain, critical hydrogen concentration was needed locally to cause macroscopic embrittlement, and that the accumulation of this critical amount of hydrogen should be favoured by an inhomogeneous slip distribution.

For the 7050 aluminum alloy, Thompson et al. (278) showed that a low (0.01%) copper content rendered all microstructures more susceptible to embrittlement than those of normal (2.1%) copper content. For a low-copper (0.01%) 7050 alloy in the peak-aged condition embrittled by hydrogen, a cleavage-like transgranular fracture resulted; however, the same alloy in the underaged condition failed by a combination of intergranular and cleavage-like fracture.

1.2.3 Fractography and Mechanisms of Crack Growth in Liquid Metal Environments

When metals such as certain steels, titanium alloys, nickel-copper alloys, and aluminum alloys are stressed while in contact with low-melting metals, including lead, tin, cadmium, lithium, indium, gallium, and mercury, they may be embrittled and fracture at a stress well below the yield strength of the alloy. If the embrittling metal is in a liquid state during exposure, the failure is referred to as liquid metal embrittlement (LME).

1.2.3.1 Cracking Characteristics of LME

Susceptibility to LME is unique to specific metals. For example, liquid gallium embrittles aluminum but not magnesium, and liquid mercury embrittles zinc but not cadmium. The equilibrium phase diagrams of most embrittlement couples show that they form simple binary systems with little or no solid solubility. Also, they usually do not form intermetallic compounds. Contact with the liquid component does not degrade the solid and the embrittlement is not affected by the length of contact time before stressing to failure (279, 280).

Under certain conditions, LME can occur with dramatic speed. For example, when an AISI 4140 steel which was heat treated to an ultimate tensile strength of 1500 MPa was tested at an applied stress of 1009 MPa (the approximate

proportional limit of the material) while in contact with liquid indium at a temperature of 158°C (indium melts at 156°C), crack formation required about 511 S. The crack then propagated and fractured the 5.84 mm diam. electropolished round bar specimen in only approximately 0.1 S (279). However, not all cases of LME occur in such short time spans.

The presence of liquid metal at the moving crack tip appears necessary for fast fracture, unless the solid is inherently notch-brittle. For instance, in high strength brittle metals, the possibility exists that the crack initiated in contact with the liquid may propagate in a brittle manner in the absence of this liquid. In low-strength materials, however, a transition may occur from brittle-to-ductile failure under similar circumstances (281).

In general, higher applied stresses and lower strain rates promote embrittlement (282), while an increase in the amount of cold work reduces embrittlement (283). The reduction in embrittlement from cold work has been suggested as due to the increase in the dislocation density within grains providing a larger number of additional diffusion paths to dilute the concentration of embrittling atoms at grain boundaries.

A smaller grain size reduces embrittlement because of the reduced stress concentration at grain-boundary dislocation pile-ups (283). However, for the embrittlement of Monel 400 by mercury, maximum embrittlement has been observed at an approximate grain size of 250 μm, with the embrittlement decreasing for both smaller and larger grain sizes (282). The decrease in embrittlement at smaller grain sizes was attributed to a difficulty in crack initiation, and for large grain sizes, the effect was attributed to enhanced plasticity (282).

When fracture occurs by intergranular decohesion, the presence of such elements as Pb, Sn, P, and As at grain boundaries can affect the embrittlement mechanism.

An increase in test temperature decreases embrittlement, which leads to a brittle-to-ductile transition that limits the temperature range of embrittlement. The transition temperature depends on grain size and strain rate (280). Severe embrittlement occurs near the freezing temperature of the liquid (281).

1.2.3.2 Fractography of LME

In general, most fractures in LME occur by a brittle intergranular or cleavage-like fracture mode; however, the dimpled ductile fracture mode has been also observed microscopically by Lynch (284). Although, LME can occur by either

a brittle or a ductile fracture model, both degrade the mechanical properties of the solid metal.

As mentioned formerly, careful fractographic and metallographic examinations of LME in b.c.c., f.c.c. and h.c.p. metals have been intensively reviewed by Lynch (284-286), who formed very small microvoids (dimples) occurred on cleavage-like fracture surfaces as well as evidence of considerable plastic strains accompanying fracture. Lynch concluded that the microvoid-coalescence process cannot only vary enormously in scale but can produce a wide variety of fracture modes and appearances, including fractures with a cleavage-like appearance (284) except at very high magnifications.

1.2.3.3 Mechanisms Proposed for LME

The precise interaction between atoms of an embrittling liquid and a stressed substrate that leads to embrittlement remains unknown. Particularly, the mechanism for the extremely rapid crack propagation for LME is not well understood (279).

There are mainly four mechanisms proposed (287) for explaining the embrittlement induced by liquid metal, as follows:

(1) decohesion

(2) enhanced shear

(3) stress-assisted dissolution

(4) embrittlement of grain boundaries by diffusion.

It appears clear that rapid brittle fracture in liquid-metal environments involves only adsorption-induced weakening of interatomic bonds precisely at the crack tip (287). Consequently, the decohesion theory is the most accepted in that chemisorbed embrittling atoms lower bond strength, at the crack tip, thereby facilitating both nucleation and propagation of the crack (288, 289). However, as mentioned in the section on HE mechanisms, the most sustained criticism of the decohesion model as applied to LME is based upon metallographic and fractographic observations of embrittled samples, most notably by Lynch (e.g. 284-286). Decohesion implies a cleavage mechanism of fracture in which atomic bonds defining a crack tip are fractured by forces acting normal to the crack plane, leading either to crystallographic cracking or to grain boundary separation. This micromechanism is not consistent with the observations of Lynch. Hence, he suggested that chemisorption facilitated nucleation of dislocations from the crack tip, i.e. enhanced shear, and proposed that atomically brittle behaviour is much less common than generally supposed. Lynch's criticism to the decohesion model also based on the following arguments:

For metals, the resistance to slip is much less than that in materials with covalent and ionic bonding, for which several observations indicate that fracture can occur by decohesion. The localized strains occurring during cleavage in metals are generally larger than those occurring during cleavage in non metals. Even though it is widely presumed that this localized plasticity does not blunt crack tips, and that cleavage in metals also occurs by decohesion, there is no direct evidence that fracture does occur by decohesion in metals. Fracture surfaces have not been examined using techniques with a sufficiently high resultion to determine whether or not they are atomically flat.

Moreover, atomically brittle cleavage fractures should occur either on planes for which the surface energy is least or, if slip accompanies cleavage, on planes and in directions for which the dislocation activity is minimized (290, 291). However, cleavage planes and directions in metals often do not agree with either or these predictions. For example, cleavage crack fronts are often parallel to the line of intersection of slip planes with the cleavage plane, thereby favouring slip on planes intersecting crack tips.

Although there remains serious criticisms of the applicability of the Lynch model to crystalline metals, his detailed metallographic and fractographic studies of environment-assisted cracking provide valuable insight into ductile versus brittle

behaviour.

The dissolution model proposed by Robertson (292), and later by Glikman et al. (293) in that rapid localized dissolution of highly stressed atoms at the leading edge of a crack is the cause of crack propagation in LME. The dissolved material would need to be carried away by diffusion through the liquid. The main problem with this approach is that dissolution would have to be rapid enough to account for crack propagation rates measured in cm/s, which is highly unlikely (287).

Krishtal (294) has proposed that LME is composed of a two step process: embrittling atoms must initially diffuse along grain boundaries in the substrate to a critical depth and concentrate on the boundaries, which are then embrittled. Dislocations produced by strains resulting from the presence of the embrittling atoms as well as dislocations produced by lowering of the base metal surface energy are responsible for the embrittlement. Gordon (283) also suggested that the grain boundary embrittlement model can account qualitatively for strain rate, solute, grain size and cold work effects, as a result of the influence of these variables on volume diffusion. Unfortunately, this mechanism provides no insight into the many recorded instances of transgranular (on single crystals) embrittlement noted in the literature. Therefore, this model cannot be a general mechanism of liquid-metal-induced embrittlement.

1.2.4 Fractography and Mechanism of Corrosion-Fatigue Cracking

Corrosive liquid environments, such as water, brines, organic fluids, basic or acid media, and molten salts, can affect the rate at which fatigue cracks propagate as well as the fracture appearance. Fatigue that occurs in environments that are corrosive to the material is referred to as corrosion fatigue.

The history of corrosion fatigue is a long one and has been described in numerous reviews (295-297). However, the micromechanisms of the phenomenon of corrosion fatigue cracking have been examined (298) only in the last quarter century.

Basically, the fatigue phenomenon is often divided into two distinct components: crack initiation and crack propagation. Accordingly, a very brief description of aqueous environmental effects on corrosion fatigue crack initiation and propagation, respectively is presented here.

1.2.4.1 Aqueous Environmental Effects on Fatigue Crack Initiation

The influence of an aggressive environment on fatigue crack initiation can include effects which facilitate the initiation of cracks or the early stages of their propagation at crystallographic deformation features, such as slip bands and twin interfaces, and effects which cause localized corrosion of one or more

microstructural constituents, such as inclusions or grain boundaries, with this localized attack giving rise to the stress or strain concentrators at which crack initiation subsequently occurs. The former type of effects can be expected to occur primarily in high-purity metals and alloys on specimens or components with polished surfaces, since it is only in the absence of significant surface defects that crack initiation occurs along crystallographic deformation features. The occurrence of fatigue crack initiation at corrosion pits which have formed at microstructural features such as inclusions is common in commercial-purity materials such as steels. Several mechanisms have been proposed in an attempt to provide meaningful explanation for the roles played by aqueous environments on fatigue crack initiation. Some of these mechanisms are summarized in the following.

1.2.4.1.1 Strain Enhanced Dissolution of Slip Steps for Crack Initiation

This mechanism is based on strain-enhanced dissolution of emerging slip bands. The preferential attack of the slip bands in turn accelerates further slip in an autocatalytic process. The preferential attack of slip bands is explained through the higher energy state of metal atoms associated with dislocations when compared to metal atoms in a lattice. A number of investigators have shown that for pure metals and alloys, such as pure copper, fatigue crack initiation is generally associated with the production of intrusions and extrusions by conventional slip processes. In aqueous solutions, the formation of the intrusion/extrusion structure

has been shown to be affected by several possible corrosion processes, and accordingly, the crack initiation could be affected. For copper (299), either active dissolution of the surface or the presence of a solid or semisolid reaction product film have been shown to alter the surface structure created by cyclic deformation. For instance, the surfaces of single copper crystals tested in air was observed that persistent slipbands (PSB's) formed early in the cyclic life (10% N_f), then, the secondary slip occurred after significant hardening occurred. However, the comparable surfaces of the specimen tested in 0.5 N NaCl solution with a small anodic current applied (100 $\mu A/cm^2$) clearly showed that slip offset heights were increased and the density of PSB's was also increased by dissolution effect. Yan and Laird (300), also demonstrated that under conditions of active dissolution, the maximum slip offset gradient was increased, thus further localizing strain in the PSB's when compared to experiments performed under cathodic current condition. The indications were therefore that the preferential dissolution and strain localization phenomena mutually enhanced each other, accounting for the synergistic interaction of the corrosion and the stress cycling responsible for the reduction of the fatigue lives.

Experiments performed on pure polycrystalline copper samples showed that if anodic currents were applied, the fatigue fracture morphology changed from a combination of transgranular and intergranular to totally intergranular (301). This

behavior has been interpreted as an indication of the enhanced deformation associated with grain boundaries that causes increased corrosive attack of the grain boundaries related to that of emerging slip bands.

It may be stated from these observations that when a metal is in the active corrosion state, strain enhanced dissolution could be as an operative mechanism which is responsible for accelerating crack initiation in corrosion fatigue.

1.2.4.1.2 Surface Film Rupture and Electrochemical Attack at the Rupture Sites

In the mechanism of surface film rupture, fatigue crack nucleation is enhanced by mechanical damage to a protective surface film. As shown in fig. 1.25, when this protective film is damaged, areas of bare metal are exposed, resulting in preferential areas for corrosive attack. This could result in geometric discontinuities which may act as stress raisers where further damage to the film can occur. Eventually, the stress intensity at the root of such a geometric discontinuity will become high enough to form a crack in the metal. An important requirement of this mechanism is that the electrochemical potential of a metal or alloy in a given aqueous environment must be in the passive region, as shown in fig. 1.25. Some evidence has been reported (302, 303) that a thin passive film also have a pronounced effect on subsequent surface deformation and crack initiation.

1.2.4.1.3 Formation of Corrosion Pits and Stress Concentration at the Base of the Pit

Some of the earlier work in corrosion fatigue (e.g., 304) indicated that a corrosive media can assist in the nucleation of fatigue crack by the formation of corrosion pits on a metal surface. The composition and electrochemical conditions in a pit can influence the initiation of a fatigue crack. A number of examples exist for which the crack initiation was clearly the result of previous pitting. Corrosion pits which usually formed at inclusions have been reported to serve as the fatigue initiation sites.

Mueller (305) reported that pitting occurred at oxide-sulfide inclusions in both 12% Cr stainless steel having a tempered martensite microstructure and an 18% Cr-2% Mo ferritic stainless steel in aerated solution of NaCl (0.5 N and 4 N) adjusted to a pH of 6.5 with HCl, under stress control at 100 Hz. For the 18% Cr-2% Mo stainless steel, cracking in the 4N solution initiated at pits produced at niobium carbonitride particles, which cracked early in the cycling, even during the tests in air. This cracking then permitted localized crevice corrosion to occur in the 4N solution producing the pits.

1.2.4.1.4 Surface Adsorption of a Specific Species from the Environment for Crack Initiation

This mechanism proposed for crack nucleation involves the lowering of the surface energy of a metal due to the adsorption of a specific species from the environment. As has been mentioned in the mechanisms of SCC and HAC, such species adsorption lowers the local atomic bond energies and therefore can promote early crack initiation either due to local brittle decohesion failure (306), or due to enhanced local plasticity (168).

If adsorption of hydrogen occurs, such as high-strength Al-Zn-Mg alloys exposed to water, the effect of enhanced crack initiation during cyclic loading has been attributed to hydrogen assisted cracking which can provide an explanation for environmentally enhanced crack initiation of metals whose corrosion potential lies in the immune region.

Fig. 1.26 gives a schematic of correspondence between regions of a polarization curve and corrosion fatigue mechanisms, indicating that the possible operative mechanism for enhanced crack initiation is strongly dependent on the corrosion state of a metal. A good example was given by Magnin et al. (303), who analyzed the influence of a 3.5% NaCl solution on the cyclic plastic deformation of a bcc Fe-26Cr-1 Mo alloy as a function of the applied electrochemical potential E,

taking into account the dislocation behavior, the formation of microcracks and the evolution of the cyclic corrosion current transient. Their experimental results show that: i) in the cathodic region (E<-300 mV/SCE), the localization of the hydrogen evolution was favoured when microcracks were mechanically formed, which induced a very marked decrease of the fatigue life especially in high strain amplitudes; ii) in the passive region for -300 < E < +500 mV/SCE, the damage mechanisms were related to the localization of the anodic dissolution due to a depassivation-repassivation process; iii) in the passive region for E > +500 mV/SCE, the cyclic strain enhanced the formation of pits which induced an early formation of microcracks. This study, therefore, clearly revealed the physical mechanisms by which an aqueous corrosive solution can affect the fatigue life of bcc stainless steels according to the applied electrochemical potential.

1.2.4.2 Aqueous Environmental Effects on Fatigue Crack Propagation

It is generally accepted that exposure to aggressive aqueous environments will increase the fatigue crack growth rate of a given material. Such results have been observed in aluminum alloys (e.g., 30, 308), steels (e.g., 309, 310), stainless steels (e.g., 303, 311), copper alloys (e.g., 299, 312), titanium alloys (e.g., 102) and nickel base alloys (e.g., 313).

There are a number of mechanisms that explain accelerated fatigue crack growth and degraded fatigue resistance in aqueous environments. These mechanisms include:

1) Preferential electrochemical attack of plastically deformed metal,
2) Mechanically rupture of and/or electrochemically damage to protective surface films,
3) Adsorption of aggressive specific species,

The essential principles of the first three mechanisms for accelerating fatigue crack propagation are almost similar to those of the mechanisms for enhanced crack initiation, and hence, the general explanations for them are not presented here.

It has been mentioned that the studies performed by Yan et al. (300), using anodic polarization on copper during corrosion fatigue further confirmed the mechanism of preferential electrochemical attack of plastically deformed metal. They also show that compressive strain is as important as tensile strain (300).

Another mechanism involving film rupture proposed by Jones (199) for explaining both corrosion fatigue and stress-corrosion cracking has been described in section 1.2.1.6.1. Although this mechanism is fairly comprehensive, little

experimental evidence exists for the different steps proposed (see Fig. 1.13).

The crack closure effects due to wedging action of corrosion products are often very important at low crack growth rates and a relatively high testing frequency, which resulted in fluid not being able to escape from the region of the crack tip during the decreasing portion of the cyclic loading. The wedging action of the trapped fluid reduced the effective stress intensity at the crack tip and thus reduced the crack growth rate (279).

In general, any environment that promotes the initiation of fatigue cracks, such as pitting, enhanced corrosion, or oxidation; that allows an embrittling species to enter the material; that promotes strain-hardening relief (which lowers the fracture stress) at the crack tip; or that interferes with crack tip slip reversal will accelerate the corrosion fatigue crack growth rate and decrease the fatigue life of the material.

1.2.4.3 Effects of Corrosion-Fatigue on the Fatigue Propagation Curve

The corrosion fatigue crack propagation process is often classified as either a true corrosion fatigue (TCF) or a stress-corrosion fatigue (SCF) phenomenon or a combination of both (314). The true corrosion-fatigue is identified as the behavior where fatigue crack growth rates are enhanced by the presence of an

aggressive environment through a synergistic action of corrosion and cyclic loading. This effect on fatigue propagation curve is shematically shown in Fig. 1.27a. The occurence of true corrosion-fatigue phenomena also underlines the fact that corrosion-fatigue effects can occur for material-environment systems which generally do not give rise to stress-corrosion cracking effects. Stress-corrosion fatigue, however, is considered to include a stress corrosion contribution to fatigue cracking which acts above a threshold K_{max} value, often assumed to be equal to K_{ISCC}, the threshold value for stress-corrosion cracking, resulting in a fatigue crack propagation curve in a manner as shown in Fig. 1.27b. This curve essentially corresponds to a fatigue propagation curve obtained in an inert atmosphere, plus a pure SCC curve, log da/dt-log K_I.

The combination of these two categories effects of corrosion-fatigue behavior (TCF and SCF) can give rise to the fatigue crack propagation curve presented in Fig. 1.27c.

The effect of crack closure induced by corrosion products at very low crack growth rates often causes the fatigue-threshold value, ΔK_{th} to increase in an aggressive environment in comparison with that in an inert environment. This effect on corrosion-fatigue propagation curve is given in Fig. 1.27d.

It can be seen that in each of above cases, the environmental effect is negligible on fatigue crack propagation at high crack growth rates where the mechanical process of fatigue damage is probably taking place too quickly for chemical effects to be important.

1.2.4.4 The Major Variables Affecting Corrosion-Fatigue Crack Propagation Response of a Material Subjected to an Aggressive Environment

1.2.4.4.1 The Effect of Testing Frequency

In contrast to fatigue tests in an inert atmosphere, important frequency effects have been found in metals when tested in an aggressive environment. In general, since the fatigue crack growth rates increase when more time is allowed for environmental attack during the fatigue process, hence, there is a critical frequency under which the corrosion effect starts to be manifested. Then, for a given ΔK value, the crack growth rates increase with decreasing cycling frequency. Fig. 1.28 schematizes the typical effect of testing frequency on corrosion-fatigue crack propagation.

1.2.4.4.2 The Effect of Load Profile

Corrosion fatigue is found to be sensitive to subtleties of the cyclic wave form. For example, for the 12Ni-5Cr-3Mo steel fatigued in a 3% NaCl solution, Imhot and Barsom (315) showed that when square and negative sawtooth wave

forms were used, the material responded as though the tests were conducted in air. On the other hand, when the load profile was that of a sine, triangle or positive sawtooth wave form, a strong environmental influence of the salt solution was observed. By contrast, no effect of load profile was detected when the steel was fatigued in air. On the basis of these and other supporting results, these investigators (315) concluded that environmental attack occurred only during the tensile loading portion of the loading cycle, or when plastic deformation occurs, and was not affected by hold time. They found that when the load rise time was small, the influence of an aggressive environment was minimized and vice-versa.

1.2.4.4.3 The Effect of Load Ratio R

Although the effect of mean stress on fatigue crack propagation in the intermediate growth rate regime was found generally to be not important, it does become a major variable during corrosion fatigue conditions (316). In general, high R ratio conditions enhance the corrosion component of crack growth. The greater importance of mean stress effects during environmentally enhanced fatigue crack propagation is possibly attributed to contribution of the sustained loading crack growth rate component developed during one load cycle. As well, higher R ratio conditions can result in less crack closure during corrosion-fatigue cracking.

1.2.4.4.4 The Effect of Test Temperature

The other major test variable relating to corrosion fatigue is that of test temperature. The general agreement is that higher fatigue crack propagation rates at higher temperatures mainly result from material-environment interactions, rather than a creep contribution, based on a series of experiments conducted at elevated temperatures in inert environments and in vacuum (317, 318), which show that neither temperature nor frequency had any effect on fatigue crack propagation rates.

1.2.4.5 Corrosion Fatigue Superposition Model

Wei et al. (319) developed a model that would account for effects of environment, test frequency, wave form, and load ratio on corrosion fatigue crack propagation behavior. They approximated the total crack extension rate under corrosion fatigue conditions by a simple superposition of the intrinsic fatigue crack growth rate (determined in an inert atmosphere) and the crack extension due to a sustained load applied in an aggressive environment (determined as the environment assisted crack growth rate). Therefore,

$$\left(\frac{da}{dN}\right)_T = \left(\frac{da}{dN}\right)_{fat} + \int \frac{da}{dt} K(t)dt \qquad [1\text{-}14]$$

where: $(da/dN)_T$ = total corrosion fatigue crack growth rate

(da/dN) = fatigue crack growth rate defined in an inert atmosphere

(da/dt) = crack growth rate under sustained loading

K(t) = time-dependent change in stress intensity factor

There are two important aspects of this model. First, its linear character implies that there is no interaction between the purely mechanical and environmental components. Second, the model also depends on the assumption that the same mechanisms control the fracture process in both environment assisted cracking and corrosion fatigue. More frequently, however, corrosion fatigue does not follow this simple superposition model, since, for example, interaction between purely mechanical and environmental components is usually involved during corrosion fatigue processes. It has been found that the values of K_{max} upon which the vertical portion of the stress corrosion fatigue crack propagation curve occurs (Fig. 1.27b), are often lower than the values of K_{ISCC}, indicating that the cycling K usually facilitates or amplifies the contribution of environmental assisted component such as SCC by the effect of the continuous deformation of material at the crack tip (152).

There are other models, such as the process competition model which is based on the assumption that fatigue crack growth rate involves competition among

various processes (320), and the process interaction model which was developed to allow interactions to occur, particularly in alloy systems that exhibit a high degree of susceptibility to stress-corrosion cracking (321).

However, the involvement of an aggressive environment in fatigue growth surely depends on a complex interaction between chemical, mechanical, and metallurgical (or microstructural) factors, thus, all of the models proposed for corrosion fatigue are semiquantitative and at worst, strictly empirical.

1.2.4.6 Fractographic Aspects of Corrosion Fatigue

The fractographic aspects of corrosion-fatigue cracking are generally similar to those produced by stress-corrosion cracking or by hydrogen-assisted cracking. A frequent feature of transgranular corrosion-fatigue is crystallographic striated facets which resemble those produced by SCC, other than that the striations, often referred to as brittle striations, are generally more marked in corrosion-fatigue. Intergranular facets can also be produced in corrosion-fatigue cracking, while striations are generally not observed in such cases. Since the aspects of brittle striations are generally considered to be an important feature in revealing the role of the environment during corrosion fatigue, these aspects will first be described in this section.

1.2.4.6.1 Brittle Striations

Forsyth, Stubbington, and Clark (78, 113) were the first to report that the Al-Zn-Mg alloys exhibit two different types of fatigue striations. Stubbington (322) further characterized these striations and differentiated them into two types, i.e. ductile and brittle striations. They found that ductile striations formed during crack propagation in dry air, while brittle striations were observed in a corrosive environment such as sea water. Their observations also provided evidence that these brittle striations lay on crystallographic {100} facets. After the initial discovery of brittle striations in aluminum alloys, other workers (306, 323, 324, 327) also noted their occurrence in some materials fatigued in an aggressive environment. The major features of brittle fatigue striations compared to the ductile striations include the following:

- The ductile striations appear as smooth, almost featureless rumplings of the surface, however, the brittle striations lie on the crystallographic cleavage-like facets with river patterns which generally normal to the crack fronts
- The brittle striations occur on a fracture surface that is on or near a {100} plane either in aluminum alloys or in the ferritic phase of steels (325)
- The spacing between brittle striations is generally wider than that of ductile striations.

The mechanism of cyclic brittle crack extension is still disputed especially for ductile materials. Stubbington (322) suggested that the {100} fracture might be the result of a lowering of the surface energy due to ion adsorption. However, Laird (326) cited a number of arguments against the idea that clearage is involved in brittle striation formation, and suggested that quasi-cleavage occurs. This quasi-cleavage is possible to occur in planar slip materials because planar slip constraints confine cracking to certain crystal planes. Specifically, Laird stated that for high strength f.c.c. materials, slip on {111} would cause the resultant crack plane to be symmetrically contained by the operative slip plane, i.e. for example, a {100} or {110} plane would be selected for crack propagation.

In response to Laird's arguments, Wanhill (327) further explained how adsorption or adsorption of hydrogen likely induces the formation of the brittle striations observed in the high strength aluminum alloy tested. He postulated the following concept: During the tensile part of a load cycle, the material can fracture by adsorption-induced cleavage in localized regions which, until fracture, are relatively undamaged. In the relatively high strength aluminum alloys, the age-hardened microstructure can provide a high density of slip barriers and a large portion of material exhibits essentially elastic behavior. This elastic behavior is necessary for environmentally-induced cleavage to occur. The cleavage crack can not run into material unaffected by the environment, because the stresses required

for cleavage are much higher and the crack is blunted by dislocation movement into the tip. Crack blunting and interference with the cleavage process by second phases and/or coarse slip results in the observed morphologies of brittle striations.

The processes of formation of brittle striations illustrated by Wanhill seem to be reasonable, some objections, however, have also been opened to Wanhill's proposal.

Stoltz and Pelloux (306, 328) studied the influence of the applied electrochemical potential and of the addition of sodium nitrate inhibitor on the striation morphology and on fatigue propagation behavior of 7075-type aluminum alloys tested at 1 Hz in NaCl solution. They found that the anodic potentials enhanced the crystallographic dependence of the fracture mode, resulting in brittle striations and in an acceleration of crack growth, while cathodic potentials resulted in ductile striations formed by shear. They showed that polarity reversal of the applied potential, for ΔK values of approximately 10 MPa $m^{1/2}$, resulted in a change in orientation of a local fracture plane from a crystallographic plane to a plane perpendicular to the tensile stress axis. The addition of a sufficient concentration of sodium nitrate to the NaCl solution also resulted in an abrupt change from brittle to ductile striations and in a return to fatigue crack growth rates similar to those obtained in air. The influence of this inhibitor on the fatigue behavior was

interpreted as indicating a corrosion-fatigue mechanism associated with an adsorption phenomenon or with a surface film.

Lynch (329) reported that for Al-Zn-Mg single crystals fatigued at 1 Hz in water, the macroscopic fracture planes were approximately parallel to {100} planes and crack growth occured in <110> directions. Slip on {111} planes intersecting {100} crack was also observed on the sections, either in the side or in the interior of specimens by ageing aftercrack growth (to "decorate" dislocations), then sectioning, polishing, and etching. Observations of Lynch indicated that significant plasticity accompanied corrosion-fatigue propagation, raising an objection to the suggestion that this cracking occurs by cleavage.

The occurrence of cleavage-like facets presenting both ductile and brittle appearing features was studied by Ait Bassidi et al. (325) on an austenitic-ferritic KCR 171 stainless steel tested in a white water environment. In these tests, it was the ferritic phase which was susceptible to corrosion-fatigue effects. Their detailed examinations showed that the occurrence of ductile features on the brittle-appearing facets was favoured by grain orientations for which the crystallographic cracking plane {100} was not close to perpendicular to the stress axis and for test conditions which combined high ΔK values with only a small corrosion-fatigue effect, such as in the region where the log da/dN-log ΔK curve obtained in the aggressive

environment rejoined that obtained in air. These authors also noticed the absence of brittle striations in the plane stress regions near the lateral edges and the presence of similar brittle features for tests in air (35-45% relative humidity) in well-oriented (a {100} fracture plane almost perpendicular to the stress axis) ferrite grains. As well a few reinitiation sites in a ferritic grain at an α-γ interface appeared to be situated ahead of the macroscopic crack front. Bassidi et al. (325) suggested that in the ferritic phase of steels and iron alloys, cleavage-like facets with very crystallographic and characteristic brittle striations can be produced by hydrogen-assisted corrosion fatigue. The same type of brittle striations were subsequently observed by Kaczorowski et al. (330) in Fe-3% Si single crystals fatigue tested in gaseous hydrogen.

1.2.4.6.2 Some of Fractographic Features of Corrosion-Fatigue in Multiphase Alloys

The fractographic aspects observed on the individual phases in dual or multi-phase alloys can be particularly useful in determining the influence of microstructure on the corrosion-fatigue behavior. As well, a good understanding of the relationships between the microstructure and the corrosion fatigue behavior can also be very useful in identifying the details of the mechanisms by which aggressive environments facilitate the initiation and propagation of fatigue cracks. Dickson et al. (331) have reviewed some of the work which has been carried out in this field.

In austenitic-ferritic KCR 171 tested in white water environment, as have mentioned above, Bassidi et al. (325) reported that brittle striations were present in the ferritic phase while the striations remained ductile in the austenitic phase. They observed that the interstriation spacings in the ferritic phase could be as much as ten times larger than in the austenitic phase. The difference in the crack growth rates between the two phases resulted in the grains of austenite within the ferritic matrix being bypassed by the local crack front in the ferrite, giving rise to the formation of some islands of austenite which then fractured behind the crack front in the ferrite. The initiation of cracking in the individual austenite grains occurred at several sites around their perimeter in the plane corresponding to crack in the ferrite. Final fracture of the center of each austenite grain generally occurred by necking or crack tip stretching of the ligament remaining between the individual cracks which had initiated in the grain. In terms of these detailed fractographic observations, these authors suggested that [the austenitic phase was not itself subjected to corrosion-fatigue effect in this environment and that the influence of the uncracked islands of austenite can limit the environmentally-accelerated crack growth rates obtained in ferrite, since the interstriation spacing in the ferrite was also observed to decrease in passing between two closely-spaced austenite grains.]

The same type of brittle fractographic features were also observed (332) on corrosion-fatigue fracture surfaces of an offshore ferritic-pearlitic steel for tests

under cathodic protection (-1.0V/SCE). Again in this steel, the cleavage-like facets with brittle striations were only present in the ferrite. Ductile striation were present in the pearlite. These observations, therefore, further demonstrated that ferrite can be susceptible to hydrogen-enhanced fatigue crack propagation even in cases when harder microstructural constituents in the same steels are not or are little affected (307, 331).

Dickson et al. (333, 334) studied the corrosion-fatigue propagation of 12-14%Mn-8%Al-2%Ni-3%Fe ship propeller bronzes at the free corrosion potential in 3.5% NaCl solution. Several material conditions were tested. These bronzes generally contained two principal phases, with the fcc α-phase present as smaller grains within large bcc β-grains. As well, κ particles rich in iron and manganese were also present within α-grains.

The general behaviour observed was that of accelerated corrosion-fatigue crack propagation at the higher ΔK values in the aggressive environment, with the difference between the crack growth curves in the NaCl solution and in air increasing with increasing ΔK up to the highest da/dN values employed in the tests (10^{-3} to 2×10^{-3} mm/cycle). Below approximately 10^{-5} mm/cycle, testing in the NaCl solution resulted in considerable corrosion-product induced crack closure effects and in slower crack growth rates than those obtained in air for similar nominal ΔK

values.

The microfractographic evidence (333, 334) indicated that the accelerated corrosion-fatigue propagation was essentially the result of decohesion being produced during tests in the NaCl solution along the portions of α-β interfaces which intersected the macroscopic crack front. Such features were not present on the fracture surfaces produced in air. These interface cracks proceeded ahead of the macroscopic crack front and facilitated crack initiation at different sites in the adjoining α-grains and possibly in the adjoining β-ligaments, although the latter had not been determined fractographically, because of the very limited plasticity in the β-phase. The decohesion at the α-β interface was also observed in the immediate vicinity of the fracture surface on metallographic profile sections. Since the maximum corrosion fatigue effect obtained occurred at the highest growth rates attained for the Mn-Ni-Al bronzes tested in the NaCl solution, Dickson et al. (333, 334) attributed the environmentally-produced decohesion at α-β interfaces to a stress-sorption effect, rather than to a dissolution mechanism.

For the stress-corrosion cracking of a cast Ni-Al bronze tested in natural sea water, Parkins and Suzuki (312) observed that over a restricted range of potentials in the vicinity of the free corrosion potential, cracking occurred at the α-K interfaces, and that some preferential dissolution of the α-phase also occurred at

the more anodic potentials. They also found that cycling in sea water reduced the threshold stress level for the fatigue cracking of smooth specimens. They interpreted the environmentally-enhanced cracking of this Ni-Al bronze as resulting essentially from a dissolution mechanism. More dissolution effects were observed by Parkins and Suzuki (312) possibly due to relatively lower strain rates employed in their experiments.

1.2.4.6.3 Intergranular Corrosion-Fatigue Cracking

Under conditions of active corrosion, a number of instances have been cited where corrosion fatigue cracks initiated and propagate in an intergranular mode even in the absence of second phases in the grain boundaries. For example, Masuda and Duquette (301) observed that for the polycrystalline copper tested in 0.5 N NaCl with applied anodic currents, the fatigue lives were reduced, which was associated with a change from transgranular to intergranular crack initiation. This intergranular cracking was attributed to preferential dissolution, during cycling, at dislocations accumulated at grain boundaries, or to intergranular cracking associated with strain accomodation and favoured by the delayed transgranular cracking. Since more continuous crack path for intergranular cracking than for transgranular slip band cracking, for which the microcracks will encounter difficulty in crossing grain boundaries, resulted in the reduce in the fatigue life.

Hahn and Duquette (335) also observed a transition to intergranular cracking for a solutionized IN838 (Cu-16%Ni-0.6%Cr) alloy tested in aereated NaCl solution. Some evidence was also found for intergranular corrosion during stress cycling under applied anodic currents, which reduced the fatigue lives with respect to those in air. The fatigue crack path in the aged alloy was mainly intergranular because of the presence of grain boundary precipitates, giving rise to the relatively weak grain boundary precipitate/matrix interfaces. Testing this alloy in the NaCl solution at the free corrosion potential resulted in severe intergranular attack, in a more completely intergranular cracking mode and in an important decrease in the fatigue strength.

The studies of Duquette and co-workers (298, 299, 335) further clearly showed the influence of preferential dissolution to delay slip band initiation when this dissolution blunted the stress concentrators produced at the slip bands. In such cases, intergranular cracking was promoted, especially when some grain boundary dissolution occurred during cycling.

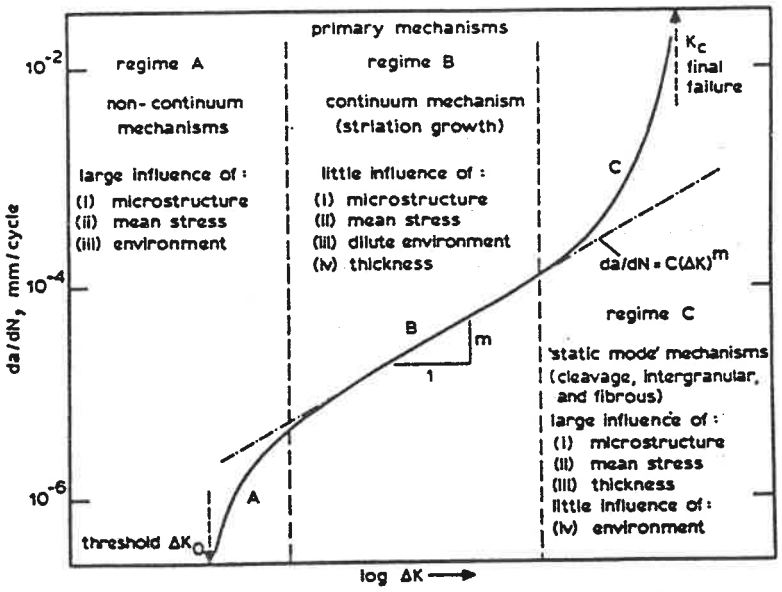
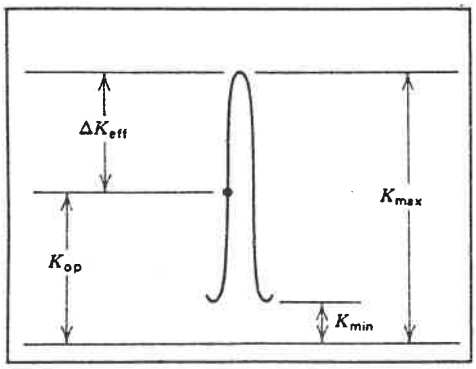


Fig. 1.1: Schematic variation of fatigue crack growth rate as function of stress intensity range (7).



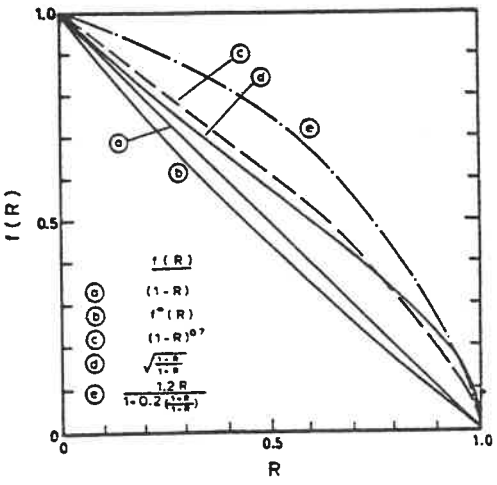


Fig. 1.2 **Fig. 1.3**

Fig. 1.2: Crack surface interference results in crack opening K_{op} to be above zero, ΔK_{eff} defined as K_{max}-K_{op}.

Fig. 1.3: Variation with the R ratio of the f(R) function in equation [1-3] (14).

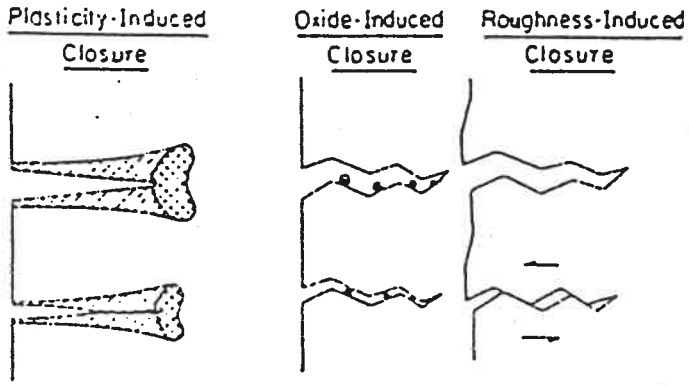


Fig. 1.4: Schematic illustration of mechanisms of fatigue crack closure (40).

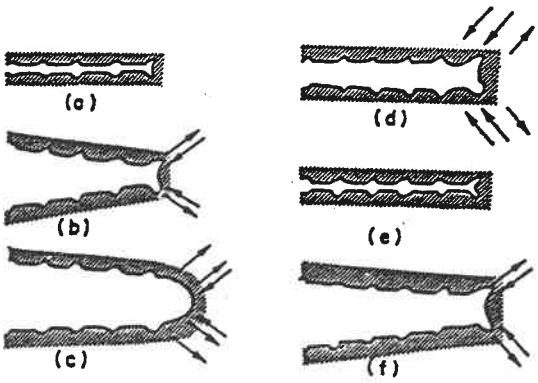


Fig. 1.5

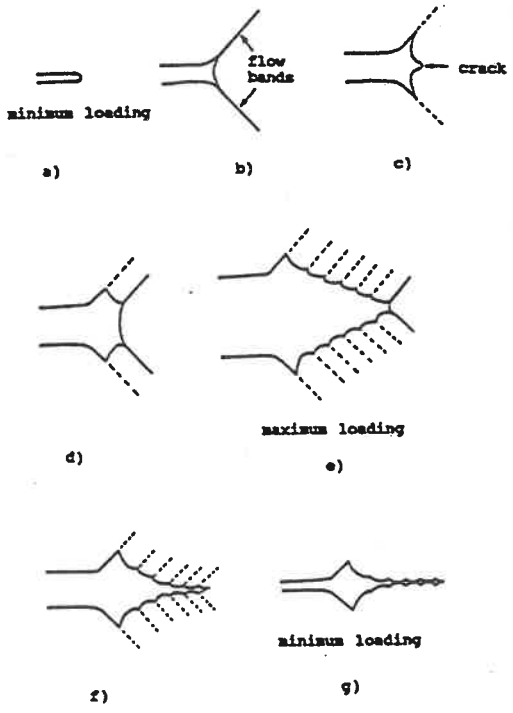


Fig. 1.6

Fig. 1.5: Schematic of the plastic blunting process of fatigue crack propagation during a loading cycle (79).

Fig. 1.6: Model of Tomkins and Biggs (80).

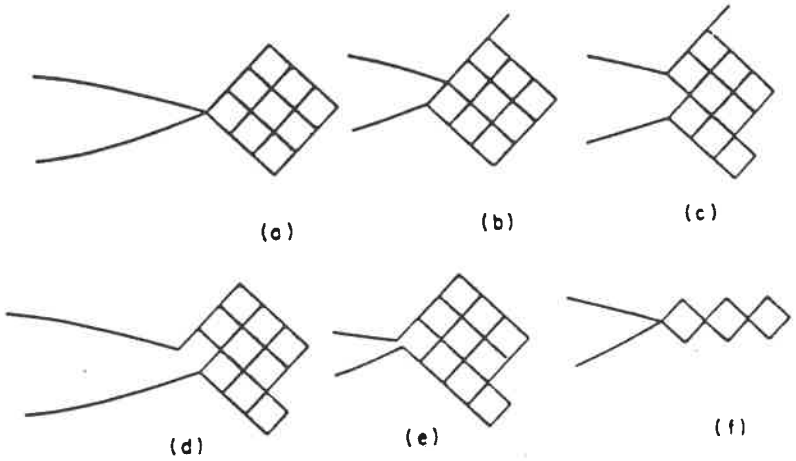


Fig. 1.7: Schematic of order of the localized slip which produces crystallographic striations (307).

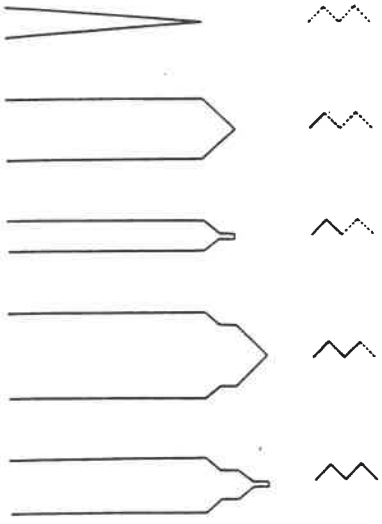


Fig. 1.8

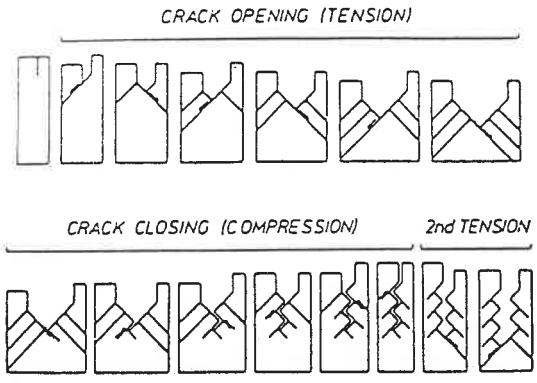


Fig. 1.9

Fig. 1.8: Model of Pelloux (81).
Fig. 1.9: Schematic of the alternate slip plane model showing the slip processes during a loading cycle (82).

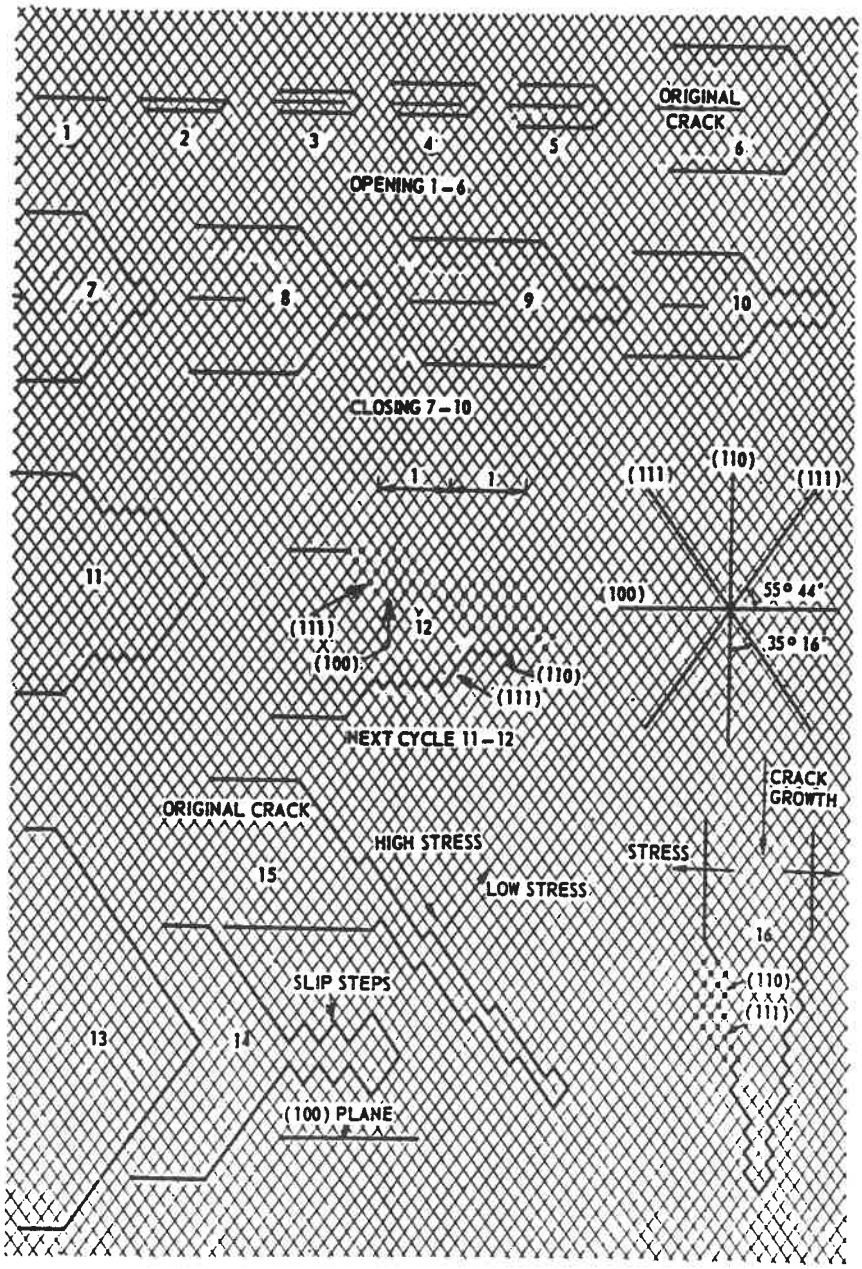


Fig. 1.10: Model of Bowles and Broek (83).

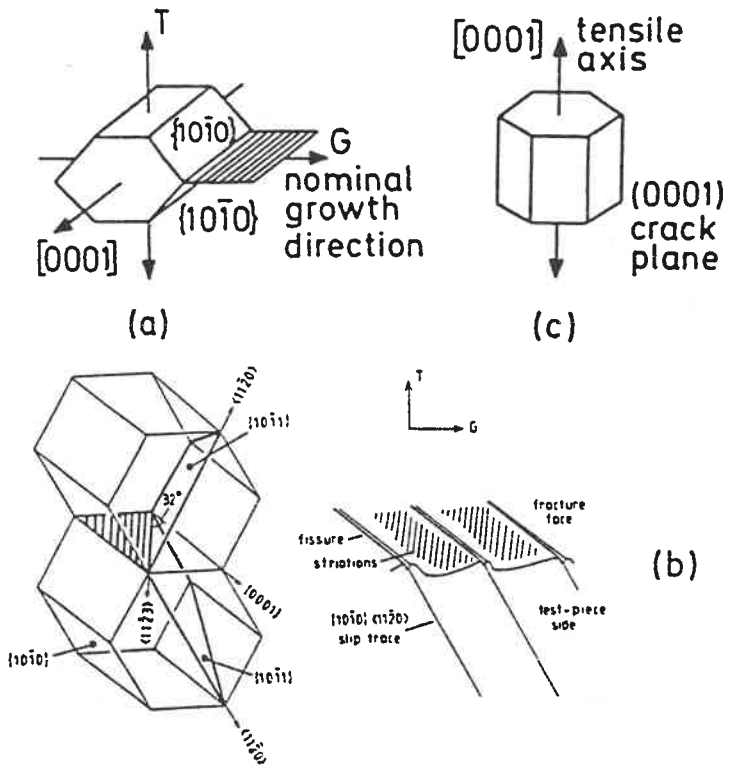


Fig. 1.11: Models of Beevers and Ward-Close (97, 102).

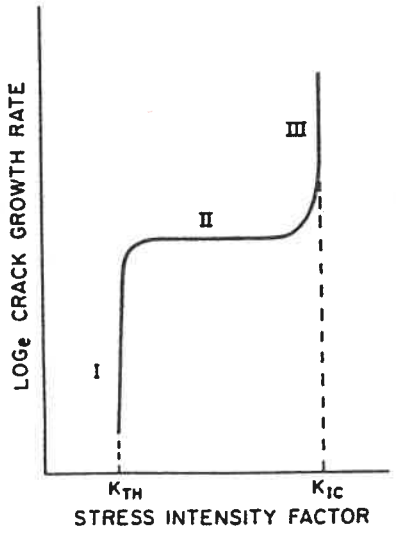
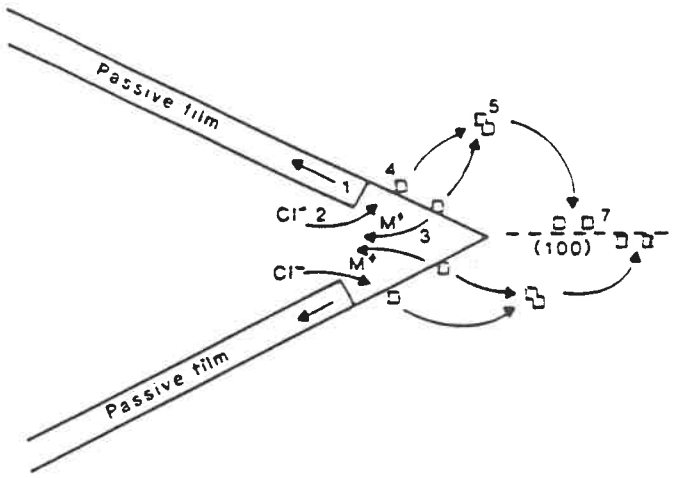


Fig. 1.12:
Schematic diagram of typical three stages curve of crack propagation rate, log da/dt vs. crack tip stress intensity, K, in SCC and HE cracking.



STEPS in SCC MECHANISM

1. Film rupture by mechanical stress
2. Retarded repassivation by competetetive adsorption of critical species, e.g. Cl^-
3. Anodic dissolution by coupling to surrounding passive surfaces
4. Vacancy formation from rapid dissolution
5. Divacancy formation and migration
6. Crack initiation (Omitted from diagram).
7. Crack propagation by cleavage due to accumulation of divacacies on prismatic planes, e.g. {100}

Fig. 1.13: Schematic diagram summarizing the model of SCC and corrosion-fatigue cracking proposed by Jones (199).

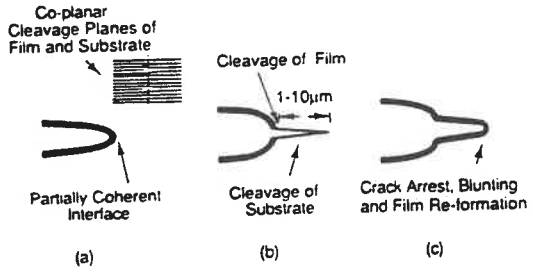


Fig. 1.14: Schematic diagram illustrating a film-induced cleavage model proposed for TSCC in copper and α-brass by Newman et al. (202).

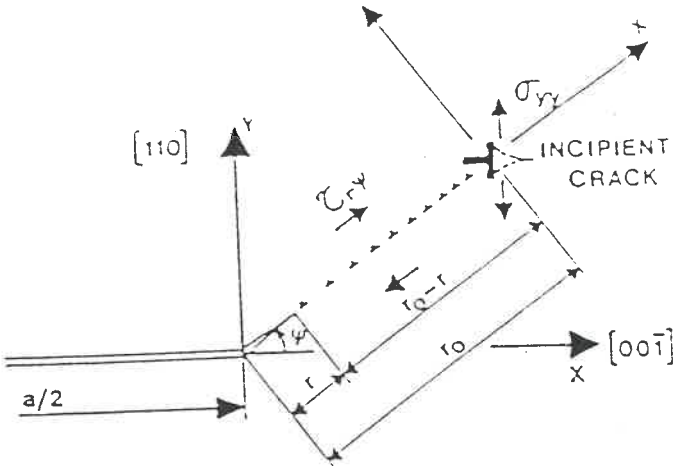


Fig. 1.15: Schematic drawing of a dog-leg crack, formed by corrosion along a slip plane, approaching a Lomer-Cottrell lock (model of Lichter et al. (175)).

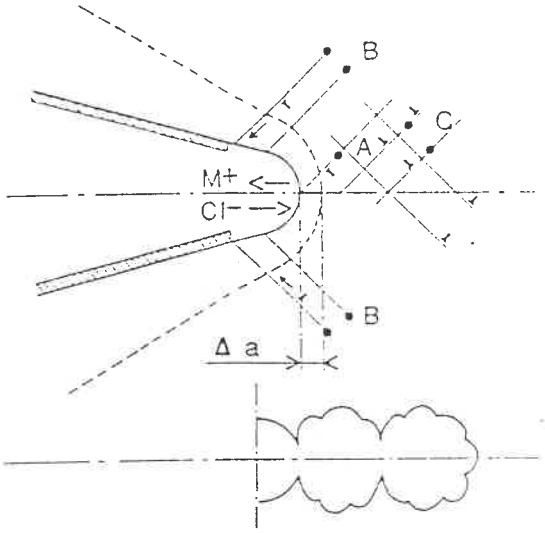


Fig. 1.16

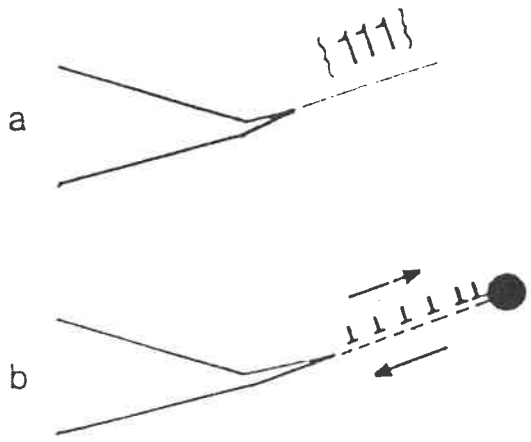


Fig. 1.17

Fig. 1.16: Schematic of the dislocation behavior at the crack tip and of the crack growth when dislocations of type B are activated and induce crack blunting (from 194).

Fig. 1.17: Schematic of the effect of the localized anodic dissolution on the plasticity at the crack tip. (a) Dislocation in a slip band and formation of a step just at the crack tip. (b) formation of dislocation pile-ups (from 194).

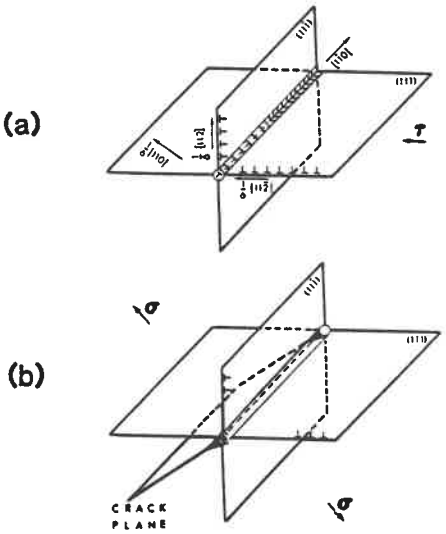


Fig. 1.18:
Crystal geometry of the slip planes, the Cottrell-Lomer dislocation barrier and their relation to the cracking plane (163).

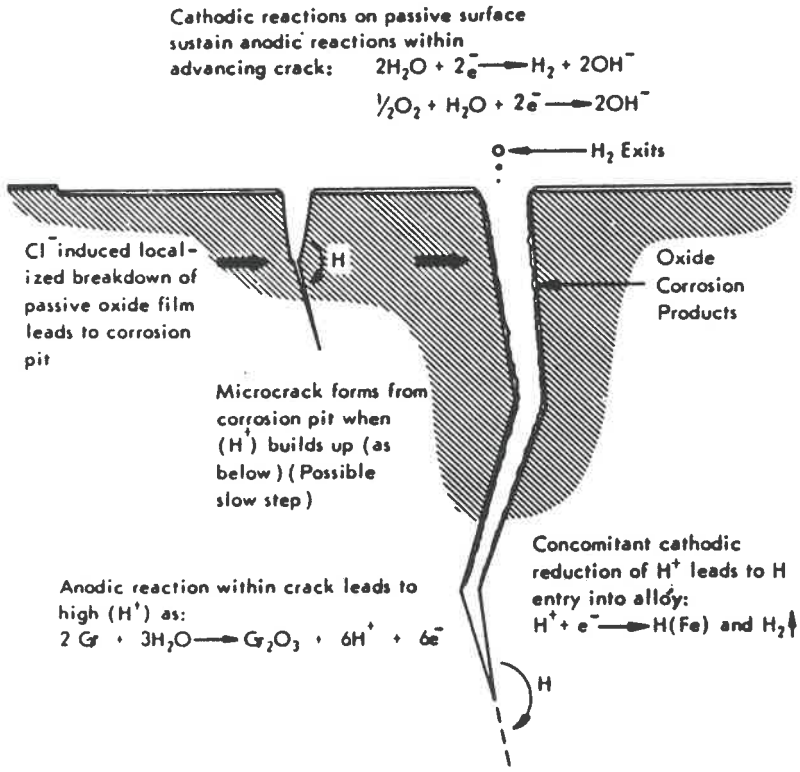


Fig. 1.19: Generalized model for crack initiation and propagation in SCC (the details here are for austenitic stainless steel in a chloride environment) (264).

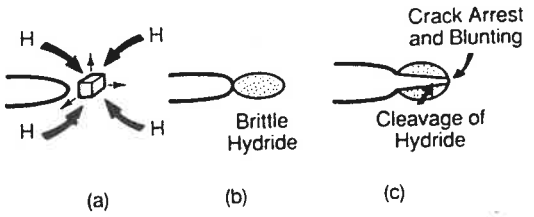
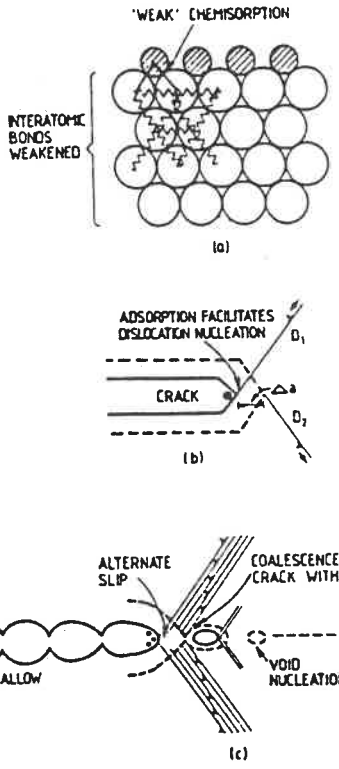


Fig. 1.20: Schematic illustrating a hydride-induced cleavage fracture processes.



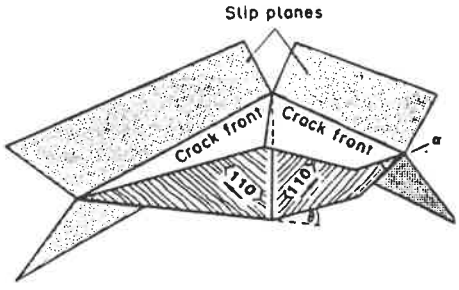


Fig. 1.21 (left)

Fig. 1.22 (above)

Fig. 1.21: Schematic illustration of the adsorption-induced localized-slip process for environmentally assisted cracking (168).

Fig. 1.22: Diagram illustrating the formation of herringbone patterns on fracture surfaces of f.c.c. and b.c.c. materials (168).

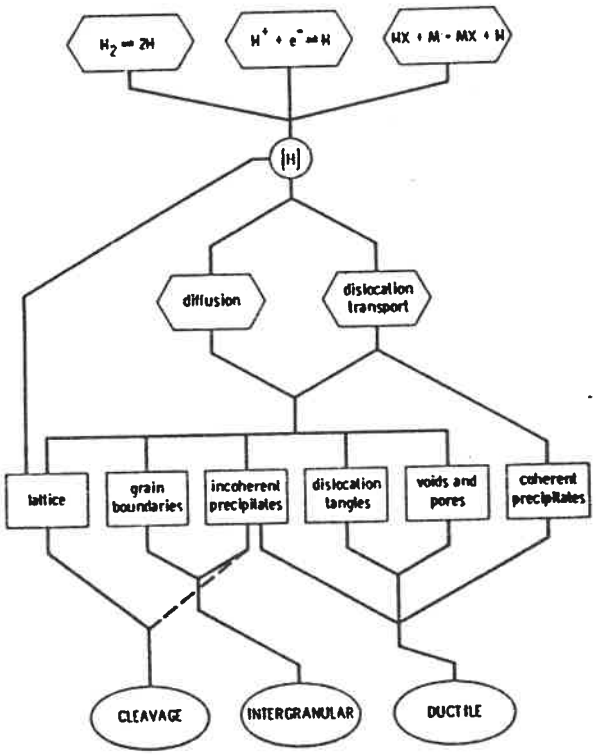


Fig. 1.23: Summary of hydrogen processes: sources leading to hydrogen in solution, transport leading to accumulation at microstructural locations, and finally fracture. Dashed line refers to cleavage of hydrides. From Thompson and Bernstein (264).

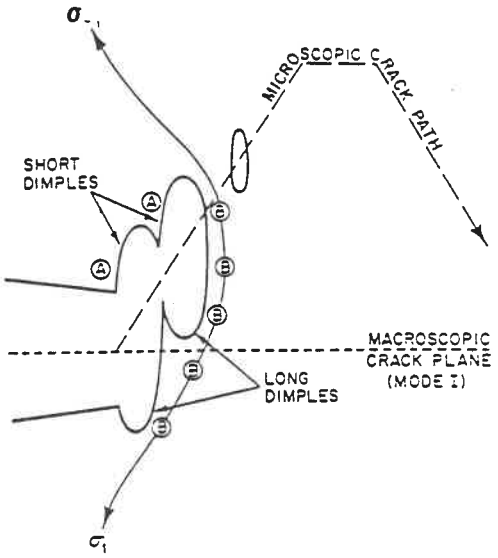


Fig. 1.24a

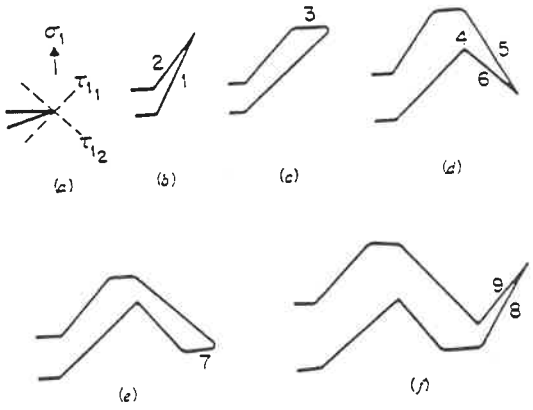


Fig. 1.24b

Fig. 1.24a: Combined tearing and shearing during the formation of dimples, which results in short shear dimples at top and long shear dimples at the bottom. Material at B continues to be stretched after stretching has stopped at A (356).

Fig. 1.24b: The unit process of elastic-plastic fracturing which best fits the observations. Four stages of continuous cracking by a blending of Modes I and II are shown, (b) up, (c) across, (d) down, and (e) across. The process is restarted in (f) (356).

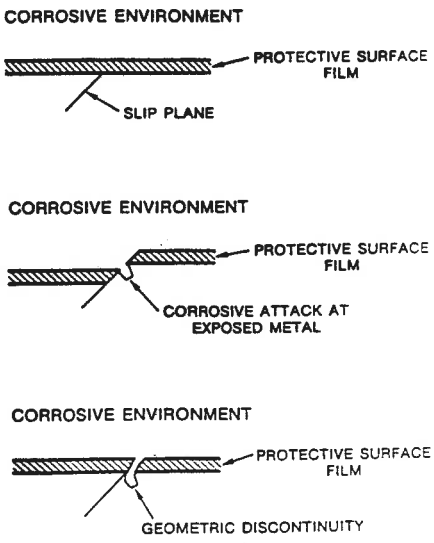


Fig. 1.25:
Mechanism of surface film rupture for environmentally enhanced crack initiation.

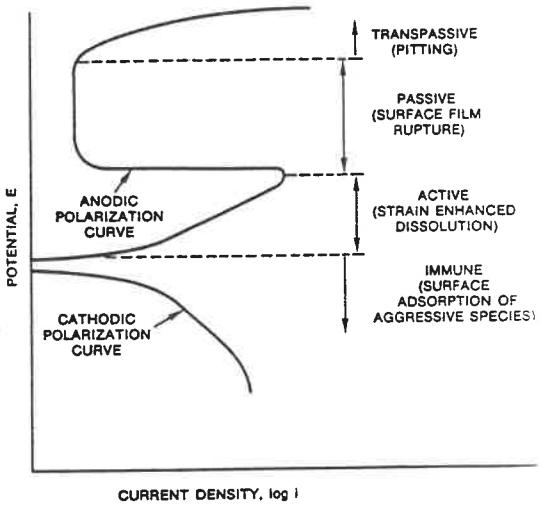


Fig. 1.26: Schematic of correspondence between regions of a polarization curve and corrosion fatigue mechanisms.

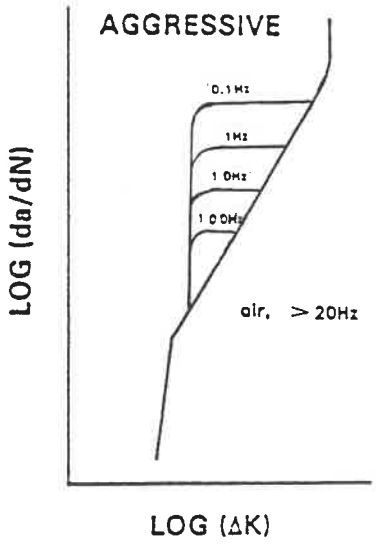


Fig. 1.28: Illustration of typical effect of testing frequency on corrosion-fatigue crack propagation (152).

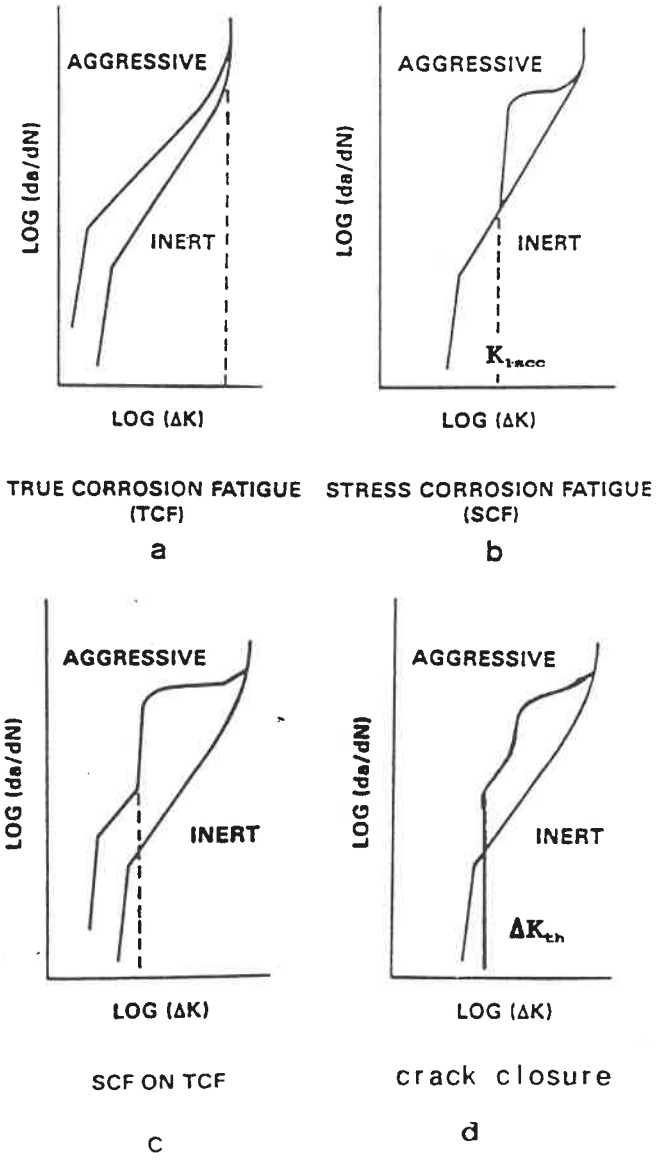


Fig. 1.27: Illustration of the four types of corrosion fatigue crack propagation curves (152).

CHAPTER 2

BASIC TECHNIQUES FOR STUDYING THE FRACTOGRAPHY AND CRYSTALLOGRAPHY OF CRACKING

2.1 MACROFRACTOGRAPHIC OBSERVATIONS

Fractography, the science of studying fracture surfaces, can be subdivided into macro-and microfractography. Macrofractography permits to observe the characteristics with the naked eye or with a low power microscope and is useful particularly for the identification of the nature and the cause of cracking in analysis of failures (108, 281). The macrofractographic study also helps to plan the subsequent microfractographic observations. In some cases, the macrofractographic observations can provide useful information regarding cracking micromechanisms and its relation to the microstructure of the material. The macrofractographic aspects which are useful in distinguishing stress corrosion from corrosion fatigue cracking include the presence of crack branching and more irregular aspect of the crack front for stress corrosion cracking (336).

Macroscopic examination of fracture surface involves relatively simple techniques. The basic equipment used for macrofractography in the present study included the eye for unaided visual observations, a low magnification stereo

microscope, a proper illumination source permitting great flexibility in choosing the direction of illumination and photographic equipment allowing satisfactory recording of the macrofractographic features.

Macrofractographic observations have also been made by scanning electron microscopy at the lowest magnification possible, generally 10-40 X. Again especially for these lower magnification observations, the positioning of the sample with respect to the electron beam and the detector determine whether the important macrofractographic evidence is highlighted or not.

Stereo pairs of photographs at relatively low magnifications taken in SEM can be useful. For instance, in the cases of studying the relationship of the orientations between the different portions of fracture surfaces and of comparing the orientation of fracture facets with respect to the tensile axis.

2.2 METALLOGRAPHIC OBSERVATIONS RELATED TO FRACTOGRAPHY

2.2.1 Introduction

Metallographic examination of polished and polished-and-etched sections by optical microscopy and scanning electron microscopy techniques has been widely employed in failure analysis and has also been used to investigate cracking

mechanisms. The examinations of metallographic sections in fractographic studies generally include observations of secondary cracks and of the profile of fracture surfaces (108, 281, 336).

The information that can be obtained by metallographic observations, especially in cases where such observations extend right to the fracture surfaces, can provide important evidence on the relationship between the crack path and the microstructure, such as the role of the different phases and inclusions on crack propagation or in crack initiation. This effect is well known to be important in the cases of environmentally assisted-cracking. Metallographic observations of secondary cracks or crack branches are generally relatively easy to interpret. For instance, some crack branching, at least on a microscopic scale, can be observed in the case of intergranular, interfacial or crystallographic transgranular cracking, hence facilitating the identification of the nature and the mode of the cracking. Moreover, crystallographic features and roughness aspects of crack propagation can also be observed by examination of the crack path profile on metallographic sections. Accordingly, the metallographic sectioning techniques were frequently employed in the present studies of SCC in 316 and 310 stainless steels in the cold worked condition and of fatigue and corrosion fatigue of Mn-Ni-Al.

2.2.2 Metallographic Sectioning Techniques and Observation Procedures

The metallographic sectioning and polishing techniques employed must prevent rounding of the specimens edges, so that, metallographic details closest to the fracture surface can be observed by optical microscopy.

Rounding of the edges during metallographic polishing can often be considerably reduced simply by placing a strip of similar metal very close to the surface that it is desired to observe (108). If no subsequent SEM observations are planned, this strip can be pressed against the fracture surface. This simple procedure may be sufficient for many purposes, especially when employed with automatic metallographic polishing with diamond paste, which considerably decreases the tendency for rounding of the edges in comparison to manual polishing.

A procedure often employed is to electrodeposit a thin layer of a different metal, such as nickel, on the fracture surface, so that the fracture edge is protected (281, 336). The metallographic features at the fracture surface can then be easily observed, at least if the hardness of two materials are reasonably similar. Since the metallographic etching usually is important, the metal chosen for depositing should not cause galvanic effects which prevents proper etching of the microstructure immediately adjacent to the fracture surface. If the deposited material on the

fracture surface is very thin, automatic polishing should also be employed.

For relatively soft metals, several layers of red "Microstop" lacquer, built up on the fracture surface and hardened by heating at 50°C or higher (108), can be employed to prevent rounding of the edges during metallographic polishing. An advantage of this technique is that, if the hardening temperature employed is low (≈ 50°C), this coating can be dissolved ultrasonically in acetone. After polishing and metallographic etching to reveal the microstructure, the sample can then be removed from its metallographic mount, the lacquer dissolved and the relationship between the microstructure and the fractographic features studied by simultaneous observations of both the metallographic section and the fracture surface at their common edge.

In the present study, this last method was employed frequently. Several steps in the procedure are important:

- Firstly, the lacquer on the fracture surface must be built up to a sufficient thickness and hardness, and must also protect the fracture surface very well during electrochemical polishing and metallographic etching. Hardening the lacquer at room temperature was also employed on some samples rather than the use of slight heating. In these cases, the fracture surface was first covered with a very thin

lacquer layer, then dried well in air at room temperature for about 6 hours. After that, the second layer of lacquer was applied and dried in the same manner. Finally, a third layer of lacquer was applied and dried at least for 3 days. The total thickness of the lacquer deposited was of 0.5 to 1 mm. A thicker layer is particularly important to protect the fracture surface from attack when an electropolishing or electro-etching procedure is to be used subsequently.

- The use of proper cutting equipment, such as a low speed circular diamond saw is also important and should be able to cut the metallographic section perpendicular to the fracture surface that it is desired to investigate.

- Thirdly, since no mounting was performed, particular care was taken to maintain the metallographic section perpendicular to the fracture surface during polishing especially when the technique was used on small specimen portions. In such cases, it is beneficial to do the final stages of polishing entirely manually without rotation of the polishing wheel.

- The microstructural features and the profile of the fracture surface as well as the characteristics of the secondary cracks can be observed on the metallographic section by optical microscopy. Afterwards, the lacquer can be dissolved, and the relationship between the microstructures and the fractographic features can be

examined in the SEM by tilting of the fracture surface at approximately 45^o to the beam direction.

2.3 MICROFRACTOGRAPHIC OBSERVATIONS

2.3.1 General Observation with SEM

A sufficiently complete understanding of the fracture process often requires high magnification microfractographic observations. Such observations are particularly useful in investigating fracture mechanisms. To improve the resolution of micrographs, the choice of appropriate working parameters, such as the acceleration voltage, the electron beam current, the working distance (WD) and the aperture size should be taken into consideration. In general, for higher magnification observations, a relatively lower acceleration voltage, a lower beam current, shorter working distance and smaller aperture size of the objective lens should be employed. In addition, the astigmatism correction is very important to obtain a high resolution SEM image. At times, in examining simultaneously the aspects of both fractographic and microstructural features on a metallographic section extending to the fracture surface, a long working distance and a smaller aperture size have to be employed in order to obtain the desired depth of field (337).

2.3.2 Observation of Stereofractographs

Because the fracture surfaces produced by SCC and fatigue near-threshold cracking generally are microscopically very rough, it is very useful and necessary to do observations of stereofractographs, which can reveal more important information concerning the microtopography of the fracture surfaces than that which can be obtained by examining individual micrographs.

Stereofractographs are taken by photographing exactly the same region of the fracture surface at two different tilt angles, which are generally chosen to differ by 6 or 7^{o} (108). The exact site of the first micrograph can be identified by marking two or three easily recognizable features on the cathodic screen with a water soluble marker, the markings of which can be easily and completely wiped away with a soft wet tissue.

As the image generally will move considerably as the tilting is performed, this site will have to be refound after tilting. This is most easily done by decreasing the magnification prior to performing the tilting and verifying that the site of interest can be easily found at this lower magnification. If necessary easily recognizable features of the lower magnification image can be marked on the cathodic screen. As the tilting is performed, the region of interest is brought back to the centre of the screen a sufficient number of times so that this region is not lost. As a

precaution against losing the region of interest, it is wise to note the original coordinates of this site on the x and y vernier displacement scales, which, at least, will permit refinding the site at the initial tilt angle. After the tilting is finished, the site is repositioned precisely as it was for the first micrograph. As the scanning electron microscope used permits fine-scale vertical displacement, this feature is used to refocus the image as best as possible so that both stereomicrographs are photographed at precisely the same magnification. The final fine focusing is then performed in the usual manner. Care should also be taken to assure that both photographs are taken with similar levels of brightness and of contrast.

In examining a pair of stereofractographs with a stereo viewer, the photograph taken at the lower tilting angle is put on the right side, in order to obtain positive stereo imaging.

2.3.3 Observation of Fractographs on Matching Microregions

The comparison of matching high magnification micrographs from opposite surfaces can be particularly useful in identifying the relationship between the detailed fractographic features and the basic mechanism by which the crack propagates (338). Such observations permit to determine whether all of the fine fractographic features on the opposite facets match perfectly, which is a general case for transgranular stress corrosion in f.c.c. and b.c.c metals and alloys. If the

matching details are not present on the opposite surfaces, it can be usually be deduced that these details are produced by corrosion or other damage after fracture.

Matching microregions on opposite fracture surfaces are most easily found by precisely aligning the opposite fracture surfaces in the same manner with respect to the x and y vernier displacement scales of the scanning electron microscope and at least initially employing a tilt angle of 0^{o} (108). A region of interest is found on one fracture surface and photographed at the desired magnification and at a considerably lower magnification but at which it can still be recognized. If this lower magnification is still relatively high, it may be useful to take another photograph at another lower magnification. Its x and y position is measured with respect to an easily identifiable feature easily recognizable on the matching surfaces. The previously taken micrographs at the different magnifications then are employed to find exactly the matching micro region of interest.

It is also useful to take stereophotograph pairs at the same magnification of the same microregion on opposite fracture surfaces. This procedure can give important and useful information in helping to understand the nature of crack process even though such a procedure is more tedious.

2.3.4 Replication TEM

TEM of secondary-carbon replicas of fracture surfaces can resolve finer details than SEM, especially when replicas are shadowed with certain metals, such as Au or Cr, at low angles ($10^o \approx 20^o$) and examined at high tilt angles ($30^o \approx 45^o$) and relatively low voltage (60 ≈ 80 kv) to enhance the contrast (279, 339).

Features as small as 5 nm can be faithfully replicated and observed using this technique. Lynch (338) has often applied this technique to observe the fractographic details for various environment-assisted cracking and proposed a recent model based on locally enhanced plasticity in the presence of hydrogen or other adsorbed species, based on the presence of very fine dimples observed on fracture surfaces.

In order to observe finer microfractographic details and also to verify for the presence of very fine microvoids, replicas ofTSCC fracture surfaces in 316 s.s produced at low K and presenting a {100} <110> crack propagation crystallography, were studied. For comparison, the replication TEM technique was also employed for fracture surfaces of 316 s.s. produced near the fatigue threshold.

Replication TEM technique was also attempted for TSCC of α - brass, but was not successful, since the fracture surfaces were too rough to be able to make replicas of sufficient quality to permit observations of the fine details.

2.3.4.1 Details of Replica Preparation

Two - stage replicas (279) were produced as follows :

1) Normally, the specimen was cleaned ultrasonically. It is of paramount importance that the fracture surface be free of contamination before replication. The first plastic replica made from a fracture surface served to extract residual dirt on the fracture surface and was discarded.

2) A cellulose acetate sheet of about 0.04 mm thickness was cut into narrow strips of 30 mm x 15 mm size. A pair of medical tweezers was used to pick up the strip, which was then dipped into analytically pure acetone. The acetate strip was softened to allow it to follow the contours of the fracture surface while not being sufficiently fluid to form bubbles at the plastic-metal interface.

3) The softened acetate film was placed on the fracture surface and left in place for about 20 minutes. During this period, an optical microscope or the naked eye was employed to check for bubble formation. By using a dust blower with a fine spray nozzle, bubbles could be actually "driven" out of the area of interest.

4) The dried plastic film was stripped off and placed on a glass slide with the impression side up. Two pieces of PVC tapes were used to fix the film in position. Then, the glass slide was put into the carbon-coating bell chamber, where a thin layer of carbon was deposited on the acetate film. The deposition of carbon was carried out after the pressure became equal to or lower than 1×10^{-5} torr. Finally the carbon layer was shadowed by depositing a thin coat of gold-platinum. The shadowing angle employed was approximately 20^{o}.

5) Each strip was carefully taken from the glass slide and cut into about 3 x 3 mm at sites corresponding to different K or ΔK values. These were then placed on individual copper grids (200 mesh), also with the impression side up. Finally, an extractor was employed to dissolve the acetate film gradually with acetone vapour. The cellulose acetate was then dissolved and dried completely before examination by TEM.

At first, the procedure employed to dissolve acetate film was as follows :

After each strip was carefully taken from the glass slide, it was immersed in acetone. As the cellulose acetate dissolved, the carbon film would float to the surface. By then the entire carbon replica had fragmented into a number of pieces. Each piece was fished out on a copper TEM grid, and transferred into a mixture

of acetone and water (10 % H_2O). The replica was kept in this solution for about 5 minutes, and then moved to the acetone-water mixtures containing first 30% and then 70% water. Finally the replica was placed into pure water for several hours. Copper grids (200 mesh) were used to pick up the replica from the water tray. After two hours of drying, the replicas were ready for TEM examination.

The technique employed the extractor allows three significant advantages. The first one is that less washing and fishing of the replicas is involved, which should reduce the probability of introducing artifacts, The second is that it is easier to recognize the corresponding relation between the topography of the fracture surfaces. The third advantage is that it permits to avoid fragmentation of the replicas into several pieces, so that, it is convenient to find the exact replica portion, which corresponds to a given region of the specimen, such as a low K or high K region.

2.3.4.2 Operation of the TEM

A JEOL 2000 - FX transmission electron microscope was used to obtain the TEM fractographs. The acceleration voltage was set at 200 KV. Most of the exposure were taken using the medium aperture with a resolution of (5 ~ 10) nm. For a quick survey of the general features of the replica, a conventional single-tilt specimen holder was used, which also permitted to tilt the replica for taking stereo

micrographs.

The procedure for taking stereofractographs in the TEM is similar to that in the SEM, which has been described in the section of 2.3.2. The main difference is that it is more difficult to photograph exactly the same field of the fracture surface at two different tilt angles in the TEM than in the SEM. The method employed in the present study was to draw more than three easily recognizable features of the replica on a sketch and to note as accurately as possible, their relative position to some markers of the screen, such as the centre and the rims of the screen. The other difference is that the tilting angle employed in the TEM for a pair of stereographs was approximately 13^{o} to enhance the stereographic effect on the high magnification image taken from a small region. A few good quality pairs of TEM stereo fractographs were obtained with this procedure.

2.4 TECHNIQUES FOR DETERMINATION OF THE CRYSTALLOGRAPHY OF FRACTURE FACETS

2.4.1 Introduction

The fractographic investigation showed that for most of the materials in the present study, the fracture surfaces produced under "environmentally-assisted cracking" (for example, transgranular stress corrosion cracking and corrosion-fatigue) and fatigue near-threshold cracking conditions, consisted of a series of flat, parallel crystallographic facets separated by steps which were also crystallographic. In establishing the cracking mechanisms, it is then useful to determine the cracking crystallography as completely possible. These crystallographic analyses included the orientation of facets and steps and the directions of markings observed on the fracture surfaces. The determination of the facet orientation is not feasible with standard two-surface trace analysis because the fracture surface consists of many small stepped parallel facets. The observed crack trace on the sectioning plane represents the averaging of these steps and does not necessarily relate to the facet crystallography. In recent years, the several methods for determination of the orientation of cracking facets have been developed. They mainly are (i) selected area electron channelling, (ii) SEM photogrammetry technique, (iii) etch-pitting and (iv) measurement of the angles between the fractographic details. The first three methods have been reviewed by Meletis and Hochman (340). The method of

measuring angles between the fractographic details have been described by Scully et al (188, 341), by Dickson et al (336) and by Ait Bassidi (307).

The advantages and limitations of each orientation determination method are in relation to the grain size of the test specimen as well as the fracture facet size and the ability to determine the orientation of the steps and surface markings on the fracture surface. Because the etchpit technique has been extensively employed in the present study to determine the crystallography of the fracture facets of TSCC, corrosion fatigue cracking and fatigue near-threshold cracking attention will primarily be focused on describing this technique.

2.4.2 Etchpit Technique

The fracture plane orientation can be determined with crystallographic etch pits developed on the fracture surface, by employing selective etching reagents. Etching in certain crystallographic directions is much faster than in others, therefore, the shape of an etchpit will be a polyhedral formed by the intersection of the surface of the crystal with the etchpit faces. Experimental results (342, 343) have shown that in cubic structures, the faces of the etchpit generally correspond to low surface energy {100}, {110} or {111} planes. The shape of the pit depends on two factors: (i) the orientations of the etchpit faces and (ii) the orientation of the fracture surface.

By examining the geometric shapes of the etch pits under the SEM and by measuring the angles between the traces of interesting etchpit faces, the orientation of the crystal surface can be determined (344). In addition to the fracture surface orientation, the crystallographic directions of the surface traces can be obtained. However, it is usually not possible to determine precise orientations of TSCC surfaces because these surfaces are generally far from the ideal orientation for etchpit development, and often etching can result in the formation of truncated pits.

In our case, the determination of the orientation of different facets and microfacets was mainly performed by comparing on pairs of stereomicrographs the orientations of average fracture facet and micro cracking facets with those of faces of etch pits produced on the fracture surface. This method was also very useful for determining with reasonable precision the orientations of the secondary microfacets on thick, crystallographic river lines or steps since which are generally tilted or perpendicular to the primary fracture facets.

The etchpit technique is an excellent way to determine the crystallography of the fracture facets only when the fracture surfaces permit its use, such as in the case of relatively large fracture facets which are not too strongly deformed and when an appropriate number and dimensions of very crystallographic etch pits can be formed on regions of the fracture surfaces of interest. Consequently, the choice

and control of the etch-pitting conditions becomes particularly important.

For etchants used in the production of "crystallographic pits", the main requirement is that the solution first produce a good protective film, before it, or a second solution, develops pits in this film (345). Toaka et al (346) have suggested a number of useful solutions for this purpose. In general, the solution chosen should avoid the occurrence of general corrosion on the fracture surface so as to not damage the fractographic details. Metals are best etched under electrochemical control. Although this necessitates more elaborate techniques, it is preferred for materials such as stainless steels. In addition, the other etching conditions of temperature, time, voltage and current as well as the cathodic materials employed all should be controlled carefully. The test procedures often employed in the present study are as follows:

1) A promising etch-pitting solution according to references on dislocation etch techniques was found in the literature, e.g. (346, 348).

2) Etching was first carried out on polished surface of the material of interest under different etching conditions in order to determine close-to-optimal conditions for the development of appropriate number and size of pits on the fracture surface.

3) Part of the fracture surface was cut using a diamond saw and most of this surface was masked with cellulose acetate (Microstop) lacquer. The remainder was etched using the etching conditions suggested as optimal by the tests on the polished surface.

4) The etched fracture surface was examined, and if successful, further etch-pitting was performed on other selected regions. If not, the etching conditions were modified for the next test in the manner which appeared appropriate from the results obtained.

It is also important to etch only on of the two matching fracture surfaces in order to be able to verify if the etching has modified the fracture surface by comparing the same regions of the etched and un-etched opposite fracture surfaces.

As the etchpit techniques strongly depends on the material, the detailed, etching conditions and procedures employed will be described in the relevant chapters.

2.4.3 Measuring Angles Between Fractographic Details

Even if crystallographic indexation of fracture facets cannot be identified directly and unambiguously by this technique, the measurement of the angles

between facets within the same grain can permit to determine the possible or probable orientations. The method employed was that of rotating in the SEM (188, 341) the two planes about an axis parallel to their intersection line.

Firstly, it is necessary to rotate the specimen until the intersection line of the two facets considered is parallel to the tilting axis of the SEM. Secondly, the specimen is inclined until the projection of one of these facets becomes a single line (the facet is then parallel to the electron beam of SEM) or passes through a maximum facet width (the facet is then perpendicular to the electron beam). Subsequently, the inclination angle is noted and the same procedure is repeated for the second facet. The difference of the two inclination angles represents the measurement of the angle between the two facets studied. This method permits greatly to limit the number of possible combinations concerning their mutual orientations.

The f.c.c. metals which are sensitive to TSCC are generally of lower stacking fault energy (SFE) and present annealing twins of {111} orientation. The measurement of the angle between the facet in the matrix and a new facet in the twin and the comparison of this angle with that calculated assuming probable orientation of these facets, can also be employed (112) for deducing the orientation of the facets which could not be directly identified by other techniques. As well, the

measurement of the angle between the traces of the annealing twins and the striation-like markings observed on the fracture facets can also help to deduce the orientations of the striations.

An example to illustrate the importance of this method employed to identify the characteristics of the crystallography of corrosion fatigue cracking in the austenitic-ferritic KCR-271 stainless steel has been described elsewhere (307, 336).

2.4.4 Selected Area Channelling Patterns

Electron channelling in the scanning electron microscope (SEM) can be used to determine the orientation of TSCC facets and steps. This method is not widely applied to the study of fracture surfaces, particularly environmentally cracked surfaces, due presumably to the presence of oxides or excessive plastic deformation developed on these surfaces. As well, in some cases, the minimum size of facet identifiable may be larger than the typical facet size.

To determine the orientation of transgranular facets, first, the fracture facet of interest should be oriented perpendicular to the electron beam (Z axis). This is usually accomplished by using a double-tilt holder and tilting the specimen around the two orthogonal axes (x,y) in order to maximize the distance between two characteristic points of the facet. Subsequently, an electron channelling pattern is

taken. The orientation of the facet examined can be identified by visual comparison with a map of patterns (349).

For determining the crystallography of step traces and markings on the fracture facet, the angle formed by their direction and the orthogonal x or y axis (side of the pictures) is measured. The crystallographic orientation of the specimen, determined by the channelling pattern, is plotted on a stereographic projection.

The ECP unit of the SEM employed usually does not permit to obtain the electron channelling patterns for small grain size of the present TSCC specimens. Many trial attempts were carried out, but no good ECP patterns were observed. An additional reason not allowing its successful use could be interference associated with the presence of oxide film and of the important plastic deformation which developed on the fracture surfaces.

2.4.5 SEM Photogrammetric Technique

The basic principles of the use of photogrammetry in the SEM and the mathematical relationships were developed by several workers (340, 350, 351). This technique can be used to determine the orientation of small facets, but its accuracy decreases as the three reference points chosen on a facet become closely spaced. Whereas, this technique has to be accomplished by means of a back reflection Laue

pattern, obtained from a side face of the specimen; this requires the use of relatively coarse grained or single crystal specimens. In the case of using selected area channeling to assist in determining the orientation of the side face, however, this technique also requires flat surfaces presenting little or no plastic deformation, relatively free of oxides to obtain good quality channelling patterns.

Because of the presence of these limitations, this technique was not applied to the present crystallographic study for the polycrystal materials with fine grains employed.

CHAPTER 3

THE FRACTOGRAPHY OF NEAR-THRESHOLD FATIGUE CRACKING IN F.C.C. AND B.C.C. METALS

3.1 INTRODUCTION

There has been considerable progress in understanding metal fatigue propagation behaviour near and at the threshold (ΔK_{th}). Crack closure and shielding effects are now widely accepted concepts, which are often invoked to explain R-ratio, environmental and microstructural effects on ΔK_{th}. Less attention, however, has been paid to the cracking mechanisms active in the threshold region.

Since the basic cracking mechanisms must be related to fractographic features, a number of studies have been performed to examine microfractographic aspects (9, 34). Generally, transgranular fatigue cracking at very low propagation rates is highly crystallographic, and terms, such as quasi-cleavage, crystallographic decohesion and slip plane decohesion, have been employed to describe the main fractographic features. Yet, the more complicated facets are difficult to reconcile with a cleavage mechanism and the facet orientations usually identified do not correspond to slip planes. In the earlier studies, Baïlon et al. (110) noticed that the near threshold fatigue cracking crystallography often appeared to be consistent with

that which would result from fine-scale decohesion on two alternating slip planes, and also noted the very strong similarity (110) of fractographic aspects of near-threshold fatigue cracking and of transgranular stress-corrosion cracking in f.c.c. metals. Such important observations indicate that understanding the cracking mechanisms associated with near-threshold fatigue should help to understand that during transgranular stress-corrosion cracking and vice versa.

The first objective of the present study was to analyze the fractographic and crystallographic features associated with near-threshold fatigue cracking in f.c.c. and b.c.c. metals in greater detail, in order to compare it with the typical fractography of transgranular stress-corrosion cracking so as to identify better the cracking mechanisms operating in these two types of very. important fracture phenomena.

For fatigue tests in laboratory air, some intergranular fracture has been observed in the near-threshold region corresponding to the knee of the log da/dN-log ΔK curve.

The occurrence of intergranular cracking has also been observed in different metals including in some carbon and alloy steels (9, 137, 138, 352, 353), copper (10, 139), α-brass (10, 34, 110), 316 stainless steel (110, 141) and α-Ti (142). Two possible mechanisms for this intergranular cracking have been proposed. One is that

this intergranular cracking results from grain boundary embrittlement by an environmental effect (10, 138, 139, 353), such as atomic hydrogen, produced by the dissociation of water vapour in contact with the fresh fracture surfaces and transported to grain boundaries by dislocations. The second mechanism proposed (137, 353) is that intergranular cracking occurs when the cyclic plastic zone size is comparable to the grain size as a result of strain incompatibilities or dislocation pile-ups in the grain boundary regions.

Another objective of the present study of near-threshold fatigue cracking was to investigate further the possibility of the influence of the environment on the occurrence of intergranular cracking in the near-threshold region for copper and 70-30 Zn α-brass alloy.

3.2 SUMMARY OF MATERIALS AND EXPERIMENTAL PROCEDURES

3.2.1 Materials

The study on the near-threshold fatigue cracking in face-centered cubic metals focused on metals of low stacking-fault energy materials, namely AISI 316 austenitic stainless steel (quenched from 1000°C, grain size d $\approx$ 25 μm) and 70 Cu-30 Zn α-brass (annealed, d $\approx$ 25 μm), based on the assumption that reducing the stacking-fault energy should increase the size of the basic decohesion steps if

these occurred on alternating slip planes. Some observations were also carried out on copper and on 2024-T 351 Al alloy as well as on the f.c.c. α-phase of 8 ~ 14% Mn - 8% Al - 2% Ni bronzes.

Two body-centred cubic materials, polycrystalline Fe-3% Si and a mild steel (AISI 1008), were also studied. The Fe-3% Si plate, obtained from the Department of Metallurgy of McGill University, was annealed at 860°C for 4 hours under the protection of argon, in order to enlarge the grain size (~ 2 mm in the longitudinal direction, 100 μm-1mm in the transverse direction), then furnace cooled. The composition of Fe-3% Si plate is given in Table 3.1 and the microstructure after annealing is shown in Fig. 3.1. No further treatment was performed on the mild steel plate employed, the microstructure of which is presented in Fig. 3.2. An approximate carbon content of 0.08% can be estimated from the percentage of pearlite contained. The average grain size of the low carbon steel employed is about 30 μm. Some observations were also carried out on the b.c.c. β-phase of the bronzes. The material conditions of the bronzes studies are described in Chapter 6.

Table 3.1: The composition of Fe-3% Si plate

Elements	C	Mn	Si	S	P	Al	Fe
%	0.029	0.032	3.20	0.004	0.003	0.009	Balance

3.2.2 Fatigue Tests

Most of the near-threshold fatigue cracking tests in f.c.c. metals were carried out former by students and coworkers of professors Baïlon and Dickson (34, 110, 354, 355). Part of the fatigue tests were repeated on 316 s.s. and on α-brass. As well, the tests on b.c.c. Fe-3% Si and on the mild steel were performed by the present author.

Compact-tension (CT) specimens, conforming to ASTM specification E-399 with width W=50.8 mm and thickness B=12.7 mm were machined from rolled plates 14-25 mm thick for a TL crack propagation orientation for all of the materials employed in the present study. The geometry and dimensions of the CT specimens employed is shown in Fig. 3.3

The fatigue tests were carried out in laboratory air or "dry argon" at R ratios of 0.1 and 0.5 and frequencies of 20 Hz or 50 Hz down to crack growth rates, da/dN, of 10^{-8} mm/cycle on an Instron servo hydraulic machine (10 T or 20 T), employing computer controlled load-shedding. Figs. 3.4 to 3.7 present the log-log plots of da/dN vs ΔK and vs ΔK_{eff} on the 316 s.s., Fe-3% Si and on the mild steel tested.

The previous fatigue tests were performed (34, 110, 354, 355) at different R-rations generally 0.1 and 0.5 and in different environments including "dry" and wet argon, silicone oil and laboratory air. However, these differences in R-ratio and test environment did not influence the cleanliness of the fracture surfaces as well as the amount of closure-induced flattening of asperities observed.

The fatigue tests in vacuum and in air on 2024-T351 Al alloy, copper and α-brass were carried out at Ecole National Superieure de Mecanique et d'Aerotechnique, Poitiers, France by Drs. J. Petit and N. Ranaganathan. The fractographic and crystallographic observations on the fracture surfaces of copper and α-brass were performed in the present study, and some observations on 2024-T351 Al alloy were also repeated by the present author.

3.2.3 Etch Pitting Procedures

Scanning electron microscopy (JEOL-840 and JSM-820), etch-pitting and stereographic observations were employed to study the detailed microfractography and crystallography of transgranular near-threshold fatigue cracking in the different metals tested.

The procedures employed for producing etch pits on different metals concerned were as follows:

3.2.3.1 Etching AISI 316 Stainless Steel

Etch pits were produced on 316 stainless steel by electro etching in a solution of H_2SO_4 (0.5 m) with 100 mg/l NH_4SCN applied potential V (SCE) = -0.15 v, T = 40°C, time = 6 min. On {100} planes, the etch-pits formed have a square base with 4 faces corresponding to {111} planes (187). Fig. 3.8 schematizes of the etch pits produced in 316 s.s., as well as the correspondence between the orientations of fracture facets and the shapes of the etch pits on the fracture facets obtained.

3.2.3.2 Etching Copper

Several etch-pitting techniques (356) for copper were tried. Although they produced well-defined etch pits on fatigue surfaces produced at higher rates, they did not yield satisfactory results on the fracture facets produced in the near-threshold region. Occasionally less defined etch pits were produced on some relatively flat facets permitting to obtain limited information for analyzing the orientations of the facets. Very recently, an improved method (357) was employed to etch the near-threshold fracture surfaces of copper. The composition of the etchant is 1 M $(NH_4)_2S_2O_8$, 6 M NH_4OH and 0.3 M NH_4Br, in doubly distilled water. The etching time is 7 to 10 seconds at 10°C, with sufficient stirring. This improvement of the etching conditions employed permitted to increase the size of etch pits. Pits with {111} faces are produced by this etchant, and hence, the

orientations of the etch pits on the fracture facets are the same as in Fig. 3.8.

3.2.3.3 Etching 70 Cu-30 Zn α-brass

A few small etch pits were produced on some facets employing electro-etching in a 30 pct-orthophosphoric acid bath at 1.0v for 20 seconds (358). Owing to some success obtained for copper recently, the etching techniques (357) employed for copper were also tested for α-brass. Although a smaller number of well-defined etch pits were produced on the fracture surfaces near the threshold in comparison to copper, the etch pits produced still revealed some important crystallographic evidence.

3.2.3.4 Etching 2024-T 351Al Alloy

The etchant (81) employed was 50ml HNO_3, 32 ml HCl and 2 ml HF, at room temperature for 1 to 2 seconds. The etch-pits are pyramidal, with {111} faces. Therefore, the orientations of the etch pits obtained in this alloy is the same as that shown in Fig. 3.8.

3.2.3.5 Etching Bronzes

Etch pits in both the α and β phases of the bronzes were produced by chemical etching in 8 M nitric acid at 17°C for 15 seconds (356). The analysis of the pit shapes indicated that the pit faces corresponded to {100} planes. Thus, the

triangular pits with three {100} side faces produced indicate that the fracture facets correspond to {111} planes. Fig. 3.9 schematizes three typical orientations of etch pits produced on {100}, {110} and {111} fracture facets, respectively.

3.2.3.6 Etching Fe-3% Si

Etch pits were produced by a three-stage etching technique (359) consisting of etching for 6 seconds in a solution of 70 ml H_2O, 30 ml H_2O_2 and 5 drops of HCl, followed by a 3 seconds etch in 30 ml HCl and 70 ml H_2O, followed again by 15 seconds in a solution of 10 gm of $Fe_2(SO_4)_3$. $6H_2O$ in 10 ml H_2O, with rinsing and drying between each stage. This produced etch pit faces which consist of {100} and of {110} faces. Therefore, the appearance of the etch pits depends on whether only {100} or both {100} and {110} pit faces are produced. Fig. 3.10 shows schematically typical etch pits bounded by {100} and {110} planes.

3.2.3.7 Etching Mild Steel

Etch pits were produced by etching in a 4% Nital solution for about 17 seconds at 22°C. The orientations of the etch pits in the mild steel were similar to those obtained in the β phase on the Mn-Ni-Al bronzes (Fig. 3.9) and were bounded by {100} faces.

3.3 OBSERVATIONS AND DISCUSSION OF THE MICROFRACTOGRAPHY OF FATIGUE CRACKING NEAR-THRESHOLD FOR FCC METALS

In order to study the basic crack propagation mechanisms near or at the fatigue threshold, the microfractographic observations focused on determining the crystallography of the fracture facets. Some of the results obtained on both f.c.c. and b.c.c. metals have been previously published (111, 141, 145, 360-363).

The fractographic features produced at very low crack growth rates are generally very crystallographic and can vary from large almost featureless facets to complex sets of fine facets. The typical microfractographic features and examples of clearly identified cracking crystallography will be presented for the different metals tested.

3.3.1 316 Stainless Steel.

For this steel, large flat facets were found to have {100} orientations (Fig. 3.11) and to be favoured by a {100} plane oriented almost perpendicularly to the tensile axis, as demonstrated by the etch-pits produced on the fracture surfaces and by examination of stereo microfractographs. The side of the square base of the etch-pits in Fig. 3.11 is in a <110> direction, and the diagonal line across the etch-pit in a <100> direction. Such {100} facets perpendicular to the tensile axis

tended to be almost featureless, while facets inclined to the tensile axis more clearly presented <110> striation-like markings (Fig. 3.11). These marking are generally referred to as striations, although the spacings between striations are much larger than the average values of the propagation rate, da/dN. Most of the river lines or tear ridges tended to lie along the <110> direction perpendicular to the striations. Some, however, were along <100> directions. More complex features were present in some grains. An example is presented in the pair of stereo fractographs of Fig. 3.12. The main aspect is the presence of many wedge-shaped facets having an edge along a <100> direction, a relatively flat side (indicated as A) corresponding to a {100} orientation and a side (B) making an angle of approximately 45^{o} with the former and having an average orientation near {110} but clearly made up of two alternating {111} microfacets, with one set generally longer than the other. The flat {100} side could generally be observed at high magnification to present fine <110> striations. A few larger facets (indicated as C) were also identified as having a {111} orientation parallel to one side face of the etch-pits (C). These larger {111} facets are also parallel to one of the finer sets of facets making up the near-{110} side of the main set of wedge-shaped facets, with the trace of this same {111} also parallel to the <110> striations observed on the {100} side of these facets. These observations therefore indicate that decohesion on three sets of {111} slip planes was involved in forming the wedge-shaped facets. Such sets of complex facets occurred for cases in which no {100} plane was well oriented for cracking with

respect to the tensile axis or occasionally with the requirement of having to fracture a ligament between a pair of neighbouring fracture facets leading the macroscopic crack front.

Fig. 3.12 (b) presents the fractographic aspect on the opposite unetched fracture surface in the same region (a) of Fig. 3.12. It is seen that the features match perfectly and that the etch-pitting technique employed has not modified the microfractographic aspects.

A few of the secondary facets along river lines were quite flat and perpendicular to the primary {100} facets and thus correspond to {110} and {100} orientations as shown in Fig. 3.13, although smaller serrations on river lines tended to correspond to alternating {111} facets. The primary {100} facets often changed orientation by rotating about the <110> striation direction, best seen on pairs of stereomicrofractographs. In some cases, deviations approaching 90° were observed to result in a strongly striated facet of near-{110} orientation, while large primary {110} facets were not observed.

Small tetrahedra-like facets were quite often observed near grain boundaries (Fig. 3.14). These consisted of three fracture facets, the orientations of which were identified as {100}, {110} or {111}, with generally at least two different families of planes involved with any such set of facets studied.

Some observations were also carried out with TEM replicas produced from the near-threshold regions of fracture surface of 316 s.s., in order to observe fractographic details on the cracking facets and particularly to examine whether some very fine ductile dimples or microcavities were present on the relatively large, flat {100} facets. These observations (Fig. 3.15) indicated that fine <110> striations could be seen clearly on the striated {100} average cracking facets and that an interstriation spacing of approximately 0.13 to 0.20μm could be estimated. As well a wavy aspect of the {100} <110> facets could then be revealed clearly on these replicas. No microdimples or cavities, however, were recognized in contrast with the observations by Lynch (285) on environment-assisted fatigue cracking of some f.c.c. metals, who often observed microdimples on fracture facets associated with {100} <110> cracking crystallography.

3.3.2 70 Cu - 30 Zn (α-brass)

The previous work (34, 110) has shown that at very low crack growth rates ($\leq 10^{-7}$ mm/cycle) the threshold fatigue surfaces of 70 Cu - 30 Zn for tests in laboratory air, silicone oil, dry and wet argon were highly crystallographic, although in moist environments, the crystallographic aspect could often be masked by oxide layers. The present study attempted to more clearly determine the orientation of these fracture facets. At first, only occasional success was achieved in producing reasonably clear etch-pits by the electro etching technique on the near-threshold

fracture facets of this alloy. The details of some of the main fractographic features, hence, were identified from their similarity with those found in the 316 s.s. and from their relative orientations with respect to interfaces of {111} annealing twins.

The relatively flat facets also appeared to have {100} average orientations and were generally very clearly striated along <110>, with the river line generally present along the perpendicular <110> direction but with some river lines present along <100> directions at 45^o to these <110>. Such facets could be seen to consist clearly of two sets of finer facets. The orientations of these finer facets appeared to be {111} from the manner in which they were tilted with respect to the average facet orientation, which was assumed to be {100}. In Fig. 3.16, an annealing twin interface is seen parallel to the striation-like markings. A few small etch-pits indicated by arrows in Fig. 3.16 appear to confirm the cracking crystallography assumed. Fig. 3.17 presents again which contains two regions of {100} <110> cracking. One region presents one set of striations along which two sets of fine facets meet and another region presents a perpendicular set of striations along which two different sets of facets meet. The fractographic features of the intermediate region between these two strongly striated regions are more complex but still often present fine striations parallel to one or the other of the sets of more marked striations. The aspect in the intermediate region is fully consistent with two sets of <110> striations contained in an average {100} fracture plane, with the four

sets of fine facets corresponding to the four {111} planes. In this case, river line in the intermediate region are present along a <100> direction at about 45° to the both <110> directions, resulting in a near-{100} <100> cracking crystallography. These three sets of river lines form a herringbone or fan-shaped pattern of river lines and also indicate that the <100> river lines were obtained in regions presenting four sets of {111} microfacets.

Striated facets of {110} average orientation were at times observed near the threshold, and verified by improving the etch-pitting technique, as shown in Fig. 3.18. The micro-facets marked as A and B can be seen to be very clearly parallel to {111} side faces 1 and 2 of the etch pits respectively, indicating that decohesion on two sets of alternating {111} planes formed the {110} average primary facets with <110> striations and a <100> average crack propagation direction. Observation of stereo micrographs showed that these {110} facets were approximately perpendicular to the tensile axis. Generally the average plane of the primary facet deviates away from being perpendicular to the tensile axis and from a {110}, and one set of microfacets is larger than the other.

Small tetrahedra-like facets were again observed principally near grain boundaries (Fig. 3.19), since these permit average local orientations with large, more complex deviations from {100} or {110}. At very low da/dN, relatively large {111}

facets can also be observed, as seen in Fig. 3.18. Similar crystallographic facets were observed in the f.c.c. α-phases of 8-14% Mn-8% Al-2% Ni bronzes at propagation rates, da/dN, of about 10^{-8}mm/cycle, the details of which will be described in the next section.

3.3.3 α-phase in 8-14%Mn-8%Al-2%Ni Bronzes

The microfractographic aspects of near-threshold fracture surfaces for the α-phase of the bronzes tested in air show considerable similarity to those observed in 70 Cu-30 Zn tested in air. The fracture surface often consists of parallel, relatively large and planar crystallographic facets for crack propagation rates, da/dN, of approximately 10^{-6} mm/cycle. The etch-pits produced on the fracture surfaces indicate clearly that these relatively large and planar facets more often had {100} orientations, but also at times had {110} orientations, which were approximately perpendicular to the tensile axis. The tear ridges or river lines observed generally correspond to a <110> direction parallel to a diagonal of the square shaped etch-pits on {100} facets (Fig. 3.20). Some river lines have also been observed to be parallel to the edge of the etch-pits, i.e., to <100> directions. The striations clearly present were always parallel to the diagonal lines of the etch-pits, i.e., along <110> direction on the {100} average planar facets.

Herringbone or fan-shape patterns of river lines were also present. A typical example is shown in Fig. 3.21, in which the two perpendicular sets of <110> striations with <110> river lines can be clearly seen in regions A and B. As well, some river lines along a <100> direction are present in the intermediate region indicated by an arrow, where two sets of very fine <110> striations at times can be recognized. This indicates that decohesion on four sets of {111} slip planes should be responsible for the occurrence of the {100} <100> cracking crystallography observed. It was also noted in this figure that in the central part of the grain, a larger number of river lines of the same sign are present, the direction of which gradually changed from approximately a <110> direction to approximately a <100> direction. Their presence also permits the average local orientation of the cracking plane to deviate significantly from {100}.

At ultra low crack growth rates, da/dN ($\leq 10^{-8}$mm/cycle) the fractographic aspect became more crystallographic. Stair-like or pyramid-like facets of relatively large size (5μm to 20μm) were frequently observed. The etch pits, produced have shown that most of these large facets correspond to {111} planes, as shown in Figs. 3.22 and 3.23.

Detailed examination of region A of Fig. 3.22 (a) at higher magnification revealed that the stair-like large facets correspond to {111} planes, as indicated by

the etch pits in the shape of equilateral triangles with a central point shown in Fig. 3.22(b). It was found that all of these stair-like or pyramid-like facets were inclined with respect to the tensile axis at least in the observations carried out on the α-phase of the bronzes. Two large facets appeared to have {100} orientations and to be almost perpendicular each other (Fig. 3.23); however, examination of stereographic pairs clearly indicated that the values of the interfacial angle between these two facets was approximately 70°, and that each of these were inclined with respect to the tensile axis. Moreover, their {111} orientations were demonstrated by the presence of the triangular etch pits. The presence of such large {111} facets indicates that a sufficiently low ΔK and da/dN values, the resulting very small crack tip plastic zone size causes this plastic zone to become concentrated locally along a single set of {111} planes which then becomes the fracture plane. This f.c.c. copper-rich phase, because of its high solute content and particularly high Al content, would also be expected to show very planar slip behaviour favouring high slip reversibility.

3.3.4 Copper

The individual facets observed in the threshold region of copper were often very fine and arranged in complex patterns (Fig. 3.24). Very recently more success was obtained in forming clear etch-pits on the complex facets permitting to determine their orientations reasonably well.

A large number of {111} sheet-like facets were often observed as shown in Fig. 3.25, and were clearly identified by the etch-pits in the shape of equilateral triangles produced on the fracture surfaces for propagation rates, da/dN, of approximately 10^{-7} mm/cycle. In the example shown in Fig. 3.26, the striations are seen to have a <110> orientation, and the river lines or tear-ridges generally had a <110> or near-<110> orientation.

Fig. 3.27 and 3.28 present examples of finely striated primary facets which are clearly seen to be made up at two sets of microfacets, which meet along the striations and both of which are inclined with respect to the average facet plane. The orientations of these two sets of microfacets are {111} as demonstrated by small triangular etch pits indicated by the arrows in Fig. 3.27. The orientation of the primary facet in this figure is inclined to the tensile stress, and the size of one set of {111} microfacets can be seen to be larger than the other, which results in the sheet-like facet and makes the average facet plane quite close to that of these larger {111} orientation microfacets. Some facets formed at very low da/dN values, such as those shown in Fig. 3.28, presented features similar to the striated {100} facets observed on 316 s.s. and on α-brass. The interfacial angle of the two {111} microfacets can be clearly seen to correspond to an acute angle, hence, suggesting that the average striated facets have a {100} orientation.

Fig. 3.29 presents small pyramid-like or triangular shaped near-threshold facets in an unetched region of copper tested in air. Such small facets have been observed to occur generally in regions near grain boundaries.

Although a number of well-defined etch pits indicative of {100} or {110} orientations were often observed on large and relatively flat intergranular-like facets produced for propagation rates, da/dN, of approximately 10^{-6} mm/cycle, such pits were observed much less often on transgranular facets, which were generally complex and made up of very fine sheet-like facets. An example of such pits formed on an intergranular-like facet is presented in Fig. 3.30. These observations suggest that etch pits form readily on grain boundary portions which have orientations near {100} or near {110}.

Occasionally well-defined etch-pits were found, which indicated transgranular facets of {110} orientation. Fig. 3.31 presents such an average facet with <110> striation-like markings and near-<100> river lines, which appears to be consistent with the {110} <100> cracking crystallography at times observed for α-brass near the threshold (see Fig. 3.18). It is seen that such {110} facets have formed from the two sets of alternating {111} microfacets; however, the size of the microfacets is smaller than observed for α-brass. This appears to be related to the lower stacking fault energy of α-brass, favouring planar slip of dislocations and larger slip plane

decohesion microfacets.

3.3.5 2024-T351 Al Alloy

Some aspects of the near-threshold fractography of 2024-T351 Al alloy have been previously described by Baïlon et al. (34, 110). For this alloy tested in air, the fracture surface often consists of parallel crystallographic sheet-like facets. The etch-pits indicate clearly that these sheet-like facets have {100} orientations, with the ridges or river lines often corresponding to <100> directions parallel to the diagonals of the etch-pits produced which are bounded by four {111} side faces. Less often, the river lines are parallel to <110> directions. Fig. 3.32 presents general aspects of {100} sheet facets with two sets of <100> river lines which are perpendicular to each other. That the details of the microfractographic features have not been modified by etching can be seen by comparison of Fig. 3.32 (a) and (b), photographed before and after etching respectively.

The presence of <100> river lines consisting of large serrations along two <110> directions contained in a {100} fracture plane is shown in Fig. 3.33. By examination of this pair of stereo fractographs, the large serrations are seen to correspond to {111} facets, and some of the small serrations along the fine river lines can also be seen to correspond to the same pair of {111} facets. A few very fine <110> striations can also be recognized, as indicated by the arrow. This

cracking crystallography is similar to that of the wedge-shaped facets present in some grains for 316 s.s., where three sets of {111} slip planes were involved in forming the more complex fractographic features.

At times, etch pits in the form of equilateral triangles were found on some fracture facets produced near the threshold in this Al alloy tested in air as shown in region A of Fig. 3.34, clearly indicating that some facets correspond to a {111} orientation. Striations on the {111} facets generally were along a <110> direction, i.e., parallel to one side of the triangular etch-pits.

When a sufficient amount of cracking was produced in vacuum at ultra-low propagation rates (da/dN $\approx 10^{-8}$ mm/cycle), the fractographic aspects became very crystallographic and the fracture surface appeared to be very rough, similar to that observed for the α-phase of the 8% Mn-8% Al-2% Ni bronze in the HT_1 condition. Again stair-like and pyramid-like facets were observed, and their orientation was identified as corresponding to {111} planes by the triangular etch-pits produced on these facets. The ridges or river lines on the {111} facets were general close to <110> directions.

Fig. 3.35 (a) presents three {111} pyramidal facets observed on an unetched fracture surface for a very low crack growth rate (da/dN $\approx 10^{-8}$ mm/cycle) in a test

in vacuum. Details of aspects in region A of the {111} pyramidal facets shown in Fig. 3.35 (b) present some evidence of rubbing in region R of this figure. The aspect of region D of this figure is shown at higher magnification in Fig. 3.35 (c), from which it can be seen that this large near-{111} facet consists of a number of sheet-like {111} microfacets with fine <110> river lines. These sheet-like facets appear to be parallel to each other and also to be nearly parallel to the large facet A. A few features which appear to resemble microcavities can be seen in the left portion in Fig. 3.35 (c). The occurrence of these features is possible associated with some microstructural effects in the alloy. Such microfractographic features observed on the large {111} pyramid-like facets as well as their tilted orientation of these facet with respect to the tensile axis indicate that these correspond to {111} planes on which crack tip slip occurred.

For 2024-T351 Al alloy, the large {111} facets produced at sufficiently low da/dN were found more often for tests in vacuum than in laboratory air. This suggests that increased reversibility of slip associated with testing in vacuum may give rise to more planar slip hence to the more highly faceted fracture surface, especially at ultra-low crack growth rates. At these very low rates, the small plastic zone size should restrict slip to only a few slip planes within a very small plastic zone. Therefore, the most favourably orientated slip plane dominates and large fracture facets is produced by cracking on individual slip planes. In moist

environments such as laboratory air, slip reversibility could be reduced by the formation of crack tip oxides or possibly by diffusion and dislocation sweeping of hydrogen into the process zone (223), resulting in the operation of other slip system and thus causing more diffuse slip at the crack tip. The fact that more {100} sheet facets were observed for the tests in air for this alloy is consistent with this suggestion. Similar observations have been reported for IN 718, a nickel base superalloy (364), in which the more planar slip behaviour was linked to grater slip reversibility in vacuum and hence to the more highly faceted fracture surfaces.

Furthermore, since the nature of slip in precipitate-strengthened materials is strongly affected by precipitates size, misfit and distribution, slip is generally highly planar when the precipitates are small enough to be easily sheared as in the case of peak-aged 2024-T 351 alloy.

3.3.6 Microfractography of Fatigue Cracking in Vacuum for Copper and α-brass at Threshold

In contrast to the results on 2024-T351 A alloy, less faceted fractographic aspects were observed for α-brass, and particularly for copper fatigued in vacuum compared to the aspects produced in air. The microfractographic aspects for α-brass, and especially for copper tested in vacuum appeared to become more complex and less crystallographic as the crack propagation rates, da/dN, decreased

to ~ 10^{-8} mm/cycle. The general aspects are shown in Fig. 3.36 and 3.37. The fracture surfaces consist of a number of fine facets separated by tear ridges or bands of dimples in both metals. Moreover, a few typical dimples can be recognized in a few regions on the fracture surfaces of copper. such dimples are present in the regions marked by arrows in Fig. 3.38, clearly indicating that multislip should be occurring during the fracture process. Crystallographic striations present on complex facets, examples of which are shown in Figs. 3.39 and 3.40, are quite often observed for α-brass but very rarely for copper. It can be seen from these two figures that relatively regular striations with an interstriation spacing of approximately 1μm tend to be perpendicular to the river line-like markings in α-brass, but that these striations are less regular in copper. At times, the relatively large, flat facets were also occasionally observed in α-brass tested in vacuum, while such facets were not observed in copper. The crystallography of such relatively flat facets appears to be the same as that identified for similar facets of α-brass tested in air, but the individual microfacets in vacuum appear to be very small (Fig. 3.41), or to be arranged in groups corresponding to wider striation-like features, such as shown Fig. 3.39.

The identification of the orientation of the fine facets for copper tested in vacuum was unsuccessful by the etch-pitting technique, even if some of fine facets appeared to have {111} orientations.

These difference of fractographic details on the fracture surfaces for copper and for α-brass tested in vacuum strongly indicate that the fracture characteristics also depend on the stacking-fault energy (SFE), since a decrease in SFE should increase the size of the basic decohesion steps.

More importantly, the striking difference in the microfractographic morphology produced in vacuum and in air for both metals imply that environmental effects play a role in determining the morphology produced in air at low da/dN values. Especially for copper, many of the fractographic characteristics including some large dimple-like features produced in vacuum bear resemblance to those produced by ductile fracture, indicating that fatigue cracking in vacuum resulted in less localized slip. Such an observation is consistent with a previous investigation on copper (365), which showed that slip homogenization in vacuum increased the initiation life. As well, observations of the external surfaces of copper single crystals tested in air or in vacuum (365) have shown that the slip band density was approximately 10 times higher for tests in vacuum than in air. The present fractographic observations are also consistent with the very recent examination of dislocation substructure produced near threshold (124), which has shown that a dislocation cell network was present near the crack tip for copper tested in vacuum, while some dipolar ladder-like dislocation structure and some larger dislocation cells were observed for the sample tested in air. These

observations (124) confirm the importance of the role of environment to modify crack tip plastic deformation characteristics and hence to alter the fatigue fracture process, especially at low da/dN values.

That, for α-brass and copper tested in laboratory air, a number of highly crystallographic and relatively large {111} facets were present at sufficient low da/dN values ($\leq 10^{-7}$ mm/cycle), and that {100} and {110} striated facets occurred frequently at somewhat higher da/dN values ($\approx 10^{-6}$ mm/cycle), must be related to environmental effects which acted to enhance the localization of plastic deformation at the crack tip. In particular, the evidence indicates that slip planarity was larger for the tests in air, resulting in relatively long slip bands and large decohesion facets following the most favourable orientated slip planes.

3.3.7 Summary of the Crystallography Identified and the Cracking Mechanisms for f.c.c. Metals Near the Threshold

The crystallography of near-threshold fatigue cracking identified for f.c.c. metals studied and the mechanisms associated with this cracking can be summarized as follows :

Firstly, relatively flat {100} fracture facets with <110> striation-like markings and near-<110> river lines were often observed for all the f.c.c. metals studied

fatigued in air. The occurrence of these {100} facets have at times been shown to result from fine-scale microscopic decohesion on two alternating {111} slip planes which meet along the <110> striations. In regions in which such {100} facets are perpendicular to the tensile axis, approximately equal amount of decohesion generally occurs along the two slip planes meeting along the <110> crack front. That this stress orientation condition particularly favours flat facets indicates that the individual decohesion steps should then be very small, which suggests that this condition also favours the emission of dislocations at or near the crack tip along sets of very closely spaced slip planes. As the {100} primary facet deviates away from being perpendicular to the tensile axis, slip on one plane in the crack tip region tends to become more important than on the other, which should result in larger decohesion steps on the favoured plane permitting to explain the more pronounced striations observed on inclined {100} facets.

In 70-30 Zn α-brass, the regions of fracture facets presenting striations often have a stepped aspect (Figs. 3.18, 3.20), with the individual steps corresponding to fine facets along a pair of {111} planes. This aspect of {111} or near-{111} steps resulting in a {100} or near-{100} average orientation of the fracture plane provides particularly strong evidence that fatigue propagation near the threshold occurs by decohesion along slip planes.

Secondly, complex near-threshold fractography corresponding to wedge-shaped {100} and near primary {110} facets as well as to {111} primary facets commonly observed in 316 stainless steel was identified as resulting from slip and decohesion occurring on three sets of slip planes, but with slip on the plane parallel to the large {111} facets being particularly important. Indeed, decohesion on this plane explains these large {111} facets and also contributes to the formation of both sides of the wedge-shaped facets which meet along a <100> edge (see Fig. 3.12).

A {100} <100> cracking crystallography can also be found particularly for 2024-T351 Al alloys and less often in 70 Cu-30 Zn α-brass with the <100> river lines often finely serrated along the two < 110> directions. In α-brass, this region of more complex fractography was quite often situated between two regions which presented, in the same grain, <110> striations, along which two sets of fine {111} facets meet, with the striations of one region perpendicular to those of the other. This observation strongly indicates that this {100} <100> fractography resulted from slip and decohesion occurring on all four sets of slip planes. It is the occurrence of this multiple slip which has produced these more complex near-threshold fractographic features. It has been noted that, although the roughness of the fracture facets can vary, these features observed on the α-brass resemble closely those often observed on 2024-T351 Al alloy (111) and Fig. 3.33 which present {100}

river lines. These river lines are also often finely serrated along two <110> directions (section 3.3.5). The explanation for the preferred occurrence of these <100> river lines at low da/dN values for this Al alloy should then be that this cracking crystallography results when slip and decohesion on four {111} slip planes occurs in the crack tip region. That the {100} <100> cracking crystallography was more often observed in 2024-T351 Al alloy near-threshold probably attributed to the formation of crack tip oxides which can reduce reversibility of slip and thus can enhance the multiple slip.

Thirdly, striated facets of {110} average orientation with <110> striations and near <100> river lines was at times observed near the threshold for the both copper and α-brass tested in air. The formation of such {110} facets has been demonstrated to consist of two sets of {111} microfacets. Generally the size of one set of such slip plane facets is larger than the other set, as the average plane of the primary facets deviate away from being perpendicular to the tensile axis and from a {110}.

Such primary {110} facets were only rarely observed for 316 s.s. and were very small. Some secondary {110} facets along thicker <100> river lines were frequently found and identified for 316 s.s. as resulting from a crack path alternating between two sets of {111} planes.

Fourthly, as the crack growth rates decreased to ultra-low values (10^{-8} ~ 10^{-9} mm/cycle), relatively large {111} facets having a stair or pyramid-like aspect were often observed for the α-phase of 8% Mn-2% Ni bronze in the HT1 condition (see section 6.2) tested in air and for 2024-T351 Al alloy tested in vacuum. Such larger {111} facets were also at times observed for α-brass in air at sufficiently low da/dN values. With copper tested in air at da/dN ≈ 10^{-7}mm/cycle, the larger near-{111} facets which were generally titled with respect to the tensile stress were observed to be made up of a number of fine sheet-like {111} facets which were parallel to each other.

The presence of such large {111} facets indicates that at sufficiently low ΔK and da/dN values, resulting in sufficiently small crack plastic zones, the plastic zone becomes concentrated locally principally along a single set of {111} plane which then becomes the fracture plane.

Fifthly, in a large number of grains of all f.c.c. metals studied, series of small tetrahedral-like or pyramid-like facets were often observed in the regions near grain boundaries. Such fractographic features firstly indicate that, in these regions, more slip planes or more different families of planes of decohesion were involved in accommodating the orientation of the average fracture plane with respect to the stress axis. These as well indicate that local stress and strain effects result in the

need for differently orientated crack segments in neighbouring regions to join up to produce the macroscopic crack front.

In consequence, the detailed microfractography of transgranular threshold cracking in f.c.c. metals examined is consistent with this cracking being produced by decohesion on planes on which slip has occurred ahead of the crack tip, often on alternating slip planes. Fig. 3.42 shows how {100} and {110} primary facets can be formed from decohesion along two alternating {111} slip planes. The type and the degree of complexity of the fractographic features observed depend on the orientations and the number of slip planes on which decohesion occurs and on the amount of decohesion which occurs on each slip plane, (i.e., on the size of the each set of microfacets produced). The number of slip planes on which decohesion occurs and the size of the microfacets depend on the orientation of the individual grain with respect to the stress axis, on local stress effects associated with the need for differently orientated crack segments in neighbouring regions to join up to produce the macroscopic crack front, on the crack growth rates, on the crack tip stress intensity values, as well as on the material conditions and the effects of environment on the degree of slip planarity obtained.

3.3.8 Fractography of Intergranular Cracking Near the Threshold

In the earlier studies of Baïlon, Dickson and coworkers (10, 34, 110, 354, 355) on the fracture surface of near-threshold fatigue cracking in the tests in laboratory air or in "dry argon", intergranular cracking was observed in 316 stainless steel, copper and α-brass. As well, it was found that the amount of intergranular cracking was related to the degree of moisture in the environment. Higher moisture levels tended to give more intergranular cracking. In the present study, it was also clearly found, as shown earlier by Marchand et al. (10), that the percentage of intergranular cracking also strongly depends on the crack growth rate (da/dN). The percentage of intergranular cracking could reach 60% at a da/dN value of approximately 10^{-6} mm/cycle, while the intergranular facets disappeared approximately above 1×10^{-4} mm/cycle or below 1×10^{-7} mm/cycle. Such findings resulted in a suggestion that the occurrence of intergranular cracking during fatigue in air is probably associated with the effect of hydrogen swept to grain boundaries by dislocations (10).

In order to verify this suggestion, the threshold fatigue tests were carried out in copper and in 70 Cu-30 Zn α-brass in vacuum and then the atmosphere was changed to air. A clear transition in fracture surface morphology associated with this change of environment was observed by SEM (Fig. 3.43 and 3.44). The presence of intergranular facets for the last portion in air at a da/dN value of $\approx 2 \times 10^{-6}$

mm/cycle is clearly evident. In contrast, the fracture surfaces obtained in vacuum for the full range of da/dN values studied (10^{-5} to 10^{-9} mm/cycle) and for both copper and α-brass were completely transgranular. This evidence clearly indicates that for these two f.c.c. metals the intergranular cracking is indeed an environmental effect, which often has been considered to be grain boundary embrittlement produced by hydrogen (10, 36, 138).

Three important fractographic aspects were noticed for the near-threshold intergranular facets for the f.c.c. metals studied.

Firstly, the presence of extrusion and intrusion features on some intergranular facets was frequently observed at relatively low da/dN values (e.g., 10^{-6} mm/cycle) for copper and α-brass tested in air. An example is presented in Fig. 3.45. This aspect indicates that the intergranular facets form prior to the transgranular facets and then act as internal surfaces in a region submitted to cyclic deformation. This aspect is consistent with that of hydrogen being transported ahead of the crack tip and producing the intergranular facets in air.

Secondly, small tetrahedra-like or pyramid-like facets were also often observed on the near-threshold intergranular facets as shown in Figs. 3.45 and 3.46. These appear as crystallographic pits and protrusions which match in an interlocking

manner on opposite fracture surfaces, indicating that they were created before or during the grain boundary separation process. Such facets correspond to small amounts of transgranular cracking which nucleate along slip traces on the intergranular facets. The shape of the pits in Fig. 3.46, on a sample which has not been etched, indicates that the three side facets correspond to {111} planes, consistent with the near-threshold transgranular cracking facets identified on a very microscopic scale for the f.c.c. metals studied. It can be also noticed that one side of these pyramids is often aligned along the slip trace on which they nucleated. In a few cases a large number of such small facets can be present and the amount of transgranular cracking on some intergranular facets can occasionally approach or surpass 50%. Considering the role of the environment in producing this intergranular cracking on at least some f.c.c. metals, it is particularly interesting to note that the nucleation of similar small transgranular facets along slip traces on intergranular facets can also occur in the case of stress-corrosion cracking of 316 stainless steel (155) for which the microscopic crack path also follows {111} slip planes (see chapters 4 and 5).

Thirdly, some intergranular facets were only partly intergranular and the observation for these intergranular portions often showed the presence of numerous very fine river lines (Fig. 3.47), indicating that the crack path was not exactly along the grain boundaries. Such quasi-intergranular facets were also observed in a recent

study of α-Ti (104). Intergranular facets with this aspect were referred to as quasi-intergranular cracking and were interpreted as actually occurring by the same cracking mechanism as the more clearly transgranular cracking, namely by microscopic decohesion along slip planes active in the crack tip region, with the slip planes along which decohesion occurred and the number of river lines present varying locally so as to constantly permit the crack path to lie close to the grain boundary. This aspect then suggests that this quasi-intergranular cracking occurs when the localized slip in the immediate vicinity of the grain boundary becomes significantly more important than within the grain.

That highly crystallographic transgranular facets, including relatively large {111} facets, were observed at sufficiently low da/dN for copper and α-brass tested in air, but not for those in vacuum, indicates that they are associated with an environmental effect which acts to enhance the localization of the plastic deformation at the crack tip (section 3.3.6). Since intergranular surfaces in both α-brass and copper tested in air were observed to be at times actually quasi-intergranular and produced by a similar mechanism as the transgranular facets, it can then be suggested that the intergranular cracking in air is associated with environmentally-enhanced localized plasticity near the grain boundary. In vacuum, this is prevented in copper and α-brass by the absence of the environmental effect, which then results in more diffuse slip associated with a greater number of slip

systems activated. More diffuse slip will favour less incompatibility and stress concentrations at grain boundaries and thus more diffuse slip will result in less intergranular cracking. On the other hand, taking into account some evidence that shear localization due to hydrogen has been clearly shown for steels (256, 366) and Fe-Ni alloys (367), the environmental effect on fatigue fracture morphology in the present observations for copper and α-brass at low da/dN values appears to be more compatible with a hydrogen enhanced local plasticity mechanism (237), however, it is not clearly evident whether hydrogen can be formed during fatigue cracking in air for both metals.

3.4 THE MICROFRACTOGRAPHY IN BCC METALS

3.4.1 The Objective of This Study

In section 3.3, the fractographic aspects of near-threshold fatigue cracking in f.c.c. metals were shown to correspond well to fine-scale decohesion along {111} slip planes often involving alternate slip. Detailed studies of the fractography of near-threshold fatigue cracking in b.c.c. metals are fewer, e.g. (127), and have indicated a variety of fracture facet orientations and crack propagation directions. Table (1.1)b (see section 1.1.1.3.2) gives a summary of results reported in different studies (94-96, 125-132), some of which were not conducted in the near-threshold regions.

Some of the microfractographic features (141) observed for f.c.c. metals suggested that slip plane cleavage could be involved in near-threshold fatigue cracking mechanism. As well, very similar microfractographic features have been found for stress-corrosion cracking in f.c.c. metals and alloys (see section 1.2.1.6), for which a cleavage-type mechanism is often proposed (157, 202).

Since the fractographic aspects of cleavage in b.c.c. metals are well known, these metals are well suited for determining whether crystallographic near-threshold fatigue cracking occurs by a cleavage of by a slip mechanism. For this reason, the detailed microfractographic aspects of near-threshold fatigue propagation in Fe-3% Si and in mild steel for tests in air at room temperature were studied. Some observations were also performed on the β-phase of Mn-Al-Ni bronzes.

3.4.2. Observations and Results

The materials and experimental procedures have been described in section 3.2. The observations and results will be presented in this section.

3.4.2.1 Observations on Fe-3% Si

The primary crystallographic fracture facets for near-threshold fatigue cracking in Fe-3% Si presented fine striation-like markings. In many cases, these primary facets could be seen to consist of much finer microfacets, with the

striation-like marking corresponding to the sites at which two sets of microfacets met or corresponding at least to the extremities of one set of microfacets. An example from an unetched fracture surface is shown in Fig. 3.48.

Different average orientations of primary facets, most often {100} and {110}, were identified from the crystallographic etch pits, which in Fe-3% Si were bounded by {100} and {110} etched faces, indicated as i and j respectively in Fig. 3.49. It can be clearly seen from this figure that the primary {100} facets consist of very fine microfacets which meet along fine striations. The cracking crystallography is consistent with that schematized in Fig. 3.50a, that is, cracking occurring by decohesion on two alternating sets of {112} slip planes. The striations and ridge or river lines are parallel to the perpendicular pair of <110> diagonals of the square {100} face of the etch pit.

Fig. 3.51 shows the other typical striated aspect of primary {100} facets in Fe-3% Si. In region A, the cracking crystallography is the same as that identified in Fig. 3.49. In region B, the striations are parallel to <100>, which is consistent with cracking occurring by decohesion on two alternating sets of {110} slip planes, as schematized in Fig. 3.50b.

Striated {110} facets with <111> striations and approximately <112> river lines are presented in region "c" of Fig. 3.52. The primary facets are parallel to the {110} face marked as "c" within the etch pits and inclined with respect to the tensile axis, as observed by examining stereographs. This cracking crystallography is thus consistent with that depicted in Fig. 3.50c, and suggests that the {110} primary facets resulted from decohesion on two {112} alternating slip planes. The <111> striations correspond to the intersection line of the pairs of {112} microfacets. In Fig. 3.53, the cracking crystallography in region "c" is also consistent with model c, namely, tilted {110} facets with <111> striations. In region D, relatively flat and large {100} facets present <110> river lines and striations consistent with a <113> orientation, in that the angle between the <100> and the striations is approximately 25^{o}. Consequently, the microfractographic aspect is consistent with that shown in Fig. 3.50d.

For the pair of stereofractographs of Fig. 3.54, the microfractographic aspect in region A agrees with the crack crystallography schematized in Fig. 3.50a. In this region, perpendicular pairs of <110> river lines to each side of central <100> spine form herringbone patterns. Fine <110> striations are also present perpendicular to each set of <110> river lines. From the orientation of the etch pit on these facets, stereographic examination showed that the facets in region "A" are almost perpendicular to the tensile axis and have orientations near {100}. The

primary facets in region "c" are parallel to a {110} face of the etch pits and present <111> striations and two sets of <112> river lines, consistent with the cracking crystallography of Fig. 3.50c. Fig. 3.55 shows the microfractographic details of unetched fracture surface at the site which matches region "M" in Fig. 3.54. This figure presents clear evidence that the etch-pitting technique used has not altered the fine microfractographic features.

Comparison of the microfractographic details on the fracture facets of the near-threshold fatigue cracking with typical cleavage {100} facets with <110> and <100> river lines (Fig. 3.56) observed in Fe-3% Si clearly indicates that the primary facets produced by near-threshold do not resemble such cleavage facets.

3.4.2.2 Observations on Mild Steel

The microfractographic and crystallographic features of near-threshold cracking in AISI 1008 steel were basically the same as those observed on Fe-3% Si, with primary {100} and {110} facets often observed and identified from the crystallographic etchpits which were simply bounded by {100} faces. Different regions consistent with the different alternate slip cracking combinations schematized in Fig. 3.50 were again identified. For example, in region D of Fig. 3.57, the near-{110} primary facets present <110> river lines and near-<113> striations in agreement with model d of Fig. 3.50. The matching region on the opposite unetched

fracture surface is shown in part (b) of this figure. Comparison of matching regions allowed to verify that the microfractographic features, including the microfacets, matched in an interlocking manner at high magnification.

For the near-threshold fatigue cracking in the mild steel, sheet-like facets were often observed in which a considerably greater amount of decohesion occurred on one of the sets of microfacets. The stereographic observations indicated that the average orientation of the primary facets then tended to deviate from that predicted for equal amounts of decohesion on the two sets of slip planes towards that of the {110} or {112} slip plane on which the largest amount of cracking occurred. This deviation in orientation occurred as a rotation in orientation about the direction corresponding to the striation-like markings, when the primary facets were slanted with respect to the tensile axis, they tended to consist of sheet-like facets (Fig. 3.58) with a greater amount of cracking following a single slip plane. Primary facets with orientations perpendicular or close to perpendicular to the tensile axis had average orientation which generally agreed well with those predicted for equal amounts of decohesion on alternating slip planes. Such facets generally presented a wavy aspect as shown in Fig. 3.59.

3.4.2.3 Observations for the b.c.c. β-phase of Mn-Al-Ni bronzes

Observations were also carried out on the b.c.c. β-phase of the Mn-Al-Ni bronzes tested in air and in 3.5% NaCl solution. It was found that very crystallographic stair-like facets were often present at da/dN 10^{-4} to 10^{-6} mm/cycle in this phase. The values of the angles between two stair-like facets estimated by observing stereofractographs were generally approximately 60^{o} degrees, but some of the stair-like facets were almost perpendicular to each other as shown in Fig. 3.60. Secondary cracks were observed on a metallographic sections in the immediate vicinity of the fracture surface. Fig. 3.61 shows an example where the crack path clearly follow slip traces, thus, further confirming the interpretation of cracking alternating between different slip planes. As well, the size of facets along the individual slip traces are often relatively large, consistent with the large flat facets observed on the fracture surface of the same 13.5% Mn-Al-Ni bronze (Fig. 3.60). The relationship between the microfractography and microstructure of the β-phase containing K_{IV} precipitates and secondary α-grains (368) in 13.5% Mn-Al-Ni bronze was examined by the metallographic sectioning technique to show that, even though a few dimples were present mainly at higher ΔK on the β facets, some fatigue striation-like markings could also be seen at high magnification (area indicated by an arrow in Fig. 3.62) on some β facets.

Etchpits produced on the β-phase facets of these bronzes were not defined well enough to allow to identify the near-threshold cracking crystallography. In particular, the size of the etchpits produced on β-phase facets was very small, leading to some difficulty in determining the orientations of the striations and river lines on the fracture surfaces. It appeared, however, that {100} and {110} facet orientations could be recognized quite often as shown in Figs. 3.63.

3.4.3 Discussion

The detailed observations on Fe-3% Si, mild steel and the β-phase of Mn-Al-Ni bronzes has shown that, on a very microscopic scale, near-threshold tansgranular fatigue cracking in these b.c.c. metals involves decohesion along slip planes, often along alternating slip planes, in much the same manner as previously shown for f.c.c. metals. Similar cracking along alternating slip planes has previously been shown to occur in b.c.c. Ti-V (126) for da/dN values of 10^{-5} - 10^{-4} mm/cycle. Because of the large number of slip planes which can be activated in b.c.c. metals, many variations in cracking crystallography can be obtained. In some cases, only one set of microfacet orientation appeared present or at least one set was highly dominant. This resulted in an average facet orientation which was approximately the same as that of the slip plane corresponding to the microfacets, which then had a sheet-like appearance. Such sheet-like microfacets were also at times identified for near-threshold fatigue cracking in copper (section 3.3.4) and have also been

observed for transgranular stress-corrosion cracking in austenitic AISI-SAE 316 stainless steel (chapter 4).

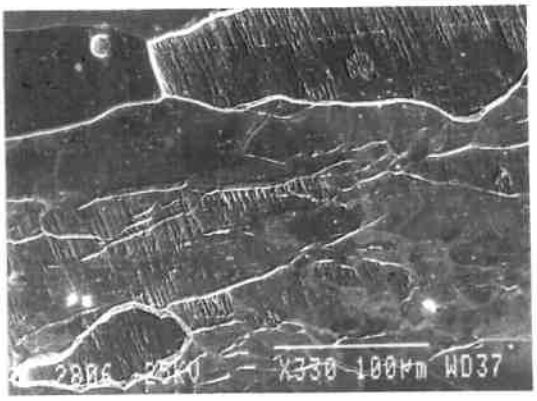
In all the observations on the Fe-3% Si and the mild steel studied, the microfacets were clearly present for near-threshold fatigue cracking. Their extremities or sites at which pairs of microfacets met then produced the fine striation-like markings. The absence of any cleavage-like facets in the b.c.c. metals studied, indicates that this cracking is at least primarily produced by slip.

The fatigue near-threshold fractographic features in h.c.p. titanium (104) also indicate that the cracking involves decohesion on microfacets which are along pairs of slip planes, with the average orientation of the primary facets then often being a bisector of the angle between these slip planes.

These results therefore strongly indicate that the transgranular near-threshold fatigue cracking in th f.c.c. and b.c.c. metals studied was produced by localized slip acting in the crack tip region, somewhat in the same manner as that which gives rise to ductile crystallographic striations (81, 93). The interstriation spacing at higher fatigue crack growth rates agrees with the macroscopic crack growth rate; however, near the threshold many cycles are required to produce each microfacet. Thus, it is not clear how continuously or discontinuously the cracking produces individual

microfacets, the knowledge of which would contribute considerably to better understanding the near-threshold propagation mechanism but remains very difficult to unambiguously establish experimentally.

Although the cracking crystallography can be explained as being produced solely by shear (reversed slip) in the case of fatigue cracking, since reversed plasticity results from the fatigue cycling, it remains possible that such cracking may also involve a cleavage or cleavage-like component to produce the decohesion on the microfacets. This is suggested by the lack of evidence of rubbing on some of the large {111} facets produced at ultra-low da/dN values such those observed for 2024-T351 Al alloy (141), or because in some cases the microfacets are often not discernible in f.c.c. metals, especially when the orientation of the near-threshold primary facets are perpendicular to the tensile axis. Possible mechanisms of decohesion and transgranular stress-corrosion cracking will be discussed further in Chapter 7.



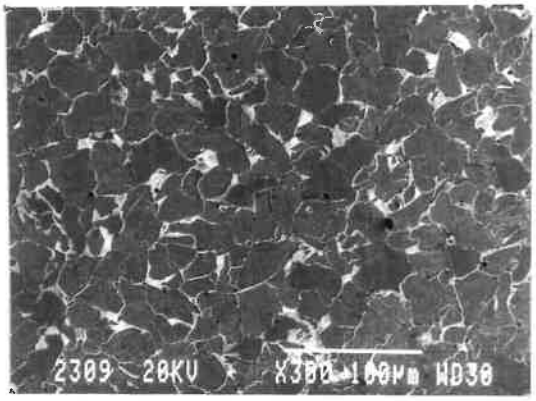


Fig. 3.1 **Fig. 3.2**

Fig. 3.1: Microstructure of Fe-3% Si
Fig. 3.2: Microstructure of the mild steel

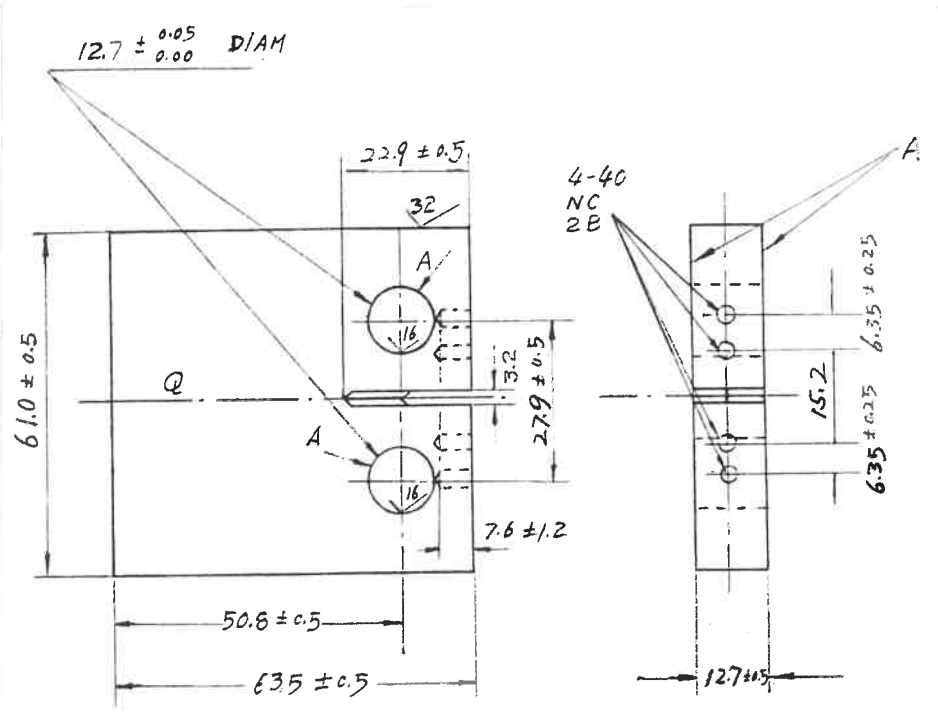


Fig. 3.3: Geometry of CT specimen

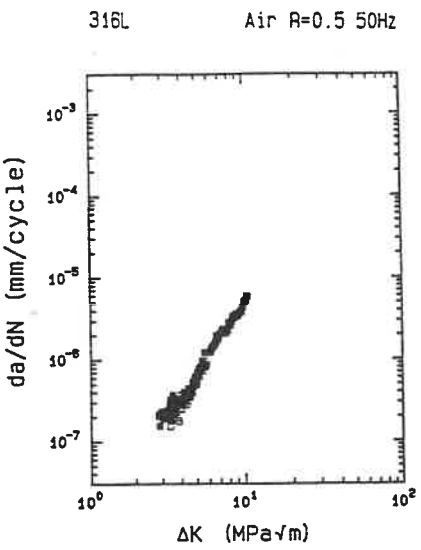


Fig. 3.4

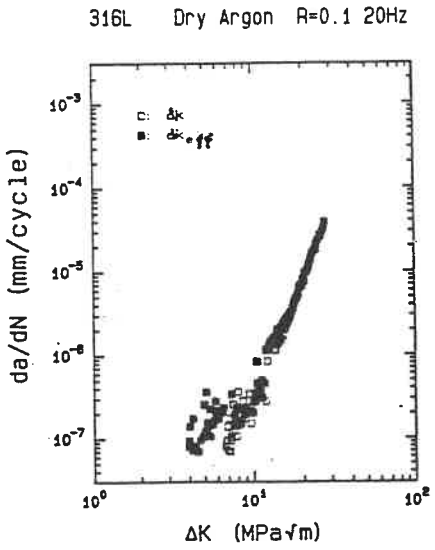


Fig. 3.5

Fig. 3.4: log da/dN - log ΔK crack growth curve for the 316L stainless steel tested in air.

Fig. 3.5: log da/dN - log ΔK (and ΔK_{eff}) crack growth curve for 316L stainless steel tested in "dry argon".

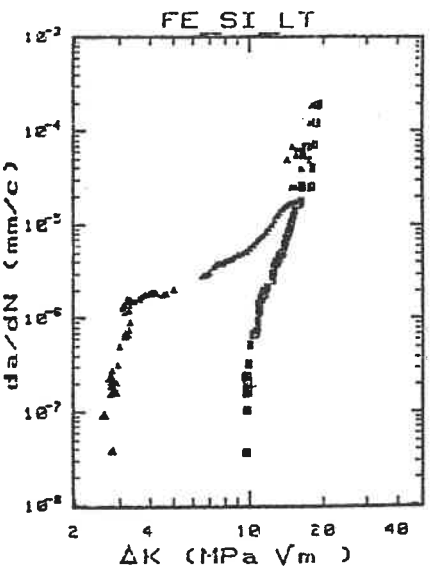


Fig. 3.6

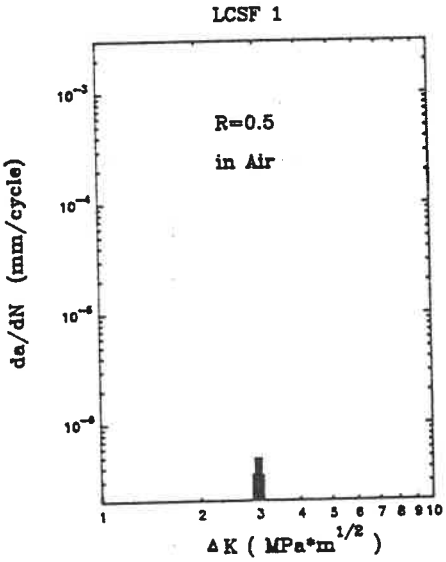
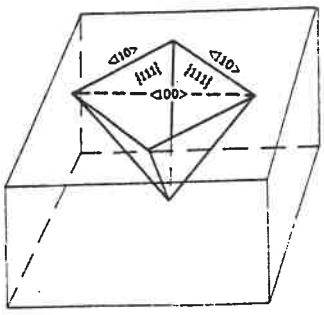


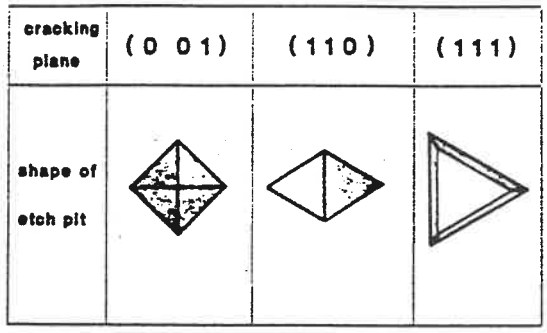
Fig. 3.7

Fig. 3.6: A typical log da/dN - log ΔK (and ΔK_{eff}) plot of Fe-3% Si tested in air. - da/dN - ΔK; Δ - da/dN - ΔK_{eff}.

Fig. 3.7: A typical log da/dN - log ΔK crack growth curve for the mild steel tested in air.

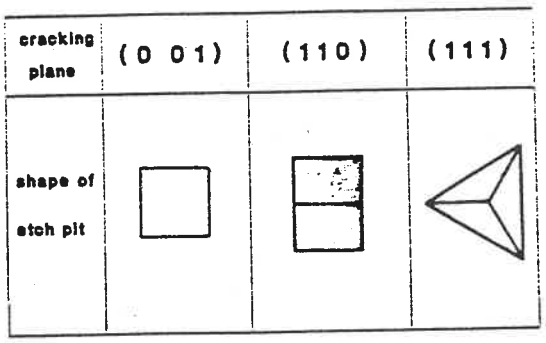


(a)



(b)

Fig. 3.8: (a) Schematic of typical etch pits produced in 316 s.s. (b) schematic of the correspondence between the orientations of fracture facets and the shapes of the etch pits.



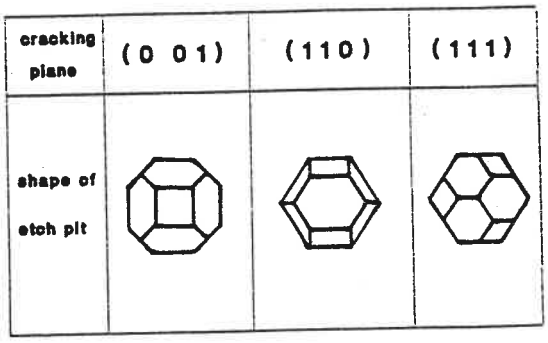


Fig. 3.9 **Fig. 3.10**

Fig. 3.9: Schematic of the correspondence between the orientations of fracture facets and the shapes of the etch pits produced in the bronzes studied.

Fig. 3.10: Schematic of etch pits bounded by {100} and {110} planes in Fe-3% Si.

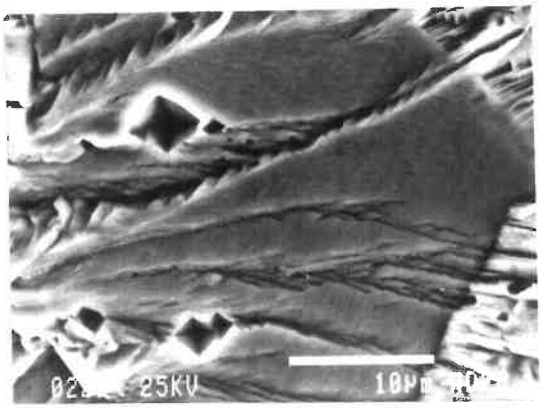
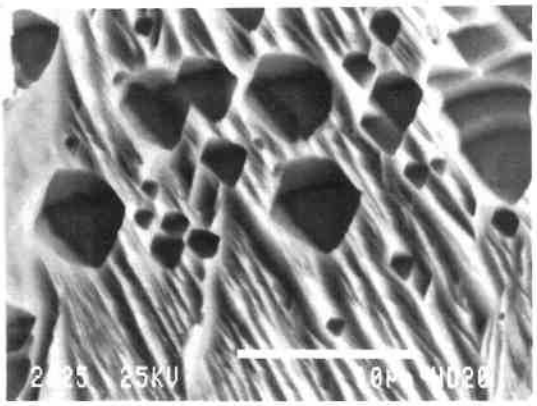
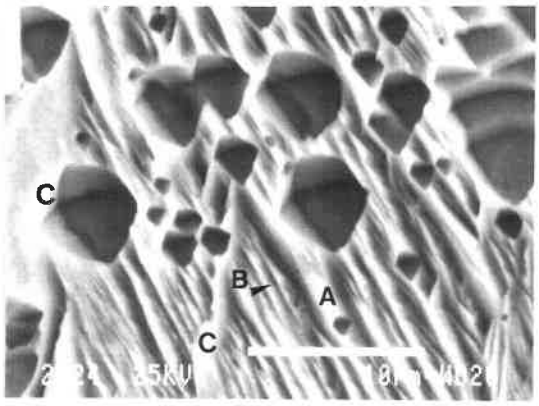
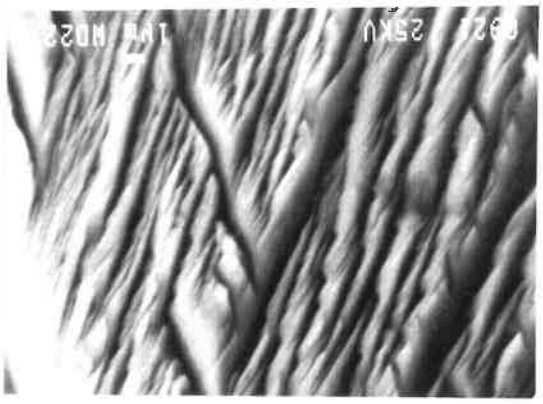


Fig. 3.11:
Large {100} facets produced in near-threshold fatigue test in air on 316 s.s.



(a)





(b)

Fig. 3.12: Complex near-threshold facets for 316 s.s. tested in air. (a) stereographs pair (b) the matching aspect on the opposite fracture surface of the same region of (a).

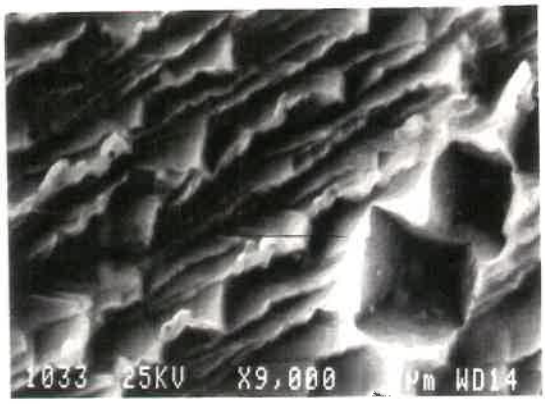


Fig. 3.13

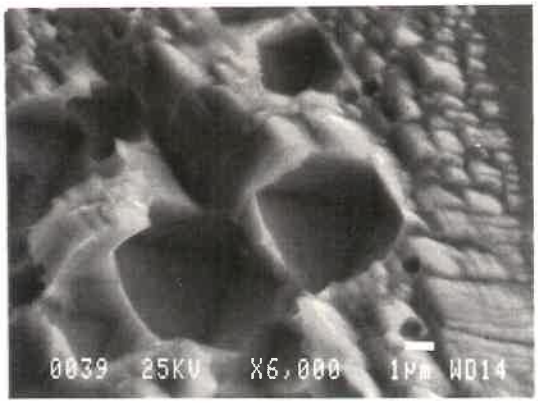


Fig. 3.14

Fig. 3.13: Serrated river lines, 316 s.s. tested in dry argon, da/dN ≈ 10^{-7} mm/cycle.

Fig. 3.14: Small tetrahedra-like facets occurred near grain boundaries for 316 s.s. tested in air.

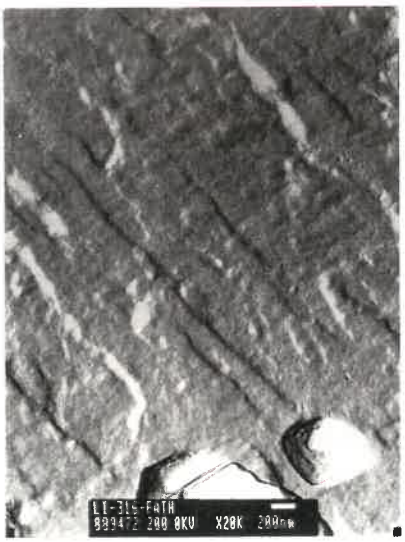


Fig. 3.15: Fractographic details on the near-threshold {100} average facets observed on TEM replicas.

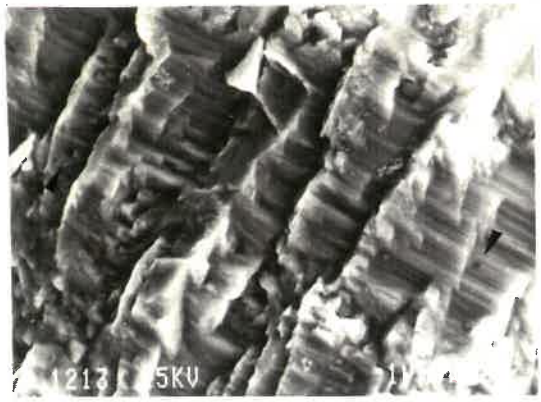


Fig. 3.16

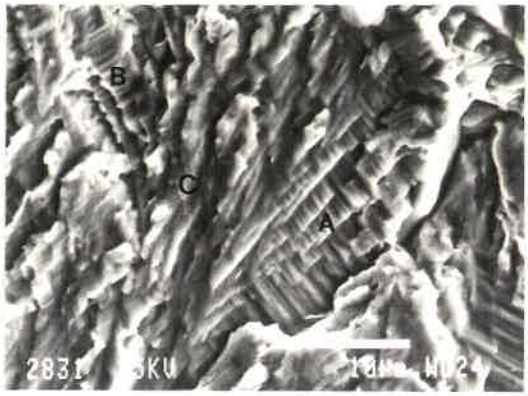


Fig. 3.17

Fig. 3.16: Striated near-threshold facet. 70-30 α-brass tested in air. Arrows indicate small etch pits.

Fig. 3.17: Near-threshold facet for 70-30 α-brass tested in air, with two regions (A and B) of striations separated by a more complex region.

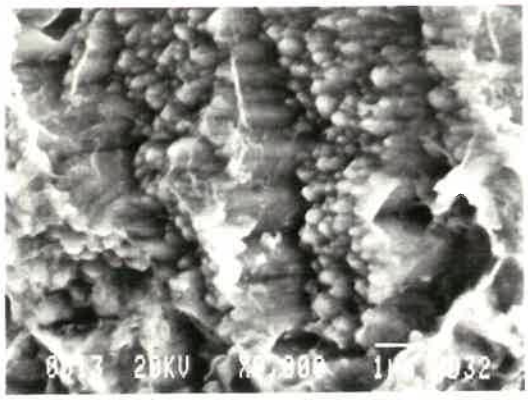


Fig. 3.18

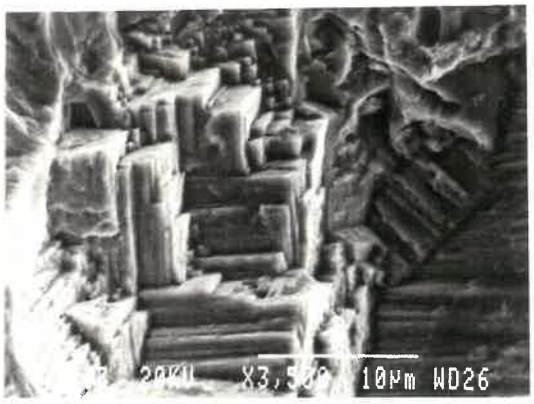


Fig. 3.19

Fig. 3.18: Striated facets of {110} average orientation are made up of two sets of alternating {111} microfacets for α-brass near-threshold fatigue cracking in air.

Fig. 3.19: Large {100} and {111} facets, 70 Cu-30 Zn α-brass, tested in air, da/dN ≈ 10^{-7} mm/cycle.



Fig. 3.20

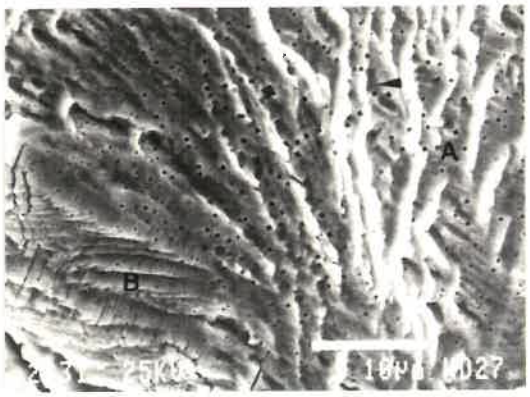
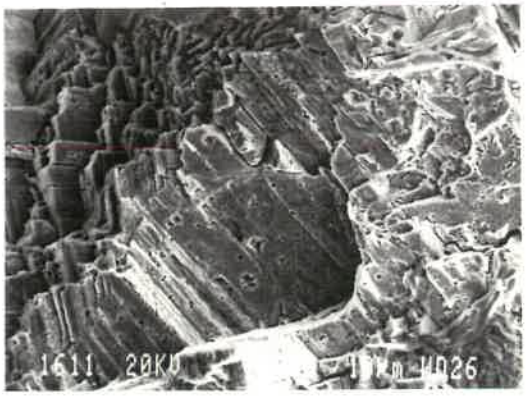


Fig. 3.21

Fig. 3.20: {100} <110> cracking crystallography observed for da/dN ≈ 10^{-6} mm/cycle in 8% Mn-8% Al-2% Ni (AC condition) bronze tested in air.

Fig. 3.21: Herringbone pattern of river lines observed at ~ 10^{-6} mm/cycle in 8% Mn-8% Al-2% Ni (AC condition) bronze tested in air.



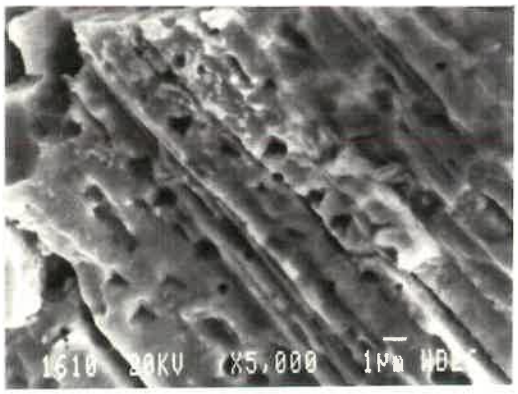


Fig. 3.22: Stair-like facets observed for ultra-low crack growth rates (da/dN ≈ 10^{-8} mm/cycle) in 8% Mn-8% Al-2% Ni bronze tested in air (HT_1 condition).

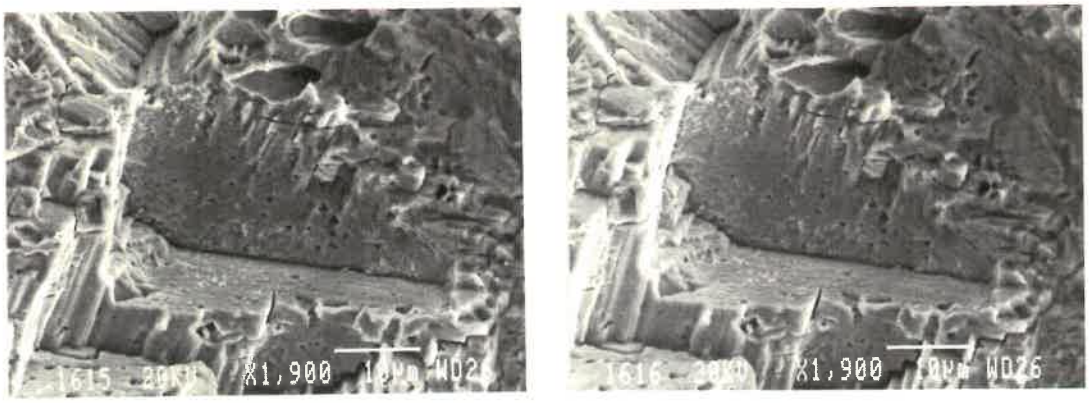


Fig 3.23: Two relatively large {111} facets observed for ultra-low crack growth rates (da/dN ≈ 10^{-8} mm/cycle) in 8% Mn-8% Al-2% Ni bronze (HT_1 condition tested in air).

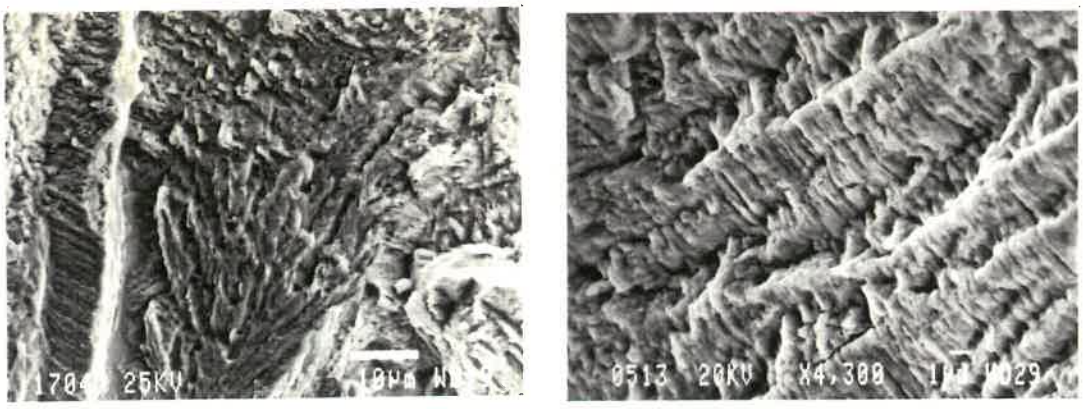


Fig. 3.24 **Fig. 3.25**

Fig. 3.24: Complex pattern of very fine facets present near the threshold for copper tested in air. (~10^{-7} mm/cycle).

Fig. 3.25: Sheet-like facets observed for copper at da/dN values of ~ 10^{-7} mm/cycle.

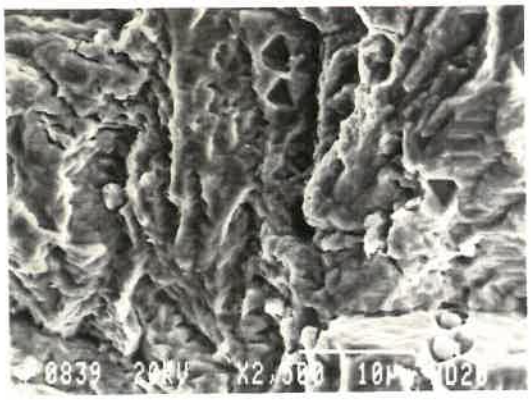


Fig. 3.26

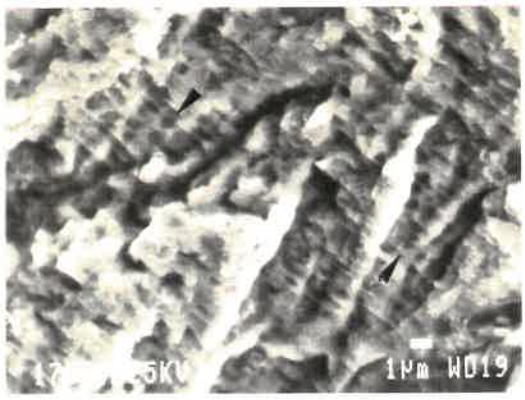


Fig. 3.27

Fig. 3.26: Sheet-like {111} facets observed for copper at da/dN values of ~ 10^{-7} mm/cycle.

Fig. 3.27: Striated near-threshold facets observed for copper tested in air. The arrows indicate etchpits produced on the small microfacets.

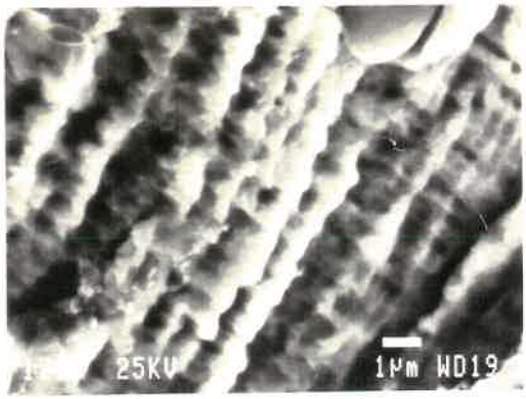


Fig. 3.28



Fig. 3.29

Fig. 3.28: Wavy primary facets made up of two sets of microfacets observed for copper tested near the threshold in air.

Fig. 3.29: Pyramid-shape facets observed near a grain boundary in copper tested near the fatigue threshold in air.

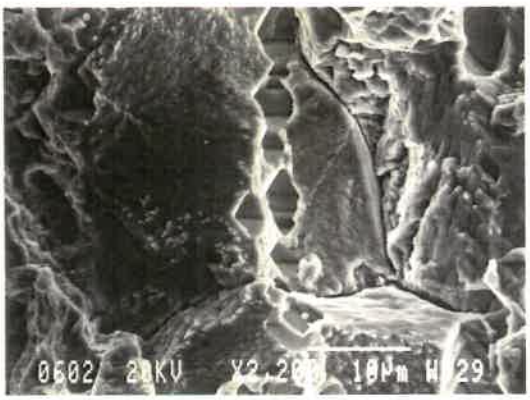


Fig. 3.30

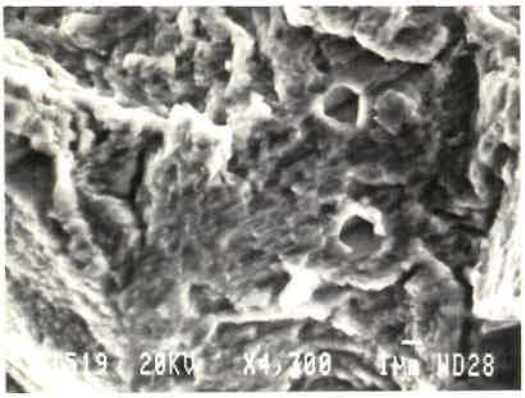
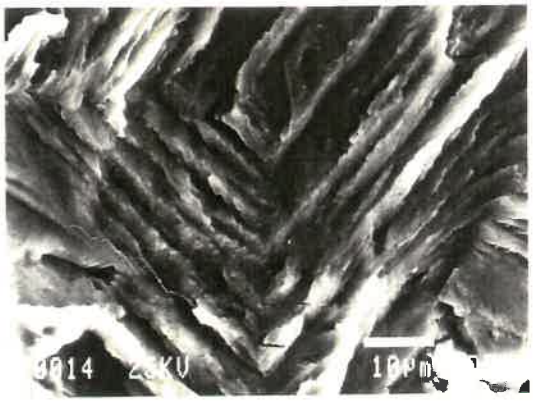


Fig. 3.31

Fig. 3.30: Well-defined etchpits indicative of a {110} orientation observed on large and relatively flat intergranular-like facets for copper tested in air (~ 10^{-6} mm/cycle).

Fig. 3.31: Striated transgranular facets of average {110} orientation observed near the threshold for copper tested in air.



(a)



(b)

Fig. 3.32: Typical aspects of {100} sheet facets presented near-threshold for 2024-T351 Al alloy tested in air observed a) before and b) after etching.

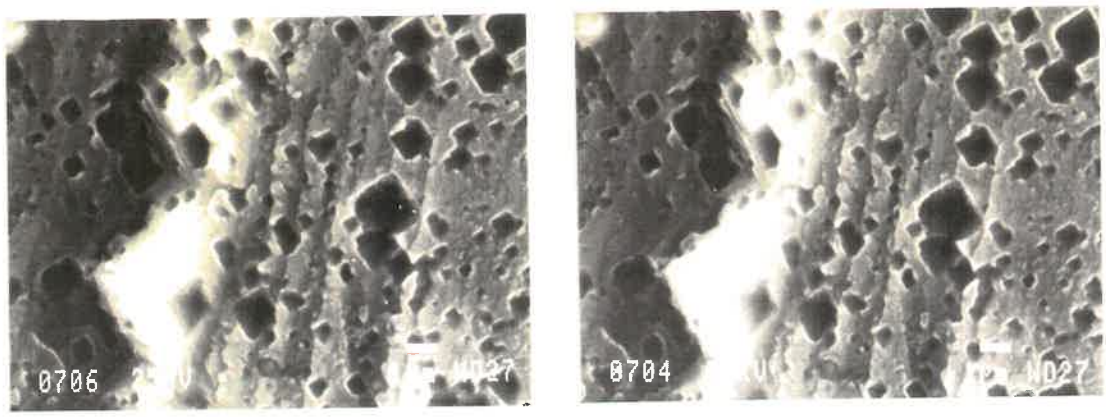


Fig. 3.33: Primary {100} near-threshold facets, with secondary {111} facets corresponding to serrated river lines in 2024-T351 Al alloy tested in air.

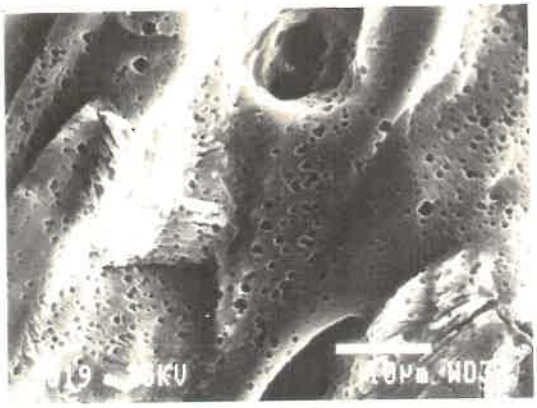
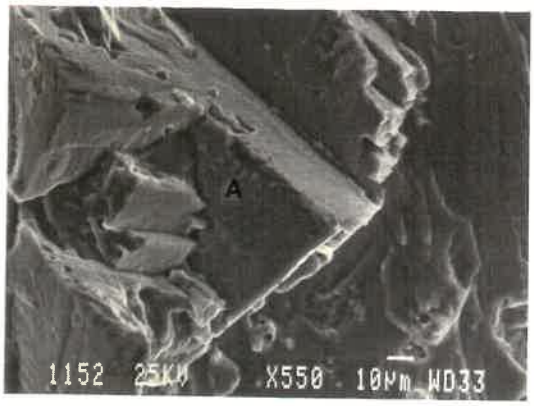
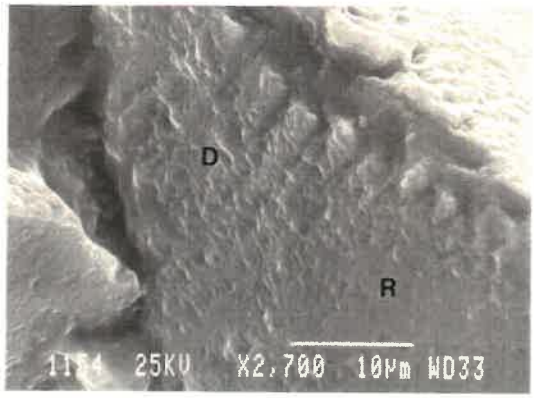


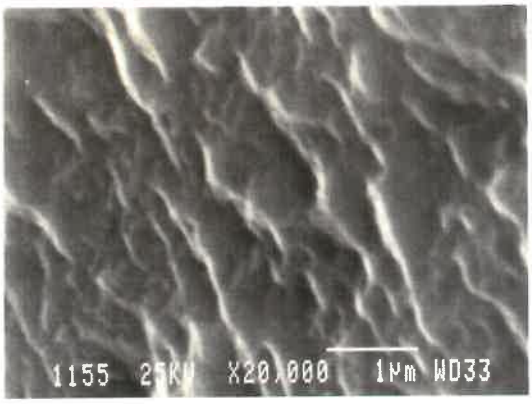
Fig. 3.34: {111} facets seen in region A of this micrograph of a near-threshold fracture surface of 2024-T351 Al alloy tested in air.



(a)



(b)



(c)

Fig. 3.35: Pyramid-like large {111} facets presented on an unetched fracture surface at ultra-low crack rates in the test in vacuum (a) aspects at low magnification; (b) details of facets A, showing rubbing appearance at region R; (c) details at region D of facet A.

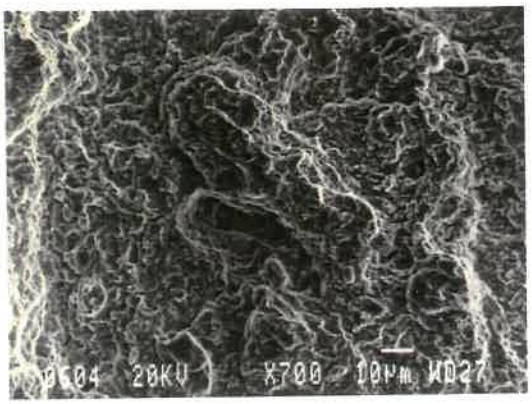


Fig. 3.36

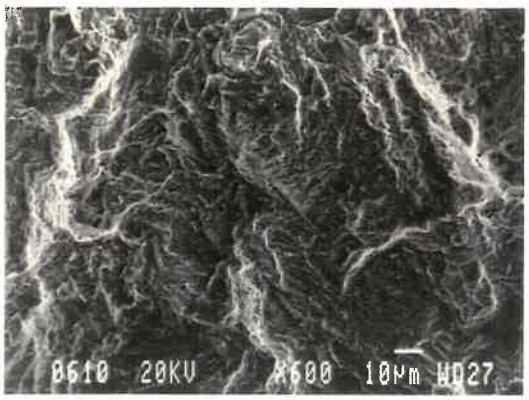


Fig. 3.37

Fig. 3.36: General fractographic aspects for copper tested in vacuum (da/dN ≈ 10^{-8} mm/cycle).

Fig. 3.37: General fractographic aspects for α-brass tested in vacuum (da/dN ≈ 10^{-8} mm/cycle).

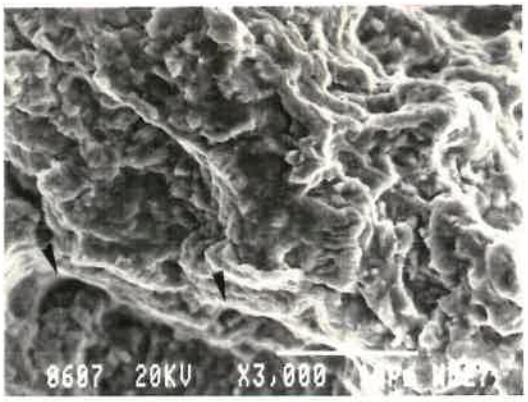


Fig. 3.38

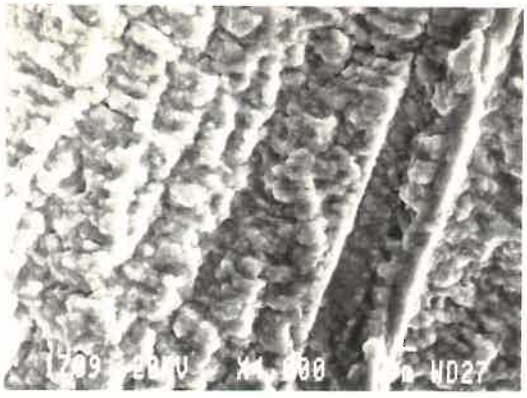


Fig. 3.39

Fig. 3.38: Dimpled aspect of the fracture surface of copper tested in vacuum at the threshold.

Fig. 3.39: Striation-like aspects observed for ~-brass tested in vacuum (da/dN ≈ 10^{-8} mm/cycle).

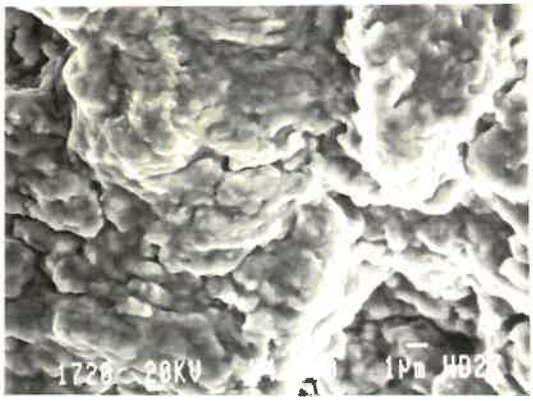




Fig. 3.40 **Fig. 3.41**

Fig. 3.40: Microfractographic aspects of copper tested in vacuum ($da/dN \approx 10^{-8}$ mm/cycle).

Fig. 3.41: Crystallographic facets observed for α-brass tested in vacuum ($da/dN \leq 10^{-8}$ mm/cycle).

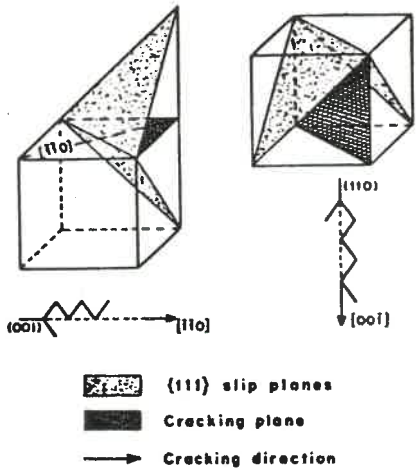


Fig. 3.42: Model for cracking along {100} or {110} by decohesion along two alternating {111} slip planes.

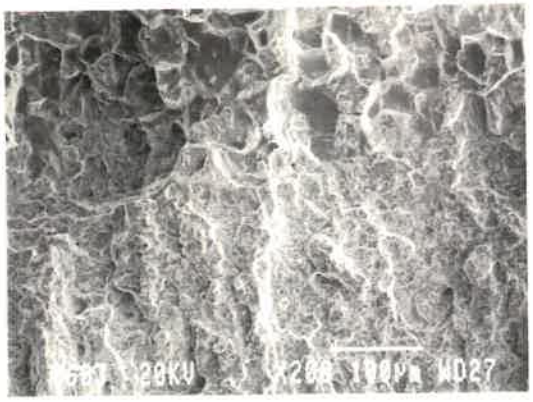


Fig. 3.43

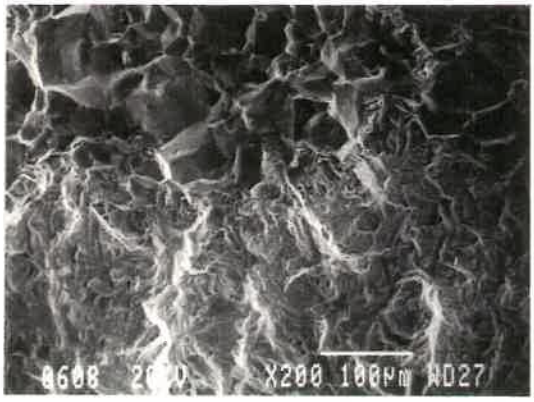


Fig. 3.44

Fig. 3.43: Transition in fracture surface morphology in copper, associated with change in atmosphere from vacuum to lab. air.

Fig. 3.44: Transition in fracture surface morphology in α-brass, associated with change in atmosphere from vacuum to lab air.

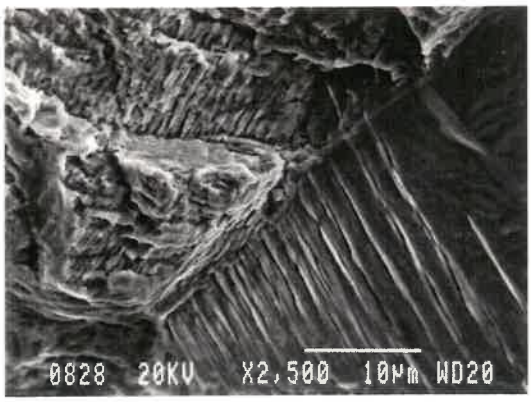


Fig. 3.45: Features resembling intrusions and extrusions observed on the intergranular facets for copper tested in air (da/dN ≈ 10^{-6} mm/cycle).

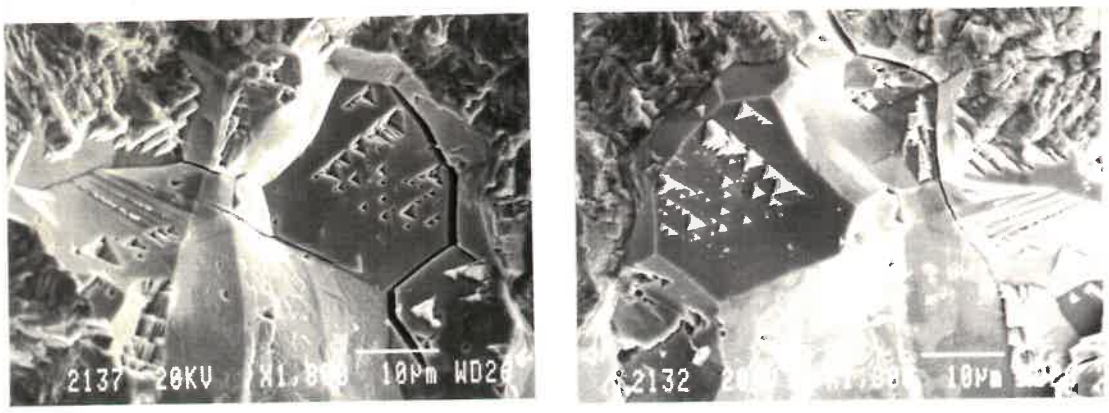


Fig. 3.46: Matching triangular pits and protrusions on opposite fracture surfaces of unetched intergranular facets for α-brass tested in air (da/dN $\approx$ 10^{-6} mm/cycle).

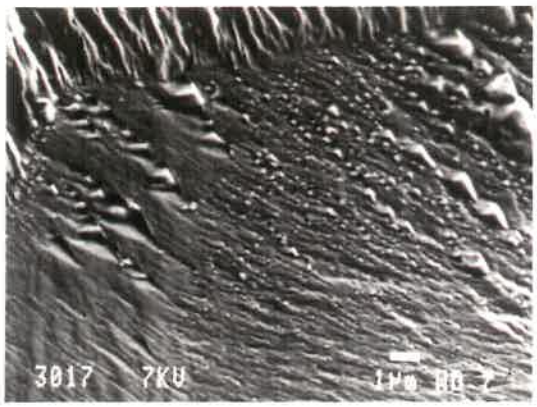
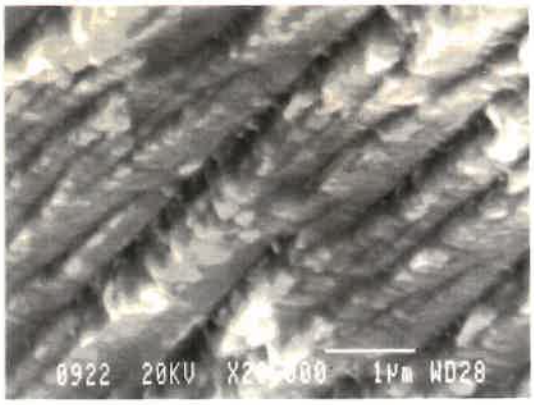


Fig. 3.47: Tetrahedra-like small facets present on the intergranular facets for 316 stainless steel tested in air at low da/dN values (~ 10^{-6} mm/cycle). Very fine river lines can also be clearly seen on the intergranular facets.



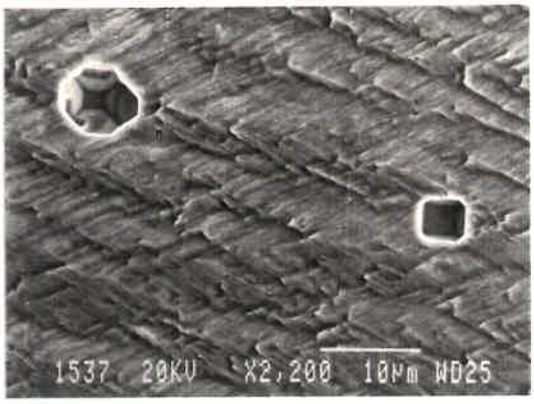


Fig. 3.48 **Fig. 3.49**

Fig. 3.48: Striation-like markings, on an unetched fracture surface of Fe-3% Si, da/dN $\approx 10^{-7}$ mm/cycle.

Fig. 3.49: Primary {100} facet with fine striation observed in Fe-3% Si for da/dN $\approx 10^{-7}$ mm/cycle.

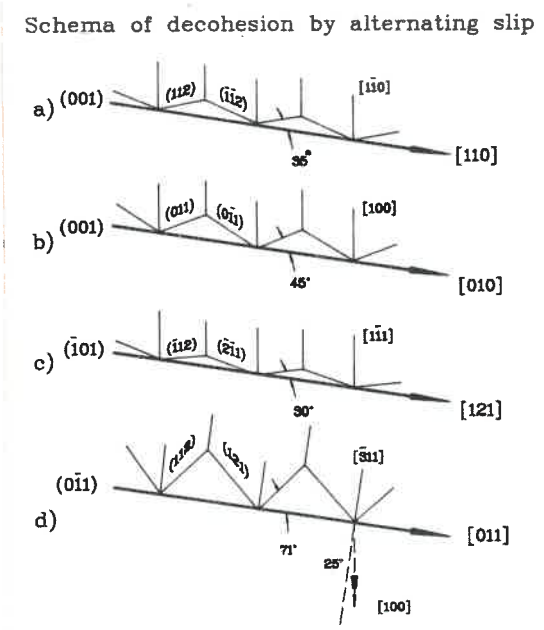


Fig. 3.50: Different alternate slip cracking combinations which are consistent with the experimental observations obtained on the b.c.c. metals studied.

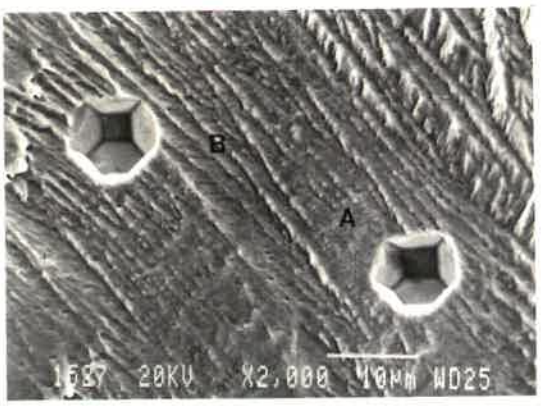


Fig. 3.51



Fig. 3.52

Fig. 3.51: Striated {100} facet on Fe-3% Si for da/dN $\approx 10^{-7}$ mm/cycle. The cracking in regions A and B is consistent with models a and b schematized in Fig. 3.50, respectively.

Fig. 3.52: {110} striated primary facets with <111> striations and near-<112> river lines observed in Fe-3%Si for da/dN $\approx 10^{-7}$ mm/cycle.

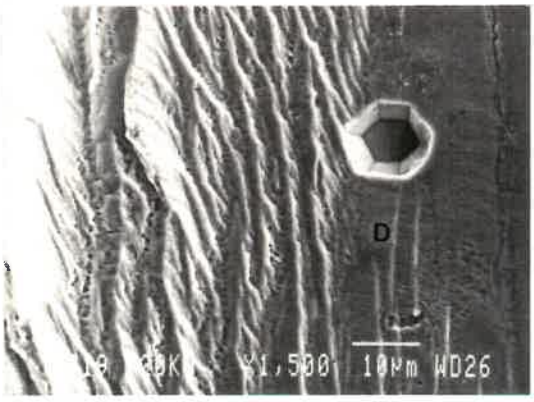


Fig. 3.53: Two different sets of {110} primary facets with <111> or <113> striations observed in Fe-3%Si for da/dN $\approx 10^{-7}$ mm/cycle.

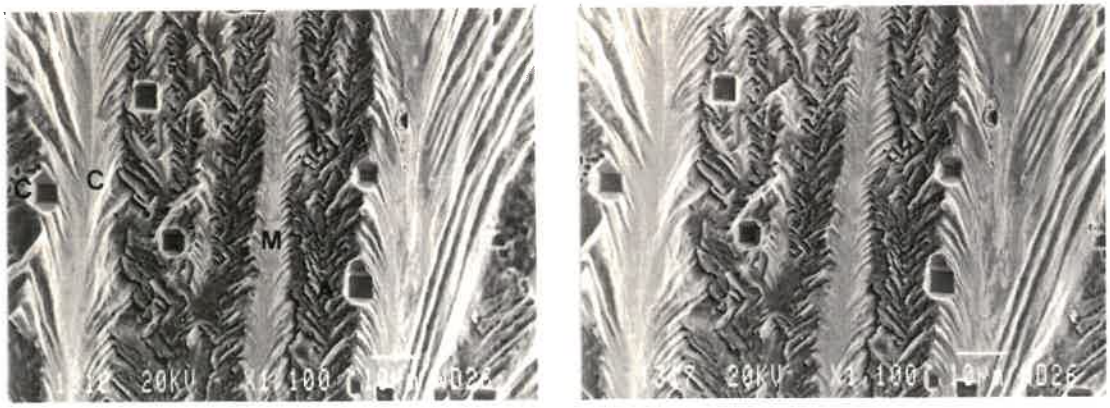


Fig. 3.54: Herringbone river lines patterns, Fe-3%Si, da/dN $\approx 10^{-7}$ mm/cycle.

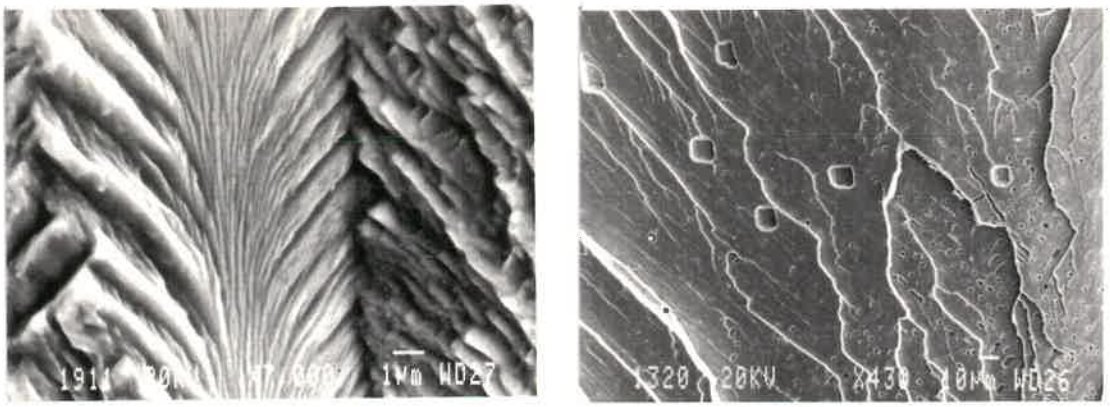
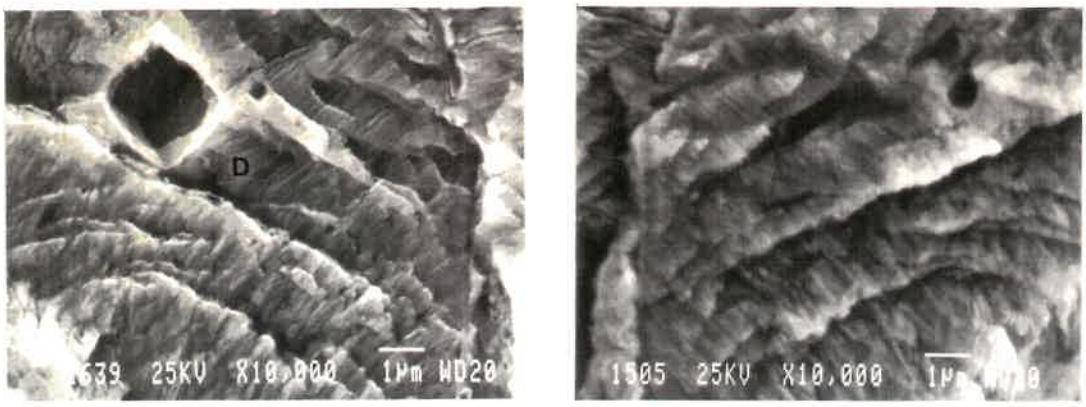


Fig. 3.55 **Fig. 3.56**

Fig. 3.55: Unetched matching surface of region "M" in figure 3.54.
Fig. 3.56: Typical {100} cleavage facets in Fe-3%Si with <110> and <100> river lines determined by comparison with the etch pits.



(a) (b)

Fig. 3.57: Near-{110} facet observed on mild steel tested in air for da/dN ≈ 10^{-7} mm/cycle. (a) etched fracture surface,
(b) matching region on the unetched fracture surface.

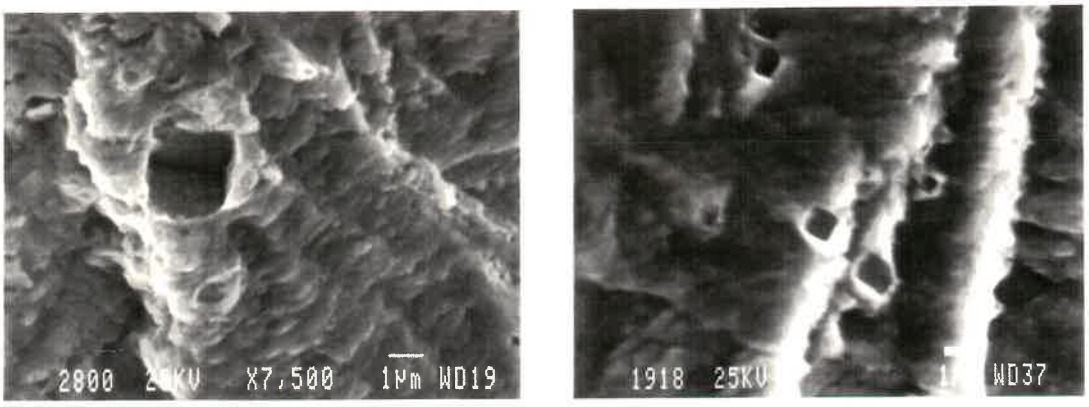
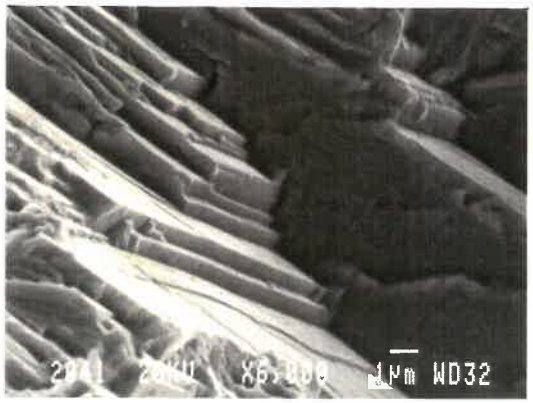


Fig. 3.58 **Fig. 3.59**

Fig. 3.58: Sheet-like fine facets observed on the mild steel at R = 0.5 for da/dN ≈ 10^{-6} mm/cycle.

Fig. 3.59: Primary wavy facets with {100} average orientation consistent with model a of Fig. 3.50, (mild steel, R = 0.5, da/dN ≈ 10^{-6} mm/cycle).



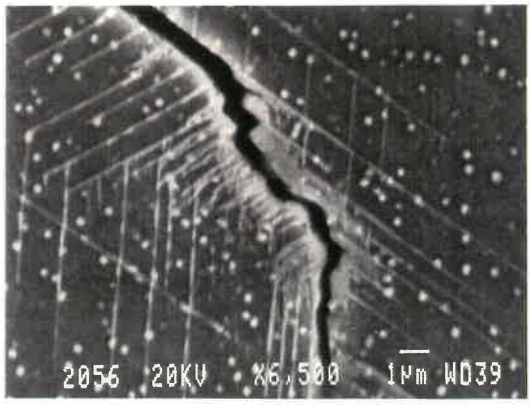
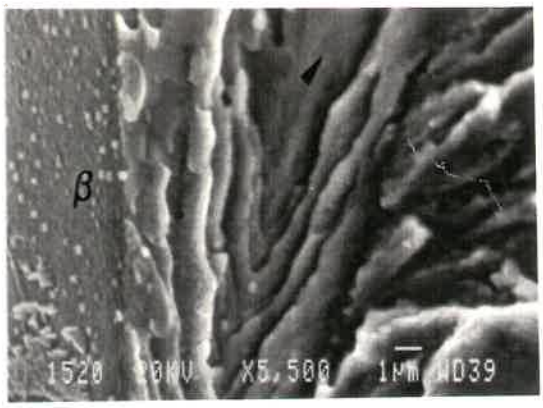


Fig. 3.60 **Fig. 3.61**

Fig. 3.60: Large flat facets in the β-phase of 13.5% Mn-Al-Ni bronze, da/dN $\approx$ 10^{-5} mm/cycle, in air.

Fig. 3.61: Path of secondary crack along slip traces in the β-phase of 13.5% Mn-Al-Ni bronze, in 3.5% NaClk solution da/dN $\approx 10^{-5}$ mm/cycle.



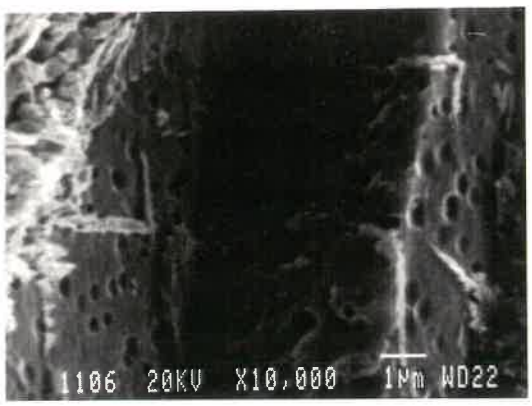


Fig. 3.62 **Fig. 3.63**

Fig. 3.62: Relationship between microfractography and microstructure of the β-phase on 13.5% Mn-Al-Ni bronze tested in air, da/dN $\approx$ 10^{-6} mm/cycle.

Fig. 3.63: {110} facets present in the β-phase of 13.5% Mn-Al-Ni bronze (HT_2), in air, R = 0.1, da/dN $\approx 10^{-5}$ mm/cycle.

CHAPTER 4

FRACTOGRAPHY OF STRESS CORROSION CRACKING OF ANNEALED 316 STAINLESS STEEL

4.1 INTRODUCTION

The fractography and crystallography of transgranular stress corrosion cracking (TSCC) in austenitic stainless steel has been the subject of considerable interest. A number of previous studies have focused on the crystallographic orientation of the microfractographic features produced by TSCC. Particular attention to this aspect has been paid by Meletis and Hochman (162, 163) and Dickson et al. (112) who have reviewed much of the previous work.

For austenitic stainless steels (s.s.), most of the detailed fractographic and crystallographic studies have been performed on AISI 304 (340, 185, 187, 188, 191) and 310 (112, 185, 186, 191) type steels. AISI 316 s.s., for which the fractography of TSCC tends to be relatively complex, has less often been the object of detailed fractographic study. Marek and Hochman (190) reported {210} as the orientation of macroscopic TSCC facets in 316 s.s. single crystals tested in boiling aqueous $MgCl_2$ solution, Silcock (186) found a strong tendency for {100} facets in 310 s.s. and a lesser tendency in 316 s.s. Neilsen (369), by examining oxide replicas of

fracture surfaces in transmission electron microscopy, found that TSCC fracture occurred preferentially on the {111} planes in 316 s.s. tested in boiling 42% aqueous solution. Other studies (112, 163, 188, 194) indicate that cracking in austenitic s.s. occurred on {100}, {110} and possibly on {111} planes. Different possible explanations of the cracking crystallography have been discussed (112, 162).

A few previous studies have also investigated the influence of the stress intensity factor K on the fractography and crystallography of TSCC. For 310 s.s., Mukai et al. (187) found a very variable interstriation spacing which appeared to be independent of K. In cold-rolled 316 s.s. tested in boiling $MgCl_2$ solution, an increasing amount of intergranular cracking with increasing K has been observed (370, 371). In the case of 70 Cu - 30 Zn, Kermani and Scully (180) found that as K increased, the presence of slip lines on the TSCC facets became more visible. On 310 s.s., Dickson et al. (112) found that, for all K values, cracking was predominantly on {100} planes with preferential crack propagation in a <110> direction, however, the striation-like markings were much more pronounced on some primary {100} facets at higher K than those observed at low K values. Recently, Magnin et al. (194) proposed that for 316 s.s. tested in boiling $MgCl_2$ aqueous solution, transgranular cracking was related to both a discontinuous microcleavage on {100} (sometimes on {110}) planes and a microshearing on {111} planes for $K_I < 20$ MPa$\sqrt{m}$, however, both transgranular and intergranular cracking

occurred as K_I was about 22 MPa√m, and mainly intergranular cracking for higher values of K_I.

Even so, many of the finer and more important fractographic features have not been adequately identified and explained. Since the fundamental cracking mechanisms must be consistent with the detailed fractographic features, the main aim in carrying out the fractographic work was to clearly identify the detailed fractographic and crystallographic features of TSCC for annealed austenitic 316 stainless steel exposed to boiling (154°C) $MgCl_2$ solution in order to better understand the possible mechanisms of TSCC.

4.2 EXPERIMENTAL PROCEDURE

The fractographic study was performed on an annealed 3.2 mm thick sample of 316 s.s. The stress corrosion cracking testing of 316 s.s. in boiling $MgCl_2$ solution was performed by Professor J.I. Dickson. The alloy composition and sample geometry as well as the testing procedures were reported earlier (371). Some of the experimental conditions, knowledge of which is useful in discussing the results of the fractographic study.

4.2.1 Material

The studies were conducted on the commercial austenitic stainless steel of AISI designation 316. The analyses, in terms of weight percentages, are shown in Table 4.1, in which the composition of AISI 310 s.s. is included in order to compare and discuss the results of the fractography observed in these two materials.

Table 4.1: The composition of 316 s.s. and 310 s.s. (wt.%) (371)

Element	316	310
Cr	16.85	24.2
Ni	12.08	21.2
C	0.07	0.05
Mo	2.13	---
Mn	1.58	1.55
Si	0.89	1.02
P	0.036	0.016
S	0.011	0.018

The steels were received as 6.4 mm thick, hot-rolled, annealed and pickled plate stock. They were rolled at 22°C, with intermediate anneals, to produce a final thickness, B, of 3.2 mm with a pre-determined amount of cold work (CW). The alloys were subsequently tested in both the annealed and CW conditions (371). All annealing was conducted in sealed Sen-pak stainless steel containers at 1050°C for 1 hr, followed by quenching in water. The 0.2% offset yield stress (σ_y) normal to the rolling direction, measured at 150°C in the case of CW material and at 22°C for annealed material, are shown in Table 4.2 for the alloy conditions studied. The

grain size for both annealed steels was approximately 35 ~ 40 μm.

Table 4.2: The yield stress of 316 s.s. and 310 s.s. (371)

Alloy	% CW	σ_y (MPa)
316	0	243
316	25	534
316	50	903
310	0	290
310	50	696

The environment was prepared from reagent grade $MgCl_2.6H_2O$ and distilled water. The composition was adjusted until a boiling point of 154 °C was achieved, corresponding to 44.7 wt% $MgCl_2$ (372). The tests were conducted under freely corroding conditions at 154 °C. The specimens were oriented so that cracking occurred parallel to the rolling direction. An incrementally increasing or decreasing value of stress intensity factor K was employed. Laboratory environments of this type generally compare favourably with industrial experience (373).

4.2.2 Specimen Geometry and Stress Corrosion Testing

The specimen geometry and dimensions were identical to those described in detail by Russell and Tromans (370). Basically, the specimen was a pin-loaded, T

notch double cantilever beam (TN-DCB), as shown schematically in Fig. 4.1. The specimen was prepared with crack starter notches of ~ 3 mm. Fig. 4.2 presents the typical three-stage log V vs. log K curves obtained for both annealed 316 s.s. and 310 s.s. of stress corrosion crack propagation.

4.2.3 SEM Fractographic Study

After testing, the samples were ultrasonically cleaned briefly in hot water to remove salt adhering to the fracture surfaces, the cleaned ultrasonically in a 5% HCl solution inhibited with 2g/l of hexamethylenetetramine. Most of the SEM micrographs were taken with a JEOL T840 scanning electron microscope. Secondary electron images and 20 KV excitation were employed. Stereo observations were routinely carried out on pairs of scanning electron micrographs photographed with a 6° difference in tilt. Observations on matching fracture surfaces were also performed. After initial SEM observations, etch pits were produced on selected regions, as described in section 3.2.3.1.

4.3 ASPECTS OF FRACTOGRAPHY AND CRYSTALLOGRAPHY

4.3.1 Terminology

The terms which will be employed to describe the fractographic and crystallographic features of TSCC are identified schematically in Fig. 4.3. According

to this terminology, the fracture facets between river lines are designated as "primary facets", some of which can be seen to be made up of two sets of alternating microfacets. The orientation of the primary facets then corresponds to an average orientation. The river lines or steps separating the primary facet can at times be seen to be serrated and to be made up of two sets of finer secondary microfacets with orientations which differ from the average orientation of the primary facets. Such river lines are designated as serrated river lines (SRL). Striations on the primary facets can often be seen to correspond to the intersection sites of microfacets. Numerous sheet-like microfacets (SMF) can at times also be observed.

4.3.2 The Influence of the Stress Intensity Factor on the Fractography

The annealed 316 s.s. showed completely transgranular cracking for the K values employed in the SCC test. Because of the occurrence of macroscopic crack branching for K > 25 MPa.$m^{1/2}$, the test was terminated prior to reaching the K values required either possibly to cause some intergranular stress corrosion cracking as observed by Magnin (194) and/or to cause ductile microvoids cracking as generally obtained in a tensile overload fracture.

4.3.2.1 Microfractography at Low K Region

At low stress intensity factors (K < 15 MPa $m^{1/2}$), the large majority of primary fracture facets produced were relatively flat and resembled reasonably well those observed on annealed 310 s.s. (112). These facets, identified by etch pits, corresponded to a plane close to {100}, as shown in Fig. 4.4. The crack propagation direction, as indicated by the direction of river lines on the {100} fracture facets, was most often near a <110> direction parallel or almost parallel to one edge of the etch pits, and at times near a <100> direction parallel or almost parallel to one of their diagonals. Fine striation-like markings generally parallel to a <110> direction were clearly present on some {100} facets (Fig. 4.4). The typical interstriation spacing at low K was of the order of 0.3-0.4 μm. At times, the {100} facets observed at low K had a microscopically wavy aspect, with the crests and the valleys of the waves parallel to the striations. Examination of regions having this aspect by stereofractography indicated that the primary facets of {100} average orientation consisted of two alternating sets of {111} microfacet which met along the <110> direction parallel to the striations. An example is shown in region "A" of Fig. 4.5 where the striation-like markings can be seen to result from microfacets parallel to sides 1 and 2 of the etchpit. Fig. 4.6 presents a further example at low K in which the waviness of the fracture surface is also seen to result from the presence of two alternating sets of {111} microfacets.

Other common features of TSCC fracture surfaces of the 316 s.s. tested were the presence of crystallographic serrations or steps on river lines and the occurrence of undercutting by some primary facets. In Fig. 4.7, facets A and B, which correspond to serration on river lines, are parallel to the {111} planes corresponding to inclined faces 1 and 2 respectively of the etch pits. Some of the serration facets on the river lines, such as those indicated by C in Fig. 4.7 have a sheet-like aspect. In this figure, these sheet-like facets can be seen to be parallel or nearly parallel to face 2 of the etch pits. Therefore, these have a {111} or near {111} orientation.

4.3.2.2 Microfractography Associated with Intermediate K

4.3.2.2.1 Occurrence of Sheet-Like Microfacets

As K increased to intermediate values (15-20 MPa $m^{1/2}$), the fracture facets generally became rougher. Etch-pitting indicated that cracking still produced primary facets of approximately {100} average orientation. The rougher fracture facets indicated larger-scale and more apparent deviation of the microscopic crack path from the average orientation of the primary facets observed at low K. The average crack plane in the portion of Fig. 4.8 below the annealing twin (i.e. lower left) is seen to consist of two sets of facets quite steeply inclined with respect to each other. Each of these sets can be seen to consist of much finer sheet-like microfacets. Stereofractographs (Fig. 4.9) taken in the portion R of Fig. 4.8

indicated that these microfacets corresponded to {111} planes. In region A of Fig. 4.9, two sets of {111} microfacets, parallel to faces 1 and 2 of the etchpit, can be seen to meet along <110> striations. A number of sheet-like microfacets in region B of Fig. 4.9 are also to be parallel either to face 1 or to face 2 of the etch pits, and therefore to have {111} orientations. A few etch pits centered on the twin interface in the upper portion of Fig. 4.8 have sides bounded by {111} planes in the matrix and {111} planes in the twin. From stereomicrographs, the change in average fracture plane in crossing the twin interface was seen to be approximately that expected (70.5° rotation about the trace of the twin interface) for a {100} plane crossing a {111} twin boundary (112).

4.3.2.2.2 Fan-Shaped Facets

As for the previous observations on 310 s.s. (112), the occurrence of fan-shaped facets was most frequently observed at intermediate K values (i.e. high K portion of stage I and low K portion of stage II of the log da/dN - log K curve in Fig. 4.2). The fan-shaped facets is defined here, as in the previous study on 310 s.s., as requiring the crack to cross a grain boundary along a narrow segment and then to fan out into the grain. Such patterns, however, were noticeably absent for $K \leq 15$ MPa $m^{1/2}$ values region, in which crack initiation in new grains tended to occur along a wide segment of grain boundary and the river lines subsequently tended to remain straight. The fan-shaped facet of Fig. 4.10 has a {100} average

orientation and includes two regions, indicated by A and B, each of which presents a different set of <110> striations parallel to etchpit edges. These two regions are separated by a region C which presents a more complex aspect. The <110> striations of region A can be seen to correspond to intersection sites of two sets of {111} microfacets. The perpendicular set of <110> striations of region B correspond to the intersection sites of two different sets of {111} microfacets. The more complex aspect in intermediate region C presents one or the other set of striations or in some areas both sets of striations. The indication is that, in region C, decohesion occurs on all four {111} planes, which gives rise to the more complex fractographic aspect and to the <100> river lines present in this region parallel to an etchpit diagonal. This identical {100} <110> and {100} <100> cracking crystallography has previously been observed for fan-shaped facets in 70 Cu - 30 Zn α-brass fatigue tested in the threshold region in air (see Fig. 3.17).

For $K \geq 20$ MPa $m^{1/2}$, the fan-shaped patterns also became less frequent, crack initiation in new grains tended to occur along wider segments of the grain boundary then at intermediate K values.

The influence of K on the occurrence of fan-shaped patterns has been explained previously (112) by considering the relative ease of crack initiation and crack propagation in a grain. When crack propagation occurs much more easily

than does the initiation of cracking in a new grain, propagation can rapidly radiate away from the crack initiation site in the grain, giving rise to fan-shaped patterns. The observations indicate that his is the situation in and near stage II of the log da/dt vs. K curve. When crack initiation and propagation occur with comparable ease (high K values) or with comparable difficulty (near the threshold value of K), fan-shaped patterns will be rare.

4.3.2.3 Microfractography at High K Region

4.3.2.3.1 Feather-Like and Sheet-Like Microfractographic Features

As K increased to high values (K > 20 MPa $m^{1/2}$), the fracture surfaces continued to become microscopically rougher and to appear more complex (Fig. 4.11). As seen in this figure, the fracture surfaces within each grain are made up of sets of fine parallel facets which give rise to feather-like and sheet-like microfractographic features. In spite of considerable effort, very few well-defined etch pits were produced on these complex fracture surface regions, complicating the identification of the cracking crystallography. In the pair of stereofractographs of Fig. 4.12, a reasonably well-defined etchpit is present. Many of the sheet-like microfacets, indicated by "A", can be seen to be parallel to face 1 of this etchpit; others such as facet "B" can be seen to be parallel to face 2. A few very fine microfacets indicated by "C" appear parallel to face 3 of this etchpit. The river lines can be seen generally to be parallel to one of the edges of the etchpit and

therefore to correspond to <110> directions. Striation-like markings which are also along <110> directions can be clearly observed on some {111} sheet-like microfacets. Fig. 4.13 presents another region of fracture surface produced at high K. The {111} orientation of the fine facets can be identified by comparison with the sides of the etch pits present. These different observations therefore suggest that all sheet-like facets have {111} orientations.

The crystallography of TSCC at high K in the unetched region presented in Fig. 4.14 can be identified by comparison with the previously identified crystallography for the very similar fractographic aspect observed for near-threshold fatigue cracking in air also on 316 s.s. as shown in Fig. 3.12(a) (see section 3.3.1). The main difference between the fractographic features observed for near-threshold fatigue in Fig. 3.12(a) and for TSCC in Fig. 4.14 is that in the latter the larger facets are made up of a large number of fine sheet-like facets, which in regions presenting etch pits on the same specimen have been found to have {111} orientations, such as in Fig. 4.13. The large facets C′ in Fig. 4.14 can be seen to be almost parallel to the finer set of sheet-like facets which it contains. The near-{111} facet C′ in Fig. 4.14 then would correspond to {111} facet C in Fig. 3.12(a). The identification of this facet orientation and the similarity between Figs. 4.14 and 3.12(a) then indicate that sides B′ and A′ of the wedge-shaped facets in Fig. 4.14 would correspond to near-{110} and near-{100} facets respectively, both of which

(but in particular A′) consist clearly of finer sheet-like facets.

4.3.2.3.2 Herring-Bone Patterns of River Lines

While the fan-shaped facets with the crack front crossing grain boundaries along narrow segments were essentially only observed for intermediate values of K, herring-bone patterns of river lines occurred for all values of K, but very few occurred near the threshold value K_{ISCC}. At quite low values of K, herring-bone patterns of river lines were present on {100} facets, with the central spine corresponding to a <110> direction and the average direction of river lines to each side corresponding to a different <100> direction as shown in Fig. 4.15. In the region of the central spine, fine <110> striations were present perpendicular to the <110> direction of the spine. In the region of the <100> river lines, this same set of striations was present; however, in some regions a perpendicular set of <110> striations could also be observed at high magnification.

At high K values (stage III and high stage II portion of the log da/dN-log K curve) the crack front typically crossed grain boundaries across wide segments, although most facets showed some tendency to fan out to the sides. Fig. 4.16 presents a typical region observed in stage II of the log da/dN-log K curve. Typical of this region, secondary microcracks are present, many of which appear to indicate previous positions of the crack front within individual grains. The curvature of

some of these secondary cracks suggests that the crack front tends to lead near the centre of the grain and at times to be held back significantly near the lateral grain boundaries, where the crack front in the adjacent grains must join up in order to be reasonably continuous. It can further be seen that the local crack front tends to be held back especially in grain boundary regions where the average orientation of the crack plane changes significantly in order to permit it to join up with the average crack plane on the other side of the grain boundary.

In the central portion of Fig. 4.16, a grain present sheet-like facets arranged in a herring-bone pattern, typically of those observed at high K values. Fig. 4.17 presents a second example of a herring-bone pattern observed at high K. In this second example, the two sets of river lines are essentially perpendicular to each other. Two twin interfaces are also present in this region and make an angle of approximately 80° with the central spine. The herring-bone patterns observed in both Figs. 4.16 and 4.17 appear reasonably consistent with a central spine corresponding approximately to a <110> direction and with two sets of river lines corresponding to near-<100> directions.

The relatively frequent occurrence of herring-bone patterns at high K values for the TSCC of annealed 316 s.s. may indicate that easier crack initiation in new grains and the large number of pronounced river lines produced are associated with

larger crack tip plastic strains. A tendency to obtain near-<100> orientations for the type of river lines which are produced at high K would also strongly favour herring-bone patterns being produced in favourably oriented grains.

4.3.2.4 Observations Near the Lateral Edges of the Specimen

For both low and intermediate values of K, a narrow (less than 150 μm wide) zone was present near the lateral edges of the specimen (Fig. 4.18). This zone presented rougher, more complex microfractographic features resembling those produced at higher K values in the mid-thickness portion of the specimen. Fig. 4.19 presents a region from this zone near a lateral edge at low K. The symmetry of the etch pits confirmed that the average crack plane was close to {100}. Two sets of <110> as well as one set of <100> river lines can be recognized. The features of the latter resemble those observed with <100> river lines on fan-shaped facets at intermediate K values. Also in region A of Fig. 4.19, the average {100} fracture facet can be seen to result from the presence of two sets of finer facets which intersect along a set of <110> striation-like markings.

4.3.3 Observations on Opposite Fracture Surfaces

Observations were also carried on opposite fracture surfaces of identical sites presenting alternate sets of microfacets and sheet-like facets. These observations demonstrated that both alternating and sheet-like microfacets were present on

opposite fracture surfaces and that they matched in an interlocking manner (particularly for those of alternating microfacets) as shown in Fig. 4.20. Alternating sets of microfacets have previously been shown to match in this manner on opposite fracture surfaces of cold worked 310 s.s. (112) tested in the same boiling $MgCl_2$ solution.

4.3.4 Stereographic Observations at Low and Intermediate Magnifications

Stereographic observations carried out at low and intermediate magnifications showed that the average crack plane in a grain could differ considerably from the primary facet orientation. It was noticed that for certain metals, in particular for austenitic stainless steels, the presence of the large majority of river lines were often of the same sign in a grain. This can permit to obtain an average orientation of the fracture surface which is favoured by the macroscopic mechanical conditions, while on a microscopic scale permitting this fracture to be produce following the crystallographic planes favoured by the stress corrosion cracking mechanism. The deviation between the average fracture plane in a region of a grain and the orientation of the primary facets, therefore, depends on the number, the size and the sign of the river lines or steps between primary facets as well as on the relative size of the sets of microfacets making up the primary facet. For this reason, it is often useless to determine the average orientation of a fracture surface produced in stress corrosion cracking in a grain or in a single crystal.

These aspects can be verified by the change in the symmetry and projected size of the four {111} faces within a {100} etchpit as shown in Fig. 4.10 of a fan-shaped pattern observed for an intermediate K value. In the right-hand portion of this fan-shaped pattern, a very symmetrical {100} etchpit indicated that the orientation of the average cracking facets was almost perpendicular to the tensile axis and relatively few river lines occurred in this local region. In the central portion of this fan-shaped pattern, however, the presence of a large number of river lines or steps almost along the same <100> direction resulted in a rotation of the average crack plane away from the orientation of the right-hand portion indicated by the dissimilar projected size of the {111} faces within the etch pits of stereographic observations.

Stereographic observations at low magnification (Fig. 4.21 (a)) showed that flatter and larger cracking facets at low and intermediate K values generally with an orientation almost perpendicular to the tensile axis; however, more complex fracture facets presenting more river lines or steps were also seen to form in order to produce a tilted average crack plane with respect to the tensile axis. It can also be seen in these figures that the average crack plane within one grain was often strongly influenced by the tendency to join up the crack front segments propagating at different heights in different grains and in different regions.

At high K, the larger number of microfacets involved in cracking resulted in more complex fractographic features which could readily produce average crack planes which differed strongly from a {100} and which were closer to those favoured by the local stress conditions. At high K, therefore, the fractographic feature appeared to be complex on a microscopic but less rough on a more macroscopic scale, since smaller orientation changes usually permitted adjacent crack segments in neighboring grains to join up as shown by the comparing the stereographs presented in Fig. 4.21(a) for lower K values to that in (b) for higher K values.

4.3.5 TEM Observations of Secondary-Carbon Replicas of Fracture Surfaces

Observations of secondary-carbon replicas (see section 2.3.4 for a description of the technique) of the TSCC fracture surfaces of annealed 316 s.s. was carried out with particularly paid attention to reveal details of striation-like markings which are often observed on the fracture primary facets, as well as to investigate whether some microcavities or small dimples could be observed on the flatter facets which present a {100} <110> cracking crystallography.

A few stereofractographs were taken by TEM in order to examine the orientation of the microfacets with respect to the tensile axis. In the TEM stereographic pair presented in Fig. 4.22, the striation-like markings can be seen

quite clearly on a TSCC facets at low K region, which would appear as a very flat facet in a SEM photography of the type shown in Fig. 4.4. With the stereo viewer, the wavy aspect can be seen very clearly on the micrographs taken on the replica and such observations indicate that these relatively flat primary facets are also made up of two alternating sets of {111} microfacets. The spacing between wave crests in this region can be estimated as approximately 0.04 to 0.08 μm. This value is smaller than that estimated from the observations by SEM in the low K region, suggesting that such striations are often too faint to be resolved by SEM. The river lines are almost parallel to each other and perpendicular to the striations. Some sheet-like facets present on river lines join up with the average facets at different height. On the other hand, some very fine details observed on these photographs could correspond to microdimples.

In order to verify whether they corresponded to artefacts, some carbon film specimens were made from primary acetate film which was not replicated on any surface. The aspect of this film is shown in Fig. 4.23. Similar very fine details are observed, indicating that they originate from the acetate film itself. However, the wavy aspect of the primary facets are only present on the replicas of TSCC fracture surfaces. It is therefore seen that TEM observations of secondary-carbon replicas of fracture surfaces can resolve finer details than those resolved by SEM; however, observations of replicas also result in some artefacts being seen, thus, requiring

additional care in interpreting the observations.

4.4 DISCUSSION

This section summarizes and discusses some of the microfractographic and crystallographic features observed for TSCC of annealed 316 s.s. A further discussion on the mechanisms of TSCC is found in chapter 7.

4.4.1 Summary of Microfractographic Observations and Results

The extensive study carried out on the fractography of stress-corrosion cracking of annealed 316 s.s. tested in boiling (154°C) $MgCl_2$ aqueous solution under freely corroding conditions showed that:

1) The cracking was entirely transgranular for K values up to 30 MPa $m^{1/2}$

2) The microfractographic features exhibited a strong variation with K. This variation possibly is the origin of the frequent differences in TSCC fractographic features published by different authors for unspecified K values.

3) At low K values, the fracture facets were relatively smooth and presented an average facet orientation close to or coincident with {100}. Also, <110>

river lines and finely spaced <110> striations were often present. Some of the primary facets had a microscopically wavy aspect. The etch-pitting studies indicated that {100} <110> cracking resulted from fine-scale decohesion occurring in an alternate manner on two sets of {111} microfacets.

4) At somewhat higher K values, herringbone patterns appeared for which the {100} primary facets presented both <110> and <100> river lines. The evidence indicated that the <100> river lines corresponded to regions in which decohesion occurred on four sets of {111} microfacets.

5) At high K values, the presence of {111} microfacets became more evident and they were identified more frequently. In addition, these {111} microfacets adopted an increasing sheet-like aspect. The only orientation identified in the present study for the sheet-like microfacets was {111}, and it appeared that the large majority, if not all, of these microfacets had this orientation. Also, as K increased, the average crack plane within a grain tended to deviate away from {100} to an orientation perpendicular to the tensile axis. This resulted in an average crack plane composed of a number of small primary facets, inclined to the average fracture plane as shown schematically in fig. 4.3. Many of these smaller facets were in turn

composed of finer sheet-like microfacets.

6) The TEM observations performed on replicas basically resemble that observed in SEM, however, more distinct striation-like markings and very small alternating microfacets were resolved on primary facets produced at low K region and which appeared flat. Features resembling very fine microdimples were observed but were shown to correspond to artefacts.

4.4.2 Discussion of the Fractographic Features

4.4.2.1 The Microscopic Crack Path

The inescapable conclusion arising from the present study was that, on the finest microscopic scale observed, TSCC occurred by decohesion on {111} planes and that combination of {111} microfacets resulted in larger primary facets with other average orientations, most notably {100}.

The microscale propagation of TSCC along the {111} planes of austenitic stainless steels is supported by the observations of a few previous workers, such as, the oxide replica observations of Nielsen (369) and the TEM observations of Nakayama and Takano (189), as well as the measurement of the interface angle of planes during stereomicrographic observations of Harston and Scully (188). Also, the fractograpic study of Dickson et al. (112) on 310 s.s. suggested the possibility

of TSCC on alternating sets of {111}, the evidence being clearer for cold-worked condition than for the annealed condition, presumably because of the inability to resolve clearly the very fine microfacets on the annealed alloy. As well, the present observations are consistent with those recently found by Magnin et al. (194), who reported discontinuous microcleavage mainly on {100} planes and microshearing on {111} planes on TSCC fracture surfaces for an annealed 316 s.s. tested in boiling $MgCl_2$ solution.

The present study showed that the increasing fractographic complexity of 316 s.s. with increasing K suggested a marked sensitivity to slip-dominated effects in the crack tip region, since increasing K should increase the amount of slip on individual {111} slip planes and increase the number of operative slip systems.

The present study also showed that the microfractography of 316 s.s. was generally more complex than that observed on 310 s.s. This was attributed to two effects: firstly, the crack propagation increment on each {111} microfacet was larger for 316 s.s., with the average microfacet size increasing with increasing K. This is possibly associated with the difference in the stacking fault energy (SFE) in these two alloys (374). The SFE is lower in 316 s.s. than in 310 s.s., favoring a larger increment of crack propagation on the individual {111} microfacets for 316 s.s. Secondly, decohesion occurred on a larger number of different sets of {111}

planes at higher K for 316 s.s. resulting in sheet-like microfacets which gave rise to the more complex fractographic aspect observed. However, the microfractography of 310 s.s. at low and high K values (112) was similar to that of 316 s.s. at low K. This indicates that the crack tip plasticity during TSCC is larger in 316 s.s. than in 310 s.s. It should be noted that the stage II propagation velocity was also larger in the 316 s.s. (Fig. 4.2). Despite differences in the fractographic complexity with increasing K for these two alloys, the basic fractographic features of TSCC could be considered to arise from the same fundamental crack propagation processes.

The present observations thus suggest strongly that the microscopic crack path follows planes on which slip has occurred. The absence of any significant crack tip blunting at least in stage I and II of the log da/dN-log K curve, furthermore, suggests that localized slip is involved. The details of the cracking mechanism proposed by Lynch (210, 285), which is based on adsorption-facilitated localized slip at the crack tip, are inconsistent with the microscopically resolvable {111} microfacets observed in the present study. However, to explain that the crack path alternates regularly between one set of {111} planes and the other in the case of a cracking mechanism produced solely by localized slip, reversed slip at the crack tip appears required (Fig. 4.24) but is not expected under the monotonic load application conditions employed. Therefore, even if localized slip plays an important role in the process of TSCC, the crack propagation cannot be produced

only by simple slip. From this study, it is evident, however, that the mechanism of TSCC in 316 stainless steel must involve microscale propagation on {111} planes on which slip has occurred. The indication is that the crack propagation of TSCC in 316 s.s. may occur by enhanced slip, microscale cleavage following slip planes or localized dissolution along {111} slip planes, or by a combination of these processes.

4.4.2.2 Complete or Incomplete Linkage Processes of River Lines During TSCC

As suggested by Pugh (206), another aspect worthy of particular attention concerns the manner in which the river lines form. Crack propagation proceeds on segments of primary facets which are essentially parallel but are not coplanar, even though they may have a similar crystallographic orientation.

Tongues of cracks on primary facets penetrate the metal and leave uncracked ligaments in their wake. Eventually, the increasing stress on the ligaments causes their failure by shear or TSCC processes and promotes a linkage between the crack tongues. The linkage process gives rise to river lines between similar orientations of primary facets and may also produce a shear or slip step on the fracture surface parallel to the local crack front.

The penetration of crack tongues and their subsequent linkage by fracture of the uncracked ligaments are shown schematically in Fig. 4.25 and 4.26, where two possible linkage situations are illustrated. The first possibility, depicted by Fig. 4.25, corresponds to the case in which the ligament fracture and linkage processes do not extend completely to the tip of the crack tongues. Thus, while a step may be produced on the fracture surface as a result of the fracture of the ligaments, the crack in general will not be blunted along the entire crack front. Small crack tongues will extend into the metal, as shown in stage 3 of Fig. 4.25. The important consequences of this process are that the crack does not have to re-initiate and the river lines will be continuous across the steps. The river lines may be displaced slightly along a step owing to the shear processes associated with step formation, but these displacement should be essentially of a continuous nature. The incomplete linkage process of Fig. 4.25 and the subsequent effect on fractographic appearance are expected to occur at low K values, and the microfractography of 316 s.s. at low K appeared to be consistent with this process.

At higher K values a second linkage possibility of river lines exists, as depicted by Fig. 4.26. In this situation, ligament failure and linkage extend completely to the tip of the crack tongues. The crack is effectively blunted and temporarily arrested and a step is produced along the entire crack front. The important consequences of this situation are that crack re-initiation has to occur at

the blunted crack front and, because it does not have to occur on precisely the same plane as the previous crack tongue, the river lines produced by ligament failure can be discontinuous across the steps and can appear to re-initiate or terminate at the individual steps. Linkage occurring in this manner was consistent with some of microfractographs of 316 s.s. and 310 s.s. (112) obtained at very high K values, in particular in stage III of the log v vs. log K curve.

The events dipicted by Fig. 4.28 and 4.29 may have important ramifications in relation to the pulse-loading experiments described by Hahn and Pugh (375). They superimposed a series of small load pulses on the applied load during TSCC of 310 s.s. and 304 s.s. in boiling (154°C) $MgCl_2$ solution. Application of the pulses resulted in pronounced striation-like features on the fracture surface. While these striations appeared curved and marked the shape of the crack front (in the same manner as the secondary cracks of Fig. 4.16), their aspect was also similar to the TSCC striations produced at high K in the absence of load pulses (112). Moreover, the published fractographs of Hahn and Pugh (375) showed that termination of re-initiation of some river lines occurred on meeting such pronounced striations. This confirmed the occurrence of blunting at the crack tip. Therefore, the striations produced by the load pulse experiments of Hahn and Pugh (375) must correspond to the high K situation depicted in Fig. 4.29. This conclusion is consistent with their statement that such "crack arrest" markings are only resolvable by SEM when

appreciable crack blunting occurs.

Having concluded that the experiments reported by Hahn and Pugh (375) were obtained under high K conditions, for which linkage of primary facets should occur as schematized in Fig. 4.26, it is now possible to account for their other observations on pulse frequency effects in terms of a more or less continuous crack propagation mechanism. For example, under high K conditions, when the load pulse is applied at sufficiently long intervals, the tongues lead the uncracked ligaments by a sufficient distance such that upon application of each load pulse the ligaments will fracture, with crack arrest not occurring until ligament failure extends to the crack front corresponding to the tip of the tongues. A one-to-one correspondence between crack arrest markings and load pulse is then obtained, as observed (375). When the load pulse interval becomes too short, insufficient time is allowed for significant penetration of TSCC tongues into the metal between pulses. Thus, the stress acting on the shorter uncracked ligaments may not be sufficient to cause their fracture. Several load pulses may be required before the tongues penetrate a sufficient distance to permit fracture of the ligaments. Consequently, the number of crack arrest marks on the fracture surface will be smaller than the number of load pulses, which is consistent with reported observations (375). This argument presents an alternative explanation for the load pulse observations of Hahn and Pugh without necessitating cleavage-like crack

jumps of a minimum size.

Even though the present fractographic observations performed on the fracture surfaces of TSCC for annealed 316 s.s. do not permit us to clearly identify the mechanism of cracking, however, they indicate that traditional microcleavage models of TSCC (e.g. by Pugh (206), Hahn and Pugh (375) and Sieradzki and Newman (202)) are not as well supported by the fractographic observations as earlier believed. In order to better understand the nature of the crack propagation process, as to facilitate identification of the mechanism of TSCC for f.c.c. metals, a detailed fractographic study was carried out for 70 Cu-30 Zn α-brass in ammoniacal solutions, and is presented in the next chapter.

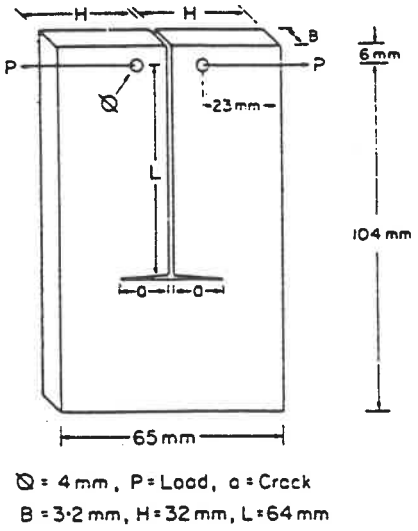


Fig. 4.1

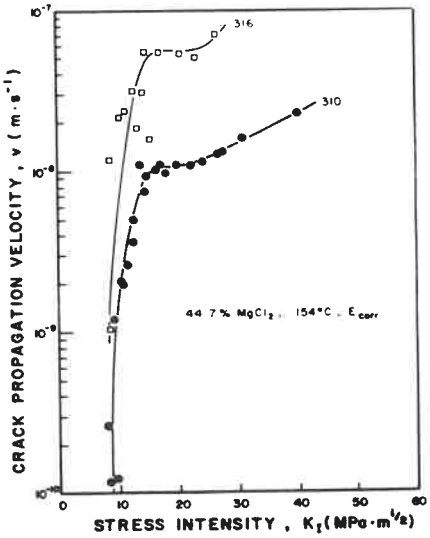


Fig. 4.2

Fig. 4.1: Dimensions and geometry of TN-DCB specimen.

Fig. 4.2: Previously obtained curves of crack velocity vs. K for annealed 316 and 310 stainless steels (112).

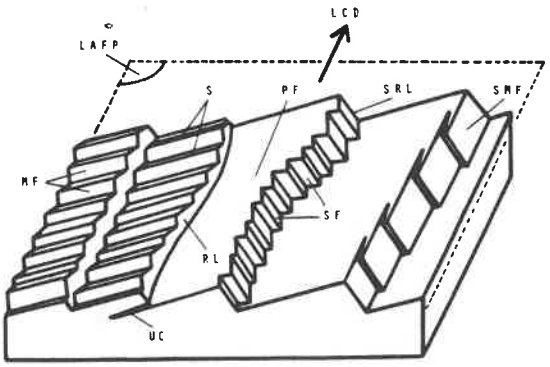


Fig. 4.3: Schematic diagram defining the fractograpic features associated with TSCC: LAFP, local average fracture plane; LCD, local crack propagation; MF, microfacet; PF, primary facet; RL, river line; S, striations; SF, serration facets; SMF, sheet-like microfacets; SRL, serrated river line, UC, undercutting (415).

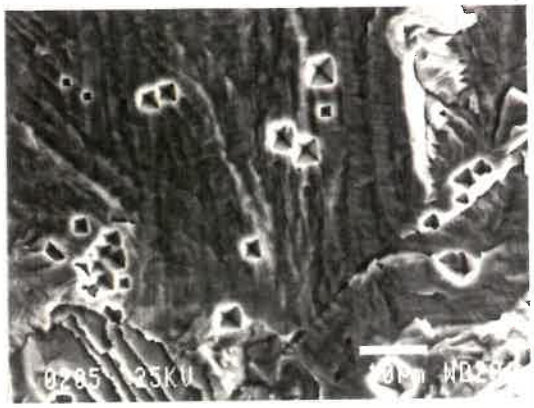


Fig. 4.4

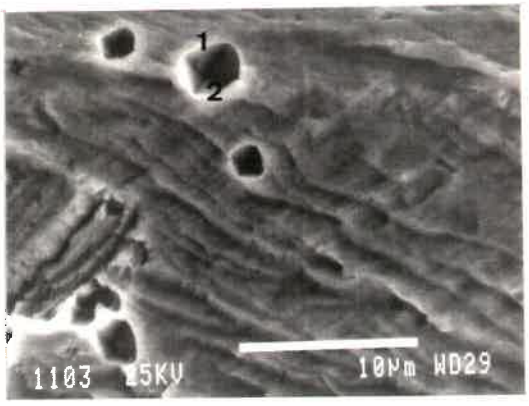
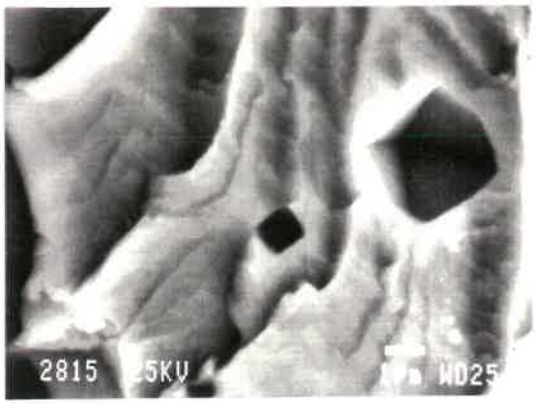


Fig. 4.6

Fig. 4.4: Aspect of the fracture surface produced near the SCC threshold. The etch pits indicate a {100} orientation of the primary facets. Fine horizontal striation-like features can be seen parallel to the <110> direction which is perpendicular to the main direction of river lines.

Fig. 4.6: In this micrograph, the striations and the waviness of fracture surface can be seen to result from the presence of sets of {111} microfacets parallel to sides 1 and 2 of the etch pits.



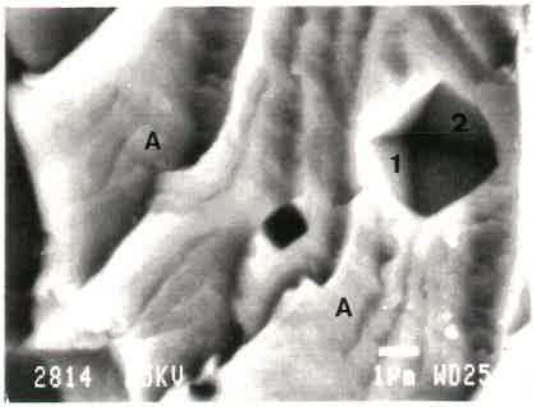


Fig. 4.5: Stereographic pair of micrographs showing fine striations which, in region "A" can be seen to result from the presence of sets of {111} microfacets parallel to sides 1 and 2 of the etch pits.

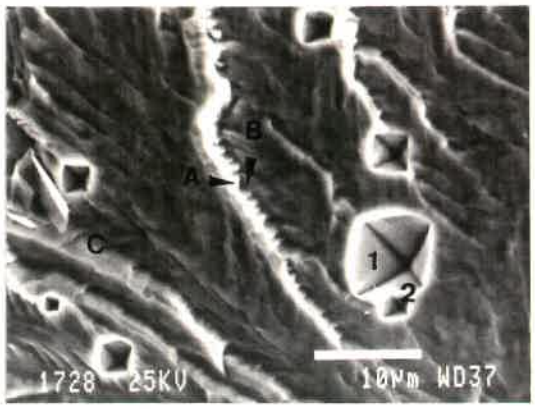
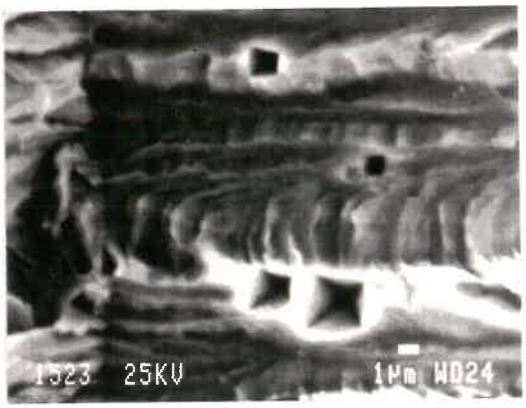




Fig. 4.7 **Fig. 4.8**

Fig. 4.7: Serration facets A and B on a prominent river line correspond to faces 1 and 2 of the etch pits. Sheet-like microfacets C on another river line correspond to face 2 of the etch pits.

Fig. 4.8: More complex fractographic aspect observed at intermediate K, presenting numerous microfacets not parallel to the average orientation of the fracture plane.



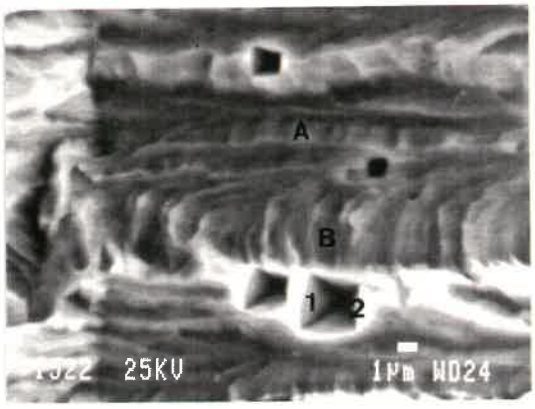
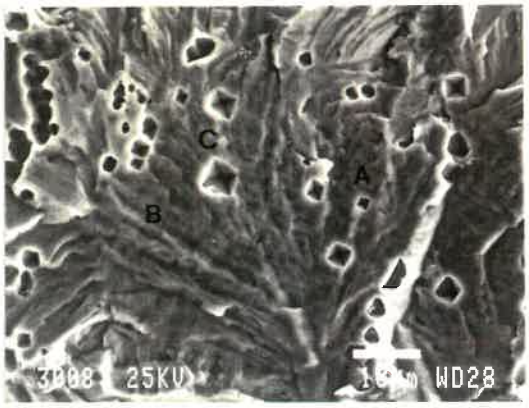


Fig. 4.9: Stereographic pair of micrographs from the region below the annealing twin in Fig. 4.8, allowing one to observe the microfractographic aspects at higher magnification. The presence of different sets of {111} microfacets can be identified. Fig. 4.9 is rotated almost 90° with respect to Fig. 4.8.



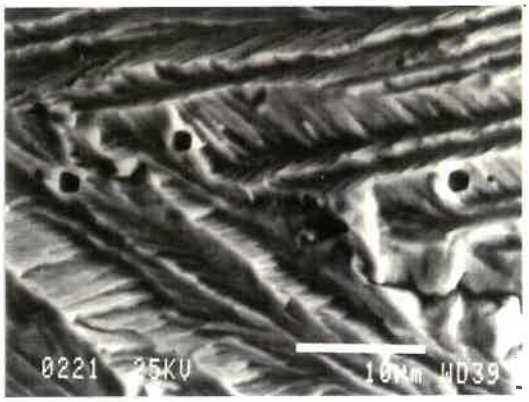
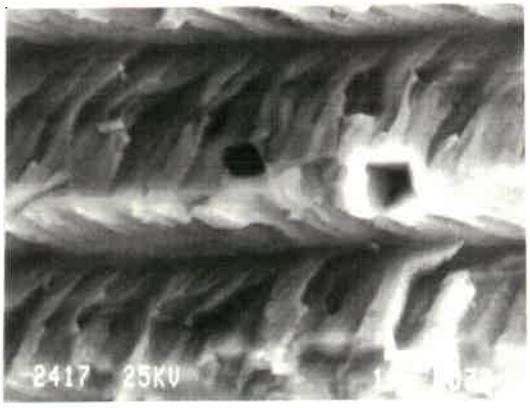


Fig. 4.10 **Fig. 4.11**

Fig. 4.10: Fan-shaped pattern of river lines observed for an intermediate value of K. River lines are parallel to the two <110> directions as well as to one of the <100> directions contained in the average {100} fracture plane.

Fig. 4.11: The more complex aspect of the SCC fracture surface observed for 316 s.s. at high K. The presence of many sheet-like microfacets results in feather-like microfractographic features.



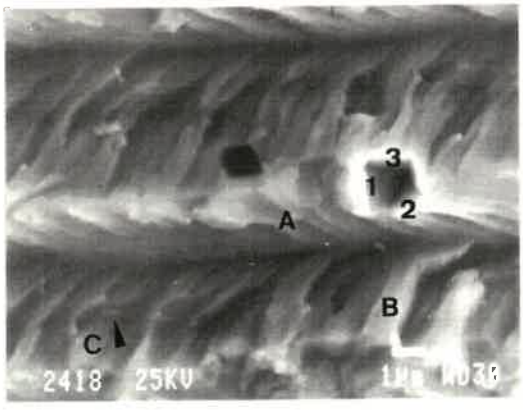
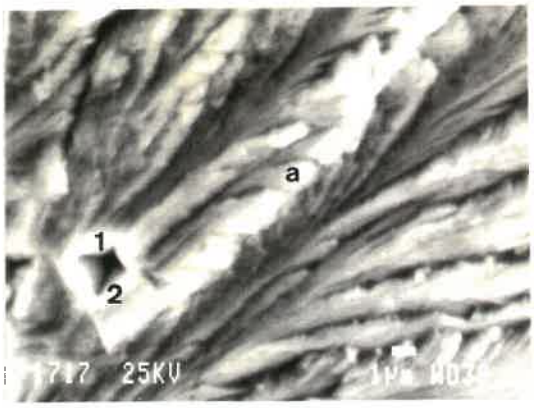


Fig. 4.12: The presence of an etchpit on this stereographic pair of micrographs permits one to identify the {111} orientations of the sheet-like microfacets. For example, the microfacets indicated A, B and C can be seen to be parallel to faces 1, 2 and 3 respectively of the etchpit.



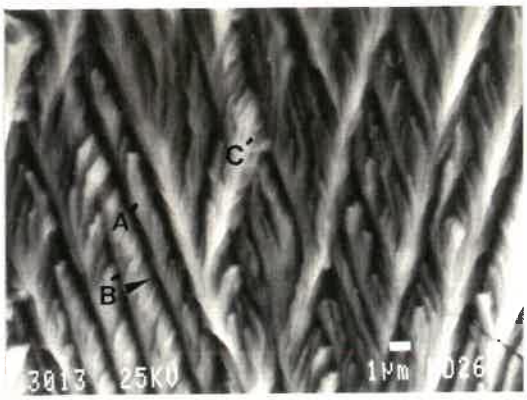


Fig. 4.13 **Fig. 4.14**

Fig. 4.13: Another etch-pitted region of SCC fracture surface produced at high K for which the {111} orientation of the sheet-like microfacets a and b were identified as parallel to sides 1 and 2 respectively of the etchpit.

Fig. 4.14: Unetched region of SCC fracture surface produced at high K, with feather-like features which result from the presence of numerous sheet-like microfacets. The crystallography of these features can be identified by comparison with Fig. 3.12(a) (see section 3).

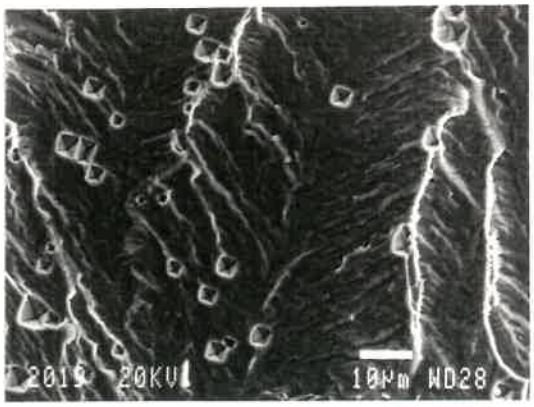


Fig. 4.15: Herring-bone patterns of river lines observed at quite low K. The {100} primary facet presents two sets of {100} river lines and a <110> central spine.



Fig. 4.16



Fig. 4.17

Fig. 4.16: Fractographic features produced in the high K portion of stage II of the log da/dN-log K curve. Secondary cracks permit one to identify intermediate positions of the crack front.

Fig. 4.17: Herring-bone pattern of river lines observed at high K.

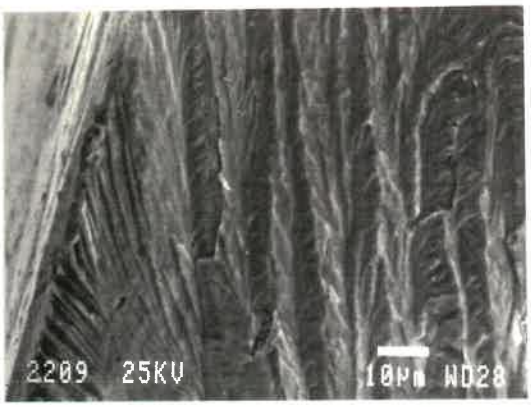


Fig. 4.18

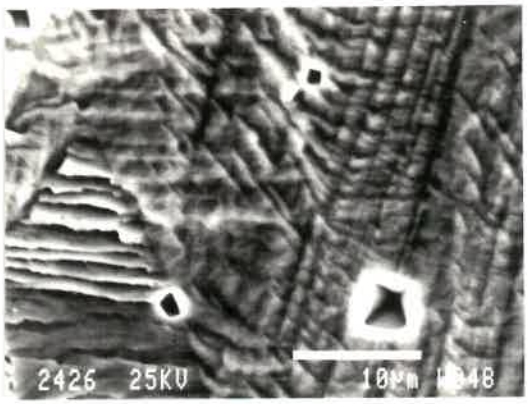


Fig. 4.19

Fig. 4.18: Region of fracture surface produced at low K at a lateral specimen edge and presenting fractographic features more typical of those observed away from the lateral edges at higher K.

Fig. 4.19: Low K region of fracture surface near a lateral edge, presenting two sets of <110> and a set of <100> river lines.

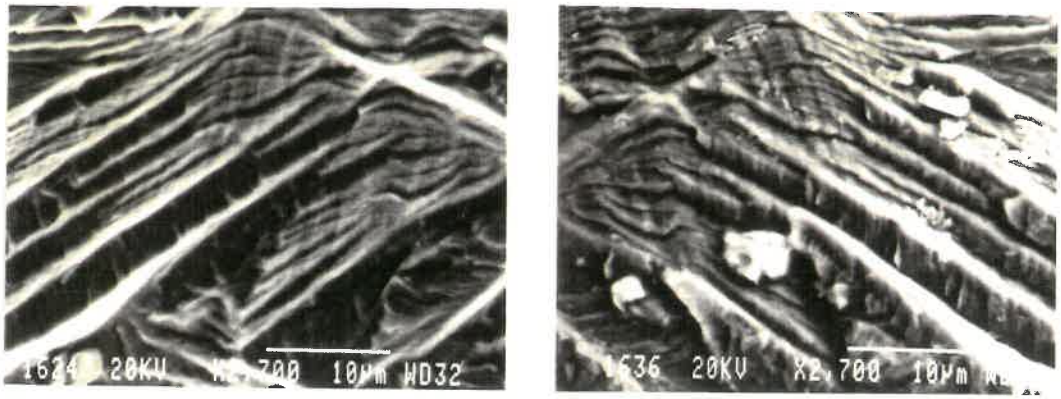


Fig. 4.20: The same site of the fracture surface observed on opposite fracture. The microfractographic features match in an interlocking manner.

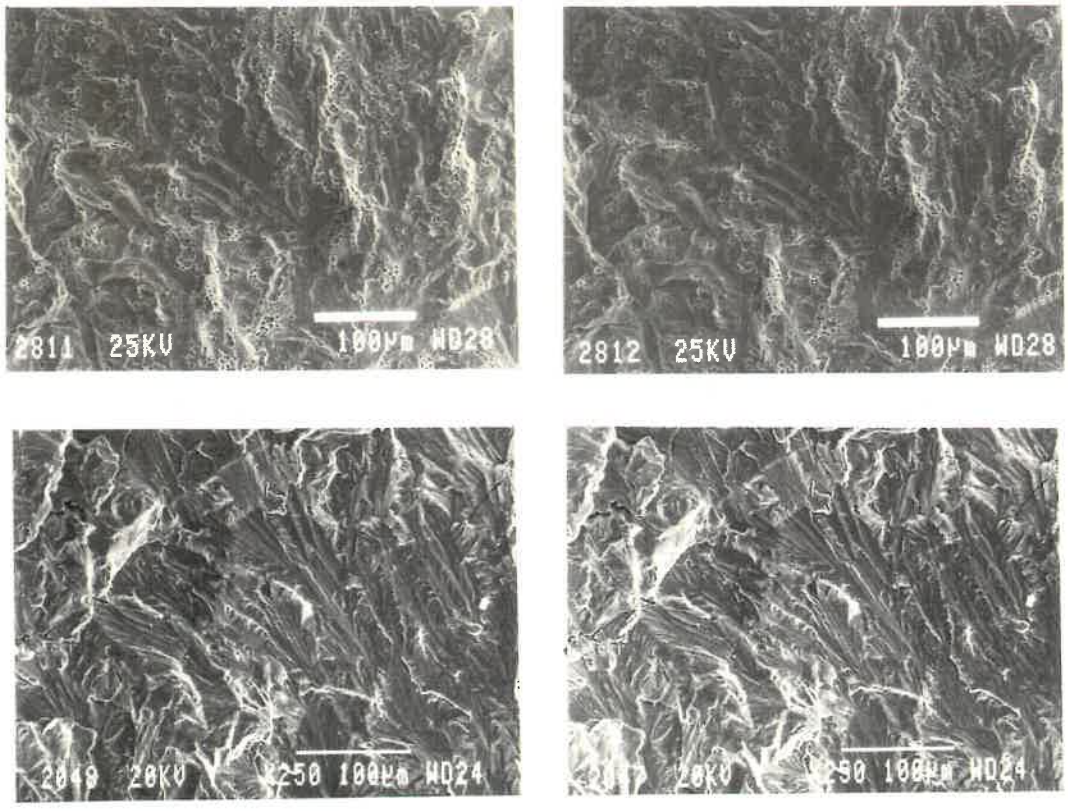
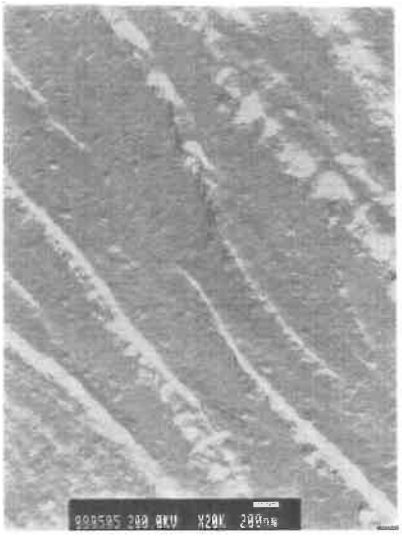


Fig. 4.21: Stereofractographic pairs of a relatively low magnification
(a) at low and intermediate K values region,
(b) at high K values region.



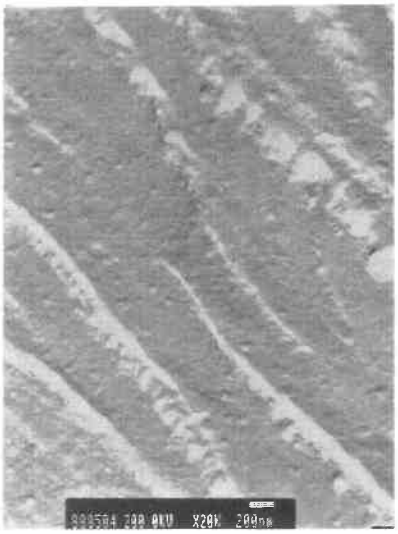
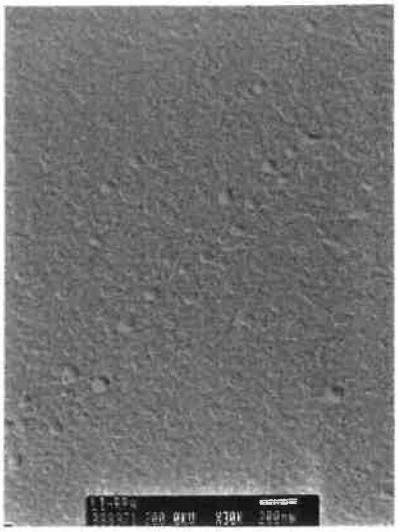


Fig. 4.22: Stereographic pair of TEM fractographs observed for a flat facet produced at low K.



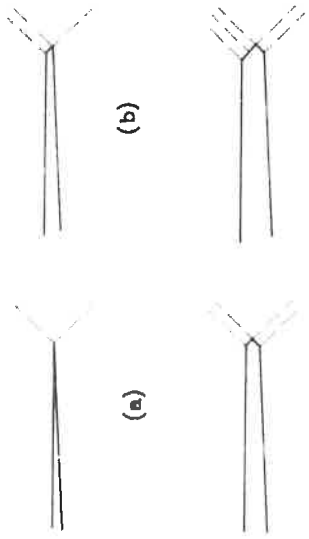


Fig. 4.23 **Fig. 4.24**

Fig. 4.23: Photograph of carbon film made from acetate film which was not replicated on any surface.

Fig. 4.24: Schematic representation of crack growth which occurs solely by alternate slip at the crack tip in the absence of reversed slip.

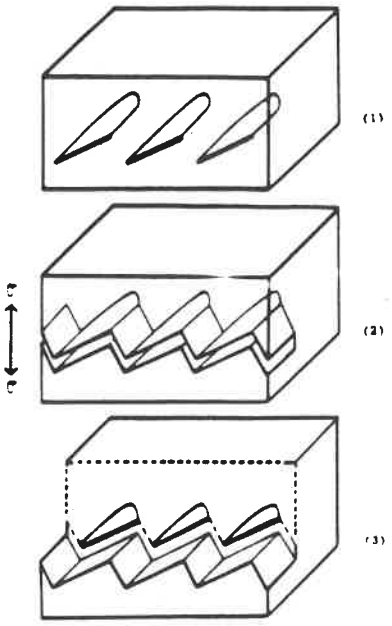


Fig. 4.25

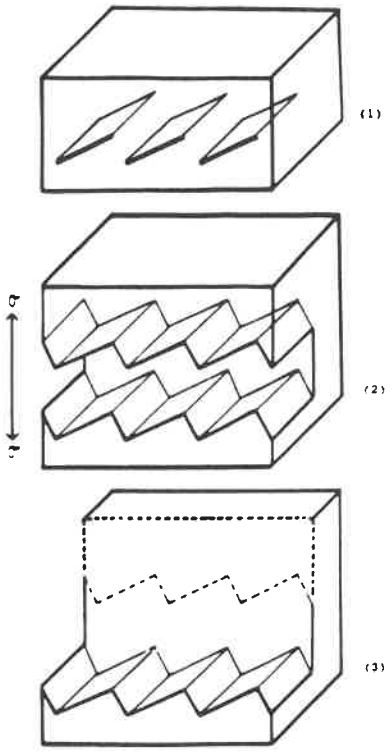


Fig. 4.26

Fig. 4.25: Schematic representation of the incomplete linkage of primary facets which extend into the metals as parallel tongues separated by uncracked ligaments. If the stress intensity factor acting on the ligaments is not sufficiently high, the discontinuous fracture of the ligaments can be expected not to extend the river lines all the way to the tips of the tongues.

Fig. 4.26: Schematic representation of the linkage process which can be expected at high K. The discontinuous fracture of the ligaments causes linkage to occur all the way to the tips of the tongues and is generally accompanied by the formation of a step along the crack front, effectively blunting the crack tip.

CHAPTER 5

FRACTOGRAPHY AND CRYSTALLOGRAPHY OF STRESS CORROSION CRACKING OF 70Cu-30Zn α-BRASS IN AMMONIACAL SOLUTIONS

5.1 DCB SPECIMEN EXPERIMENTS

5.1.1 Introduction

There have been many attempts to correlate the fractographic details with possible mechanisms of stress corrosion cracking (SCC) of α-brass and other copper alloys (157, 161, 163, 175, 179, 202). However, the fractography is complex and many fractographic features have not been explained clearly. Some important fractographic details including some of the crystallographic features have not yet been identified fully. It is therefore not surprising that, even considering the improvement in understanding the mechanisms of SCC of α-brass achieved by studying the fractography, that it is difficult to give a full interpretation of the fractographic features observed.

In light of the success of the fractographic study carried out on 316 stainless steel, we decided to perform a detailed fractographic study for 70 Cu-30 Zn α-brass in ammoniacal solutions. The objectives of this study were the following.

Since the usual orientation of the primary facets for α-brass containing about 30% Zn and for some other copper alloys have been identified frequently as being {110} planes by other investigators (157, 163, 175, 202), the first objective was to determine whether the primary {110} facets are formed from two sets of alternating {111} microfacets. A second objective was to determine whether {110} cracking is produced preferentially or uniquely in a <100> direction with a <110> crack front. In previous orientation studies of TSCC for the copper alloys, the microscopic details of crack propagation directions were not reported. Yet, knowledge of this feature should be important in identifying the cracking mechanisms of TSCC.

The third objective was to determine whether primary {100} or {111} facets could also be found and to identify the conditions giving rise to their appearance.

5.1.2. EXPERIMENTAL METHODS

5.1.2.1 Material

The composition of 70 Cu-30 Zn α-brass employed is given in Table 5.1.

Table 5.1: The composition of 70Cu-30Zn (wt%) (376)

Elements	Cu	Zn	Sn	Pb	S	Fe	As	O
	Bal.	29.9	<10ppm	47	110	140	<5ppm	<10ppm

Two plates of α-brass from the same lot with dimensions of 150 x 100 x 19 mm were cut from as-received material and annealed at 650°C for 2 hours in an argon atmosphere followed by furnace cooling. This resulted in a grain size of 100 to 400 μm and in a hardness of HB80.

The microstructure of the material after annealing is given in Fig. 5.1. The etching solution used for displaying the microstructure was 15 ml of HCl (Conc.), 5 g of $FeCl_3$ and 60 ml of double distilled H_2O. The etch time was approximately 30 seconds.

5.1.2.2 Specimen Geometry

The specimens employed were bolt-loaded double-cantilevered beams (DCB) specimens of dimensions 19 x 14 x 127 mm. Fig.5.2 shows details of the specimen geometry.

The stress intensity factor K of DCB specimen (377) can be calculated by equation [5-1]:

$$K = \frac{VEH\ [3H(a + 0.6H)^2 + H^3]^{1/2}}{4\ [(a + 0.6H)^3 + H^2 a]} \qquad [5\text{-}1]$$

where,

V is the total deflection of two arms of DCB specimen at the load point.

E is the modulus of elasticity (109800 MPa for α-brass)

2H = 19 mm

B = 14 mm

a is the crack length measured from the load point (centerline of the loading bolt).

5.1.2.3 Preparation of the Specimens

After machining, the specimens were prepared as follow :

1) Sharpen the root of the chevron notch using a jeweller's saw;

2) Polish both lateral surfaces (finishing with 0.05 μm alumina powder) to obtain a flat, reasonably scratch-free surface of high reflectivity.

3) Ultrasonically rinse the specimens in acetone, in distilled water and finally in methanol, followed by air-drying.

4) Coat all surfaces of the specimen including the inside of the notch with lacquer.

5) Fatigue precrack at R=0.1 some specimens to produce a sharp crack of about 2mm, measured from the tip of the notch. To avoid a large plastic zone at the crack tip, a decreasing ΔK program was employed starting at

da/dN ≈ 10^{-5}mm/cycle and ending in a range of 10^{-6} to 10^{-7}mm/cycle. Because bending of the arms of some DCB specimens occurred during fatigue, some notched specimens were employed directly for stress corrosion test.

6) Bolt-load the specimens, measuring the value of displacement V with a travelling microscope having an accuracy of 0.01 mm. After loading, coat the bolt surfaces with lacquer, with special attention paid to properly coat the contact regions between the bolts and the specimen in order to avoid any electrochemical effect during SCC testing.

7) Attach a polyethylene beaker to the specimen using a silicon rubber adhesive. One side of this beaker had previously been cut to attach a viewing window with acetate foil. The adhesive was then dried in air for at least 48 hours.

5.1.2.4 Composition of the Testing Solutions

The following testing solutions were employed :

1) A typical non-tarnishing aqueous solution of 15M ammonia solution to which 6 g/l of copper added as Cu $(NO_3)_2$ (158, 180).

2) An aqueous solution of 15M ammonia to which 6 g/l of copper has been added as pure copper powder. For this solution, because the dissolution of the copper powder was performed in air rather than under an oxygen pressure of 10 p.s.i., the copper powder had not been dissolved completely

and hence the concentration of copper in the solution was less than 6 g/l, which did not meet the requirements of a standard tarnishing solution (158, 180).

Since these two solutions were prepared and tested in air, they should contain a certain amount of dissolved oxygen and both presented a blue colour, but the colour was lighter for the second solution described.

5.1.2.5 Experimental Procedures

The stress corrosion test were performed under open circuit conditions in the test cell schematized in Fig. 5.3.

The tests were conducted under constant displacement and therefore decreasing stress intensity. In general, for most of precracked specimens, the "stress intensity" employed to initiate cracking was in a range of 10 to 20 MPa $m^{1/2}$, as suggested in reference (378). For the notched specimens, an approximate value of the stress intensity was (over) estimated, considering the notch length as corresponding to an equivalent crack length. Furthermore, since the cracks were always branched upon initiation at the notches, the true value of the stress intensity at the notch tip should be much less than the nominal values calculated, which were between 20 to 25 MPa $m^{1/2}$.

The stress corrosion crack initiation and propagation process was observed by removing the solution approximately every 24 hours and measuring the crack lengths with the travelling microscope through the viewing window on the beaker. The SCC testing was performed generally for a period of 100 to 200 hours.

At the end of each test, the solution was removed and the specimen was washed then dried. The fracture surfaces were obtained after almost complete sawing of the remaining cross section.

A detailed fractographic examination was performed on JEOL JSM-840 and JSM-820 scanning electron microscopes. The cracking crystallography was determined from etch pits produced on the primary facets during SCC testing and by measuring the angles between the different facets.

5.1.3 RESULTS AND DISCUSSION

5.1.3.1 The Plot of log V vs. K

Fig. 5.4 presents the plot of log V (da/dt) vs. K. The data in this plot were from 3 specimens which were tested in 15M ammonia solution containing 6 g/l of copper added as $Cu(NO_3)_2$, which was an oxygenated non-tarnishing solution.

At low values of stress intensity factor K, a region of constant velocity was obtained (a plateau region), with the crack growth rate being approximately 1 x 10^{-8} m/s for this annealed material. This value is slightly lower than that obtained by Scully et al. (378), who reported that the crack velocity da/dt in the plateau region was 3.1 x 10^{-8} m/s at low K (~10 MPa $m^{1/2}$) for annealed material tested in 15M ammonia solution containing 6 g/l of copper added as copper powder. A relatively large data scatter band can be seen in Fig. 5.4, possibly associated with the crack branching and the crack length measurements introducing error in the stress intensity K and cracking velocity da/dt measurements, as discussed in section 5.1.2.

5.1.3.2 Intergranular and Transgranular Cracking

A relatively large transgranular cracking region occurred after a narrow (≈ 1 mm wide) initial predominantly intergranular cracking region for the specimens tested in both solutions employed in the present study. The typical macroscopic aspect of the fracture surface is shown in Fig. 5.5, taken from a precracked specimen tested in 15M ammoniacal solution with 6 g/l of copper added as $Cu(NO_3)_2$. The regions indicated A,B, and C in this figure correspond, respectively to those of fatigue precracking, of intergranular stress corrosion cracking (ISCC) and transgranular stress corrosion cracking (TSCC). It should be noted that the intergranular cracking region in this figure is situated not only near the fatigue precrack but also near the lateral edges of the fracture surface. The colour of

TSCC portion of the fracture surface appeared yellow but the ISCC portion displayed a bluish colour.

The cracking path of Cu-Zn alloys in oxygenated 15M non-tarnishing ammoniacal solution containing 8 g/l of copper was reported by Pugh et al (379) as transgranular in the alloys in which dislocations form planar arrays (Zn > 18 wt%) and intergranular in alloys displaying cellular dislocation configurations (Zn ≤ 18 wt%). Kermani and Scully (180) reported that in all their experiments on 70 Cu-30 Zn α-brass SCC was always transgranular in 15M NH_3 solution containing 6 g/l of copper and was not affected by the manner in which the 6 g/l of copper was added or whether the alloys were in the as-received or annealed condition. The occurrence of transgranular cracking in the present study is therefore in agreement with these previous studies, but the occurrence of intergranular cracking in the non-tarnishing solution is not.

The present observations in which more intergranular cracking occurred near both lateral edges of the fracture surface as well as near the site of initiation of SCC suggests that this ISCC is associated with a difference in the composition of the solution near the edges and near the precrack compared to that in contact with the crack tip further in the interior of the crack. This result suggests that when more oxygen is present in the solution, more ISCC will be favoured. Further

evidence indicating a role of oxygen in solution in favouring intergranular cracking will be presented in section 5.2.3.3. The mechanism by which oxygen in the ammoniacal solution facilitates ISCC of α-brass is not very clear. However, as indicated by Pugh and Green (380), oxygen can increase the amount of cupric complexes ($Cu(NH_3)^{2+}_4$) in the solution, the essential role of which in conventional open-air tests is simply to provide an efficient cathodic reaction and, hence, either to permit rapid preferential dissolution of grain boundary materials (380) or to permit preferential adsorption of some anodic or cathodic species at the grain boundaries (381, 405).

5.1.3.3 Fractography of ISCC of α-Brass

The appearance of the intergranular stress corrosion cracking facets in α-brass was generally very smooth and relatively featureless (Fig. 5.6). On some of the intergranular facets, parallel line markings were observed and were generally found to correspond to slip traces (Fig. 5.7). Such markings generally did not continue across grain boundaries, and frequently a single grain boundary facet contained more than a single set of parallel markings. Examinations on a number of matching fracture facets demonstrated that the sets of line markings, in general, were not present on the matching facets. This indicates that they generally correspond to slip traces produced on the fracture surface behind that crack front. These observations are consistent with those of Pugh et al (158). On the other

hand, McEvily and Bond (382) and Kermani and Scully (180) reported that they observed the presence of crack-arrest markings on some intergranular facets of α-brass, but for tests performed in Mattsson's tarnishing solution (ASTM G 37). Since the main aim of the present fractographic study was to investigate the nature of TSCC, the study of the intergranular fractography was limited to that just described.

5.1.3.4 Fractography of TSCC of α-Brass

The aspects of TSCC fracture surfaces of α-brass in both 15M ammoniacal solutions employed are very similar to that reported in previous studies (158, 161, 180, 379, 382), in that they are cleavage-like in appearance. Most of transgranular fracture surfaces consist of a series of relatively large and flat facets. Within the individual grain, these large and flat facets are made up of several parallel facets which are separated by steps. In general, these steps are very crystallographic, exhibiting a serrated appearance, and vary in height from several microns to dimensions barely resolvable by the SEM. Frequently, the steps form "river" "fan" or "herringbone" patterns, common in conventional cleavage of brittle solids.

Careful examination, however, reveals some important features. Firstly, the microfractographic appearance varies with the stress intensity factor K. The microfractographic features are more complicated at higher K values, which

correspond to the region near the interface with the intergranular fracture surface in the present tests performed under conditions of constant displacement. More triangular shape facets of different size in different orientations are frequently observed in the individual grains at higher K values (~ 20 MPa $m^{1/2}$), as shown in Fig. 5.8.

Secondly, large flat cleavage-like facets were observed frequently on the fracture surfaces produced in the lower K regions (e.g. 10 ~ 15 MPa $m^{1/2}$). Most of the flat facets, however, presented very crystallographic striation-like markings, some of which were not perpendicular to the serrated river lines (Fig. 5.14). By examination of stereofractographs, these striated facets appeared to be made up of two sets of fine microfacets which were inclined with respect to the large primary facets and intersected along the striation-like markings.

Thirdly, the surface steps on the individual grain facets were more visible, crystallographic and numerous than on ordinary cleavage facets. All of these features clearly revealed that the microfractographic aspects of TSCC for α-brass again varied with the stress intensity factor K.

5.1.3.5 Crystallography at High K (K ~ 20 MPa $m^{1/2}$)

For convenience of presentation, the results pertaining to the crystallography of cracking will be separated into those produced at high K values and those produced at intermediate and low K values. The results presented are taken mainly from one specimen tested in 15M ammoniacal solution containing 6 g/l of copper added as Cu $(NO_3)_2$, which is the typical non-tarnishing solution used by previous workers (158, 180). Specimens tested in 15M ammoniacal solution containing 6 g/l added as copper powder generally gave identical or very similar TSCC fractographic aspects.

As already mentioned, the fracture surface produced at high K displayed a very complex microfractographic appearance. The triangular-like facets in Fig. 5.8 are very similar to those reported by Kaufman and Fink (161), (Fig. 6c in the reference (161)) as typical of the fracture surface produced towards the end of their slow constant extension rate tests on 70 Cu-30 Zn single crystal tested in a cupric ammonia solution containing 8 g/l of copper added as Cu $(NO_3)_2$.

An attempt to determine the orientation of these complex triangular facets in the present study was performed by measuring the interfacial angles between the facets observed on pairs of stereo fractographs. Fig. 5.9 clearly reveals this complex aspect, with the presence of four sets of {111} microfacets, indicated as A, B, C

and D. This result is similar to that obtained in our previous study of TSCC (section 4.3.2.3) in annealed 316 s.s. at high K values, in which the various {111} orientation facets combined to form sheet-like or feather-like patterns resulting in complex microfractographic features. Kermani and Scully (179) also reported the identification of {111} facets for α-brass tested at high K in neutral ammoniacal solution.

The other fractographic feature at times observed in the relatively high K region, is that of numerous parallel river lines or serrated steps separating a series of relatively flat and narrow fracture facets, as shown in Fig. 5.10 (a). These serrated triangular facets on the river lines can be seen to consist of two sets of alternating {111} facets, the angle between which is approximately 70°. Some of the serrated secondary facets or steps between primary facets have a relatively important height and often result in an average plane having a near-{100} orientation, with the river line on the primary facet corresponding to an average near-<110> direction, determined from the angle between {111} facets. Since the relatively flat primary facets are almost perpendicular to the average {100} plane of the secondary facets which are clearly made up of two sets of {111} serrated facets and since the trace of the relatively flat primary facets and the average {100} secondary facet meet along a <110> direction, the primary facets have a {110} orientation. Careful examination of Fig. 5.10 (a) showed that these relatively flat

{110} facets also consist of some very fine microfacets, the orientation of which can be determined as corresponding to the other two {111} planes (those not perpendicular to the primary facet). In this region, however, these microfacets meet in the direction parallel to the average orientation of the river lines, and therefore do not alternate parallel to the crack front. Fig. 5.10 (b) schematizes the orientations of the cracking facets identified in Fig. 5.10 (a). When the secondary facets separating primary {110} facets have a strong tendency to form a {100} average cracking plane perpendicular to the primary facets and to consist of alternating {111} facets with an average <110> propagation direction, this {100} <110> cracking crystallography applicable to the secondary facets making up the river lines is the same as that observed for the primary facets in TSCC of 316 s.s. at low and intermediate K values. However, no large primary {100} facets were observed in the present study on 70 Cu-30 Zn α-brass.

At high K, however, the presence of numerous river lines with relatively important step heights permits the local average orientation to deviate strongly from the {110} orientation of the relatively flat primary facets. An example is presented in Fig. 5.11, from which, it is also noticed that if unequal amounts of decohesion occurs on the two sets of alternating {111} planes, the local direction of the serrated river line would change from a <110> orientation towards a <112> direction, indicated by the arrow in this figure.

5.1.3.6 Crystallography At Low K (≈ 15-10 MPa $m^{1/2}$)

The relatively low K regions of the fracture surfaces correspond to those portions which are located in the middle part of the TSCC fracture surface of Fig. 5.5 and in the portion produced near the end of the TSCC crack propagation region.

5.1.3.6.1 {110} <100> and {110} <112> cracking crytallography

In this region, the fractographic features have often reported cleavage-like appearance. They are characterized by parallel crystallographic primary facets separated by steps or serrations on the river lines which are also crystallographic in nature.

The primary fracture facets are identified as corresponding to {110} planes, with preferential propagation in a <100> or in a near-<100> direction and occasionally propagation in a <110> direction. The identification of the orientation of the primary facets in this region was aided by etch pits produced during the tests. An etchpit shown in Fig. 5.12 (a) indicates that the primary cracking facets have a {110} orientation. This type of etchpit was reported by Young (342) for grown-in dislocations on {110} face of preannealed copper crystals. The two large side faces of the etchpit, which are inclined with respect to the primary facets, have {111} orientations. The striation-like markings on the {110} primary facets can clearly be

seen to be parallel to a <110> direction which is the orientation of interfaces between the large {111} faces within the etchpit. If the average crack propagation direction was perpendicular to these striations, this direction would be a <100> direction. The two sets of serrated secondary facets on the river lines are perpendicular to the primary {110} facets and have {111} orientations. The traces of these sets of serration facets correspond to two <112> orientations. Usually, one set of <112> traces is more favoured than the other, resulting in an average crack propagation direction close to a <112>.

5.1.3.6.2 Nature of the Wavy Aspect on the Primary {110} Facets

The primary {110} facets often present a wavy aspect, especially when produced at intermediate or high K values as shown in Figs. 5.12 and 5.13. This wavy nature clearly suggests that the primary {110} facets result from the cracking occurring on two sets of very fine microfacets inclined with respect to the average crack plane orientation and intersecting this plane along the striation-like markings, which are often close to perpendicular to the microscopic propagation direction. The orientations of the microfacets were determined by the examination of stereofractographs (e.g. Fig. 5.12) and indicated that the two sets were parallel to the two large inclined {111} faces of the etch pits. Thus, they should have {111} orientations. Such microfacets can also be observed very clearly in a micrograph from an intermediate K region of the TSCC fracture surface of 70 Cu-30 Zn single

crystal, which was published by Kaufman and Fink (161). These authors carried out slow strain rate tests and found the fractographic aspect progressively became more complex as the crack propagated further from the initiation region.

It was also found that the size of microfacets decreased as the stress intensity K decreased. Fig. 5.13 presents an example showing that the primary {110} facets are made up of the two alternating sets of very fine {111} microfacets. This photo was taken from a region corresponding to $K \approx 10$ MPa $m^{1/2}$. Moreover, the {111} microfacets were often not visible on the primary {110} facets produced at very low K (≤ 10 MPa $m^{1/2}$), especially when the average facet was almost perpendicular to the tensile axis. An example is presented in Fig. 5.14. The appearance of the fractography in this figure is quite similar to the TSCC micrographs which have been published for Cu-25 Au tested in aqueous $FeCl_3$ (174, 209) and for Admiralty brass tested in non-tarnishing ammoniacal solutions (157, 158). At high resolution, however, even on such very smooth primary {110} facets, some striation-like markings can at times faintly be seen (see arrow in Fig. 5.14), but the interstriation spacing becomes very small indicating that the size of the two sets of {111} microfacets is then very small.

5.1.3.6.3 Matching of {111} microfacets and striations

It is important to verify if the fine {111} microfacets observed on primary {110} planes match on the opposite fracture surface or whether they can be interpreted as corresponding to slip steps produced after fracture. Previous work on α-brass have not reported the presence of these microfacets.

Matching {111} microfacets are clearly shown in Fig. 5.15. For example, microfacet A_1 matches in an interlocking manner with facets A_2 on the mating fracture surfaces. However, the details of the microfacets, because of their very small size, could not be resolved very clearly by SEM. As a result, it is difficult to say whether the microfacets match "perfectly" or not, however, they appear to match very well.

Having shown that the microfacets match in an interlocking manner, the nature of the striation-like markings on the {110} primary facets should be considered. Striations have been frequently reported to be associated with TSCC (158, 174, 180). Generally speaking, the striations on TSCC facets are considered to correspond to crack-arrest markings produced presumably by plastic deformation during the temporary crack arrests. They have therefore been interpreted as indicative of discontinuous crack propagation (157, 375). The main properties of crack-arrest markings are that they are normal to the crack growth direction (i.e.

the surface steps on a facet) and match perfectly on opposite fracture surfaces. On the other hand, slip traces which are produced behind the crack front, such as those observed on some intergranular facets (section 5.1.3.3), appear only on one of the fracture surfaces. In addition, they do not necessarily lie parallel to the microscopic crack front.

The striations shown in Fig. 5.15 match well and are approximately normal to the crack growth direction, as indicated by the average orientation of the serrated river lines. In this context, the present striation-like markings have the characteristics of crack front markings. However, it must be emphasized that the striations on the mating fracture surfaces match in an interlocking peak-to-valley manner rather than as mirror images. Moreover, the striations on the primary average cracking facets produced at intermediate K have been shown to be intersection lines of two alternating {111} microfacets and, accordingly, to be very crystallographic. This indicates that the nature of the striations produced in TSCC of α-brass is similar to that observed for TSCC of 316 stainless steel.

5.1.3.7 Comparison of the Relative Ease of Cracking for the Different Crystallography Identified of TSCC Facets

Table 5.2 summarizes the cracking crystallography identified in the present study of TSCC for α-brass in (DCB) bulk specimens. The combinations of crack

plane and direction identified are {110} <112>, {110} <110> and {110} <100>, consistent with those of TSCC for Cu-25 Au reported recently by Lichter et al (175). However, these authors did not mention the {111} <110> crystallography obtained at high K or the two sets of alternating {111} microfacets associated with the primary {110} facets at lower K values. While these two cracking features have clearly been demonstrated in the present study of TSCC for α-brass.

The {110} <100> crystallographic cracking and particularly those of {110} primary facets with a preferential <112> or near-<112> orientation of river lines, were frequently found at relatively low and intermediate K values (see Figs. 5.12 and 5.14). However, cracking on a {110} plane in a <110> direction was only very rarely observed at low K values but was more frequently observed at high K values.

The study of facets which present fan-shaped patterns of river lines can be expected to provide evidence concerning the relative ease of cracking in different crystallographic directions. Fig. 5.16 presents an example of a facet presenting a fan-shaped pattern of river lines. The directions of the river lines on the {110} primary cracking facets are predominantly in two near-<112> directions; however, in a quite narrow region near the middle of the fan shape, a smaller number of river lines are in a near-<110> propagation direction. This aspect implies that the crack propagation on a primary {110} facets is relatively difficult in a <110>

direction, resulting in only a narrow region of cracking in this direction, with the cracking fanning out preferentially to follow near <112> direction. This result is consistent with that obtained by Lichter et al. (175) in the study of TSCC for disordered Cu-25 Au single crystals anodically polarized in a 0.6M NaCl solution to potentials between 300 and 430 mV (SCE) and tested in tension at low strain-rates between 10^{-6} - 10^{-7} sec^{-1}. They found that faster macroscopic crack growth propagation occurred for {110} cracking in an average <110> direction, but the aspect of their river lines indicates that microscopically the propagation occurs in two <112> directions. They associated this faster propagation with fewer crack arrests compared to {110} propagation in a <100> direction.

Table 5.2: Crystallography identified for TSCC facets of α-brass in bulk DCB specimens.

K (values)	Primary facets	Average propagation direction	Characteristics of microfacets	Orientations of striations
Relatively high K values (~ 20MPa $m^{1/2}$)	{111}	<110>	different sets and different sizes of {111} microfacets	<110>
	{110}	<110>	two sets of {111} microfacets deco-hesion meeting parallel to the crack propagation direction	<110>
	{100} (average secondary facets planes)	<110>	Two serrated alternating sets of small {111} secondary facets on river lines	<110>
Intermediate and low K values (10 ~ 15 MPa $m^{1/2}$)	{110}	<100> (often) <112> (more often>	two alternating sets of {111} microfacets	<110>
	{110}	<110> (least often)	two sets of {111} facets decohesion meeting parallel to the crack propagation direction	<110>

It can be noted that most of the <110> river lines observed in the present study are relatively thick and present two sets of serrated secondary {111} facets to give rise to an average {100} orientation of the secondary facets, corresponding to these river lines (see Fig. 5.10 and 5.11). However, most of preferential <112>

river lines are defined very sharply. Therefore, the relative ease in crack propagation direction may also be partly associated with the effect that when an average growth direction is in a <112> or near-<112>, the formation of the river lines for joining up the parallel primary {110} facets on different levels only requires cracking primarily on one set of {111} slip planes and also involves fracture over shorter distances. This would be expected to minimize the resistance to crack growth in this direction.

It also should be noted that under the effect of a tensile stress acting on a {110} crack plane, the {111} slip planes submitted to the highest shear stresses will be the two which share the <110> direction contained in the crack plane, since the other two {111} planes are parallel to the tensile stress. That two sets of inclined {111} microfacets often can be observed on the {110} primary facets, even in the case of a <110> crack propagation direction, is therefore, consistent with the crack propagation following microscopically planes on which slip has occurred, these being principally the same two {111} planes for all average crack propagation directions on this plane.

To summarize, the present observations demonstrate that the TSCC of α-brass occurs microscopically on different sets of {111} microfacets and that the presence of relatively large {111} microfacets of several orientations occur at

relatively high K values for which a relatively important amount of slip should accompany crack propagation. Therefore, the present observations on TSCC of α-brass, similar to those on 316 austenitic stainless steel, indicate that microscopically the crack path follows {111} planes on which slip has occurred and that this plastic deformation plays a role in the crack propagation mechanism. However, the details of the decohesion on the {111} planes and the relationship between the amount of slip and the decohesion which occurs on these planes remains to be clarified.

5.2 SUPERFICIALLY DEALLOYED Cu-30Zn RIBBON EXPERIMENTS

5.2.1 Experimental Ojbectives

As mentionned in the section 1.2.1.6, the film-induced cleavage model (202, 206, 209, 383), which proposes that thin surface films, usually monoporous metallic layers, can nucleate cleavage crack advance of approximately 1 μm in ductile materials including α-brass, austenitic stainless steels and pure copper, has recently attracted particular attention since it accounts for discontinuous cleavage-like cracking. Cassagne et al. (209) has reported that some cracks in a gold copper alloy appeared to cross the interface between a de-alloyed layer and the unattacked substrate, however, most of the evidence in favour this model is indirect (206). Some authors (383) pointed that it was not conclusively established if this occurred

as a single brittle event in air, or as a series of events in the corrosion solution, due to induced stresses from de-alloying. Therefore, after the ammonia-induced transgranular stress-corrosion cracking of α-brass had been correlated precisely with the onset of de-alloying (selective zinc dissolution) at ~ 20% Zn (384), Newman et al. carried out a series of experiments (383) which have been considered as providing important evidence to support the film-induced cleavage mechanism.

In these experiments, α-brass ribbons (65 Cu-35 Zn, with thickness of ~ 12.5 μm) were immersed for 100 minutes at room temperature in 15 M ammonia solution stirred under nitrogen in a glass flask with enough cuprous oxide (Cu_2O) to give 0.04 M cuprous complex ions ($Cu(NH_3)_2^+$) and in the presence of several grams of copper powder to remove traces of cupric ions. This solution rapidly produces a superficial dezincification layer. Electrochemical measurements of the zinc dissolution indicate that the first 30-40 nm of de-alloying occurs within one minute, but that the anodic current then drops to such a low value that it takes many hours of further immersion to obtain a thickness of 100 nm (383). After 100 minutes immersion, the ribbons were rapidly fractured mainly under the following conditions (383):

1) Ribbon strained rapidly to fracture in the cuprous ammonia test solution;

2) Ribbon removed from the test solution, immediately rinsed with deionized water and methanol; air-dried and then fractured in air at room temperature;

3) A similar procedure as the preceding (no. 2) was employed but with the ribbon immersed with liquid nitrogen after air-drying and then fractured near 77 K;

4) Ribbon removed from solution; plunged immediately into liquid nitrogen without rinsing; fractured near 44K, rinsed with deionized water and methanol and air dried.

Newman et al. (383) reported that brittle fractographic aspects were observed for the ribbons broken directly in solution and in liquid nitrogen without rinsing after the ribbons were removed from test solution; however, ductile fractographic aspects were observed for ribbons broken in air or in liquid nitrogen after rinsing. Accordingly, these authors interpreted that the occurrence of the crystallographic cracking of brittle appearance as supporting a mechanism of TSCC, in which brittle cracking initiates in the very thin de-alloyed layer and proceeds for some distance into the ductile substrate before being arrested by the increasing plastic crack tip deformation (383).

It was noted that the testing conditions employed in their experiments, such as thin foils at high strain rates in liquid nitrogen are not relevant to those of the normal stress corrosion cracking testing of bulk materials at low strain rates at room temperature or above. However, they intended to separate the effects of stress and

corrosion or adsorption of the environments in the cracking process, so as to facilitate the determination of the applicability of the different SCC models proposed.

The observations reported by Newman et al. stimulated us to repeat their experiments in order to carry out observations at higher magnification and to compare the microfractographic details and the crystallographic aspects obtained with those of typical TSCC fracture surfaces produced in the bulk DCB α-brass specimens. Such a comparison should contribute to our understanding of the mechanism of film-induced-cleavage for f.c.c. ductile materials.

5.2.2 Experiments

In order to obtain the same results as those in the experiments of Newman et al. (383), the test conditions employed in the present study attempted initially to duplicate those described by these authors. Since no details were reported about the preparation of the test solution in reference (383), the solution preparation procedure described by Bertocci (385) was adopted.

5.2.2.1 Material Condition

Half-hard brass foil was employed with a nominal composition of Cu-30Wt% Zn, which was verified by the results of EDS analysis shown in table 5.3 (the

primary data recording).

The α-brass foil was clamped between two copper sheets to prevent zinc evaporation and was annealed at 550°C for one hour in an argon atmosphere and then furnace-cooled. The microstructure after annealing is presented in Fig. 5.17.

5.2.2.2 Preparation of the Specimens

The tests can be divided into two series according to the preparation procedure employed.

For the first series tests, ribbon specimens, 70 x 5 mm in dimensions, were cut from the annealed foil with scissors. These specimens were gently abraded on both sides with a piece of polishing cloth placed over the index finger and with emery powder of 15 μm and then 1 μm diameter, rinsed with water and methanol and then air-dried. The final thickness of ribbon was approximately 20 μm. The width of the central portion of some specimens were reduced to about 3 mm, and some of these specimens were edge-notched with scissors. The geometries of the first series specimens are schematized in Fig. 5.18.

For the second series of tests, the geometry and the width of the ribbon specimens were the same as (b) of Fig. 5.18, but the length of the specimen was

increased to 80 mm so as make it more convenient to fracture the ribbon specimen while holding their ends with tweezers after immersion in the test solution.

An important difference of the preparation process of the ribbon specimens in the second series of tests was that the ribbon specimens were first cut from the foil and their surfaces polished using the same procedure described. The specimens were then superposed, and were then wrapped in the same α-brass foil to prevent zinc evaporation and oxidation of the specimens during the subsequent annealing. The objective of cutting and polishing specimens prior to annealing was to avoid any residual stresses left on the surfaces and on the edges of these ribbons.

5.2.2.3 Composition of the Test Solution

The aqueous test solution used was 1000 ml of 15 M NH_4OH at room temperature, stirred under nitrogen of 1.5 psig in a glass chamber, to which 3.6 gm/l of Cu_2O and 8 gm/l of Cu powder were added to give 0.05 M of cuprous complex $(Cu(NH_3)_2^+)$ ions and to remove traces of cupric ions.

5.2.2.4 Test Procedure

Before testing, the ribbon specimen was fixed on a fine glass tube with teflon then rinsed with doubly de-ionized water, methanol and air-dried.

In the first series tests, after the test solution was stirred for more than 3 hours, the cover of the chamber was removed and 3 or 4 ribbon specimens were introduced into the cell and immersed in the test solution as quickly as possible. The chamber was then re-covered and replaced under 1.5 psig pressure of nitrogen. The test cell was sealed with rubber stoppers and silicon vacuum grease. It was noticed that the almost colourless test solution generally turned a slightly bluish colour, indicating that a very small amount of oxygen was introduced into the solution in placing the specimens into the cell.

Therefore, in order to decrease the amount of oxygen introduced into the solution, in the second series tests, the following procedure was employed:

1) Cuprous oxide and copper powder was placed in the chamber, then the chamber was sealed very well with rubber stoppers and silicon vacuum grease.
2) Nitrogen was introduced in the chamber under 1.5 psig pressure of nitrogen for at least 1 hour, then the 15M NH_4OH aqueous solution was introduced into the test cell through a small inlet in the cover of the chamber.
3) The test solution was stirred under 1.5 psig pressure of nitrogen for 3 hours, followed by verification that a colourless solution has been obtained.
4) One small inlet of the cover was opened and one or two ribbon specimens were rapidly inserted into the cell. The specimens had been fixed at one

end of a fine glass bar with teflon tape.

By means of this improved procedure, it was confirmed that less oxygen was introduced in the test solution, since there was no change in the aspect of the colourless solution during immersion of the specimen. As well, in this second series of the tests, the transfer of the specimens from the almost colourless ammoniacal solution to the rinsing solution was generally done more quickly than in the first series of tests. This procedure can also result in diminution in the amount of oxygen involved before straining and during cracking. Fig. 5.19 shows one example of the test arrangement.

Most of the specimens were immersed in the cuprous ammoniacal solution for 100 minutes, this time being chosen since Newman et al. (383) reported that tests carried out after 10 minutes immersion gave similar results to those after 100 minutes immersion, but that the brittle fractures were not as clear-cut microscopically after 10 minutes immersion. Hence, in the present experiments, specimens were immersed in the test solution for times of 1, 10 or 15 minutes, only for the purposes of comparison.

After immersion, the ribbon specimens were strained to failure by hand (or using tweezers wrapped with teflon), holding the ends with rubber gloves. The

strain rate could not be estimated accurately, most of the specimens were strained quickly, but few were strained smoothly. No distinct difference was observed for the specimens strained quickly and slowly.

A number of control tests were performed. These were divided into two series. The details of the procedures of the first series of tests are listed in table (5.4). As already mentionned, for this series, the specimens were cut and abraded after annealing and less care was taken to prevent oxygen contact with the test solution than in the second series.

Table 5.4: Summary of the procedure employed in the first series of tests

Test number	Test procedures
1	Fractured in air at room temperature without any exposure to the test solution.
2	Fractured near 77K without any exposure to the test solution.
3	Immersed for 100 minutes, strained rapidly to fracture in the test solution.
4	Immersed for 100 minutes, removed from the test solution, immediately fractured in air, then rinsed and dried.
5	Immersed for 100 minutes, removed from the test solution, immediately rinsed with deionized water and methanol, air dried, then fractured in air at room temperature, rinsed and air-dried.
6	Immersed for 100 minutes, removed from the test solution, plunged immediately into liquid nitrogen without rinsing, fractured near 77 K, rinsed with deionized water and methanol, air-dried.
7	The specimen surfaces were polished carefully, after 100 minutes immersion, they were removed from the test solution, rinsed with dionized water, methanol, then air dried. They were not stressed and their surfaces were examined by SEM.
8	After immersion for 100 minutes, the specimen was removed from solution; immediately rinsed with deionized water and methanol and air dried; cleaned ultrasonically in deionized water, then in methanol for 5 minutes; air-dried; strained rapidly and fractured in air.
9	Same procedure as for test 8, but strained slowly.
10	After immersion of 100 minutes; specimen removed from solution; immediately rinsed with deionized water and methanol and air-dried; polished gently on both sides by hand with polishing cloth and emery of 1 μm; rinsed and air-dried again; cleaned ultrasonically for 5 minutes; dried and fractured rapidly in air.

Table 5.4 (cont'd)

Test number	Test procedures
11	Same procedure as for test 4, but employing a specimen with a notch.
12	Same procedure as for test 8, but after ultrasonic rinsing and drying, the specimen was placed in a vacuum of 50 millitorr for approximately 30 minutes, then strained rapidly to fracture.
13	Same procedure as for test 12, but strained very smoothly.
14	Same procedure as for test 12, but rewetted with deionized water before straining to fracture.
15	Same procedure as for test 12, but the specimen was kept in vacuum within the chamber of SEM for 25 hours before straining it rapidly to fracture.
16	After immersion of 100 minutes, the specimen was removed from the test solution; immediately rinsed with deionized water, but not rinsed with methanol, strained but not smoothly to fracture without prior air drying.
17	Same procedure as for test 4, but immersed in the test solution for only 10 minutes.
18	Same procedure as for test 4, but immersed in the test solution for only 1 minute.
19	Same procedure as for test 6, but employing a notch specimen and an immersion time of 15 minutes.
20	The notched specimen was wrapped and attached to a glass rod with teflon tape and immersed in older solution after the first experiment had been finished. Part of the notched region was above the solution, and the surfaces near the interface between the solution and N_2 environment turned dark blue. After immersion for 100 minutes, the cleaning, drying and fracturing procedures followed were the same as those of test 5. The experimental arrangement is shown schematically in Fig. 5.20.

Table 5.5: Summary of the procedure employed in the second series tests

Test number	Test procedures
1	Same procedure as for test 3 in table 5.4. After 100 minutes of immersion in the almost colourless cuprous ammoniacal test solution, the specimen was strained rapidly to fracture in the solution.
2	Same procedure as for test 4 in table 5.4. After 100 minutes of immersion, the specimen was removed from the test solution, immediately fractured in air then rinsed and dried.
3	Same procedure as for test 5 in table 5.4. The specimen was fractured rapidly in air after rinsing and drying.
4	Same procedure as for test 6 in table 5.4. The specimen was fractured rapidly in liquid nitrogen, near 77 K, without rinsing.
5	Same procedure as for test 1 in this table, but fractured rapidly in the test solution after 13 hours of immersion.
6	Same procedure as for test 3 in this table, but with 13 hours of immersion in the solution, then fractured in air after rinsing and drying.
7	The composition of the test solution was changed to 1000 ml of 15 M NH_4OH aqueous with 7.5 gm of Cu_2O and 10 gm of copper powder. After 17 hours of immersion in the colourless test solution, the specimen was fractured rapidly in the solution.
8	The composition of the test solution and the immersion time were the same as for test 7 above, but the specimen was fractured in air after rinsing and drying.

In the second series of tests, tests no. 1 to no. 4 were generally repeated more than three times. Only a single test was carried out for tests no. 5 to no. 8, because of the reproducibility of the results in tests 1 to 4. In contrast the amount of crystallographic fracture zones obtained in the first series of tests varied greatly. For this reason, tests no. 3 to 13 in table 5.4 were repeated at least three times. Furthermore, the differences in immersion time period, in rinsing process and in solution composition were chosen to help distinguish how the brittle behavior is related to the mechanical and environmental effects. This will be discussed in section 5.6.

5.2.3 Fractography and Discussion

Because of the different results obtained for the two series of tests, the fractographic characteristics observed for each series will be described separately.

5.2.3.1 Results of the First Series of Tests

5.2.3.1.1 General Observations of Fractographic Aspects

Fracture surfaces produced by the procedures of test 1 and test 2, i.e. fractured in air at room temperature and fractured near 77 K without any exposure to the test solution, were completely ductile. Fig. 5.21 displays a typical ductile fracture aspect of the ribbon specimen fractured in air.

For the tests performed on the ribbon specimens immersed in the test solution for 10 or 100 minutes before fracturing, the fracture surfaces generally presented some crystallographic fracture zones surrounded by zones of ductile necking, although the amount of crystallographic fracture zones varied greatly between test samples. In contrast to the results described by Newman et al. (383), rinsing with deionized water and methanol did not permit to suppress the occurrence of crystallographic fracture in the present tests, as shown in Fig. 5.22.

The percentage of crystallographic fracture zones varied very much from one sample to the other even when they were immersed simultaneously in the same test cell. For example, on certain specimens immersed in the test solution for 100 minutes and fractured in air after rinsing with deionized water and then methanol, some fracture surfaces presented approximately 50% of crystallographic zones, while others present only approximately 5% of such zones.

However, the percentage of crystallographic fracture zones appeared to be related to the rinsing conditions and to the immersion time period. As concerns the effect of the different rinsing procedures on the amount of crystallographic fracture zones after 100 minutes immersion, in general, a relatively large percentage (such as 50% or more) of typical crystallographic fracture regions were obtained on specimens rinsed with deionized water, methanol and air-dried. Almost no

difference in the amount of the crystallographic zones was found between these specimens rinsed then fractured in air and those which were fractured directly in solution. However, if the specimens were rinsed ultrasonically and particularly if vacuum evaporation was employed after rinsing generally only a few small regions of crystallographic fracture were present separated by ductile fracture regions (Fig. 5.23). It was also noticed that if the surfaces of the specimen were polished (test 10 in table 5.4) before fracturing, almost no clearly crystallographic fracture zones were observed, suggesting that the polishing procedure destroyed the crack initiation sites, which were either corrosion slots and etchpits or the de-alloyed layer, resulting in a completely ductile fracture aspect. As well, more crystallographic fracture zones were observed on the ribbon samples immersed for 100 minutes than for 1 or 10 minutes.

5.2.3.1.2 Crystallography Near the Initial Cracking Site

Crystallographic etch pits produced during the tests were at times observed on the external surfaces of the immersed specimens as well as on some fracture surfaces. Their presence facilitated the identification of the crystallography of cracking. The side faces of the etch pits consisted of {111} faces since their plane projection often appeared in the shape of equilateral triangles.

The initial cracking was generally quite flat and planar along a typical depth of 5-10 μm and followed {111} planes with the propagation direction along <110> (Figs. 5.24 to 5.26), which gave rise to {111} <110> cracking crystallography. Examination of the stereo microfractographs (Fig. 5.25) indicated that these relatively large {111} facets were generally perpendicular to the tensile axis, which suggests that they were produced by a cleavage mechanism. That no actual cracks were observed on the surfaces of non-fractured ribbon specimens after 100 minutes of immersion (Fig. 5.28), indicates that at least some mecanical effects were involved in the fracture process which produced the relatively large flat cleavage-like {111} facets.

The cracking observed either initiated along crystallographic {111} erosion slots (Fig. 5.24, 5.26) or at lines of etch pits (Fig. 5.27). Similar etch pits and corrosion slots were observed on samples immersed in the test solution but not fractured, as shown in Fig. 5.28. In the case of cracking initiated at the lines of etch pits (Fig. 5.27), the initial cracking involved two sets of narrow {111} microfacets, which met parallel to a <110> crack propagation direction, which resulted in an average primary facet with a {110} or near-{110} orientation giving rise to the {110} <110> cracking crystallography. This cracking crystallography is similar to that identified in TSCC for the bulk DCB specimens observed at high and intermediate K values (see Fig. 5.10a).

5.2.3.1.3 Crystallography of Subsequent Crack Propagation

With subsequent crack propagation, the fracture surfaces then became more complex and generally the crack followed in an alternating manner two or more sets of {111} microfacets to produce an average {110} primary facet orientation (Figs. 5.24 to 5.27), or an average {100} primary facet orientation (Fig. 5.29). The frequent {110} orientations of the primary facets as well as their aspect (Fig. 5.26) are very similar to those produced in TSCC of this material. From this figure, it can be seen that not only the alternating {111} microfacets but also the relatively large {111} facets near the initiation sites match very well, which again offers an important evidence to indicate that the large {111} facets were fractured by a cleavage mechanism.

That the microfacets decreased in size as the crack grew can be seen clearly in Figs. 5.26, 5.27 and 5.30, probably indicating that decreasing in the environmental effect as crack propagation would give rise to less localized plasticity at the crack tip and less amount of decohesion along slip planes.

That the crystallographic cracking at times arrested before arriving at the other external surface, as shown in Fig. 5.24 and Fig. 5.30, indicates that the plasticity increased continuously as the crack propagated and finally resulted in crack arrest. This observation is consistent with the proposed mechanism (202, 383,

386) of arrest of the brittle cracking in the ductile metal by the increasing amount of plasticity.

In general, the present observations of plasticity playing an important role in crystallographic crack growth in the ribbon specimens is clearer than in bulk DCB specimens. While the number of primary facets with average {100} orientations observed remain less than those of {110} orientations, the {100} facets are more frequently observed than for TSCC on bulk specimens. Furthermore, on the ribbon specimens, it is also very evident that the non-{111} primary facets consist of two sets of alternating {111} microfacets which give rise to a {110} <100> or a {100} <110> cracking crystallography and to <110> crystallographic striations. These aspects strongly indicate that the crack propagation involved very localized plastic deformation or that the plastic deformation accompanied cracking resulted in a change of the {111} crack plane on a microscopic scale. The matching aspects of these {111} microfacets were also verified from the observations carried out on the corresponding regions of the opposite fracture surfaces. That the cracking initiated on a large {111} facet approximately perpendicular to the tensile axis then propagated in an alternating manner on two or more series of {111} microfacets indicates that this plasticity increased continuously as the crack propagated in the ductile metal, and finally resulted in crack arrest. Such a picture also indicates that if the two stages of the

crystallographic cracking are to be considered as a real cleavage fracture process, this cleavage must occur following {111} planes on which some localized slip has been produced, at least in the second stage of cracking.

5.2.3.1.4 Occurrence of the Etch Pits

Etch pits were observed even on fracture surfaces of samples rinsed prior to fracture, which indicates that the rinsing in the present tests did not remove all the solution from the corrosion slots and pits or from the de-alloyed layer. Part of the control tests from the number 7 to 16 in the table 5.4 were carried out to better verify this aspect.

Only a very few, small etch pits were found on the fracture surfaces for samples ultrasonically rinsed. For samples dried under vacuum for more than 30 minutes, no etch pits were observed on the small brittle-like crystallographic fracture zones located near ductile fracture surfaces (see Fig. 5.23). In this case, primary facets of average {110} or {100} orientation were not observed and these brittle-appearing zones may have been corrosion slots. This aspect, therefore, indicates that the occurrence of the average {110} <100> and {100} <110> crack propagation crystallography on the ribbon specimens should involve some effects of the environment.

To identify whether the etch pits occurred during or after cracking process, these were examined on mating fracture surfaces. Indication is that the etch pits on the opposite surfaces are never exactly at the same sites on the two surfaces although some are near the same sites. These observations demonstrate that the etch pits on the fracture surfaces were produced after cracking (Fig. 5.26). This evidence furthermore demonstrated that traces of the test solution were not completely removed from the corrosion slots and that pits occurred after fracture even if the ribbon specimens were rinsed and air-dried. A similar effect of solution not being removed from the dealloyed sponge can also explain the results of Cassagne et al. (386) on Cu_3Au, where a crystallographic crack continued into the ductile substrate.

Consequently, the occurrence of the crystallographic crack propagation for the rinsed and air dried ribbon specimens in the present tests probably resulted from the combination of the traces of ammoniacal solution left within the corrosion slots, the etch pits or others defects on the external surfaces of the ribbon specimens and the final strain supplied. Since the strain rate employed for the ribbon specimens generally was high, the crack propagation should be sufficiently rapid that a chemical dissolution reaction should not be able to control the crack growth process, however, an adsorption phenomenon cannot be ruled out.

5.2.3.2 Results of the Second Series of Tests

In the first series of tests, the testing conditions resulted in some confusion in the identification of the role of the de-alloyed layer in initiating brittle cracking. Corrosion slots and etch pits occurred on both the external surfaces and the fracture surfaces of the ribbon specimens, which indicated the presence of some cupric complex ions in solution permitted the dissolution of copper in the α-brass and also possibly did not allow the presence of complete dezincified layer before fracture. As well, residual stresses may have been introduced by polishing and cutting the ribbons after annealing. In order to verify whether the formation of corrosion etch pits and slots or of the de-alloyed layer was responsible for initiating brittle crystallographic fracture, a second series of tests was performed, in which greater precautions were taken to minimize the presence of oxygen in the test solution, and therefore to minimize the dissolution of copper hence avoiding the formation of etch pits.

Unexpected results were obtained in the second series tests, in that, all fracture surfaces of 8 groups of different test procedures listed in table 5.5, presented completely ductile aspects, i.e., not a single microscopic, brittle fracture zone was found. Careful examination showed the rare presence of a few very small pits distributed on the surfaces of the ribbon samples, but no crystallographic corrosion slots were observed, even on the specimens immersed in the solution for

13 or 17 hours. The fully ductile fracture in this series appeared not to be affected by the rinsing conditions, however, as mentioned, in this second series, the transfer of the specimens from the ammoniacal solution to the rinsing solution was always done very quickly, generally more quickly than in the first series of tests.

The present results obtained in the second series tests are in agreement with those of Kaufman and Fink (161), who only obtained ductile fracture on 70 Cu-30 Zn α-brass specimens at very low strain rate when the tensile tests were performed taking great precautions to avoid the presence of cupric ions or oxygen in their ammoniacal solution. These authors (161) concluded that their experimental results raised serious questions concerning the theory of the role of dezincified layer on TSCC in f.c.c. ductile α-brass of the order of 70 Cu-30 Zn compositions. Recently, Cassagne (387) argued that the conflicting results obtained previously by Kaufman and Fink and by other authors (202, 385) possibly resulted from the different concentration of copper dissolved in the solutions (387). Kaufman and Fink used a solution with 0.13 M concentration of copper instead of 0.05 M solution employed by Bertocci et al. (385). However, in the present study, the solution with 0.05 M concentration of copper was employed, and completely ductile fracture surfaces were always obtained, when sufficient precautions were taken to minimize the presence of oxygen in the solution.

5.2.3.3 Intergranular Fracture on Ribbon Specimens

In section 5.1.3.2.1, it was suggested that the greater intergranular cracking which occurred at the initiation sites of TSCC and near the edges of bulk DCB specimens was possibly associated with more oxygen or more cupric complex ions being present in the ammoniacal solution in contact with these sites. To verify this suggestion, the procedure of test no. 20 described in table 5.4 was carried out.

Firstly, during immersion, it was seen that the colour of the surfaces of the ribbon specimens immersed near the interface between the solution and the N_2 environment turned dark blue, perhaps indicating that an oxidation film had formed on the surfaces. Secondly, after 100 minutes of immersion, the sample was removed from the solution, immediately rinsed and air-dried, then fractured in air. It was noted that it was particularly easy to fracture the upper portion of such ribbon specimens. Some of these were extremely brittle and broke into several small fragments. In these cases, the fracture was intergranular, as shown in Fig. 5.31. The fractography resembled that of ISCC on the bulk DCB specimens (Fig. 5.6). This sort of tests were repeated four times, and the same results were obtained on all four specimens.

Although no quantitative measurements of amount of oxygen in the solution were carried out, the amount of oxygen present in the upper portion of the solution

should be greater than in the lower portion. A detailed metallographic examination was performed on the surfaces of an un-stressed ribbon specimen immersed in the same solution as employed in the first series tests. It was observed that more corrosion pits or slots occurred at the grain boundaries for the upper portion of the ribbon, while more etch pits were distributed within grains in the lower portion of the same ribbon. Typical examples are shown in Figs. 5.32 a and b, respectively. The reason for the occurrence of this difference in cracking characteristics has not been investigated further in the present study. However, such observations may be a reflection of the fact that intergranular cracking occurred when more oxygen was present in the ammoniacal solution. Pugh et al. (388) also found that when un-stressed 70 Cu-30 Zn brass specimens were immersed for 72 hours in 15 M aqueous ammonia preconcentrated with 8 g/l copper, the ribbon specimens became very brittle. Handling of such specimens in the absence of the environment caused them to break into many small fragments also as a result of intergranular fracture. These authors proposed that this behaviour was the result of penetration of the grain boundaries by the tarnish (389).

5.2.3.4 Summary of the Results

The major results and conclusions obtained from the study of the ribbon specimens fractured after immersion in ammoniacal solution are as follows:

1) Crystallographic cracking in the superficially de-alloyed Cu-30 Zn ribbons were not obtained without the occurrence of dissolution of copper.

2) Crystallographic cracking usually initiated from corrosion slots or lines of etch pits present on the ribbon surfaces in the first series of tests where the precaution to minimize the presence of oxygen was not as stringent as for the second series of tests.

3) More crystallographic cracking zones were observed on fracture surfaces for those ribbons fractured either in the test solution or after rinsing with de-ionized water and methanol then air-drying. But the percentage of crystallographic cracking zones varied greatly within batches of specimens for nominally identical testing conditions; however, the time between removing the specimens from solution and producing fracture varied. Much fewer crystallographic cracking zones were observed for the ribbons rinsed with ultrasonic vibration cleaning and then dried employing vacuum evaporation prior to fracture, indicating the presence of traces of the solution could be important for the occurrence of the crystallographic crack propagation.

4) The crack propagation for the ribbon specimens generally was sufficently rapid, which indicates that a chemical dissolution reaction should not be able to control entirely the crack growth process.

5) Fractographic aspects of crystallographic cracking on the ribbons are strongly similar to that observed for TSCC at intermediate and high K values on bulk

specimens of α-brass as well as of 316 stainless steel, demonstrating that the mechanical stress must be play an important role in the fracture process of the ribbons.

6) The cracking initiated on the relatively large {111} facets approximately perpendicular to the tensile axis, suggesting that these large {111} facets were possibly produced by a cleavage mechanism. That then the crack propagation by alternating between two or more sets of {111} microfacets, indicating that the plasticity increased continuously as the crack propagated in the ductile metal, and finally resulted in crack arresting. The matching aspects of these {111} microfacets and the fractographic details, again indicate that cracking on {111} planes is not simply produced by slip process but may possibly involve cleavage fracture following slip planes in which some localized slip has been produced.



Fig. 5.1: Microstructure of α-brass employed.

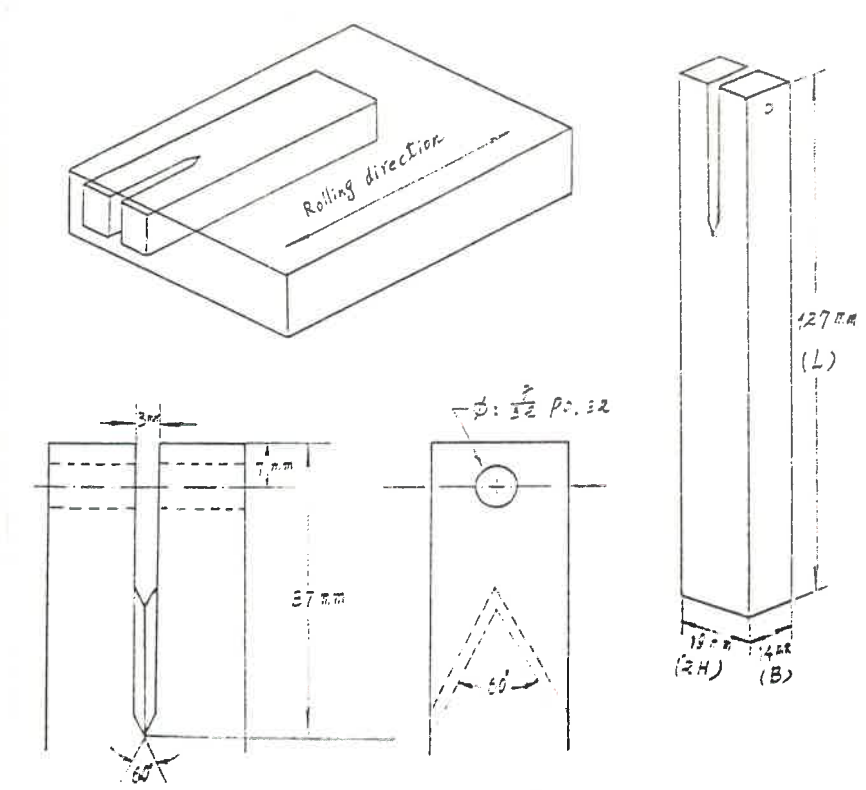


Fig. 5.2: Dimensions and geometry of DCB specimen.

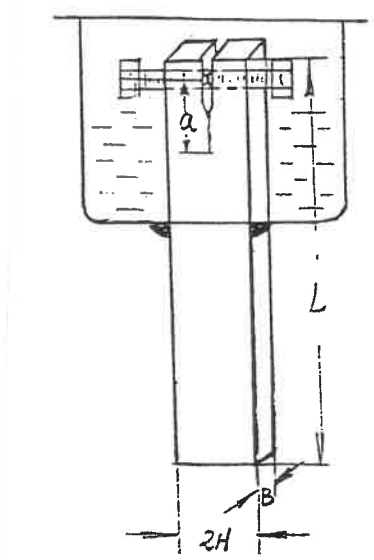


Fig. 5.3

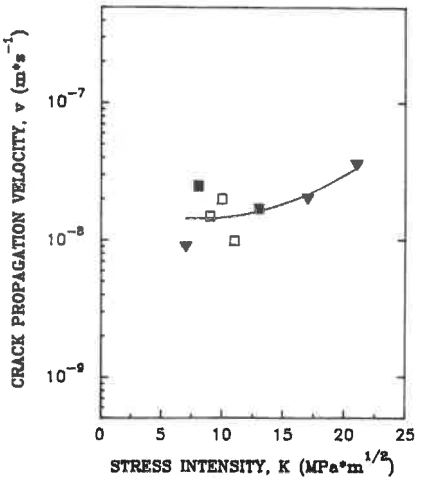


Fig. 5.4

Fig. 5.3: Schematic of test cell.

Fig. 5.4: The plot of log V vs K for tests performed in the non-tarnishing solution on three specimens.

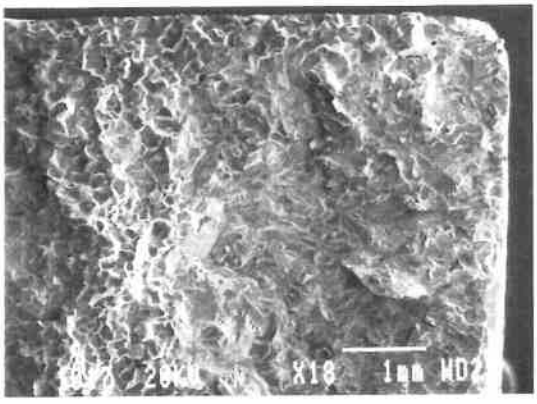


Fig. 5.5: Aspect of SCC of α-brass viewed at low magnification

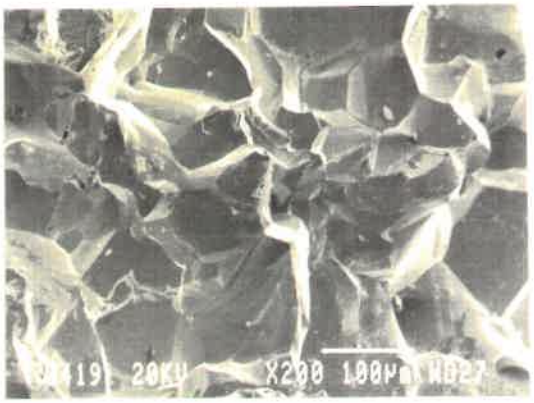




Fig. 5.6 **Fig. 5.7**

Fig. 5.6: Typical intergranular facets observed for α-brass tested in the non-tarnishing ammoniacal solution.

Fig. 5.7: Slip traces observed on some of intergranular facets for α-brass tested in the non-tarnishing ammoniacal solution.

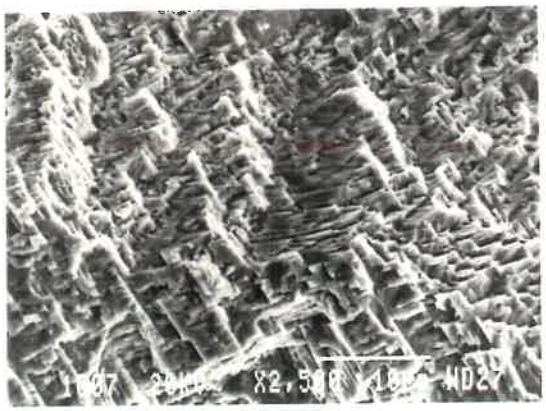


Fig. 5.8: Complicated fractographic aspect observed in higher K region (~ 20 MPa $m^{1/2}$)

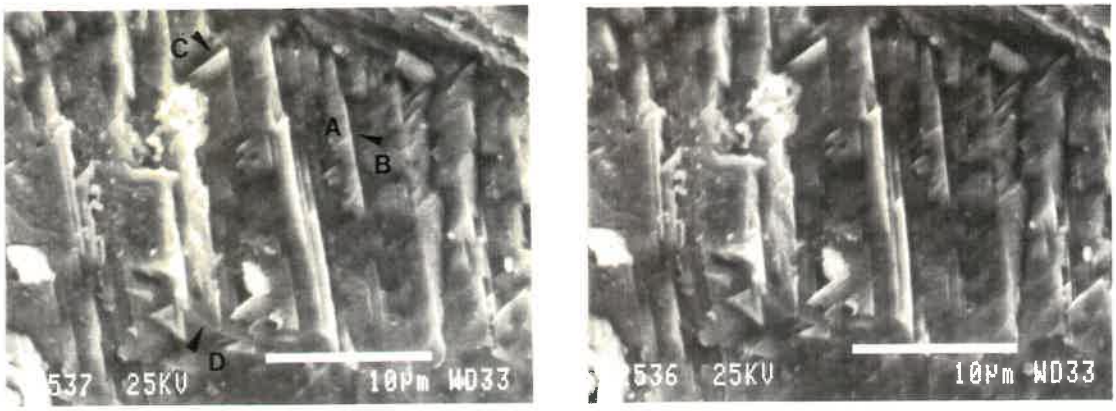
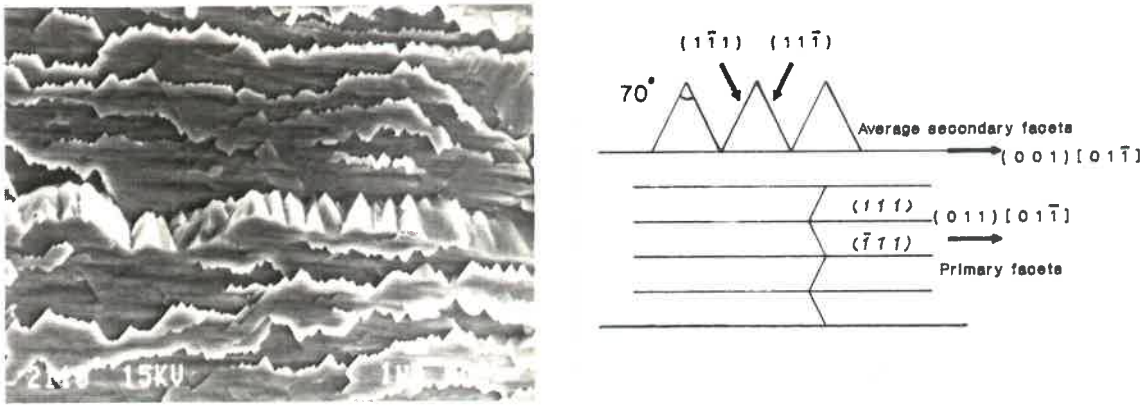


Fig. 5.9: Stereo pairs shows complex aspect with presence of four sets of {111} microfacets observed on TSCC of α-brass (K ≈ 20 MPa $m^{1/2}$).



(a) (b)

Fig. 5.10: (a) {110} <110> crystallography of the primary facets and of the {100} <110> average secondary facets identified on the TSCC fracture surface produced at K ~ 20 MPa $m^{1/2}$.
(b) Schematic of the cracking crystallography observed in (a).

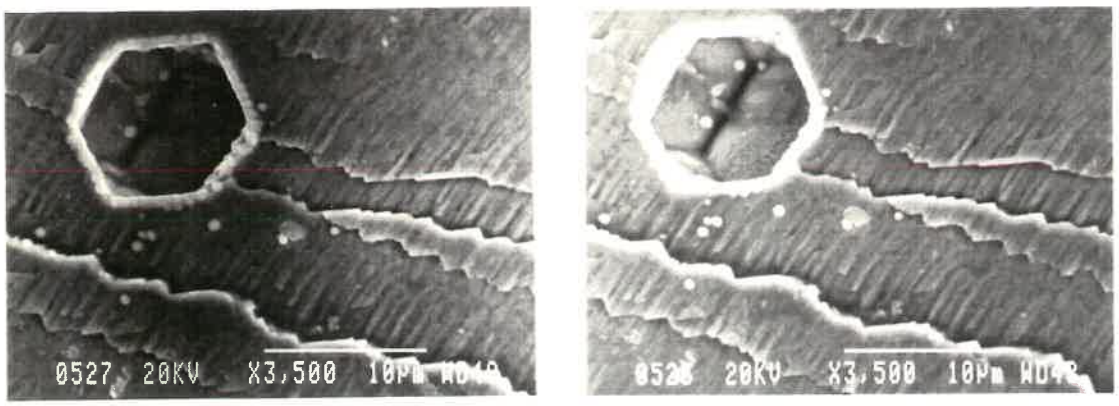


Fig. 5.12: Stereo pairs shows {110} <100> cracking crystallography identified on TSCC facets produced in the region corresponding K ≈ 15 MPa $m^{1/2}$.

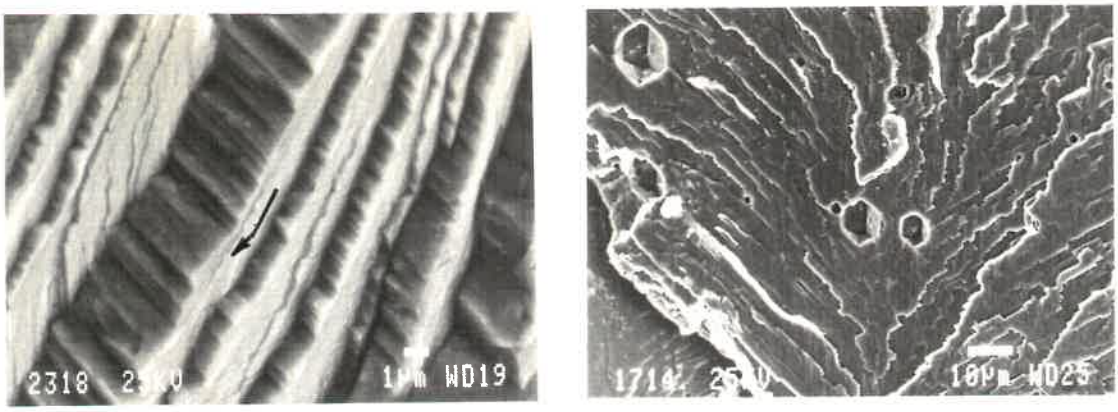
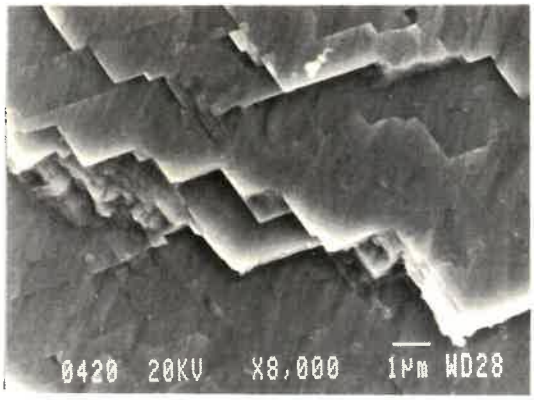


Fig. 5.11 **Fig. 5.16**

Fig. 5.11: The presence of numerous river lines with relatively important step heights observed on TSCC fracture surface produced at relatively high K values.

Fig. 5.16: Fan-shaped {110} primary facets with two <112> orientations of river lines and an average <110> orientation of serrated river lines observed at relatively low K values.



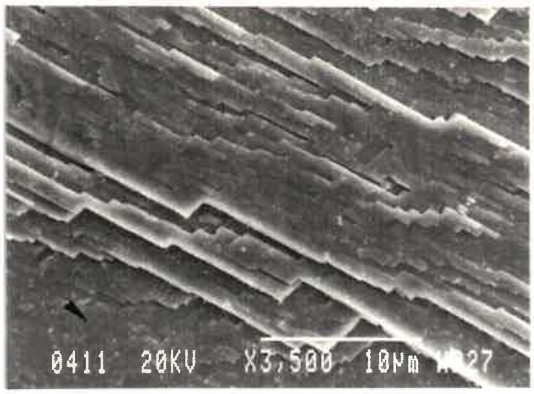


Fig. 5.13 **Fig. 5.14**

Fig. 5.13: Small size {111} microfacets observed in the low K region (K ≥ 10 MPa $m^{1/2}$).

Fig. 5.14: Relatively flat facets observed at low K. Some very fine striation-like markings can be seen in the region as indicated by the arrow.

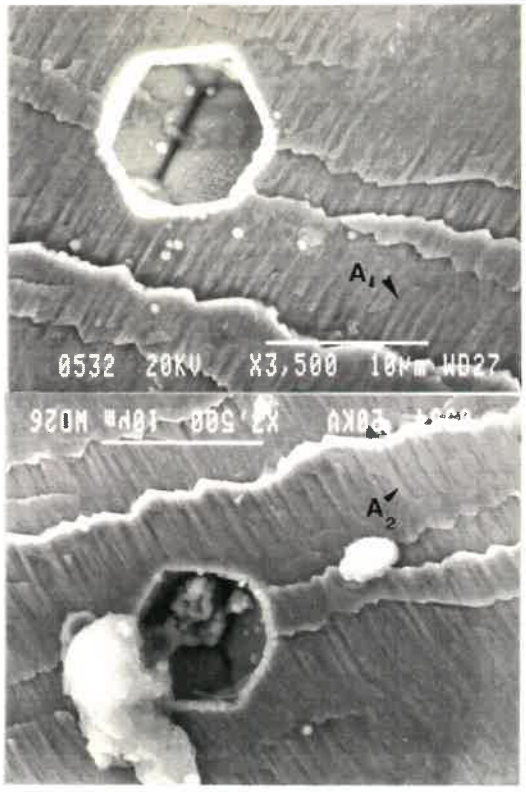


Fig. 5.15: The {111} microfacets can be seen to match in an interlocking manner. For example the facet indicated A_1 matches to that indicated A_2 on the mating fracture surfaces.

Table 5.3: The primary data recording of EDS analysis of the α-brass ribbon specimens

LIVETIME (spec.) = 60

ENERGY	RES	AREA
- 12.4	58.57	39328

TOTAL AREA = 38315

Peak at .92 keV omitted?
FIT INDEX = .43

ELMT	APP.CONC	ERROR(WT%)
Cuk : 0	89.626	1.772
ZnK : 0	38.537	1.562
FeK : 0	-.033	.328* < 2 Sigma*
NiK : 0	-.064	.386* < 2 Sigma*
CrK : 0	-.023	.234* < 2 Sigma*
SiK : 0	.099	.086* < 2 Sigma*
MnK : 0	.182	.265* < 2 Sigma*
S K : 0	.476	.559* < 2 Sigma*
P K : 0	.053	.166* < 2 Sigma*
MoL : 0	-.860	1.278* < 2 Sigma*

..[2 ZAF'S]

20.00 kV TILT = .00 ELEV = 40.00 AZIM = .00 COSINE = 1.000

Spectrum:

All elmts analysed, NORMALIZED

ELMT	ZAF	%ELMT	ATOM.%
CuK : 0	.997	69.412	69.490
ZnK : 0	.999	29.768	28.967
FeK : 0	1.258	.000	.000
NiK : 0	1.181	.000	.000
CrK : 0	1.100	.000	.000
SiK : 0	.515	.149	.337
MnK : 0	1.147	.122	.142
S K : 0	.761	.483	.959
P K : 0	.812	.051	.104
MoL : 0	.660	.000	.000
TOTAL		99.985	100.000

Table 5.3 (Cont'd)

LIVETIME (spec.) = 60

ENERGY	RES	AREA
- 12.4	57.68	39217

TOTAL AREA = 36869

Peak at .92 keV omitted?
FIT INDEX = .28

ELMT	APP.CONC	ERROR(WT%)
Cuk : 0	88.305	1.751
ZnK : 0	36.644	1.535
FeK : 0	.013	.312* < 2 Sigma*
NiK : 0	.041	.388* < 2 Sigma*
CrK : 0	.004	.222* < 2 Sigma*
SiK : 0	.055	.088* < 2 Sigma*
MnK : 0	-.145	.253* < 2 Sigma*
S K : 0	.188	.544* < 2 Sigma*
P K : 0	.058	.167* < 2 Sigma*
MoL : 0	-.499	1.243* < 2 Sigma*

..[2 ZAF'S]

20.00 kV TILT = .00 ELEV = 40.00 AZIM = .00 COSINE = 1.000

Spectrum:

All elmts analysed, NORMALIZED

ELMT	ZAF	%ELMT	ATOM.%
CuK : 0	.999	70.488	70.839
ZnK : 0	1.001	29.207	28.531
FeK : 0	1.262	.008	.009
NiK : 0	1.180	.028	.030
CrK : 0	1.102	.003	.003
SiK : 0	.514	.086	.195
MnK : 0	1.150	.000	.000
S K : 0	.761	.197	.393
P K : 0	.811	.000	.000
MoL : 0	.660	.000	.000
TOTAL		100.016	100.000

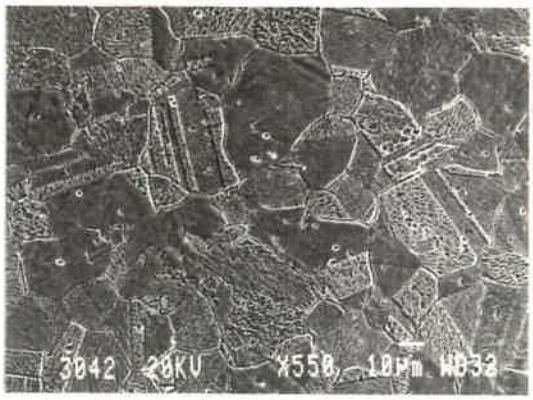


Fig. 5.17

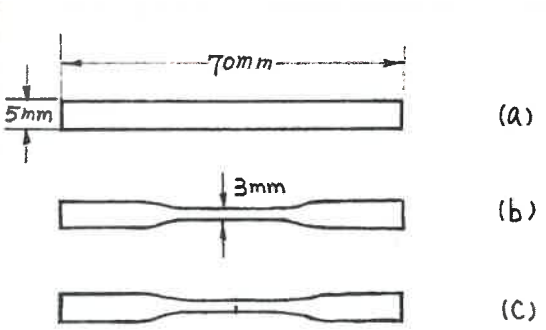


Fig. 5.18

Fig. 5.17: Microstructure of α-brass foil after annealing (etching conditions: 30 ml of HCl + 10 gm of $FeCl_3$ + 120 ml of methanol, at 24°C for 1 minute)

Fig. 5.18: Schematic of the geometries of ribbon specimens employed for the first series of tests. Only the geometry shown in (b) was employed for the second series of tests.

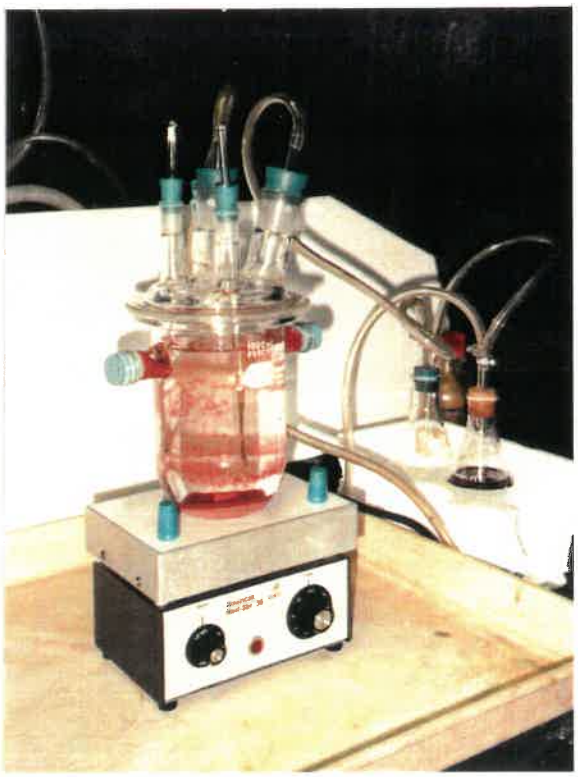


Fig. 5.19: Test arrangement

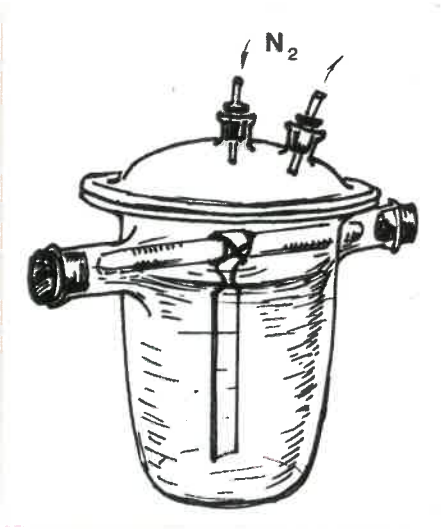


Fig. 5.20: Schematic of the experimental arrangement for test 20 in table 5.4

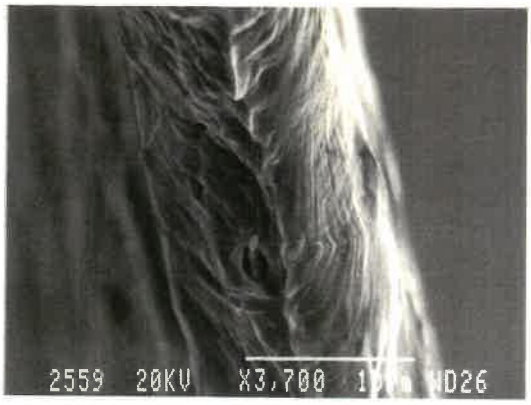


Fig. 5.21

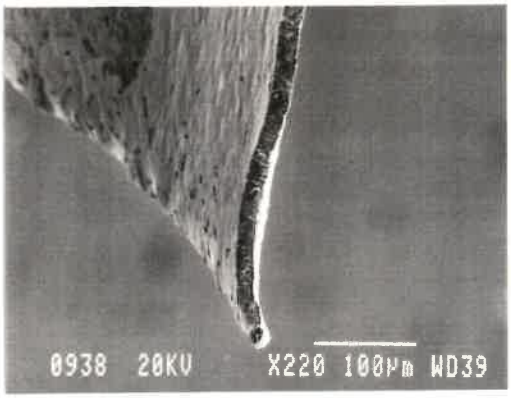


Fig. 5.22

Fig. 5.21: Fracture surface produced in air without any exposure to the test solution.

Fig. 5.22: General aspect of crystallographic fracture surfaces fractured in air after 100 minutes of immersion then rinsing with deionized water and methanol and air-drying.

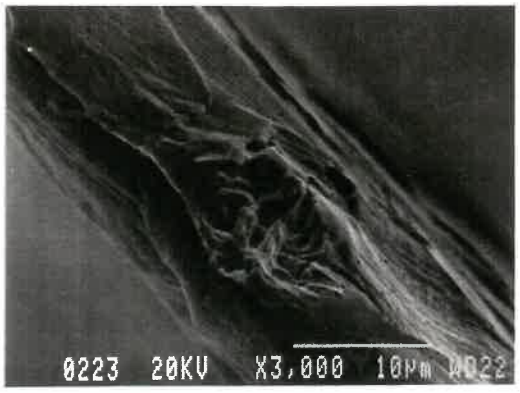


Fig. 5.23

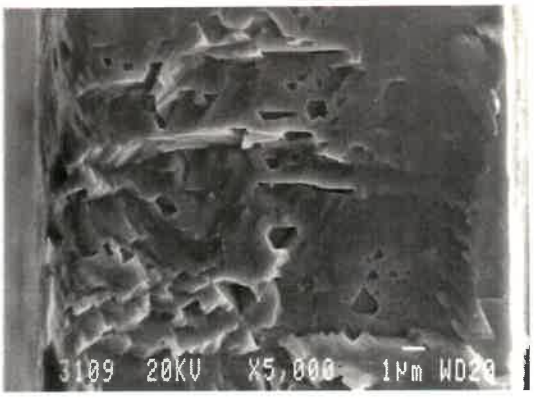


Fig. 5.24

Fig. 5.23: A small crystallographic region present near ductile fracture surface produced after 100 minutes of immersion, rinsed, dried and then kept 25 hours in the vacuum chamber of the SEM.

Fig. 5.24: Crystallographic cracking initiated following the relatively large {111} facets with subsequent propagation on two or more sets of alternating {111} microfacets observed on rinsed specimens (100 minutes of immersion).

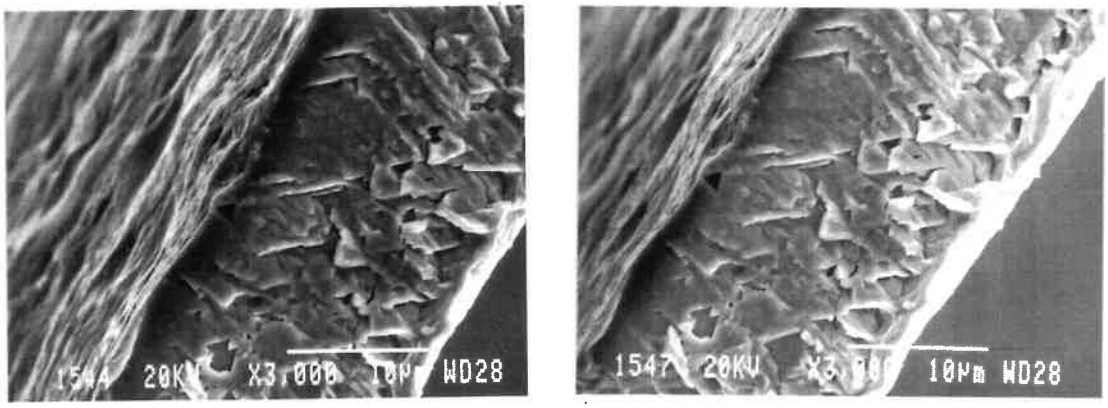


Fig. 5.25: Stereomicrofractographs show that crystallographic cracking initiated following the relatively large flat {111} facets which are almost perpendicular to the tensile axis (fractured in air after 100 minutes of immersion).

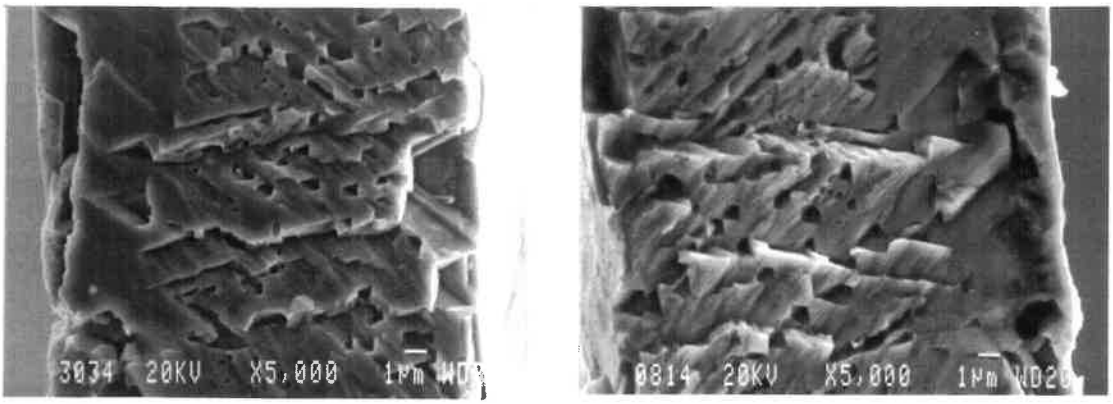


Fig. 5.26: Matching fracture surfaces for crystallographic cracking observed after fracture of a ribbon specimen, rinsed and dried after immersion and then fractured. Initiation occurred along a dissolution slot; cracking then followed large {111} facets and then two alternating sets of {111} microfacets.

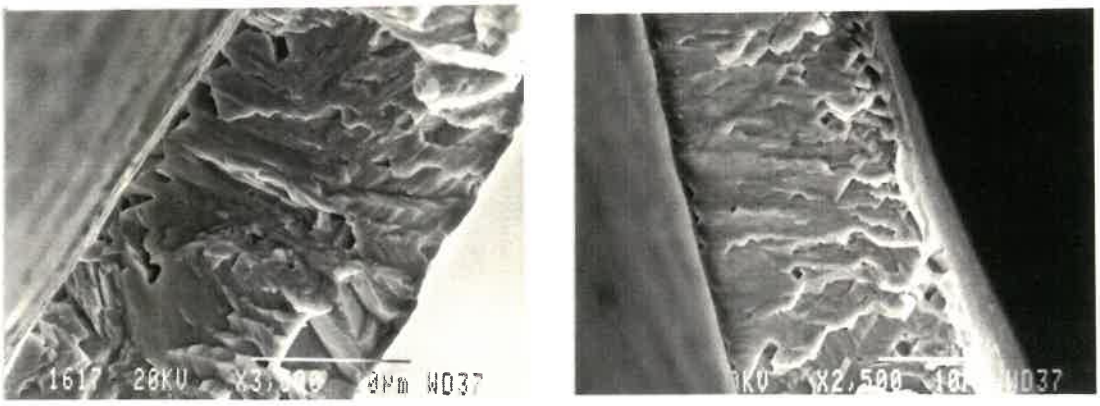


Fig. 5.27: Crystallographic cracking initiated at lines of the etch pits and propagated on two or more sets of {111} facets decohesion observed on the specimens rinsed after 100 minutes of immersion and then fractured in air.

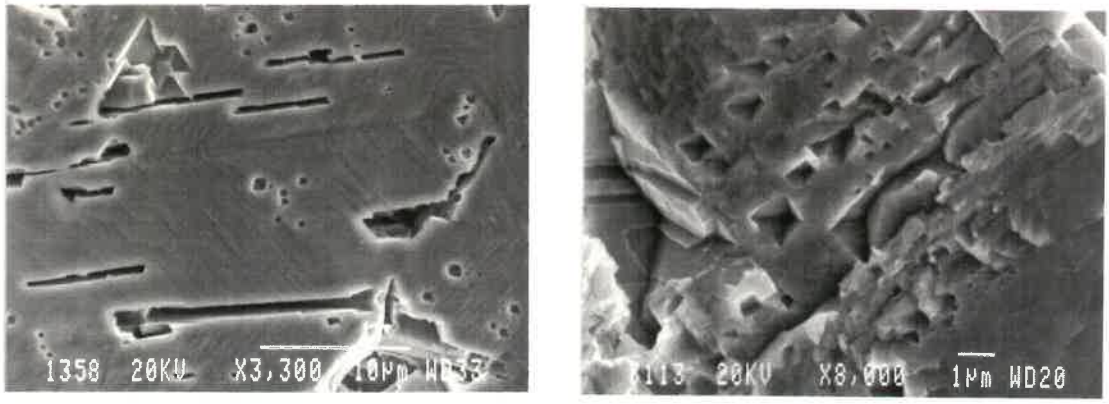
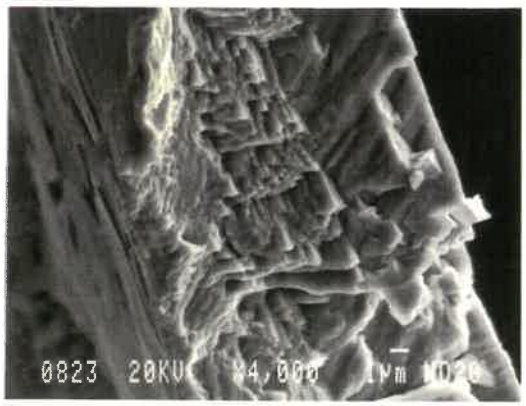


Fig. 5.28 **Fig. 5.29**

Fig. 5.28: Dissolution slots and etch pits on ribbon surface not fractured after 100 minutes of immersion.

Fig. 5.29: Crystallographic cracking observed after fracture of a ribbon, rinsed and dried after immersion and then fractured. Average primary facets with {100} <110> cracking crystallography resulted from two alternating sets of {111} microfacets.



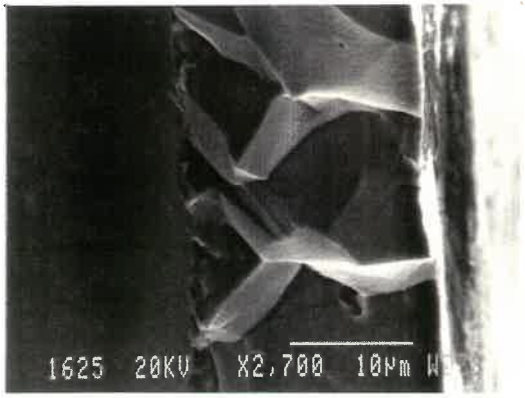
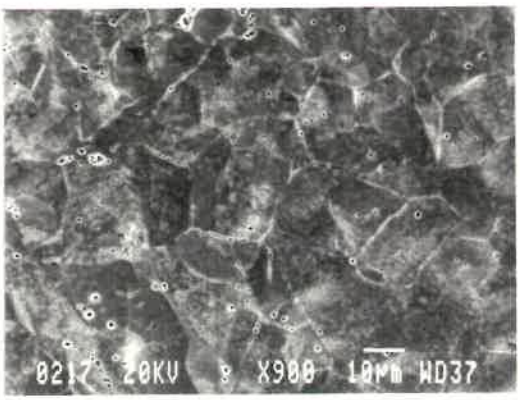
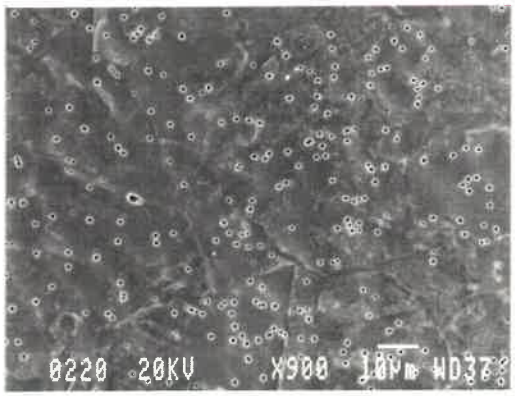


Fig. 5.30 **Fig. 5.31**

Fig. 5.30: Crystallographic cracking on a ribbon ultrasonically rinsed before fracture, with presence of dissolution slots near initiation site, and with increasing plasticity accompanying the crack propagation.

Fig. 5.31: Intergranular cracking occurred on the upper portion of the ribbon specimen immersed in the solution (first series of tests) for 100 minutes.





(a) (b)

Fig. 5.32: Metallographic observations of the (a) upper part, and (b) lower part of the surfaces on the same ribbon specimen immersed for 100 minutes in the solution of the first series of tests.

CHAPTER 6

FRACTOGRAPHY OF CORROSION-FATIGUE CRACK PROPAGATION OF 8-14%Mn-8%Al-2%Ni BRONZES

6.1 INTRODUCTION

The corrosion fatigue behaviour of ship propeller bronzes in salt water is of practical interest, since propellers are subjected to cyclic stresses at frequencies for which corrosion-fatigue effects can be expected. The corrosion-fatigue propagation behaviour in air and in aqueous 3.5% NaCl solution of 12-14% Mn-8% Al-2% Ni bronzes, Cu alloy C95700, ASTM B-148, has previously been reported (334,390). Accelerated propagation was observed at higher crack growth rates in the NaCl solution at a cycling frequency of 1 Hz and was associated with facilitated propagation across or along α - β interfaces. A subsequent study (391,392) showed that beneficial influence on the fracture toughness of Mn compositions lower than those of C95700 alloys specifications. As well, a beneficial effect of annealing at 720°C was also noted on the fracture toughness/tensile strength ratio of the C95700 compositions.

As part of the thesis work, the present author participated in a study which has as the primary objective of the evaluation and comparison of the fatigue and

corrosion-fatigue crack propagation behaviour of Mn-Al-Ni bronzes, namely bronzes nominally containing 8 and 10% Mn in three different material conditions, bronzes containing 12 and 14% Mn in a HT2 heat-treatment condition (see section 6.2), and at 13.5% Mn-Al-Ni bronze from the blade portion of a large propeller which had fractured in service (393). A second objective was to identify the influence of microstructure on the fatigue crack propagation of these different materials in each of the test environments.

A detailed report of this study has been published (394). The contribution of the present author to this study concerned the detailed examination of the fracture surfaces in order to identify any evidence related to the corrosion-fatigue mechanisms. The objective of this chapter, therefore, is to describe some fractographic features which can illustrate effects by which corrosion or testing in an aggressive environment influences crack propagation, so as to facilitate better understanding of the active corrosion-fatigue mechanisms.

6.2 EXPERIMENTAL PROCEDURES

The experimental procedures employed were essentially identical to those described previously (334,390). Plates 295 mm x 148 mm x 25 mm were cast at the Metals Technology Laboratories, CANMET. Two compact tension specimens of

thickness B = 22.3 mm and width W = 101 mm were machined from a plate. Material in the laboratory as - cast condition will be referred to as AC material. To obtain a microstructure more typical of a large casting, the AC plates were first annealed two hours at 900°C followed by cooling at 10°C per hour to 230°C. Material in this slowly-cooled (NSC) condition subsequently annealed for two hours at 690°C and then water quenched will be referred to as in the HTI condition. NSC material annealed for 24 hours at 720°C and air cooled will be referred to as in the HT2 condition. The microstructure of the 8-10% Mn-Al-Ni bronzes has been reported elsewhere (391,392) and consists principally of f.c.c. α grains, with small ligaments of b.c.c. β phase at some of the α grain boundaries. In addition, fatigue propagation tests were performed on specimens taken from the blade of a large 13.5% Mn bronze ship propeller, referred to as propeller #2 by Couture and others (393).

The test performed on each specimen can be identified from Table 6.1. The chemical analysis of each lot employed is given in Table 6.2. The fatigue tests were carried out at room temperature, employing a sinusoidal waveform, a cycling frequency of 20 or 1 Hz and an R-ratio (K_{min}/K_{max}) usually of 0.1. The tests in well-aerated 3.5% NaCl solution were performed under freely-corroding conditions in a plexiglass cell attached to the specimen.

The fracture surfaces tested in the NaCl solution were ultra-sonically cleaned in a 0.3% solution of Micron commercial cleaner and then in a solution of a few drops of Teepol 610 wetting agent in methanol, prior to observations by scanning electron microscopy (SEM). Metallographic observations of fracture surface profiles near the specimen mid-thickness were also carried out.

6.3 RESULTS AND DISCUSSION

6.3.1 Fatigue Propagation

All of the fatigue and corrosion-fatigue tests on the bronzes were performed by Dr. L. Handfield, who also analyzed the data to obtain the crack propagation curves. The typical log-log curves of crack propagation rate da/dN as a function of ΔK, the range of stress intensity factor, or as a function of ΔK_{eff}, the effective range, (which is often lower than ΔK as a result of crack closure reducing the stress or strain amplitude at the crack tip) are presented in Figs. 6.1 and 6.2. The values of ΔK_{eff}= Kmax-K_{op}, where K_{op} corresponds to the stress intensity value at which the crack tip starts to open, were obtained by regression analysis of the load and crack mouth opening displacement data points for the hysteresis loops recorded.

For the 8 and 10% Mn-AC bronze, slightly accelerated corrosion fatigue propagation was noted on a log da/dN - log ΔK basis for the tests at 1 Hz in the

NaCl solution for da/dN values above approximately 2 x 10^{-5} mm/cycle, as shown in Fig. 6.1. No corrosion-fatigue effect was noted for a cycling frequency of 20 Hz. At low da/dN, the crack propagation curves in NaCl solution generally were to the slower crack growth side compared to those in air, as a result of the important corrosion product induced crack closure effect in the NaCl solution. Comparison of the curves of log da/dN as a function of log ΔK_{eff} (Fig 6.2) generally indicated some accelerated cracking at 1 Hz in the NaCl solution for da/dN values in the range of 10^{-5} to 10^{-4} mm/cycle. This effect was not evident in comparing results on a ΔK basis, where it was masked by the important corrosion product crack closure effect obtained for da/dN values up to approximately 10^{-4} mm/cycle for tests in the NaCl solution.

Comparison of the curves of log da/dN as a function of log ΔK, or of log ΔK_{eff}, for the test in air and at 1Hz in the NaCl solution for the 8 and 10% Mn HT1 and HT2 alloys (Figs. 6.3, 6.4 and 6.5) did not indicate any clear corrosion-fatigue effect of accelerated cracking in the NaCl solution. At high da/dN, the curves obtained at 1Hz in the NaCl solution for both the 8 and 10% Mn HT1 alloys lay to the left of those obtained at 20 Hz in this aggressive environment. Comparison on a ΔK_{eff} basis, however, suggested that this could be associated, at least in part, with more important corrosion-product induded crack closure obtained in the NaCl solution at 20 Hz, the macrofractographic evidence for which will be

described in the next section.

Only slight differences were noted between the crack propagation curves in air for the 8 and 10% Mn alloy conditions studied, with somewhat more important differences observed between the propagation curves for the tests in NaCl solution at 1 Hz (R = 0.1). This comparison of the crack propagation curves for the 1 Hz tests in the NaCl solution with those for the tests in air indicated that the HT1 and HT2 heat treatments reduced the magnitude of the corrosion-fatigue crack propagation effect compared to that for the AC material, which was already smaller than that obtained for the higher Mn alloys (334).

The test carried out in air on the 13.5 % Mn propeller given the HT2 heat treatment was only carried out to a da/dN value of approximately 2.6 x 10^{-4} mm/cycle, because of a power failure which resulted in an important stress overload. Nevertheless, the test performed covered the crack growth region of primary practical interest (Fig. 6.6) and showed that the HT2 heat treatment was very effective in improving the resistance to fatigue crack propagation for long cracks, as characterized by the log da/dN -log ΔK curve. The HT2 heat treatment caused this curve to be displaced considerably to the right compared to the test on the as-received propeller material, with this heat treatment having a clearly beneficial effect on both the near threshold portion and the high da/dN portion of the log

da/dN - log ΔK crack propagation curve. For da/dN $\approx 7 \times 10^{-5}$ mm/cycle, the HT2 heat treatment resulted in a displacement of the crack growth curve to ΔK values approximately twice as high as for the-non heat treated propeller specimen. The influence of this HT2 heat treatment was expected since the HT1 heat treatment (referred to as HT in (334,390)), which also strongly increases the β volume fraction, had previously been shown to result in a very significant shift of the crack propagation curves to higher ΔK values.

For the test carried out in the NaCl solution on the 13.5 % Mn HT2 propeller specimen, similarly good or better crack propagation behaviour (Fig. 6.6) was obtained as in the test in air. The crack propagation on a ΔK basis was slower in the NaCl solution than in air below da/dN $\approx 6 \times 10^{5}$ mm/cycle and at higher da/dN values the crack growth curve was similar to that obtained in air or to the extrapolation of the curve obtained in air, the results in the NaCl solution having been obtained up to da/dN $\approx 2 \times 10^{-3}$ mm/cycle. Compared to the test for the propeller specimen in the as-received condition, the entire log da/dN - log ΔK curve obtained in the 3.5 % NaCl solution for HT2 propeller specimen has been displaced to ΔK values which are approximately twice as high for the same da/dN values.

More results of fatigue propagation, which have been described elsewhere (394), are omitted here in order to focus on the portion of this study related to this

thesis.

6.3.2 Macrofractography

The fracture surfaces produced in the 3.5 % NaCl solution in general were smoother than in air. In particular, the propeller specimens tested in air presented very large fractographic facets (Fig.6.8), associated with crystallographic cracking in the matrix β phase, while such facets were absent for the test in the NaCl solution.

For the tests in air, the fracture surface produced at da/dN values approximately less than 3×10^{-5} mm/cycle were covered with dark brown corrosion product, which was particularly dark for the lowest growth rates and for the 8 - 10 %Mn Ac alloys (Fig. 6.7). This rate agreed well with that at which log da/dN - log ΔK curves changed from a very steep slope below this da/dN value to a more gradual slope above it. Similar observations were previously reported for the 12 and 14% Mn alloys (334,390). For the tests in the NaCl solution, corrosion product covered the entire fracture surfaces, however, after ultrasonic cleaning, the fracture surfaces presented a similar sharp transition in appearance, which corresponded well to the transition in slope of the crack growth curves.

For the 8 and 10% Mn alloys, the fracture surface corrosion product produced in the salt solution appeared considerably thicker and was more difficult

to clean for tests at 20 Hz than at 1 Hz. These different observations indicate the occurrence of important corrosion product crack closure especially in the NaCl solution and at 20 Hz. This important crack closure also allows to explain the differences in the low da/dN portions of the log da/dN - log ΔK crack growth curves employing an increasing ΔK procedure and those obtained with a decreasing ΔK procedure. At low da/dN, the corrosion product on the fracture surface increases in thickness as da/dN decreases. As a result, the crack growth curve obtained employing an increasing ΔK procedure results in a thicker amount of corrosion product in the wake of the crack and therefore in greater crack closure and slower crack growth for a given nominal ΔK value.

6.3.3 Microfractography

Chapter 3 presented some of the crystallographic aspects observed and identified on the fracture surfaces of the 8-14% Mn-8% Al-2% Ni bronzes fatigued in air and in the NaCl solution. The present section therefore will concentrate on the fractographic features which could be taken as indications of corrosion-fatigue effect and which could assist in identify the corrosion-fatigue cracking mechanisms activated.

6.3.3.1 Intergranular Cracking

For tests in air on the 8 and 10% Mn AC, HT1 and HT2 alloys, the transgranular cracking at low crack growth rates was highly crystallographic. For da/dN between 3 x 10^{-5} to 10^{-4} mm/cycle. The fractographic feature was primarily that of ductile, crystallographic striations, while above 10^{-4} mm/cycle, the striations were less crystallographic.

The 8% and to a lesser extent the 10% Mn AC bronzes tested in air showed some intergranular cracking at low da/dN. This intergranular cracking was a maximum (≈ 40% for the 8% Mn AC alloy) for a da/dN range of approximately 10^{-6} to 5 x 10^{-6} mm/cycle. Similar intergranular cracking for tests in air has been noted in a number of previous studies ((10, 34, 139, 141, 144) and section 3.3.8) including on copper-based alloys. The evidence indicates that it is an environmental effect, which is associated with the presence of water vapour (10, 34, 141) and/or of hydrogen (144). It was noted, however, that some fine dimples as well as precipitates were often present on these intergranular facets such as shown in Fig. 6.9. Moreover, the observations by SEM on the metallographic sections containing a few secondary cracks showed that these cracks were not truly intergranular but were situated in the α-phase in the immediate vicinity of α-β interfaces, where a large number of precipitates were present (Fig. 6.10). This suggested that their occurrence was also possibly related to the difference in the deformability of the

two phases and to the large number of precipitates present in the α-phase near the α-β interfaces of these lower Mn bronzes. The metallographic observations on these AC materials showed the presence of a large number of fine κ_{II} precipitates (391) near the α-β interfaces and in the β-phase (Fig. 6.11). Such precipitates were not found for the HT1 and HT2 bronzes for which such intergranular-like facets were not observed.

The fracture surfaces produced in the NaCl solution presented a greater amount of intergranular cracking than for tests in air. A low cycling frequency, a low Mn content and the AC material condition favoured intergranular cracking at low da/dN values. For the 8% Mn AC specimens in the NaCl solution, intergranular cracking was observed up to da/dN $\approx 3 \times 10^{-4}$ mm/cycle for the tests at 1 Hz and up to da/dN $\approx 2 \times 10^{-5}$ mm/cycle at 20 Hz. These results suggest that the maximum crack growth rate at which intergranular cracking occurs is approximately inversely proportional to the cycling frequency, in general agreement with results reported on Ni - Al bronzes by Suzuki and Parkins (312).

High magnification observations of intergranular facets showed that those produced in the NaCl solution were considerably rougher than in air and, at lower propagation rates, wide secondary cracks (Fig. 6.12) were often present between such facets, strongly suggesting the occurrence of dissolution along these interfaces

or grain boundaries. Observation on metallographic profile sections often indicated noticeable preferential dissolution of the β-phase (Fig. 6.13) in the immediate vicinity of an interface with an α grain at secondary cracks. Preferential crack tip dissolution of the β phase is consistent with the interfacial cracking observed at lower growth rates in the NaCl solution of these 8-10% Mn alloys.

For the da/dN range in which this intergranular cracking was obtained, accelerated propagation at 1 Hz in the NaCl solution for the 8 and 10 % Mn AC was generally only observed on the log da/dN - log ΔK_{eff} curves (Fig. 6.2). These results indicate that the increased corrosion product-induced crack closure at low da/dN values in the NaCl solution masked, on a ΔK basis, the accelerated crack growth. Accelerated propagation was not observed for the 8 and 10% Mn HT1 and HT2 bronzes tested in the NaCl solution, for which much less intergranular cracking was observed.

6.3.3.2 Influence of the Environment on Striations

For the high da/dN values for which accelerated propagation in the NaCl solution was indicated on the crack growth curves for 8 and 10% Mn AC bronzes, the fracture surfaces were covered with ductile striations. A relationship was found between the manner in which striations interacted with grain boundaries and the occurrence of corrosion-fatigue propagation. For tests in air, the striation aspect

indicated that the crack frequently had difficulty to cross grain boundaries. The striations showed some tendency to change orientation from grain to grain (Fig. 6.14), the interstriation spacing quite often decreased as the crack front approached grain boundaries and, immediately after crossing a boundary, striations at times had a semi-elliptical shape (Fig. 6.14), indicating crack initiation in the new grain along a small segment of the boundary. In contrast, for tests at 1 Hz in the NaCl solution, the observations at high da/dN generally indicated that the crack crossed grain boundaries easily (Fig. 6.15) along a wide segment and with the interstriation spacing generally not decreasing on approaching these boundaries. The ductile striations observed at high da/dN were generally almost perpendicular to the macroscopic propagation direction for the tests at 1 Hz in the NaCl solution, while, for tests in air, the striations were often more crystallographic. The striations observed at high da/dN for tests at 20 Hz in the NaCl solution (Fig. 6.16) indicated that the crack crossed grain boundaries only slightly more easily than for tests in air.

The aspects of striations observed for the 8 and 10 % Mn HT1 and HT2 alloys tested at 1Hz in the NaCl solution indicated that the fatigue crack experienced considerable difficulty to cross boundaries containing a sizeable β ligament (Fig. 6.17). The curved aspect of the striations at times indicated that the crack crossed the boundary by causing initiation in the new α grain along a small segment of the β - α interface. The striation aspect indicated that the crack

experienced less difficulty in crossing boundaries containing only a very thin β ligament and little difficulty in crossing boundaries in which no β ligament was observed. Since many of the boundaries between α grains in the 8 and 10 % Mn HT2 bronzes contained β ligaments, these observations were consistent with the absence of accelerated cracking at 1 Hz in the NaCl solution for these bronzes with respect to the tests at 20 Hz in air or in the NaCl solution. The aspect of striations on the 8 and 10% Mn HT1 bronzes suggested the occurrence of a corrosion-fatigue effect intermediate between that for the AC and HT2 alloys, with testing at 1 Hz in the NaCl solution facilitating propagation across some α grain boundaries at high da/dN. The corresponding propagation results for the 8 and 10 Mn HT1 alloys did not show clear accelerated propagation compared to tests in air but did show faster propagation than for the tests at 20 Hz in the NaCl solution.

6.3.3.3 Microfractography of the As-Received (AR) Propeller Specimens

For the AR propeller specimen tested in air, metallographic section of the profile of the primary crack and of secondary cracks which branched off the primary crack showed that the crack path was primarily in the α phase, with some portions following α-β interfaces or crossing β ligaments (Fig. 6.18). For da/dN $< 3 \times 10^{-5}$ mm/cycle, the amount of β phase cracking appeared to be close to the minimum required to assure macroscopic crack growth. For higher da/dN values, the fractographic observations indicated that, while more β phase cracking

occurred, the presence of this phase and of α-β interfaces still acted as obstacles to propagation. Fractographic observations which indicated that the crack had difficulty crossing β - α interfaces, included the frequent presence of a finer interstriation spacing near the site at which initiation of fatigue cracking occurred in an α grain and the frequent presence of curved striations near β - α interfaces (Fig.6.19), indicating that the crack front was held back at the interface. Striations were generally not visible on the β facets. The fractographic observations, however, also frequently showed that the crystallographic cracking in the β phase generally preceeded locally ahead of the macroscopic crack front, with the cracking then spreading laterally into the adjacent α grains (Fig. 6.20). Therefore, while initiation of cracking in the β phase was an obstacle to crack propagation, once initiated, the crack propagated rapidly in this phase.

Both the macroscopic and microscopic crack path for the test on the AR propeller specimen in the NaCl solution tended to be significantly less irregular than in air at all da/dN values and crossed α - β interfaces with little deviation, even for lower da/dN. The observations also indicated that the microscopic fracture facets in both phases were also flatter than for the test in air. The microfractographic observations for da/dN > 10^{-4} mm/cycle were similar to those observed in air for high crack growth rates, except in the vicinity of α - β interfaces, where the aspect of striations suggested that, in the NaCl solution, the crack crossed α - β interfaces

with little difficulty (Fig. 6.21). Some of the β ligaments presented striations as also shown in Fig.6.21. These observations indicate that the corrosion-fatigue effect in the NaCl solution is largely associated with easier propagation across α - β interfaces. The metallographic observations also often showed some dissolution at interfaces of large κ_I particles, situated very near the fracture surface (Fig. 6.22).

6.3.3.4 Microfractography of the HT2 Propeller Specimens

For the 13.5 % Mn propeller specimen given the HT2 heat treatment and tested in air, an approximately equal amount of cracking was observed in both phases. At higher propagation rates, the crystallographic β facets (Fig. 6.23) presented some dimples, formed at fine κ_{IV} particles, similar to those observed on crystallographic β facets in fracture toughness tests (391,392). The number of dimples observed increased with increasing da/dN. For this test in air, observations of secondary cracks (Fig. 6.24) showed that the cracking in the α phase was quite devious, while the crack path in the β phase was crystallographic and cleavage-like, with crack segments often roughly parallel to elongated Widmanstatten secondary α grains within the β matrix. The crack appeared to have trouble to propagate across such α grains, resulting in frequent propagation along or near their interfaces or occasionally in secondary cracks terminating at such interfaces. The facets in the portions of β phase containing many secondary α grains presented many river lines and crystallographic features resembling tear ridges associated with these fine

secondary α grains arranged in Widmanstatten patterns (Fig. 6.25). In regions in which the secondary α grains did not significantly influence the microfractographic features in the β phase, stair-like arrangement of very crystallographic facets were present. The orientations of the stair-like facets in β phase were identified as {100} and {110} by etch-pitting of the fracture surface as shown in Figs. 3.63. and 3.64.

For the HT2 propeller specimen tested in the NaCl solution, the profile of the fracture surfaces was rougher than for the as-received (AR) propeller specimen tested in this solution, but not as rough as profile of the HT2 propeller specimen tested in air. The crack path was crystallographic in the β phase and deviated on crossing α - β interfaces (Fig. 6.26). The crack path within the α grains quite often was close to an α - β interface (Fig. 6.27). On metallographic sections some dissolution at interfaces between α grains and large propeller shape κ_I precipitates was observed in the immediate vicinity of the fracture surfaces (Fig. 6.28). One of the secondary cracks observed contained segments in the β phase along three different sets of slip traces, as shown in Fig. 3.61. This observation indicates that the fatigue cracking in the β phase involves slip deformation and that testing in the NaCl solution increases the crack tip plasticity.

The good resistance to fatigue propagation in both test environments of the 13.5% Mn propeller after the HT2 heat treatment can be associated in part with

this microstructure requiring an important amount of crack propagation in the harder β phase. The crack often has difficulty to cross from the β into the primary or into the secondary α grains indicating that the microstructure contains many obstacles tending to retard, deviate or arrest the crack. The devious crack path and rough fracture surface which resulted for the tests produced on the HT2 propeller specimen in both the air and NaCl solution environments also contributes to the good resistance to crack propagation, by causing ΔK_{eff} to be significantly lower than the nominal ΔK value.

The observations on the 12 and 14 % Mn HT2 bronzes as those on the propeller specimen indicated that testing in the NaCl solution at 1 Hz favoured the presence of observable fatigue striations on β ligaments (Fig. 6.29), which were rare or absent for the tests in air. This result clearly indicates a corrosion-fatigue effect of increased crack tip plasticity in the β phase. This result is consistent with the often observed effect, reviewed recently (331), of corrosion-fatigue to facilitate crack initiation by resulting in more important localized slip at the surface in contact with the aggressive environment. A similar effect of greater crack tip plasticity resulting from the crack tip being contact with the aggressive environment also permits to explain the less crystallographic striations observed in the α - phase, which, at a given value of ΔK, results in the crack crossing grain boundaries or interfaces more easily. For the 8 and 10 % Mn AC materials, the observations indicated that this

type of effect occurred for the striations produced in the α phase at high da/dN. For the propeller specimen as well as for the 12 and 14 % Mn HT1 bronzes (334,390), the observations indicate such an effect for both phases.

6.3.3.5 Microfractographic Evidence Related to the Influence of Precipitates

Besides the influence of the κ_{IV} precipitates in the β phase of the HT2 bronzes containing 12 % or more of Mn to result in the formation of ductile tearing dimples during the fatigue cracking, a number of other observations were made on the different bronzes studied pertaining to the manner in which the fatigue crack interacted with precipitates present within the microstructure.

For the 10 % Mn HT2 bronze tested in air, evidence was found for interaction between fine κ precipitates and the fatigue crack front for da/dN of the order of 2×10^{-5} mm/cycle. As shown in Fig. 6.30, small microvoids formed about certain precipitates and then joined up with the local crack front. As a result, the crystallographic crack plane started to go partially around the microcavity. Cracking on the neighbouring parallel facet at times bypassed that which intersected the microcavity, which indicates that the formation of the microcavity tends to impede the crack propagation at least locally. The microcavities tend to be aligned, with this alignment at times being along river or ridge lines. These observations suggest that a greater amount of local plasticity in the vicinity of such lines facilitates the

formation of these microcavities. Local plasticity is favoured at river lines to produce the local tearing which produces these lines. As well, the existence of a microcavity at the crack tip may facilitate the formation of another microcavity slightly ahead of it.

Fig. 6.31 shows very similar formation of microvoids around κ_{IV} precipitates in the β phase of the HT2 propeller specimen at low da/dN as that observed in Fig. 6.30. In both cases, dimples with a semi-elliptic shape tend to be created by the crack initially going around the microcavity formed.

The β phase of the 10% Mn HT2 material also presented a few fine, shallow microcavities or a few similarly shaped precipitates sticking out of the fracture surface for da/dN greater than 2 x 10^{-5} mm/cycle as shown in Figs. 6.32.

At high da/dN values for tests in air as well as in the NaCl solution, microcavities formed on the fracture surfaces of the different bronzes around large ($\geq$ 2 m) κ precipitates intersecting the crack plane. An example is shown in Fig. 6.33 for the 8 % Mn AC bronze tested in air. The local variation in interstriation spacing showed that these microcavities resulted in a few cycles of local acceleration of the fatigue crack growth rate followed by a few cycles of slower fatigue crack growth before a crack front presenting no local bulge was reobtained. The

observations indicated that these effects were only local and that they did not influence the macroscopic rate.

Evidence for local dissolution in the immediate vicinity of interfaces of large κ particles at the fracture surface was also obtained (prior to cleaning the fracture surfaces) for the 8 and 10 % Mn HT1 and HT2 materials tested in the NaCl solution. An example is presented in Fig. 6.34 for the 8 % Mn HT1 material tested at 1 Hz. Whether this dissolution occurred at or behind the crack front was not ascertained. For da/dN values which produced fatigue striations on the fracture surfaces, the presence of regions of dissolution about κ particles was not observed to affect the local striation spacing or the crack front shape, which suggests that this dissolution had little influence on the fatigue propagation and that most of it did not occur at the crack front.

Therefore, the observations indicate that the influence of the precipitates present in the 8 and 10 % Mn bronzes depends on whether microcavities formed about these precipitates, with the influence on the local crack growth rate being that produced by the microcavity. In the tests in air, at high da/dN, such microcavities tended to accelerate very briefly the local crack growth rate, without influencing the macroscopic rate. However, the density of particles producing such microcavities for these alloys was low. Acceleration of the macroscopic rate, hence, could be expected

in the presence of a sufficiently high density of similar particles. At lower da/dN, some of the fine precipitates in the α phase of the 10 % Mn HT2 bronze resulted at da/dN $\approx 2 \times 10^{-5}$ mm/cycle in the formation of microcavities, which were observed to retard locally the crack propagation rate and which could possibly also retard somewhat the macroscopic rate. Little influence of the presence of either large or fine particles on the fatigue propagation was observed for the tests in the NaCl solution for the 8 and 10% Mn HT1 and HT2 materials for da/dN values which produced fatigue striations on the fracture surfaces, although the presence of regions of dissolution about κ particles was observed.

6.4 CONCLUSIONS

From the present study, the following conclusions can be drawn:

1) A relatively small effect of accelerated corrosion-fatigue crack propagation occurred for the tests at 1 Hz in the NaCl solution for the 8 and 10 % Mn bronzes studied.

2) The corrosion-fatigue effect at high da/dN for the 8 and 10 % Mn AC bronzes was associated with less crystallographic striations and easier propagation across grain boundaries and interfaces, as a result of increased crack tip plasticity.

3) Corrosion-fatigue effects at lower da/dN values for the 8 and 10% Mn bronzes were associated with cracking along α - β interfaces, with the observations indicating that preferential dissolution of the β phase was involved.

4) No corrosion-fatigue effect was noted for a cycling frequency of 20 Hz, which is consistent with the general dependence of cyclic frequency on corrosion-fatigue propagation, in that there is a critical frequency below which the corrosion effect starts to be manifested.

5) The considerably improved resistance to fatigue crack propagation displayed by the 12-14 % Mn HT2 alloys with respect to the 8 and 10 % Mn alloys, can be related to the volume fraction and distribution of the β phase in their microstructure, which results in a more important amount of the fatigue crack propagation occurring in this hard phase. As well, a strong tendency for crystallographic cracking in the β phase and the large β grain size produces a microscopically very rough fracture surface which gives important roughness-induced crack closure effects as well as important crack deviation effects, both of which tend to cause ΔK_{eff} to be substantially lower than ΔK. For the tests in the NaCl solution, the fracture surfaces of the higher Mn HT2 alloys were less rough but covered with important amount of corrosion product inducing crack closure effects.

6) It also appeared that the complexity of the microstructure produced by the HT2 condition, which resulted in the crack often having some difficulty to cross from the β into the primary or into the secondary α phase also contributed significantly to the improved resistance to crack propagation, since the complex microstructure in HT2 alloys contained many obstacles tending to retard, deviate or arrest the crack in particular for the tests in air. However, the dissolution effects which occurred in the immediate vicinity of α - β interfaces and of interfaces of precipitates at lower crack growth rates for the tests in the NaCl solution, as well as the tendency to favour enhanced plasticity at a surface in contact with the aggressive environment suggest that similar effects could also give rise to corrosion-fatigue facilitated crack initiation.

Table 6.1: Fatigue propagation tests performed on the Mn-Al-Ni bronzes

Specimen	Nominal % Mn	Material Condition	Environment	Frequency Hertz	R-ratio
3330.1A	8	AC	air	20	0.1
3288.1B	8	AC	air	20	0.1
3288.1D	8	AC	3.5% NaCl	20	0.1
3288.1C	8	AC	3.5% NaCl	1	0.1
3330.1B	8	AC	3.5% NaCl	1	0.1
3303.2D	8	HT1	air	20	0.1
3303.3B	8	HT1	3.5% NaCl	20	0.1
3303.3A	8	HT1	3.5% NaCl	1	0.1
3303.1B	8	HT2	air	20	0.1
3303.1D	8	HT2	3.5% NaCl	20	0.1
3303.2B	8	HT2	3.5% NaCl	1	0.1
3289.1B	10	AC	air	20	0.1
3302.2A	10	AC	air	20	0.1
3289.1D	10	AC	3.5% NaCl	20	0.1
3289.1C	10	AC	3.5% NaCl	1	0.1
3302.2B	10	AC	3.5% NaCl	1	0.1
3335.2C	10	HT1	air	20	0.1
3335.3A	10	HT1	3.5% NaCl	20	0.1
3335.3D	10	HT1	3.5% NaCl	20	0.1
3335.2D	10	HT1	3.5% NaCl	1	0.1
3335.2A	10	HT2	air	20	0.1
3335.1A	10	HT2	3.5% NaCl	20	0.1
3335.2B	10	HT2	3.5% NaCl	1	0.1
3277.3C	12	HT2	3.5% NaCl	1	0.5
3278.3C	14	HT2	3.5% NaCl	1	0.5
Prop	13.5	AR	air	20	0.1
Prop	13.5	AR	3.5% NaCl	1	0.1
Prop.H1	13.5	HT2	air	20	0.1
Prop.H2	13.5	HT2	3.5% NaCl	1	0.1

Table 6.2: Chemical analysis (wt%) Mn-Al-Ni bronzes

HEAT NO.	Mn	Al	Fe	Ni	Si	Pb(1)	Pb(2)
3288	8.7	6.8	3.3	2.1	0.01	-	≤0.001
3330	8.4	7.0	2.9	2.0	≤0.01	0.034	0.012
3303	8.8	6.7	3.2	2.0	0.04	0.023	≤0.001
3289	10.9	6.9	3.2	2.1	0.02	-	0.002
3302	10.7	6.7	3.0	2.0	0.02	0.023	≤0.001
3335	10.5	7.1	3.2	2.1	0.02	0.06	0.0085
3277	12.3	7.9	3.3	2.1	0.04	-	0.0024
3278	14.2	8.0	3.4	2.2	0.01	-	≤0.001
PROP	13.5	7.4	3.2	2.5	-	-	0.016

(1) Original Pb analysis supplied by MTL-CANMET.

(2) Pb analysis performed by Laboratoire de Géochimie Analytique - École Polytechnique.

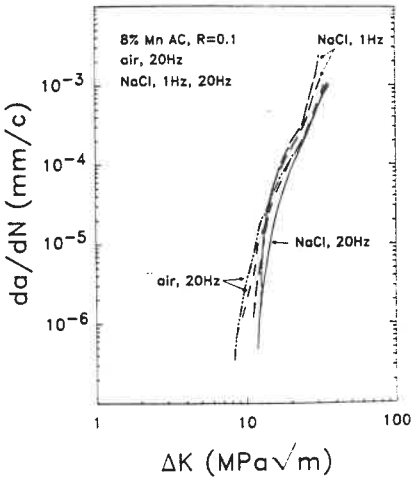


Fig. 6.1

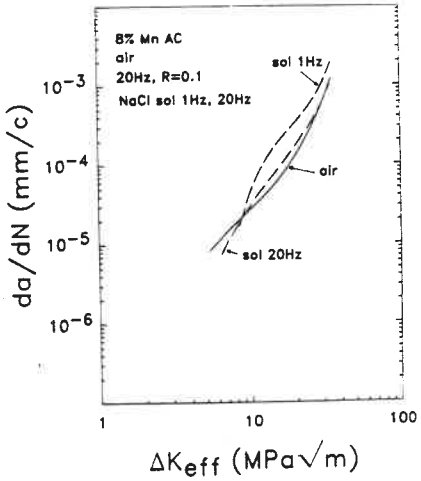


Fig. 6.2

Fig. 6.1: Comparison of the crack growth curves for the 8% Mn Ac alloys.

Fig. 6.2: Examples of log da/dN-log ΔK_{eff} crack growth curves for the 8% Mn AC alloy.

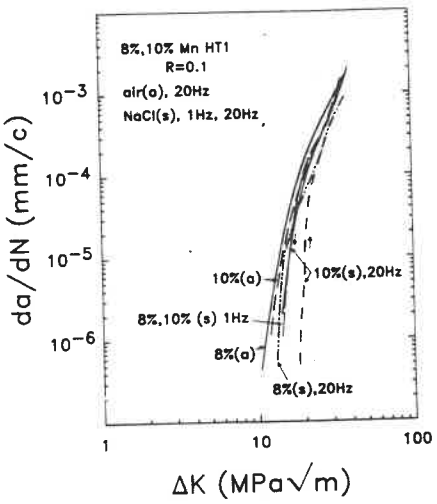


Fig. 6.3

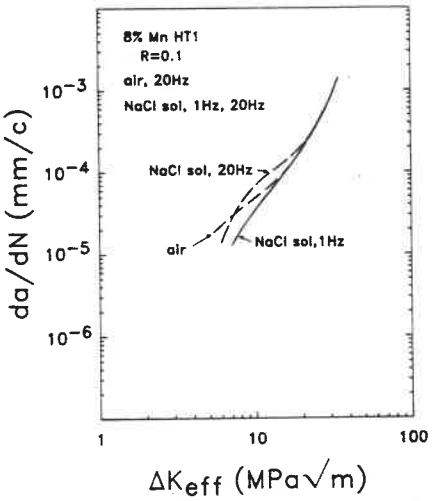


Fig. 6.4

Fig. 6.3: Comparison of different crack propagation curves for the 8 and 10% Mn HT1 alloys.

Fig. 6.4: Comparison on a ΔK_{eff} basis of the high da/dN portion of crack growth curves for the 8% Mn HT1 alloy.

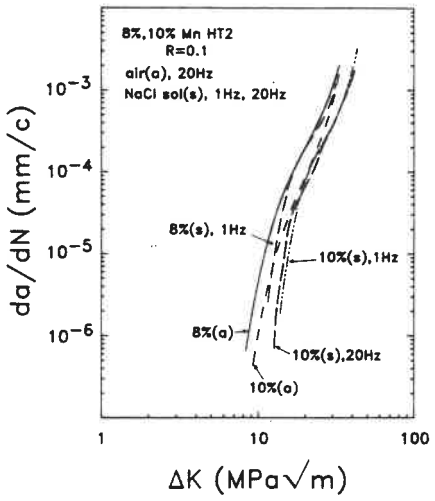


Fig. 6.5: Comparison of different crack propagation curves for the 8 and 10% Mn HT2 alloys.

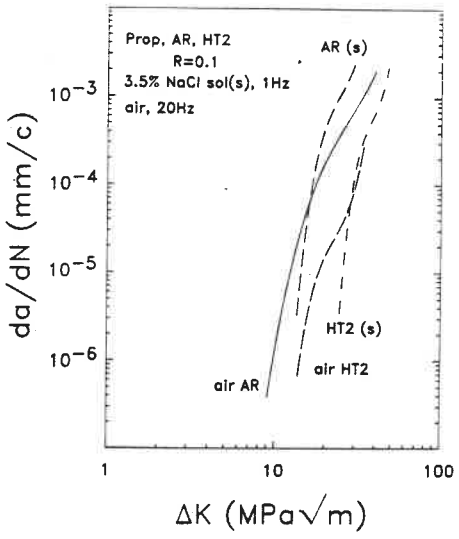


Fig. 6.6: Comparison of the crack growth curves in air and in the NaCl solution for the propeller specimens in the as-received and HT2 conditions.

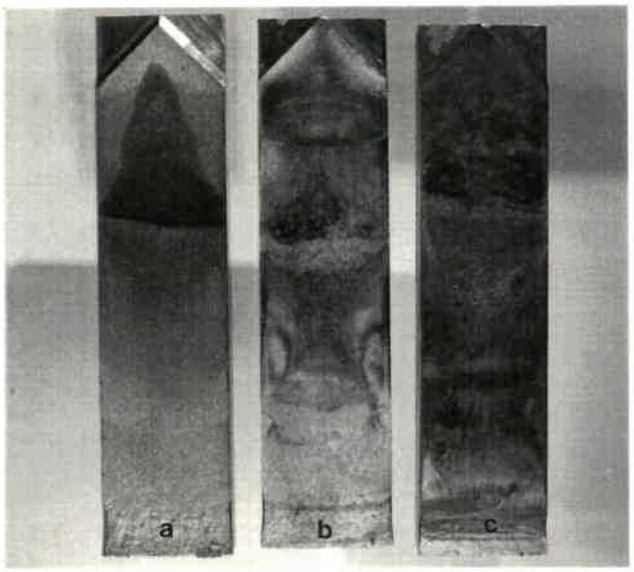


Fig. 6.7: Macroscopic aspect of fracture surfaces of the 8% Mn AC specimens tested in air at 20 Hz (a) and in 3.5% NaCl solution at 1 (b) and 20 (c) Hz.

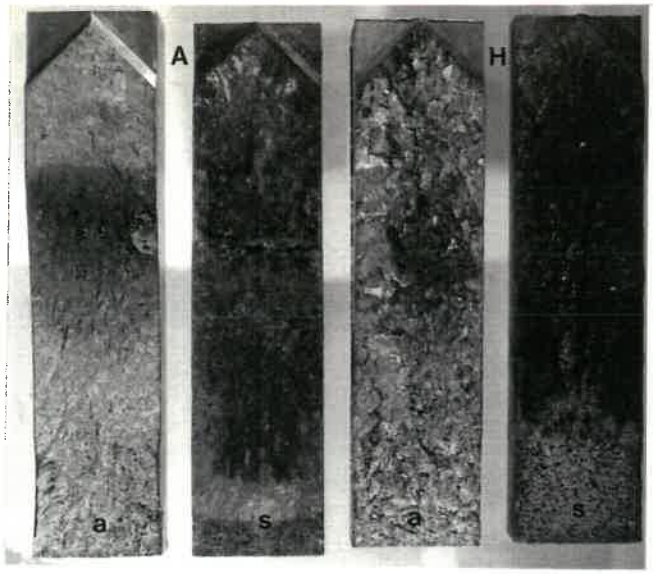


Fig. 6.8: Macroscopic aspect of fracture surfaces of the as-received (A) and HT2 (H) propeller specimens tested in air (a) and in NaCl solution (s).

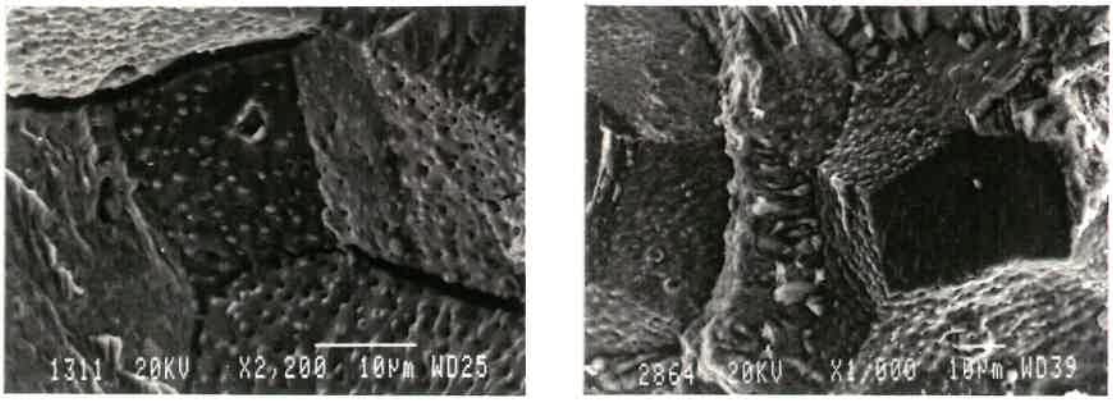
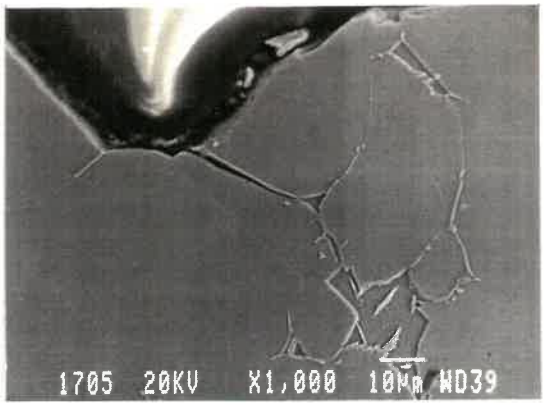


Fig. 6.9: Small precipitates and dimples on the intergranular-like facets produced in air for 8% Mn AC bronze at da/dN $\approx 10^{-6}$ mm/cycle.



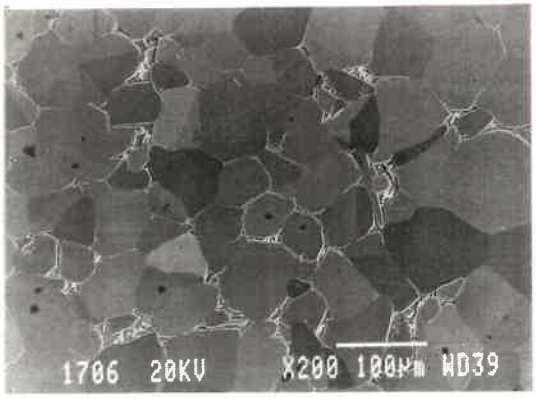
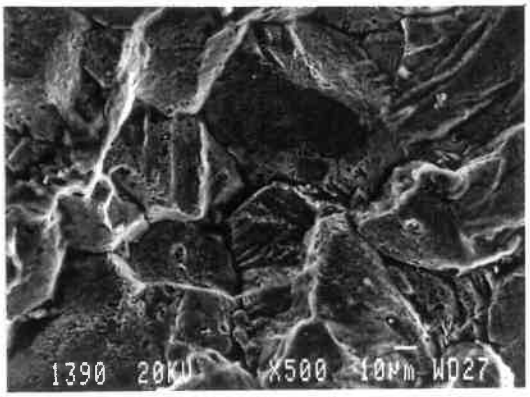


Fig. 6.10 **Fig. 6.11**

Fig. 6.10: Path of secondary crack observed on the metallographic section of the 8 % Mn AC specimen tested in air, showing that the intergranular-like cracks are situated in the α-phase in the immediate vicinity of the α-β interface (da/dN ~ 10^{-6} mm/cycle).

Fig. 6.11: Microstructure of the 8% Mn AC bronze specimen tested in air, showing the presence of fine κ_{II} precipitates in and near the regions of the β phase.



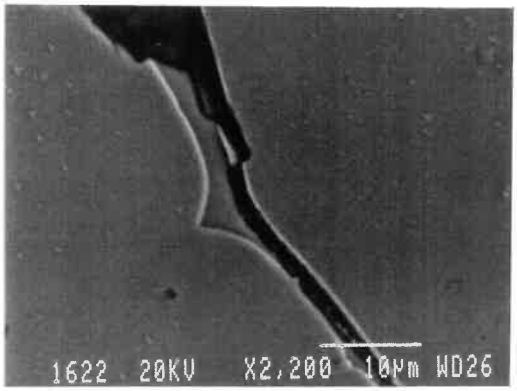
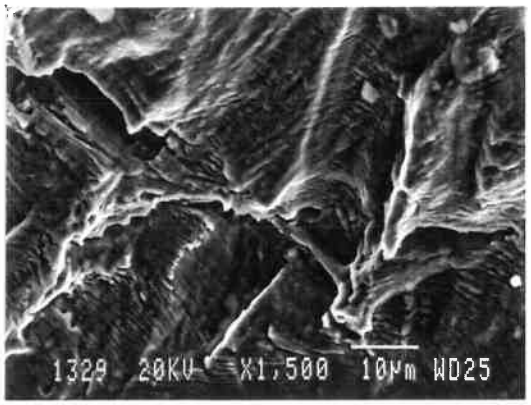


Fig. 6.12 **Fig. 6.13**

Fig. 6.12: Intergranular facets in 8% Mn AC alloy tested in NaCl solution, 1Hz $\approx 10^{-6}$ mm/cycle.

Fig. 6.13: Dissolution of β-phase in 10% Mn HT1 alloy, tested in NaCl solution at 1 Hz.



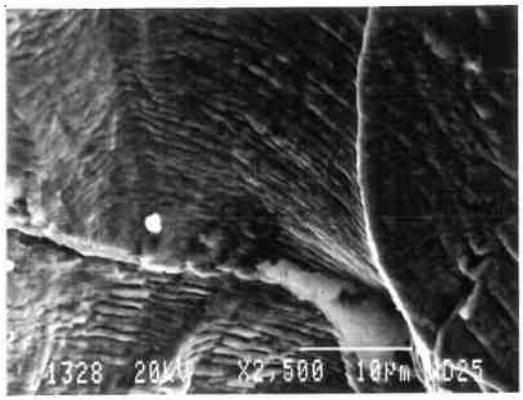


Fig. 6.14: Curved aspects of striations for the 8% Mn AC alloy tested in air, indicating that the cracks encounter some difficulty to cross boundaries between α grains, da/dN $\approx 10^{-3}$ mm/cycle.

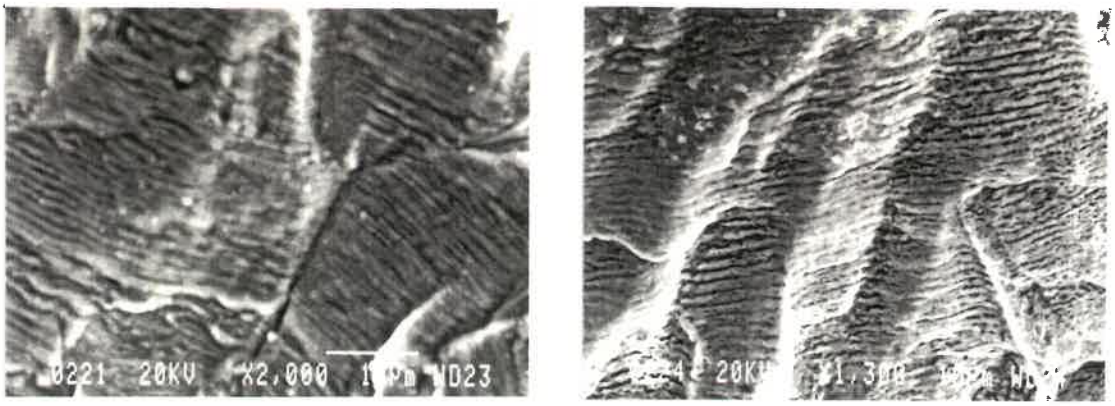


Fig. 6.15: Striations which cross boundaries between α grains with no apparent difficulty, 8% Mn AC alloy tested at 1 Hz in the NaCl solution, da/dN $\approx 10^{-3}$ mm/cycle.

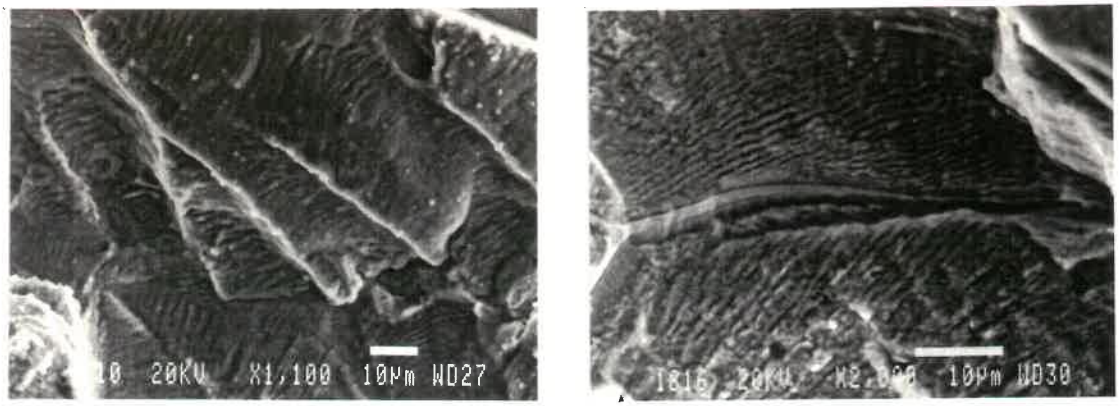


Fig. 6.16 **Fig. 6.17**

Fig. 6.16: Aspect of striations in 8% AC alloy, NaCl solution at 20 Hz, da/dN $\approx 10^{-3}$ mm/cycle.

Fig. 6.17: Aspect of striations in 10% Mn HT2 alloy, NaCl solution, 1Hz, da/dN $\approx 10^{-3}$ mm/cycle.

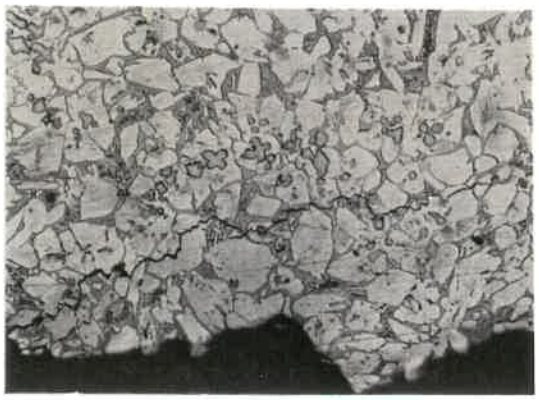


Fig. 6.18

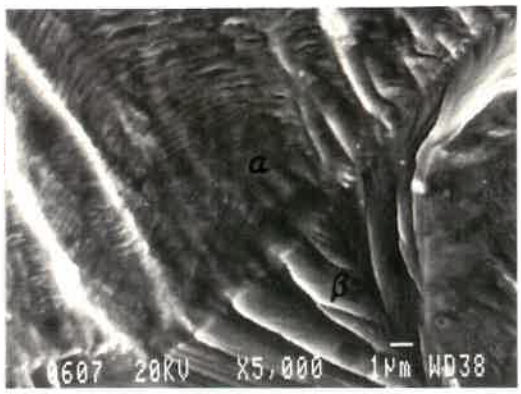


Fig. 6.19

Fig. 6.18: Profile of the fracture surface and secondary crack observed for the AR propeller specimen tested in air, da/dN $\approx 10^{-5}$ mm/cycle.

Fig. 6.19: Curved striations near a site at which the fatigue crack crossed a β - α interface, AR propeller, tested in air, da/dN $\approx 7 \times 10^{-4}$ mm/cycle.

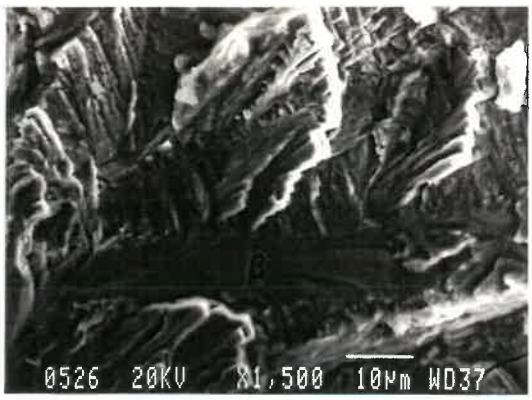


Fig. 6.20

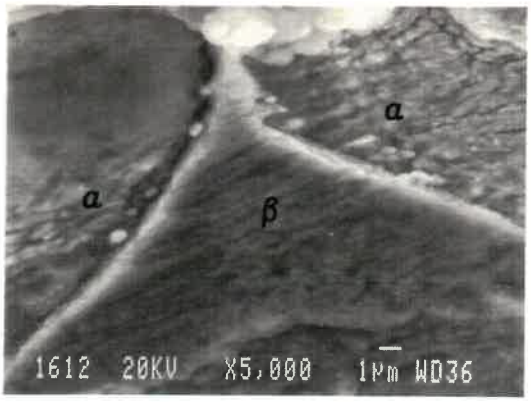
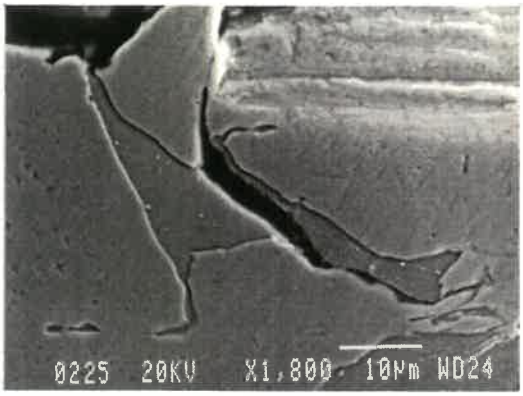


Fig. 6.21

Fig. 6.20: Fracture facets showing the cracking leading in the β phase, AR propeller tested in air, da/dN $\approx 10^{-5}$ mm cycle.

Fig. 6.21: Striations which continue across α-β interfaces, AR propeller, da/dN $\approx 10^{-3}$ mm/cycle.



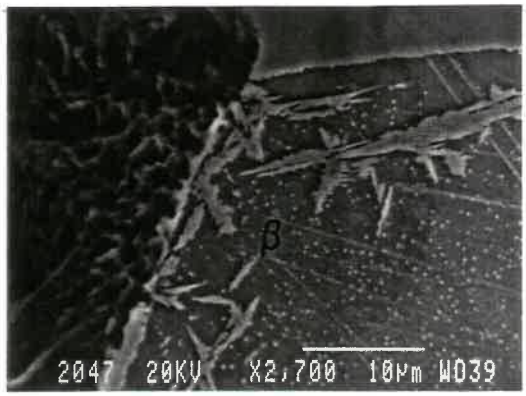
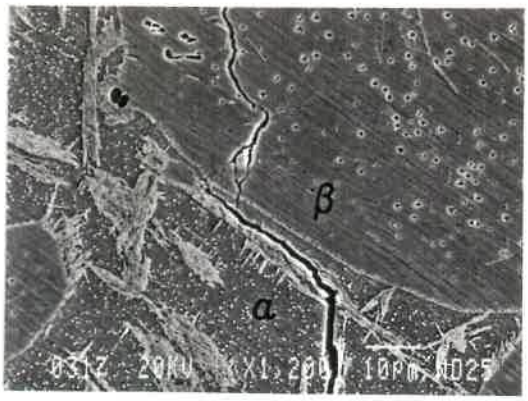


Fig. 6.22 **Fig. 6.23**

Fig. 6.22: Secondary crack in the immediate vicinity of the fracture surface, showing β phase dissolution near an α-β interface, AR propeller, da/dN $\approx 5 \times 10^{-5}$ mm/cycle.

Fig. 6.23: Dimples in β phase of HT2 propeller, tested in air, da/dN $\approx 2 \times 10^{-4}$ mm/cycle.



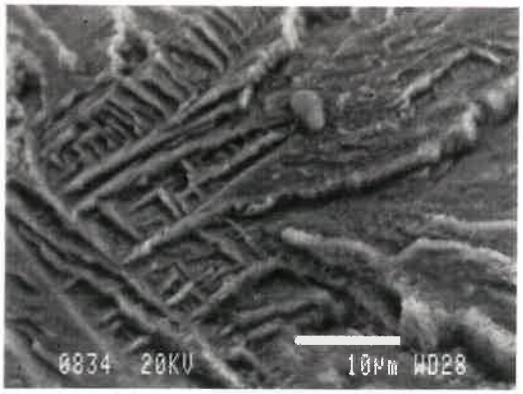
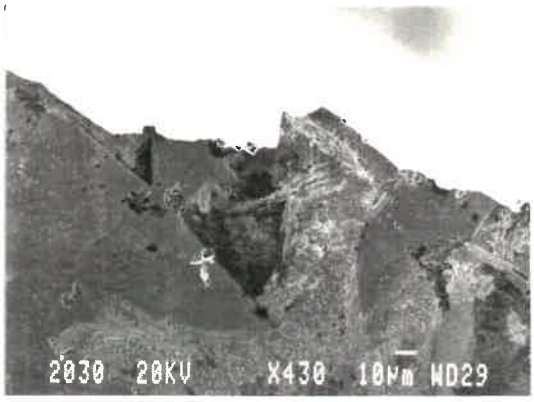


Fig. 6.24 **Fig. 6.25**

Fig. 6.24: Crack path in the α and β phases, HT2 propeller tested in air, da/dN $\approx 10^{-5}$ mm/cycle.

Fig. 6.25: β fracture facet presenting ridges corresponding to secondary α grains arranged in Widmanstatten patterns, HT2 propeller, tested in air, da/dN $\approx 10^{-5}$ mm/cycle.



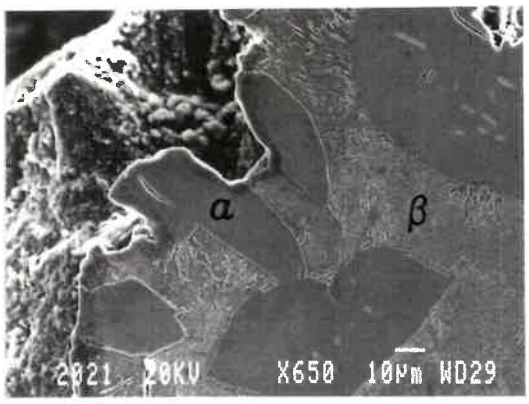
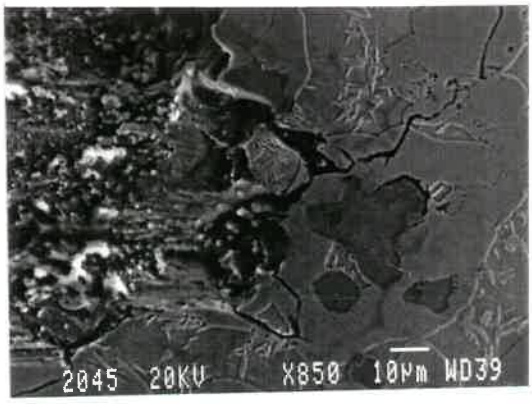


Fig. 6.26 **Fig. 6.27**

Fig. 6.26: Profile of the fracture surface of the HT2 propeller specimen tested in the NaCl solution, showing the crack path in the β phase tended to be crystallographic with the crack orientation deviating on crossing α - β interfaces, da/dN $\approx 1 \times 10^{-5}$ mm/cycle.

Fig. 6.27: Profile of the fracture surface of the HT2 propeller specimen tested in the NaCl solution, showing a tendency for cracking to follow a path near α - β interfaces, da/dN $\approx 10^{-4}$ mm/cycle.



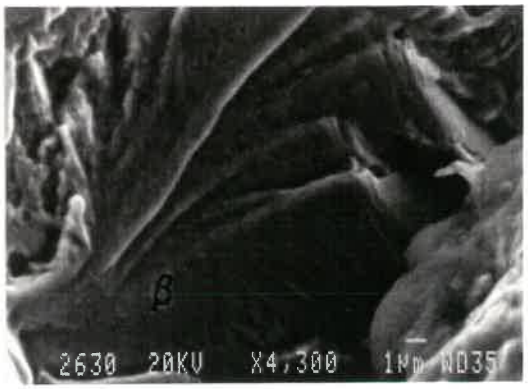
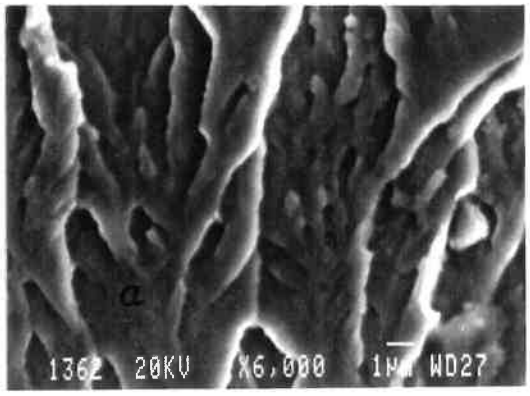


Fig. 6.28 **Fig. 6.29**

Fig. 6.28: Dissolution in the vicinity of the interfaces of κ_I precipitates, HT2 propeller specimen tested in the NaCl solution, da/dN $\approx 10^{-4}$ mm/cycle.

Fig. 6.29: Striation on β facets at da/dN $\approx 9 \times 10^{-4}$ mm/cycle for 14% Mn HT2 specimen tested at 1 Hz in the NaCl solution.



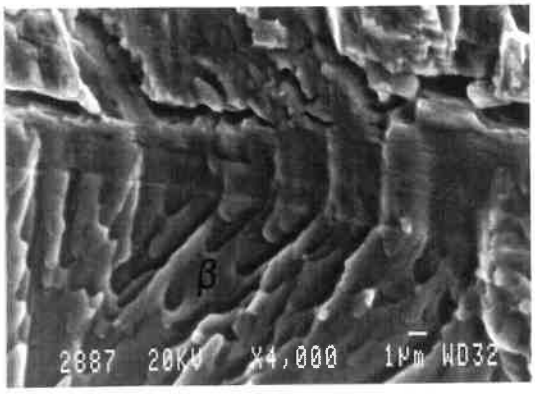
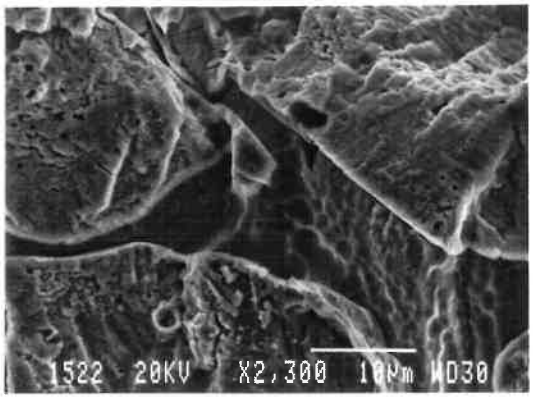


Fig. 6.30 **Fig. 6.31**

Fig. 6.30: Influence of fine κ precipitates on the microfractographic features in the α phase, 10% Mn HT2 alloy tested in air, da/dN ≈ 2 x 10^{-5} mm/cycle.

Fig. 6.31: Semi-elliptical dimples formed in the β phase of the HT2 propeller specimen tested in air, da/dN ≈ 10^{-5} mm/cycle.



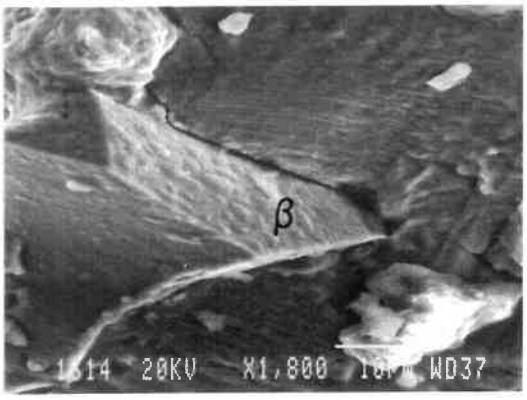


Fig. 6.32: (Left) Dimples in the β phase of the 10 % Mn HT2 alloy tested in air, da/dN ≈ 10^{-5} mm/cycle. (observed after etch-pitting).
(Right) Precipitates present on the β phase of the 10% Mn HT2 alloy tested in air, da/dN ≈ 10^{-4} mm/cycle. (observed on a surface not etched).

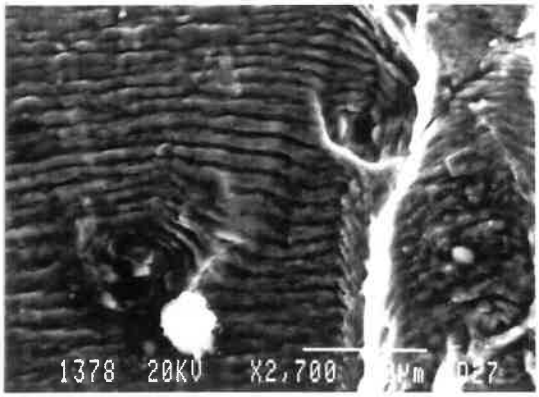


Fig. 6.33: Interaction of medium-size κ precipitates with fatigue striations in the α phase, 8% Mn AC bronze tested in air, da/dN ≈ 10^{-3} mm/cycle.

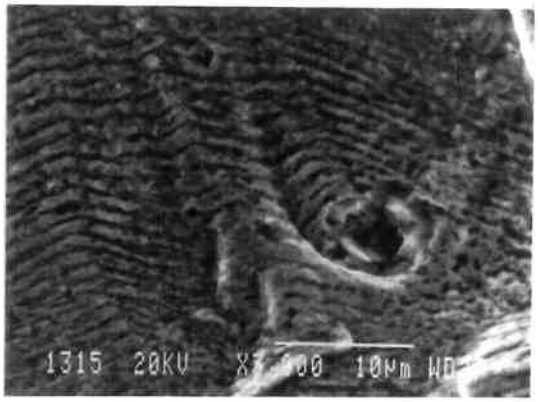


Fig. 6.34: Presence of dissolved medium-size κ precipitates on the fatigue fracture surface of the 8% HT1 specimen tested at 1 Hz in the NaCl solution, da/dN ≈ 10^{-3} mm/cycle.

CHAPTER 7

GENERAL DISCUSSION

Now that the results have been presented in detail, it is important to reconsider the main objective of this study which was to analyze the fractographic and crystallographic features associated with near-threshold fatigue cracking and to compare them with the typical fractography of transgranular stress-corrosion cracking so as to identify better the operating cracking mechanisms. Therefore, in this chapter, the main similarities and differences of the microfractographic aspects between these two types of fractures will be summarized and discussed further.

7.1 MICROFRACTOGRAPHIC SIMILARITIES BETWEEN TSCC AND NEAR-THRESHOLD FATIGUE CRACKING

The principal similarities observed in the f.c.c. metals studied between TSCC and near-threshold fatigue cracking are that both types of cracking often result in primary facets which present microfacets corresponding to {111} slip planes in f.c.c. metals (Figs. 3.16, 3.17, 3.31, 4.5, 4.6, 5.15). In b.c.c. metals, the microfacets associated with near-threshold fatigue cracking also correspond to slip planes (Figs. 3.49, 3.57). As well, the microfacets identified for both types of cracking matched well in an interlocking manner (Figs. 3.57, 4.20, 5.15). In the case of stress-

corrosion cracking, the microfacets on both 316 stainless steel and 70 Cu-30 Zn α-brass became larger and clearer with increasing stress intensity factor K (section 4.3.2, 5.1.3.5, 5.1.3.6), indicating that these facets indeed followed planes on which crack tip slip had occurred. In contrast, for near-threshold fatigue cracking in f.c.c. metals, large {111} facets are favoured by very low da/dN and ΔK values (section 3.3.3, 3.3.5), since this favours slip which is highly localized on individual slip planes.

For both types of cracking, the nominal orientation of the primary facets have been confirmed to correspond generally to a plane bisecting one of the angles between the planes of the microfacets. For 316 stainless steel, during SCC, as well as during near-threshold cracking the primary facets often correspond to {100}. For α-brass (section 5.1.3.5, 5.1.3.6) and other copper alloys (172, 174), the primary facets produced during TSCC correspond generally to {110}, and this primary facet orientation also appeared more frequently in near-threshold fatigue of 70 Cu-30 Zn α-brass and of copper than for the other f.c.c. metals studied.

In f.c.c. metals, when the orientation of the near-threshold primary facets is perpendicular to the tensile axis, the microfacets are often not discernible resulting in difficulty in recognizing the striations. This is also often the case for stress corrosion cracking in f.c.c. metals at low K values. While, the visibility of the microfacets also depends on the material, especially on the SFE or tendency to

obtain planar slip in the material for both cases of SCC and near-threshold fatigue cracking (section 3.3, 4.4.2). When the microfacets are not visible, the present study indicates that this is most probably because they are too fine to be resolved.

Near-threshold fatigue and SCC cracks not only produce the same orientations of primary facets, such as {100} and {110}, but also propagate along the same crystallographic directions, as indicated by the orientations of the river lines.

That the similarities in cracking crystallography and the result that on a microscopic scale cracking occurs on planes on which slip has occurred explains the strong similarity in fractographic features for SCC and near-threshold fatigue. The details of the fractographic features observed for both types of cracking have been clearly shown to depend strongly on the number of slip planes on which decohesion occurs and on the amount of decohesion which occurs on each slip planes. In the case of near-threshold fatigue, these two factors depend on the orientation of the individual grain with respect to the stress axis and on the local stress and strain effects associated with the need for differently oriented crack segments in neighbouring regions to join up to produce the macroscopic crack front. As shown in section 3.3, a large number of small tetrahedral-like or pyramid-like facets in the regions near grain boundaries indicate that more slip planes or more different

families of planes of decohesion were involved in accommodating the orientation of the average fracture plane in these regions. In the case of stress corrosion cracking, more complex fractographic features at high K values and near the lateral edges of specimens (section 4.3.2.3, 4.3.2.4) indicate a marked sensitivity to slip-dominated effects in the crack tip region.

From the microfractographic features and crystallographic aspects identified in the present study, an inescapable conclusion is that the crack path on a very microscopic scale follows planes on which localized slip has occurred both for TSCC in f.c.c. metals and for near-threshold fatigue in f.c.c., b.c.c. and h.c.p. (104) metals.

Since two different mechanisms of crack growth are unlikely to produce fractures with the same crystallography and similar fine fractographic details, such as crystallographic striations and serrated river lines, some consideration must be given as to whether there are similarities in the cracking mechanism responsible for the fractures following on a microscopic scale planes on which localized slip has occurred.

7.2 MECHANISMS OF TRANSGRANULAR NEAR-THRESHOLD FATIGUE CRACKING

The discussion concerning the mechanisms of transgranular near-threshold fatigue cracking has been presented in section 3.4.3. The detailed microfractography is consistent with this cracking being produced by decohesion on different slip planes, often on alternating slip planes. The absence of any cleavage-like facets in b.c.c. metals studied, indicates that this cracking is at least primarily produced by slip. Although the cracking crystallography can be explained as being produced solely by shear (reversed slip) since reversed plasticity results from the fatigue cycling, such cracking may also involve a cleavage or cleavage-like component to produce the decohesion on the slip planes. Supporting evidence for such a cleavage-like component include the lack of evidence of rubbing on some of the large {111} facets produced at ultra-low da/dN values (141) and the inability to resolve microfacets on some of the primary facets in f.c.c. metals, especially when the orientation of the primary facets is perpendicular to the tensile axis. Since many cycles are required to produce each microfacet, it is not clear how continuously or discontinuously these are produced.

One cracking process which can be considered for near-threshold fatigue is that firstly, reverse slip over a large number of cycles on a favourably orientated slip

plane ahead of the advancing crack front weakens sufficiently the cohesive strength of atomic bonds on this plane (119), so that in a single or small number of cycles, a low tensile stress initiates local separation resulting in the formation of the microfacet. The details of weakening of the cohesive strength of atomic bonds by reverse slip is not clear but may involve an increase in the density of dislocations and vacancies on the slip plane.

The other possibility which could be attributed to facilitating microscopic scale decohesion on slip planes is associated with the effects of the environment in promoting localized plastic deformation at the crack tip. In support of such an effect, the present study has shown the striking difference in microfractographic morphology produced in vacuum and in air for copper and α-brass fatigued near the threshold. Especially for copper (section 3.3.6), many of the fractographic characteristics produced in vacuum, including some large dimple-like features, bear resemblance to those produced by ductile fracture. These observations indicate clearly that fatigue cracking in vacuum for these two materials resulted in less localized slip thereby giving rise to less crystallographic faceted cracking. The highly crystallographic cracking produced near the threshold in air, including some large {111} facets at sufficiently low da/dN values ($\sim 10^{-7}$ mm/cycle), must be attributed to the environment effects by which the localization of plastic deformation at the crack tip was enhanced, giving rise to more planar slip and thus resulting in large

decohesion facets following the most favourably orientated slip planes. As mentioned in section 3.3.6, this difference in fractographic aspects produced in air and in vacuum is also consistent with the very recent examination of dislocation substructures found near the crack tip at relatively low da/dN values (124), which indicates the important role of a laboratory air environment in modifying the crack tip plastic deformation characteristics and hence in altering the fracture features.

The environmental effects which can be considered as possibly influencing the crack tip plasticity behaviour for near-threshold fatigue testing in air include an adsorption effect, the formation of a surface film or the production of hydrogen from a reaction with water vapour and its absorption into the crack tip region. As mentioned in section 1.1.4.1, bulk oxides produced in the front of crack tip can decrease the tendency for slip reversibility for aluminium and its alloys tested in air (25). The lack of reversibility would promote the operation of multiple slip system. Furthermore, some investigations (28) have associated surface energy reduction due to adsorption effects with the easy formation of slip bands. As well, McMahon (259) reviewed much of the literature on how hydrogen affects the slip character in steels and concluded that hydrogen promotes planar slip by inhibiting the cross slip of screw dislocations. Later, Hwang and Bernstein (256) demonstrated this to be the case in hydrogen-charged Fe-Si single crystals. McMahon (259) emphasized how this might lead to strain-controlled mode II cracking, by glide plane decohesion

on {110} and {112} planes, or to {110} and {112} "quasi-cleavage" in steels because of the blockage of dislocations at carbides formed along matensitic lath boundaries. The resulting build-up of stress normal to the slip plane, combined with the reduction in cohesion due to the entrained hydrogen would thus promote slip plane decohesion.

Although it is not clearly evident whether hydrogen can be formed during fatigue cracking in laboratory air near the threshold for copper and α-brass metals, the argument that slip planarity enhances slip plane decohesion is probably also valid here. Such considerations are also applicable to explain the occurrence of the quasi-intergranular cracking produced in the case of fatigue tests carried out in laboratory air at relatively low da/dN values in many metals. More planar slip enhanced by environment will promote more incompatibility and stress concentrations by dislocation pile-ups at grain boundaries, hence favouring quasi-intergranular cracking. This consideration is also consistent with the effect of the stacking fault energy (SFE) on the fractographic features observed in the present study, since the size of the microfacets and the amount of intergranular fracture are larger in α-brass than in copper at a given da/dN value. This can be attributed to the lower SFE and greater slip planarity in α-brass than in copper, resulting in larger decohesion increments on each set of {111} microfacets.

The occurrence of some apparently true intergranular facets observed at relatively low da/dN values for copper and α-brass tested in laboratory air suggests that these facets were produced by decohesion along the grain boundaries. This is consistent with an hydrogen-embrittlement effect involving hydrogen swept to grain boundaries by dislocations as proposed by Marchand et al. (10). The occurrence of quasi-intergranular facets at times observed in the present study can also be explained based on hydrogen enhanced localized plasticity in the vicinity of the grain boundaries as suggested by some investigators (237, 210). The fractographic aspects of the intergranular cracking observed are therefore also consistent with hydrogen-assisted cracking associated with hydrogen swept to grain boundaries by dislocations.

7.3 THE TSCC MECHANISMS INDICATED BY THE FRACTOGRAPHIC OBSERVATIONS

The TSCC mechanisms which are related to the fractographic features observed in the 316 s.s. and in the α-brass have been discussed in chapters 4 and 5. That the orientations of the primary facets of TSCC identified in the present study predominantly corresponded to {100} for the 316 s.s. and to {110} for the α-brass, is consistent with the findings of previous studies (e.g. 175, 194, 202). However, the new findings in the present study is that these {100} or {110} primary facets present microfacets, the orientations of which were clearly demonstrated on

a microscopic scale to correspond usually to two sets of alternating {111} slip planes. Most of the TSCC mechanisms proposed previously were based on the observations of apparently discontinuous cleavage propagation involving small crack advances (i.e., microcleavage) on the primary facets. The TSCC mechanisms proposed by Magnin (194) and Lichter et al. (175), which have been described in section 1.2.1.6, can indeed be applicable for explaining the occurrence of the TSCC primary facets on which {111} microfacets are not present or not resolved, but such model must at least be modified to explain the presence of {111} microfacets since the operative cracking mechanism should be fully consistent with the fractographic features.

The present observations on pre-immersed α-brass ribbon specimens (section 5.2.3.1.2) clearly showed that the cracking initiated on relatively large {111} facets (5~10 μm) approximately perpendicular to the tensile axis. This aspect implies that these relatively large {111} facets were probably produced by a cleavage mechanism. Then the crack propagated by alternating between two or more sets of {111} microfacets, indicating that the plasticity increased continuously as the crack propagated in this ductile metal, with this increased plasticity often finally resulting in the final portion of the fracture across the specimen thickness occurring by ductile necking. These microfractographic features suggest that the transgranular stress corrosion cracking mechanism incorporates aspects of the theories based on

environment enhanced localized plasticity (237, 210), and those on environmental embrittlement of a small zone of the material in the vicinity of the surface or of the crack tip (240, 241). The other important result obtained from the tests on the brass ribbon specimens is that some dissolution was necessary to initiate environmentally-induced crystallographic cracking.

In general, cleavage cracks are not expected in f.c.c. metals, presumably because of the multiplicity of slip system, high dislocation mobility and ease of cross slip. Cleavage can occur on {100} and {111} planes in f.c.c. irridium which has covalent atomic bonds, resulting in a resistance to slip which is inherently high. Irridium can be considered to be a f.c.c. metal only by accident. F.c.c. metals which fail by "cleavage" on {111} planes in the presence of some liquid metal environments has been reported (326). Fuller, Laws and Thompson (396) analyzed the effect of chemically induced bond rupture at the tip of sharp cracks. Their approach offers insight into brittle failure behaviour in ductile metals, although it is clearly oversimplistic in relation to real structural materials. Recently, several investigators have considered the effect of dislocations interactions near the crack tip on the local stress intensity, based on which several models have been proposed (249, 397-399). These models have also offered the possibilities for interpreting the brittle fracture behaviour in ductile metals under certain conditions; nevertheless, the interaction between a dislocation and a crack tip is complicated and still not

very clear.

Our lack of success in obtaining crystallographic cracking on superficially dealloyed 70 Cu-30 Zn ribbons in the absence of some dissolution certainly raises serious doubts about the applicability of a surface film or dealloyed layer in initiating cleavage which continues in the ductile substrate (202). A similar conclusion was arrived at by Kaufman and Fink (160, 161), who on bulk specimens during slow strain-rate testing were not able to produce SCC of 70 Cu-30 Zn α-brass in the quasi-total absence of oxygen in the solution. The film-induced or dealloyed-layer induced cleavage model also does not explain well the observations that the crack path changes to follow planes on which localized slip has occurred. That the crack does microscopically follow planes of localized slip is important in that it indicates that the cracking mechanism obtained on the ribbon specimens is similar to that which produces TSCC on bulk specimens of 70 Cu-30 Zn α-brass. Fritz et al. (400) showed that Cu-18% Au dealloyed to a depth of about 50 μm produced 50 μm-size cleavage cracks upon subsequent bending, which could not have propagated more than 0.5 μm into the ductile substrate. On the other hand, Cassagne et al. (401) reported that Cu-25% Au produced cracks that ran 5 μm beyond the dealloyed layer. Based on their calculations, Gerberich et al. (399) also argued that a 30-nm film generating a 2000-nm substrate crack would be overstating the effect for small cracks. Our results on ribbon specimens suggest that the brittle

crack in the ductile substrate observed by Cassagne et al. (401) can also be explained by some solution remaining in the dealloyed sponge and producing this cracking in the substrate.

Considering the contribution of dissolution on decohesion along slip planes, the results obtained on the ribbon specimens of α-brass (section 5.2) clearly indicated that dissolution was indeed necessary for the crystallographic crack initiation along slip planes in α-brass, based on the fact that no crystallographic fractures were obtained without the presence of corrosion slots or etch pits produced on the surface of the ribbon specimens during the pre-immersion. It is always possible that the necessary role of dissolution was only to produce sharp stress concentrators, but this should be less applicable to the slow strain rate experiments of Kaufman and Fink (160, 161). The role of dissolution for the crystallographic crack propagation appears less important, since the crack growth rates were generally sufficiently rapid to preclude a chemical dissolution reaction, such as the fine scale dissolution on {111} slip planes which has been suggested for TSCC on 316 stainless steel (section 4.4.2.1), being able to control the crack propagation. Moreover, the observations, such as decohesion occurring sequentially on two sets of alternating {111} slip planes, and the matching fractographic aspect of the {111} microfacets, are difficult to explain solely by a dissolution model.

The mechanism of TSCC which appears to be that which is most compatible with the microfractographic observations obtained on the brass ribbon specimens as well as on the stress-corroded bulk specimens of 316 stainless steel and of α-brass, including the variation in microfractography with K, is that adsorption of some species facilitates both localized plasticity in the crack tip region and decohesion along slip planes. Since adsorption at room temperature is a relatively fast process, it can account for the high crack velocities obtained on the ribbon specimens. However, identification of the adsorbed species for the present SCC systems, especially for the α-brass in the ammoniacal solutions employed, is not clear.

Concerning the possibility of hydrogen-assisted cracking (HAC), the necessary condition for any of the HAC models to apply is that there is a source of hydrogen for the condition under which cracking occurs. For the case of α-brass alloys-ammonia systems, Bertocci (402) has concluded that it is thermodynamically impossible for hydrogen to be produced when the brass is dissolving in stationary conditions. The possibility of hydrogen adsorption or discharge at the crack tip could not be excluded during the transient in terms of Bertocci's calculation (402). He also argued, however, that because of the inconclusiveness of the considerations and calculations, the study of other alloy systems with analogous cracking characteristics, but different chemical behaviour, should be considered as particularly

important. The example considered was that of cracking of Au-Cu alloy in acidic chloride solution, for which the possibility of hydrogen evolution has been ruled out (403), the cracking behaviour, however, in Au-Cu alloys is similar to that of brass. This suggests that HAC mechanisms generally can be discounted for copper alloys. As to the SCC of austenitic stainless steels in boiling aqueous magnesium chloride, such as for the annealed 316 s.s. and 310 s.s., it often has been considered to be not directly attributable to hydrogen (e.g. 404).

The alternate-slip/microvoid-coalescence mechanism proposed by Lynch (e.g. 168) for interpreting the cleavage-like fractographic aspects produced in the environment-assisted cracking, cannot explain well the microscopically resolvable {111} microfacets observed in the present study. Moreover, microvoids or small dimples were not observed by means of TEM replicas on both TSCC and near-threshold fatigue fracture surfaces (see Figs. 3.15, 4.22), also indicating that Lynch's model is required to be modified to account for these aspects. Nevertheless, the theory of locally enhanced plasticity due to contact with the environment is very consistent with the results of the present microfractographic observations. The more ductile dimple-like fractures which he observed were possibly due to the experimental conditions employed which were generally under high stresses and at high propagation rates. Such conditions would favour greater amounts of plastic deformation accompanying the crack propagation.

The very strong similarity of fractographic and crystallographic aspects observed between near-threshold fatigue cracking and TSCC in f.c.c. metals can be attributed to the influence of the environment and probably adsorption effects in both fracture processes on favouring localized slip and on promoting slip plane decohesion. The importance of the role of adsorption in both cracking processes is also suggested by the occurrence of predominantly {110} primary facets in TSCC of 70 Cu-30 Zn α-brass and a relatively large number of {110} primary facets in the near-threshold fatigue cracking in air of the same material as well as of copper. The occurrence of {110} primary facets is not favoured from purely mechanical considerations (81) and the occurrence of such facets was rarely observed in 316 stainless steel. The more frequent {110} facets observed for TSCC of α-brass than for near-threshold fatigue is also consistent with a more important chemical role in TSCC than in near-threshold fatigue. In the case of fatigue cracking at or near the threshold, the small plastic zone size with respect to the grain size always results in a tendency for localized slip and the fractographic features can theoretically be produced solely by reversed localized slip. For 2024-T351 aluminum alloy, a very reactive metal, adsorption cannot be ruled completely out even though for the fatigue tests being carried out in vacuum. That the very crystallographic cracking was obtained for very low da/dN in vacuum can mainly be attributed to the effect of the ultra-low crack propagation rates ($\leq 10^{-8}$ mm/cycle) at which there is strong tendency to get planar slip in peak-aged and overaged aluminium alloys. In

supporting this consideration, some {111} facets were occasionally observed for those fatigue cracking produced in laboratory air at relatively low da/dN (~ 10^{-6} mm/cycle).

That less crystallographic striations and easier propagation across grain boundaries and interfaces observed on corrosion-fatigue fracture surfaces at high da/dN values (~ 10^{-3} mm/cycle) for the 8 and 10% Mn AC bronzes (section 6.3.3) is also consistent with environment-enhanced plasticity, and in particular, because of the high da/dN values involved, consistent with adsorption-enhanced crack tip plastic deformation. However, in this case adsorption enhances more generalized plasticity by facilitating egress of dislocations nucleated from near crack tip sources instead of the nucleation and injection of dislocations at just the crack tip. Of course, the sharpness of the crack tip is rather different between cracking at high ΔK at which a mechanism of fatigue striation formation dominates and at low ΔK, where the crack tip remains very sharp. During TSCC of austenitic stainless steel and α-brass, the crack tip even the tip of the individual crack branches at high K tends to remain relatively sharp favouring localized slip. That environment enhances localized plasticity during TSCC and near-threshold fatigue cracking but enhanced more generalized plasticity during fatigue-cracking of bronze in 3.5% NaCl at high ΔK can be associated with differences in the sharpness of the crack tip. The very crystallographic near-threshold fatigue cracking of 2024-T351 Al alloy

obtained in vacuum can be associated with the tendency of the microstructure of this peak-aged alloy to strongly favour localized plasticity at low ΔK, since the shear of numerous very fine precipitates tends to favour planar slip behaviour. The crack growth rates obtained in vacuum were nevertheless considerably lower (10 times) than those obtained in our experiments for the same ΔK value (65).

In summary, based on the present observations, it is proposed that the fractography of TSCC in 70 Cu-30 Zn and in austenitic stainless steels involves simultaneously localized plasticity, a cleavage or a cleavage-like decohesion on slip planes, with both the localized slip and the cleavage-like decohesion being associated with crack tip adsorption effects. This proposal is also based on the strong similarity of the fractography of TSCC in comparison with that of the near-threshold fatigue cracking in the same metals, for which the comparison between tests in air and in vacuum on copper and 70 Cu-30 Zn indicates environment-enhanced localized plasticity in crack tip region as well as slip plane decohesion. That the corrosion-fatigue observations on 8-10% Mn-Al-Ni bronzes suggest that adsorption effects enhance more generalized plasticity at high da/dN and therefore on a blunted crack tip provides further support for this proposal, the more generalized plasticity being the result of the blunted crack tip.

CONCLUSIONS

1) The detailed microfractography of transgranular near-threshold fatigue cracking in both the f.c.c. and b.c.c. metals examined is consistent with this cracking being produced on a microscopic scale by decohesion on planes on which slip has occurred ahead of the crack tip, often on alternating slip planes.

2) In the case of all the f.c.c. metals tested in air, transgranular cracking near the threshold occurred predominantly along {100} planes in <110> or <100> directions. A relatively large number of {110} average orientations with <110> striation-like markings and near-<100> river lines were at times observed near the threshold for copper, for 70Cu-30Zn α-brass and for the f.c.c. phase of 8-10% Mn-Al-Ni bronze studied. Such primary {110} facets, however, were only rarely observed and when observed very small for the 316 stainless steel studied. On a microscopic scale, the primary {100} or {110} facets have at times been demonstrated to consist of two sets of alternating {111} microfacets, resulting in a striated or wavy microfractographic aspect. As well, these {111} microfacets have been identified to match well in an interlocking manner on opposite fracture surfaces.

3) In the case of the b.c.c. metals tested in air, different average orientations of primary facets, most often {100} and {110} were identified for both Fe-3% Si and AISI 1008 steel, and were also found to involve cracking following slip planes on a microscopic scale, and often alternating between two different sets of slip planes in much the same manner as that observed for the f.c.c. metals. The absence of any cleavage facets for both the b.c.c. metals studied, confirms further that near-threshold fatigue cracking is at least primarily produced by slip.

4) The type and the degree of complexity of the fractography observed during near-threshold fatigue cracking depended on the number of slip planes on which decohesion occurred and on the amount of decohesion on each slip plane. Both of these aspects, however, mainly depend on the orientation of the individual grain with respect to the stress axis; on the local stress effects associated with the need for differently oriented crack segments in neighbouring regions to join up to produce the macroscopic crack front; on the material conditions (e.g., relative tendency to obtain planar slip); and on the effect of the environment on the degree of slip planarity obtained.

5) A {100} <100> cracking crystallography was demonstrated to result from slip and decohesion occurring on all four sets of slip planes in the region of more complex fractography for 70Cu-30Zn α-brass tested in air at low da/dN values. That {100} <100> cracking crystallography was more often observed

in 2024-T351 Al alloy near-threshold propagation can be attributed to the formation of crack tip oxides which can reduce slip reversibility and thus can enhance multiple slip.

6) The highly crystallographic transgranular facets, including relatively large {111} facets observed at sufficiently low da/dN values both for α-brass and copper tested in air, but not for tests in vacuum, suggests that they are associated with an adsorption effect which acts to enhance the localization of the plastic deformation at the crack tip and thus, to promote slip plane decohesion. However, extremely low cracking rates favour larger {111} facets for 2024-T351 Al alloy tested in vacuum. This appears to be mainly attributed to the effect of the ultra-low crack propagation rates at which there is strong tendency to get planar slip in peakaged and overaged aluminium alloys. Moreover, these are very active metals and adsorption cannot be completely ruled out for the tests in vacuum.

7) Intergranular cracking occurred at relatively low da/dN values for copper and α-brass tested in air, but disappeared in the tests in vacuum. This behaviour indicates that for both metals this cracking is indeed an environmental effect, probably involving hydrogen-swept to grain boundaries by dislocations, which either produces grain boundary embrittlement facilitating apparently true intergranular cracking or enhances localized plasticity in the vicinity of grain boundaries promoting the occurrence of quasi-intergranular facets. In

vacuum, however, this is prevented in both metals by the absence of such an environmental effect. An alternate possible explanation is that more diffuse slip produced by testing in vacuum produces less incompatibility and stress concentration at grain boundaries.

8) On the finest microscopic scale observed, the TSCC of annealed stainless steels tested in boiling (154°C) $MgCl_2$ solution and of 70Cu-30Zn α-brass of DCB specimens tested in the ammoniacal solutions occurred by decohesion on {111} slip planes. The combination of the different sets of {111} microfacets resulted in larger primary facets, the orientations of which predominantly corresponded to {100} for the austenitic stainless steels and to {110} for the α-brass studied.

9) The microfractographic features and the cracking crystallography exhibited a strong variation with the stress intensity factor K both for the annealed 316 stainless steel and the α-brass examined. This variation possibly is the origin of the frequent differences in TSCC fractographic features published by different authors for unspecified K values.

10) For TSCC of the 316 s.s., at low K (< 15 MPa $m^{1/2}$), the fracture facets were relatively smooth and presented an average facet orientation close to or coincident with {100}. Also <110> river lines and finely spaced <110> striation-like markings were often present. The etch-pitting studies indicated that {100} <110> cracking resulted from fine-scale decohesion occurring on

an alternating manner on two sets of {111} microfacets. At somewhat higher K values (15~20 MPa $m^{1/2}$), herringbone or fan-shaped patterns of river lines appeared for which the {100} primary facets presented both <110> and <100> river lines. The evidence has indicated that the <100> river lines corresponded to regions in which decohesion occurred on four sets of {111} microfacets. At high K values (K > 20 MPa $m^{1/2}$), cracking occurred on a large number of sets of {111} slip planes on which an important amount of decohesion occurred, giving rise to the formation of more evident {111} microfacets which adopted an increasing sheet-like appearance resulting in more complicated fractographic aspects observed.

11) For TSCC of 70Cu-30Zn α-brass, the {110} <100> crystallographic cracking and particularly those of {110} primary facets with a preferential <112> or near-<112> orientations of river lines, were frequently found at relatively low and intermediate K values. Cracking, however, on a {110} plane in a <110> direction was only very rarely observed at low K values but was more frequently observed at high K values. Also, it was demonstrated that {110} <100> and {110} <112> cracking resulted from fine-scale decohesion occurring in alternating manner on two sets of {111} microfacets, however, {110} <110> cracking resulted from decohesion on two sets of {111} microfacets meeting parallel to the crack propagation direction. The size of the alternating {111} microfacets increased with increasing K and the

occurrence of large {111} microfacets of several orientations at high K values for TSCC of α-brass. These last two aspects are similar to the observations on 316 s.s. and clearly indicate that microscopically the crack path follows {111} planes on which slip has occurred and that this plastic deformation plays an important role in producing crack propagation.

12) The replica TEM observations performed on the fracture surfaces produced by near-threshold fatigue cracking or by transgranular stress-corrosion cracking for 316 stainless steels studied indicated that the visibility of {111} microfacets present on an average primary facet was higher in the observations by the replica TEM techniques. For the 316 stainless steel, the microfacets were generally visible on the TEM replicas. These observations on replicas indicate that, for SEM observations, the apparent absence of microfacets on some relatively smooth {100} primary facets resulted from the microfacets present being too small to be adequately resolved by SEM.

13) The study of the 70Cu-30Zn ribbon specimens fractured after immersion in the ammoniacal solutions clearly indicated that the cracking initiated on relatively large {111} facets (5~10 μm) approximately perpendicular to the tensile axis, suggesting that these large {111} facets were probably produced by a cleavage mechanism. The crack then propagated by alternating between two or more sets of {111} microfacets, which indicates that the plasticity increased continuously as the crack propagated in the ductile

material, with this increased plasticity often resulting in the final portion of the fracture across the specimen thickness occurring by ductile necking. Furthermore, fractographic aspects of crystallographic cracking on the ribbons are strongly similar to those observed for TSCC at intermediate and high K values on the bulk specimens of both α-brass and 316 s.s., demonstrating that the mechanical stress must play an important role in the fracture processes of the ribbons. All of these fractographic features observed on the ribbon specimens suggest that the TSCC mechanism may incorporate aspects of the theories based on environment enhanced localized plasticity and those on environmental embrittlement of a small zone of the material in the vicinity of the crack tip.

14) That no crystallographic cracking was obtained on pre-immersed ribbon specimens of α-brass in the absence of crystallographic corrosion slots or etch pits larger than ≈ 0.1 μm indicates that dissolution was indeed necessary for the initiation of such crystallographic cracking along slip planes in α-brass. However, the possible role of dissolution in promoting crystallographic crack propagation appears less important, since the crack growth rates for the ribbons were generally sufficiently rapid to preclude a chemical dissolution reaction.

15) That the lack of success in obtaining crystallographic cracking on superficially dealloyed 70Cu-30Zn α-brass ribbons in the absence of microscopically visible

dissolution, raises serious question about the applicability of a surface film or dealloyed layer in initiating cleavage which continues in the ductile substrate.

16) The mechanism of TSCC which appears to be most compatible with the microfractographic observations obtained on the stress corroded bulk specimens of 316 stainless steel and of α-brass as well as on the brass ribbon specimens is that adsorption of some species facilitates both localized plasticity in the crack tip region followed by decohesion along the planes on which this slip has occurred. This proposal is also consistent with the near-threshold fatigue cracking in the same metals for which the comparison between tests in air and in vacuum on copper and 70Cu-30Zn indicates the occurrence for tests in air of environment-enhanced localized plasticity in the crack tip region as well as slip plane decohesion. Therefore, the very strong similarity of fractographic and crystallographic aspects observed for near-threshold fatigue cracking and TSCC in f.c.c. metals can be attributed to the similar important role of localized slip in both fracture processes, for which the crack tips remain relatively sharp. The environment plays a role on favouring localized slip and on promoting slip plane decohesion, with this role being of particular importance during TSCC.

17) That less crystallographic striations and easier propagation across grain boundaries and interfaces observed on corrosion-fatigue fracture surfaces at

high da/dN values for 8-10% Mn-Al-Ni bronzes tested in the NaCl solution is also consistent with environment-enhanced crack tip plasticity. In particular, these results are consistent with the occurrence of adsorption-enhanced more generalized plasticity for the blunted crack tip.

18) Detailed microfractography is one of the most important tools in identifying fracture mechanisms. If the fracture surface has not been damaged after fracture, any proposed fracture mechanism must be fully compatible with the detailed aspects of the fracture surface. Theories previously proposed for TSCC which show significant compatibility with the present study include those of Lynch, of Magnin*, and of Lichter et al. None of these theories are fully compatible with the present results in that none predicts a fracture path which microscopically follows slip planes. The theory of Lynch is that which shows the best agreement with this thesis in emphasing the important role of adsorption-enhanced localized slip in producing TSCC in f.c.c. metals. The present study, however, showed further disagreement with the mechanism proposed by Lynch in that the fine microvoids or dimples which he has observed on some materials were not observed on TEM replicas in the present study.

* Magnin (416) has very recently shown that this model can explain an alternating {111} fracture path, although some true {100} cracking would also be expected to occur.

RECOMMENDATIONS

The following experimental work is recommended for further research on this subject:

1) Detailed microfractographic examinations of TSCC fracture surfaces on other systems, particularly for f.c.c. metals displaying strong slip planarity would be useful in further confirming the role of {111} slip plane cracking.

2) A detailed microfractographic study of transgranular cracking produced by liquid metal embrittlement would also be useful to compare to the results of the present study, since for liquid metal embrittlement the role of adsorption on promoting fracture is widely accepted.

3) Detailed microfractographic studies of TSCC on single crystal of chosen orientations would be and useful to investigate the role of the tensile stress component on producing {111} facets decohesion and on clarifying further the relationship between slip and decohesion on {111} planes in f.c.c. metals during TSCC.

4) Experiments on 70Cu-30Zn ribbon specimens fractured in liquid nitrogen after immersion in ammoniacal solutions are required to clarify the validity of the adsorption effect on the occurrence of the crystallographic features in this type of fracture.

5) Auger analysis of the superficial de-alloyed layers on α-brass ribbon specimen

surfaces after immersion in ammoniacal testing solutions are required to verify the presence of the de-alloyed layers, and in particular to verify whether this layer is required for initiating brittle fracture during TSCC as suggested by some investigators.

6) Detailed examination of the dislocation structures produced near the crack tip, associated with the near-threshold fatigue cracking in different environments and during TSCC would be beneficial in understanding how environment modifies the dislocation structure characteristics at a propagating crack tip region and its influence on the fracture processes. However, care should be taken to avoid any additional artifacts during preparing of the foil for TEM examination.

REFERENCES

(1) J. Ruppen, P. Bhowal, D. Eylon, and A.J. McEvily, Fatigue Mechanisms, J.T. Fong, ed., ASTM, STP675, Philadelphia, p. 47 (1979).

(2) C. Laird, Metallurgical Treatises, J.K. Tien and J.F. Elliot, ed., AIME, Warrendale, PA, p. 505 (1981).

(3) H. Mughrabi, 5th Int. Conf. On Strength of Metals and Alloys, P. Haasen, V. Gerold, and G. Kostorz, ed., Pergamon Press, Oxford, England, p. 1615 (1980).

(4) W.H. Kim and C. Laird, Acta Metall., 26, 777 and 789 (1978).

(5) S. Taira, K. Tanaka, and M. Hoshina, p. 135 in ref. 1.

(6) P.C. Paris and F. Erdogan, J. Basic Eng. Trans., ASME, Series D, 85 (4), p. 528 (1963).

(7) R.O. Ritchie, Fatigue Thresholds, J. Backlund et al., ed., Warley, W. Midlands, p. 503 (1982).

(8) R.O. Ritchie, Intl. Metals Review, 24 (Nos. 5 and 6), 205 (1979).

(9) C.J. Beevers, Metals Sci., 11, 362 (1977).

(10) N.J. Marchand, J.-P. Baïlon, and J.I. Dickson, Metall. Trans. A, 19A, 2575 (1988).

(11) R.G. Forman, V.E. Kearney, and R.M. Engle, J. Basic Engng. Trans., ASME, 89, 459 (1967).

(12) W. Elber, ASTM STP 486, p. 230 (1971).

(13) R.W. Hertzberg, Deformation and Fracture Mechanics of Engineering Materials, John Wiley and Sons, ed., p. 545 (1983).

(14) J.I. Dickson, J.P. Baïlon and J. Masounave, J. Can. Metall. Quart., 20, 317 (1981).

(15) C.J. Beevers, R.J. Cooke, J.F. Knott, and R.O. Ritchie, Metals Sci., 9, 119 (1975).

(16) J. Masounave and J.P. Baïlon, Scripta Metall., 10, 165 (1976).

(17) M. Klesnil and P. Lukas, Mater. Sci. Engng., 9, 231 (1972).

(18) R.W. Hertzberg, p. 550 in ref. 13.

(19) N. Thompson, N.J. Wadsworth, and N. Louat, philos. mag., 1, 113 (1956).

(20) D.J. Duquette, Mechanisms of Environment Sensitive Cracking of Materials, P.R. Swann, F.P. Ford and A.R.C. Westwood, Metallurgical Society, U.K., p. 305 (1977).

(21) R.M. Latanision and A.R.C. Westwood, Adv. Corros. Sci. Technol., 1, 51 (1970).

(22) H. Shen, S.E. Podloseck, and I.R. Kramer, Acta Metall., 14, 341 (1966).

(23) N.J. Wadsworth, Philos. Mag., 6, 387 (1961).

(24) C. Laird and G.C. Smith, Philos. Mag., 8, 1945 (1963).

(25) T.S. Sudarshan and M.R. Louthan, Jr., International Materials Reviews, 32, No. 3, 121 (1987).

(26) J.C. Grosskeutz and C.Q. Bowles, Environment Sensitive Mechanical Behavior, A.R.C. Westwood and N.S. Stoloff, ed., Gordon and Breach, 1967.

(27) W.A. Wood, M.S. Cousland, and K.R. Sargent, Acta Metall., 11, 643 (1963).

(28) B.J.R. Hodgson, Met. Sci. J., 2, 235 (1968).

(29) W.E. Krupp, D.W. Hoeppner, and E.C. Walker, Corrosion Fatigue, O.F. Deveraux, A.J. McEvily and R.W. Staehle, ed., NACE, Houston, p. 486 (1972).

(30) R.P. Wei, P.S. Pao, R.G. Hart, T.W. Weir, and G.W. Simmons, Metall. Trans., 11A, 151 (1980).

(31) G.M. Scamans and C.D.S. Tuck, p. 482 in ref. 20.

(32) D.L. Davidson and J. Lankford, Int. J. Fract. Mech., 17, 247 (1981).

(33) W.J.D. Shaw and I. LeMay, Can. Metall. Q., 23, 1 (1984).

(34) J.P. Baïlon, M. Elboujdaini and J.I. Dickson, Fatigue Crack Growth Threshold Concepts, D.L. Davidson and S. Suresh, ed., p. 63 (1984), The Metallurgical Society of AIME.

(35) B. Bouchet, J. de Fouquet and M. Aguillon, Acta Metall., 23, 1325 (1975).

(36) A.T. Stewart, Engng. Fract. Mech. 13, 463 (1980).

(37) R.O. Ritchie, C.M. Moss and S. Suresh, J. Engng. Mater. Tech. H, 102, 293 (1980).

(38) R.P. Skelton and J.R. Haigh, Mater. Sci. Engng. 36, 17 (1978).

(39) K. Minakawa and A.J. McEvily, Scripta Metall. 15, 633 (1981).

(40) R.O. Ritchie and S. Suresh, Metall. Trans. A, 13A, 937 (1982).

(41) J.L. Yuen and P. Roy, p. 185 in ref. 34.

(42) J.N. Vincent and L. Rémy, Fatigue Thresholds, J. Backlund, A.F. Blom and C.J. Beevers. ed., EMAS, p. 441 (1982).

(43) J.P. Hickerson and R.W. Hertzberg, Metall. Trans. 3, 179 (1972).

(44) R. Kumble and A.J. McEvily, Int. J. Fract. Mech. 8, 209 (1972).

(45) B. Tomkins and W.D. Biggs, J. Sci., 4, 544 (1969).

(46) C.E. Feltner and C. Laird, Acta Metall. 5, 1621, and 1633 (1967).

(47) A. Abel, M. Wilhelm and U. Gerold, Mater. Sci. Engng. 37, 187 (1979).

(48) H. Mughrabi, R. Wang, K. Differt and V. Essmann, Fatigue Mechanisms (Advance in Quantitative Measurements of Physical Damage), J. Lankford, D.L. Davidson, M.L. Morris and R.P. Wei, ASTM, STP 811, 5.45 (1983).

(49) R.W. Landgraf, Fatigue and Microstructure, ASM, Metals Park, Ohio, p. 439 (1979).

(50) P. Lukas and M. Klesnil, Mater. Sci. Engng., 11, 345 (1973).

(51) G. Chalant and L. Rémy, Acta Metall. 28, 75 (1980).

(52) P. Lukas and W.W. Gerberich, Mater. Sci. Engng., 51, 203 (1981).

(53) E.K. Priddle, Scripta Metall., 12, 49 (1978).

(54) J.P. Benson and D.V. Edmonds, Metal. Sci., 12, 223 (1978).

(55) J.P. Benson, Metal. Sci., 13, 535 (1979).

(56) J. Lanteigne, Ph.D. Thesis, Ecole Polytechnique, Montreal (1979).

(57) J.L. Robinson and C.J. Beevers, Metal. Sci. 7, 153 (1973).

(58) J. Lindigkeit, G. Terlinde, A. Gysler and G. Lütjering, Acta Metall., 27, 1717 (1979).

(59) J.P. Baïlon, J. Masounave and J. Lanteigne, Scripta Metall. 12, 607 (1978).

(60) R. Dang, G. Yu and H. Li, Theor. Appl. Fract. Mech., 7, 37 (1987).

(61) W.W. Gerberich and N.R. Moody, Fatigue Mechanisms, J.F. Fong, ed. ASTM, STP 675, Philadelphia p. 292 (1979).

(62) H. Kitagawa, R. Yunki and T. Ohira, Engng. Fracture Mech., 7, 515 (1975).

(63) H.C. Heikkemen, Fu Shiong Li and E.A. Starke Jr., Mater. Sci. Engng., 51, 17 (1981).

(64) M.C. Lafarie-Frenot and C. Gasc, Fatigue Engng. Mater. Struct., 6, 329 (1983).

(65) J. Petit, p. 3 in ref. 34.

(66) J.E. King, Mater. Sci. Tech., 3, 750 (1987).

(67) S.R. Mediratta, V. Ramas Wamy and P. Ramarao, Int. J. Fatigue, 7, 101 and 107 (1985).

(68) H. Suzuki and A.J. McEvily, Met. Trans. A 10A, 475 (1979).

(69) I.C. Mayes and T.J. Baker, Mater. Sci. and Tech., 2, 133 (1986).

(70) M.E. Fine, Metall. Trans. A, 11A, 365 (1980).

(71) R.O. Ritchie, J. Engng. Mater. Tech., Trans. ASME, Series H, 99, 195 (1977).

(72) H. Kitagawa, H. Kishitani, and J. Matsumoto, in Proc. 3rd Intl. Cong. on Fracture (ICF-3), Dusseldorf, Verein Deutsher Eisenhuttenleute, 5, V-444/A (1973).

(73) H. Kitagawa and S. Takahashi, in Proc. 2nd Intl. Conf. on Mech. Beh. of Materials, Boston, MA, p. 627 (1976).

(74) G.G. Garrett and J.F. Knott, Acta Met. 23, 841 (1975).

(75) S. Suresh and R.O. Ritchie, p. 227 in ref. 34.

(76) P.K. Liaw, T.R. Leax, R.S. Williams, and M.G. Peck, Metall. Trans. A, 13A, 1607 (1982).

(77) R.W. Hertzberg and W.J. Mills, ASTM STP 600, p. 220 (1976).

(78) P.J.E. Forsyth and D.A. Ryder, Metallurgia, 63, 117 (1961).

(79) C. Laird and G.C. Smith, Phil. Mag., 7, 847 (1962).

(80) B. Tomkins and Biggs, J. Mater. Sci., 4, 544 (1969).

(81) R.M.N. Pelloux, Trans., ASM, 62, 281 (1969).

(82) P. Neumann, Acta Metall., 22, 1155 (1974).

(83) C.Q. Bowles and D. Broek, Int. Journ. of Fract. Mech., 8, 75 (1972).

(84) R. Koterazawa, M. Mori, T. Matsni, and D. Shimo, J. Eng. Mater. Technol., (Trans. ASME) 95, No. 4, 202 (1973).

(85) R.J.H. Wanhill, Metall. Trans., 6A, 1587 (1975).

(86) W. Weibull, Acta Metall., 11, No. 7, 725 (1963).

(87) D.O. Swenson, J. Appl. Phys., 40, 3467 (1969).

(88) C.D. Beachem, Fracture I, Liebowitz, Academic Press, 243 (1968).

(89) R.W. Hertzberg, ASTM STP 415, 205 (1967).

(90) D.A. Meyn, Trans. ASM, 61, No. 1, 42 (1968).

(91) D.L. Davidson and J. Lankford, Metall. Trans. A, 15A, 1931 (1984).

(92) H. Vehoff, and P. Neumann, Acta Metall. 27, 915 (1979).

(93) P. Neumann, H. Vehoff and H. Fuhlrott, ICF4, Fracture 1977, 2, 1313 (1977).

(94) P. Neumann, H. Vehoff and H. Fuhlrott, p. 371, in ref. 5.

(95) P. Rieux, J. Driver and J. Rieu, Acta Metall., 27, 145 (1979).

(96) C.E. Richards, Acta Metall., 19, 583 (1971).

(97) C.J. Beevers, Metal Science, p. 418, August (1980).

(98) J.C. Chesnutt and J.C. Williams, Metall. Trans. A, 8A, 515 (1977).

(99) D.A. Meyn, Metall. Trans. 2, 853 (1971).

(100) R.J.H. Wanhill, Metall. Trans. A, 7A, 1365 (1976).

(101) A.W. Bowen, Acta Metall., 23, 1401 (1975).

(102) C.M. Ward-Close and C.J. Beevers, Metall. Trans. A, 11A, 1007 (1980).

(103) D. Hoeppner, Metallography, 11, 129 (1978).

(104) D. Larouche, Ph.D. Thesis, Ecole Polytechnique de Montréal (1989).

(105) R.M.N. Pelloux, Trans. ASM, vol. 57 (1964), p. 511.

(106) D. Broek, in Fracture, Chapman and Hall, p. 754 (1969).

(107) C.D. Beachem, Trans. ASM, vol. 60 (No. 3), p. 325 (1967).

(108) J.I. Dickson, text book, A Tool in Failure Analysis and in Fracture Research, Ecole Polytechnique de Montréal.

(109) J.I. Dickson, A.E. Geckinli, and I. Uribe-Perez, Mater. Sci. Engng., 60, 231 (1983).

(110) J.P. Baïlon, P. Chappuis, J. Masounave and J.I. Dickson, p. 277 in ref. 7.

(111) J.I. Dickson, Li Shiqiong, and J.P. Baïlon, Fatigue 87, R.P. Gangloff, R.O. Ritchie, E.A. Starke, Jr., and J.A. Wert, ed., EMAS, vol. 2, p. 759 (1987).

(112) J.I. Dickson, D. Groulx, Li Shiqiong and D. Tromans, Mater. Sci. Engng. 94, 155 (1987).

(113) P.J.E. Forsyth, C.A. Stubbington, and D. Clark, J. Inst. Metals, 90, 238 (1963).

(114) C.A. Stubbington, Metallurgia, 68, 109 (1963).

(115) K.R.L. Thompson and J.V. Craig, Metall. Trans., 1, 1042 (1970).

(116) Z.X. Tong, S. Lin and C.M. Hsao, Scripta Metall. 20, 967 (1986).

(117) G.R. Yoder, P.S. Pao, M.A. Imam and L.A. Colley, Scripta Metall. 22, 1241 (1988).

(118) K.T. Venkateswara Rao, R.J. Bucci and R.O. Ritchie, Fatigue 90, H. Kitagawa and T. Tanaka, ed., MCEP Ltd., p. 963 (1990).

(119) M. Gell and G.R. Leverant, Acta Metall. 16, 553 (1968).

(120) S. Purusthothaman, and J.K. Tien, Metall. Trans., 9A, 351 (1978).

(121) P.A.S. Reed, P. Woolin, and J.E. King, p. 1085 in ref. (118).

(122) P.K. Liaw and W.A. Logsdon, Acta Metall. 36, No. 7, 1731 (1988).

(123) H. Müllner, B. Weiss and R. Stickler, p. 423 in ref. (7).

(124) Z.X. Tong and J.P. Baïlon, to be published, Ecole Polytechnique de Montréal.

(125) J.P. Baïlon et al., Microstructure, 1, 277 (1982).

(126) J.A. Carlson, and D.A. Koss, Acta, Metall. 26, 123 (1978).

(127) R. Koterazawa, and D. Shimo, Materials (in Japanese), 26, 12 (1977).

(128) A. Otsuka, K. Mori and S. Tsuyama. Materials (in Japanese), 29, 42 (1980).

(129) R.P. Wei and A.J. Baker, Phil. Mag., 12, 1005 (1965).

(130) K. Asami, and M. Terasawa, Journal of the Society of Materials Science (Japan), 30, 803 (1980).

(131) T. Tanaka and M. Korugi, Basic Questions in Fatigue, J.T. Fong and R.J. Fields, ed., ASTM, STP 924, Philadelphia, vol. 1, p. 98 (1988).

(132) H.D. Williams and G.C. Smith, Phil. Mag., 13, 835 (1966).

(133) D.E. Neal and P.A. Blenkinsop, Acta Metall. 24, 59 (1976).

(134) M. Sugano and C.M. Gilmore, Metall. Trans. A., 11A, 559 (1980).

(135) P.J.E. Forsyth, Acta Metall. 11, 703 (1963).

(136) C.D. Beachem and D.A. Meyn, Electron Fractography, ASTM, STP 436, p. 59 (1968).

(137) R.J. Cooke, P.E. Irving, C.S. Booth and C.J. Beevers, Eng. Fract. Mech. 7, 69 (1975).

(138) R.O. Ritchie, Metals Sci., 11, 368 (1977).

(139) Y. Higo, A.C. Pickard and J.S. Knott, Metals Sci., 15, 233 (1981).

(140) J. Congleton, R.N. Parkins and J. Yu, Mater. Sci. Techn., 1, 1046 (1985).

(141) J.P. Baïlon, J.I. Dickson and Li Shiqiong, Basic Mechanisms in Fatigue of Metals, P. Lukas and J. Polak, ed., Academia, Prague, p. 361 (1988).

(142) J.L. Robinson and C.J. Beevers, Titanium Science and Technology, R.I. Jaffee and H.M. Burte, ed., Plenum, New York, vol. 2, p. 1245 (1973).

(143) K.S. Ravichandran, E.S. Dwarakadasa, and Kishore, Mater. Sci. Engng. 83, L11, (1986).

(144) T.S. Sudarshan, M.R. Louthan, Jr., T.A. Place, and H.H. Mabie, Fatigue Life Analysis and Prediction, V.S. Goel, ed., ASM Metal Park, OH, p. 47 (1986).

(145) J.P. Baïlon, J.I. Dickson, Li Shiqiong, and D. Larouche, vol. 3, p. 1333 in ref. (118).

(146) R.P.V. Evans, N.B. Owen and B.E. Hopkins, Eng. Fract. Mech., 3, 463 (1971).

(147) J.D. Frandsen and H.L. Marcus, Scripta Met. 9, 1089 (1975).

(148) A.T. Stewart, Eng. Fract. Mech., 13, 463 (1980).

(149) H. Moore and S. Beckinsale, J. Inst. Met. Vol. XXIII, No. 1, 225 (1920).

(150) W.Y. Chu, J. Yao, and C.H. Hsiao, Corrosion, 40, 302 (1984).

(151) R.W. Staehle, Fundamental Aspects of Stress-Corrosion Cracking, R.W. Staehle, A.J. Forty, D. Van Rooyen, ed., NACE, Houston, p. 1, (1969).

(152) J.I. Dickson, Course notes, Micromechanism of Fracture, Ecole Polytechnique de Montréal.

(153) D.P. Williams, P.S. Pao, and R.P. Wei, Environment Sensitive Fracture of Eng. Mat., Z.A. Foroulis, ed., (TMS) New York, p. 3 (1979).

(154) M.O. Speidel, The Theory of Stress-Corrosion Cracking of Alloys, J.C. Scully ed., NATO, Brussels, p. 345 (1971).

(155) J.I. Dickson, P. Martin, A. Febres and J.P. Baïlon, Microstructural Science, vol. 15, p. 113 (1987).

(156) P. Martin, J.I. Dickson and J.P. Baïlon, Mater. Sci. Engng., 69, L9, (1985).

(157) J.A. Beavers and E.N. Pugh, Metall. Trans. A, 11A, 809 (1980).

(158) A.J. Bursle and E.N. Pugh, p. 18 in ref. (153).

(159) J.I. Dickson and J.P. Baïlon, Time-Dependent Fracture, Martinus Nijhoff Ltd. Dordrecht p. 69 (1985).

(160) M.J. Kaufman and J.L Fink, Acta Metall., 36, No. 8, 2213 (1988).

(161) M.J. Kaufman, and J.L. Fink, Metall. Trans. A, 18A, 1539 (1987).

(162) E.I. Meletis and R.F. Hochman, Corros. Sci. 26, No. 1, 63 (1986).

(163) E.I. Meletis and R.F. Hochman, Corros. Sci. 24, No. 10, 843 (1984).

(164) W.K. Blanchard, Jr. and L.A. Heldt, Metall. Trans. A, 20A, 1439 (1989).

(165) D.N. Fager and W.F. Spurr, Trans. ASM, 61, 283 (1968).

(166) R.W. Lyceti and J.C. Scully, Corros. Sci., 19, 799 (1979).

(167) H. Kimura, Trans. Japan Inst. Met., 26, 527 (1977).

(168) S.P. Lynch, Acta Metall., 36, No. 10, 2639, (1988).

(169) D.A. Mauney, E.A. Starke, Jr., and R.F. Hochman, Corrosion, 29, 241 (1973).

(170) B. Cox, Corrosion, 28, 207 (1972).

(171) P. Majumdar, M. Golozar and J.C. Scully, Hydrogen Effects in Metals, AIME, Warrendale, PA, p. 881 (1983).

(172) J.A. Beavers, J.C. Griess and W.K. Boyd, Corrosion, 36, 292 (1981).

(173) R. Bakish, Trans. AIME, 9, 494 (1957).

(174) B.D. Lichter, T.B. Cassagne, W.F. Flanagan and E.N. Pugh, Microstructural Science, 13, 361 (1985).

(175) W.F. Flanagan, P. Bastias and B.D. Lichter, Submitted to Acta Metall.

(176) W.D. Sylwestrowicz, Corrosion, 26, 552 (1970).

(177) G.M. Sparkes and J.C. Scully, Corros. Sci., 11, 641 (1971).

(178) K. Sieradzki, R.L. Sabatini and R.C. Newman, Metall. Trans. A, 15A, 1941 (1984).

(179) M. Kermani and J.C. Scully, Corros. Sci. 19, 111 (1979).

(180) M. Kermani and J.C. Scully, Corros. Sci., 19, 489 (1979).

(181) J.L. Nelson and E.N. Pugh, Metall. Trans. A, 6A, 1459 (1975).

(182) S.P. Lynch, Metals Science, 15, 463 (1981).

(183) K. Kon and N. Ohtani, J., Jpn. Inst. Met. 40, 1082 (1976).

(184) R.E. Reed and H.W. Paxton, First International Congress on Metallic Corrosion, Butterworths, London, p. 301 (1962).

(185) R. Liu, N. Narita, C. Altstetter, H. Birnbaum and E.N. Pugh, Metall. Trans. A, 11A, 1563 (1980).

(186) J.M. Silcock, Br. Corrosion, J. 16, 78 (1981).

(187) Y. Mukai, M. Watanabe and M. Murata, Fractography in Failure Analysis, ASTM STP 645, p. 164 (1978).

(188) J.D. Harston and J.C. Scully, Corrosion, 26, 387 (1970).

(189) T. Nakanayama and M. Takano, Corrosion, 37, 229 (1981).

(190) M. Marek and R.F. Hochmann, Corrosion, 27, 361 (1971).

(191) M. Ahlers and E. Riecke, Corros. Sci., 18, 21 (1978).

(192) G.M. Scamans and P.R. Swann, Corros. Sci., 18, 983 (1978).

(193) D. Tromans and J. Nutting, Corrosion, 21, 143 (1965).

(194) T. Magnin, R. Chieragatti and R. Oltra, Acta Metall. 1313 (1990).

(195) D.J. Duquette Corrosion, 46, No. 6, 434 (1990).

(196) F.A. Champion, Symposium on Internal Stresses in Metals and Alloys, Institute of Metals, London, p. 468 (1948).

(197) H.L. Logan, J. Res. Natn. Bur. Stand., 48, 99, (1952).

(198) F.P. Ford, Corrosion Process, R.N. Parkins, ed., Applied Science, p. 271 (1982).

(199) D.A. Jones, Metall. Trans. A, 16A, 1133 (1985).

(200) J.C. Scully, Corros. Sci., 7, 197 (1967).

(201) R.N. Parkins, Corros. Sci., 20, 147 (1980).

(202) K. Sieradzki and R.C. Newman, Phil. Mag. A, 51, No. 1, 95 (1985).

(203) R.C. Newman and K. Sieradzki, Scripta. Metall. 17, 621 (1983).

(204) W.F. Flanagan, P. Bastias and B.D. Lichter, Acta Met. Mat., 39, No. 4, 695 (1991).

(205) H.W. Pickering, P.R. Swann, Corrosion, 19, No. 11, 373t (1963).

(206) E.N. Pugh, Corrosion, 41, No. 9, 517 (1985).

(207) W.F. Flanagan, E. Chammas, P. Bastias, and B.D. Lichter, Third International Conference on Fundamentals of Fracture, Irsee, June 19-24, 1989.

(208) R.C. Newman, T.S. Shahrabi, and K. Sieradzki, Scripta Metall., 23, 71 (1989).

(209) T.B. Cassagne, W.F. Flanagan and B.D. Lichter, Metall. Trans. 17A, No. 4, 703 (1986).

(210) S.P. Lynch, Metallography, 23, 147 (1989).

(211) A.N. Stroh, Phil. Mag., 1, 489 (1956).

(212) R.H. Jones, Metals Handbook, 9th ed., Corrosion ASM, Metals Park, OH, 13, 145 (1987).

(213) J.R. Galvele, Corrosion Sci., 27, No. 1, 1 (1987).

(214) H.H. Uhlig, Physical Metallurgy of Stress-Corrosion Fracture, Interscience,

New York, 1 (1959).

(215) H.H. Uhlig, Fundamental Aspects of Stress Corrosion Cracking, R.W. Staehle, A.J. Forty, D. Van Rooyen, ed., NACE, Houston, p. 86 (1969).

(216) C.D. Beachem, Metall. Trans., 3, 2 (1972).

(217) W.H. Johnson, Iron, 1, 291 and 452 (1873) (quoted from "Introduction" of Hydrogen Damage, p. xiv).

(218) C.A. Zapffe and C.E. Sims, Trans. AIME, 145, 225 (1941).

(219) A.S. Tetelman and W.D. Robertson, Acta Metall., 11, 415 (1963).

(220) A.S. Tetelman, p. 446 in ref. (215).

(221) M. Smialowski, SCC and HE of Iron Base Alloys, NACE, 5, p. 405 (1977).

(222) P. Bastien and P. Azou, C.R. Acad. Sci., Paris 232, p. 1845 (1951).

(223) J.K. Tien, A.W. Thompson, I.M. Bernstein and R.J. Richards, Metall. Trans. A, 7, 821 (1976).

(224) J.K. Tien, S.V. Nair and R.R. Jenson, Effect of Hydrogen on Behavior of Materials, I.B. Beinstein and A.W. Thompson, ed., TMS-AIME, Warrendale, PA (1981).

(225) M. Kurkela and R.M. Latanision, Scripta Met. 13, 927 (1979).

(226) C. Paes de Oliveria, M. Aucouturier and P. Lacombe, Corrosion, 36, No. 2, 53 (1980).

(227) N.J. Petch, Phil. Mag., 1, No. 8, 831 (1956).

(228) H.K. Birnbaum, p. 326, in ref. (153).

(229) D.G. Westlake, Trans. ASM, 62, 1000 (1969).

(230) S. Gahr, M.L. Grossbeck, and H.K. Birnbaum, Acta Metall., 25, 125 (1977).

(231) B. Baranowski, quoted from paper of J.P. Hirth, Metall. Trans., 11A, 887 (1980).

(232) H.K. Birnbaum, Atomistics of Fracture, R.M. Latanision and J.R. Pickens, ed., Corsica, France, Plenum, N.Y., p. 733 (1983).

(233) J.P. Hirth, Chemistry and Physics of Fracture, R.M. Latanision and R.H. Jones, ed., NATO ASI Series E: Applied Science No. 30, p. 538 (1987).

(234) S. Koike and T. Suzuki, Acta Metall., 29, 553 (1981).

(235) C.D. Cann and E.E. Sexton, Acta Metall., 28, 1215 (1980).

(236) K. Nuttall and A.J. Rogowski, J. Nucl. Mater., 80, 279 (1979).

(237) H.K. Birnbaum, in Hydrogen Effects on Materials Behavior, N.R. Moody and A.W. Thompson, ed., TMS, p. 639 (1990).

(238) L.B. Pfeil, Effect of Occluded Hydrogen on the Tensile Strength of Iron, Proc. Roy. Soc., London, A112, 182 (1926).

(239) R.P. Hohmberg, W.J. Barnett and A.R. Troiano, Trans. ASM, 47, 892 (1955).

(240) A.R. Troiano, Trans. ASM, 52, p. 54 (1960).

(241) R.A. Oriani: Ann. Rev. Mater. Sci., 8, 327 (1978).

(242) R.A. Oriani, p. 351, in ref. (221).

(243) C.D. Beachem, Hydrogen Damage, C.D. Beachem, ed., p. IX, (1977).

(244) R.A. Oriani, and P.H. Josephic, Acta Metall. 22, 1065 (1974).

(245) M.S. Daw and M.I. Baskes, Phys. Rev. B, 29, 644 (1984).

(246) R.P. Messmer and C.L. Briant, Hydrogen DEgradation of Ferrous Alloys, R.A. Oriani, J.P. Hirth, and M. Smialowski, ed., p. 140 (1985).

(247) M.E. Eberhart, R.M. Latanision and K.H. Johnson, Acta Metall., 33, 1769 (1985).

(248) H. Vehoff, W. Rothe, Acta Metall., 31, 1781, (1983).

(249) J.R. Rice and Thomson, Phil. Mag., 29, 73 (1974).

(250) M.J. Morgan and C.J. McMahon Jr., p. 608, in ref. (246).

(251) T. Tabata and H.K. Birnbaum, Scripta Met., 18, 231 (1984).

(252) I.M. Robertson and H.K. Birnbaum, Acta Metall., 34, No. 3, 353 (1986).

(253) I.M. Robertson, T. Tabata, W. Wei, F. Heubaum and H.K. Birnbaum, Scripta Met., 18, 841 (1984).

(254) G.M. Bond, I.M. Robertson and H.K. Birnbaum, Acta Metall., 35, 2289 (1987).

(255) A. Kimura, H. Matsui and H. Kimura, Mater. Sci. Engng., 58, 211 (1983).

(256) C. Hwang and I.M. Bernstein, Acta Metall., 34, No. 6, 1011 (1986).

(257) R.A. Oriani, Corrosion, 43, No. 7, 390 (1987).

(258) W.Y. Chu, C.M. Haiao and S.Q. Li, Scripta Met., 13, 1057 (1979).

(259) Y. Takeda and J. McMahon, Jr., Metall. Trans. A, 12A, 1255 (1981).

(260) T.D. Lee, T. Goldenberg, and J.P. Hirth, Metall. Trans., A, 10A, 439 (1979).

(261) M.S. Daw and M.I. Baskes, Phys. Rev., B29, 6443 (1984).

(262) M.S. Daw and M.I. Baskes, Chemistry and Physics of Fracture, R.M. Latanision and R.H. Jones, ed., Bad Reichenhall, F.R.G., p. 196 (1986).

(263) J.P. Hirth, p. 677, in ref. (237).

(264) A.W. Thompson, p. 379 in ref. (153).

(265) R.P. Gangloff and R.P. Wei, p. 78, in ref. (187).

(266) P.N. Duy, R.B. Lu and J.I. Dickson, to be published in Proc. of "International Conference and Exhibits on Failure Analysis", 8-11, July 1991, Montreal, Quebec.

(267) B.D. Craig, Corrosion (NACE), 37, 530, (1981).

(268) J.I. Dickson, S. Lalonde and Li Shiqiong, Focus on Mechanical Failures: Mechanisms and Detection, Proc. of the 45th Meeting of the Mechanical Failures Prevention Group. Annapolis Maryland, p. 65 (1991).

(269) A.W. Thompson, Hydrogen in Metals, I.J. Bernstein and A.W. Thompson, Ed., ASM, Metals Park, Ohio, p. 91 (1974).

(270) R.M. Vennett and G.S. Ansell, Transactions of the American Society for Metals, 60, 242 (1967).

(271) G.R. Caskey, Jr., Scripta Met., 11, 1077 (1977).

(272) H.E. Hanninen, International Metals Reviews, No. 3, Review 241, 85 (1979).

(273) R.B. Benson, R.K. Dann, and L.W. Roberts, Trans. ASM, 242, 2199 (1968).

(274) N. Narita and H.K. Birnbaum, Scripta Metall. 14, 1355 (1980).

(275) N. Narita and C. Altstetter, and H.K. Birnbaum, Metall. Trans. A, 13A, 135 (1982).

(276) G.R. Caskey, Jr., Fractography and Materials Science, ASTM, STP 733, p. 86 (1981).

(277) J. Albrecht, A.W. Thompson and I.M. Bernstein, Metall. Trans. A, 10A, 1759 (1979).

(278) D.A. Hardwick, A.W. Thompson, and I.M. Bernstein, Metall. Trans., A, 14A, 2517 (1983).

(279) Metals Handbook, 9th edition, ASTM, Metals Park, Ohio, 12 (1987).

(280) C.F. Old, Metals Science, August-September, 14, 433 (1980).

(281) Metals Handbook, 9th Edition, ASTM, Metals Park, Ohio, 11 (1986).

(282) C.E. Price and R.S. Fredell, Metall. Trans., A, 17A, 889 (1986).

(283) P. Gordon and H.H. An, Metall. Trans. A, 13A, 457 (1982).

(284) S.P. Lynch, Materials Forum, 11, 268 (1988).

(285) S.P. Lynch, Acta Metall., 29, 325 (1981).

(286) S.P. Lynch, Acta Metall., 32, 79 (1984).

(287) N.S. Stoloff, p. 921, in ref. (232).

(288) N.S. Stoloff and T.L. Johnston, Acta. Metall., 11, 251 (1963).

(289) A.R.C. Westwood and M. Kamdar, Phil. Mag., 8, 787 (1963).

(290) R.A. Ayres, J.E. Hack and D.F. Stein, Scripta Metall. 12, 979 (1978).

(291) G.M. Pharr, D.M. Barnett and W.D. Nix, Scripta Metall. 12, 973 (1978).

(292) W.M. Robertson, Metall. Trans., 1, 2607 (1970).

(293) E.E. Glikman and Yu V. Goryunov, Fiz. Khim Mekh. Mater., 14, 20 (1978).

(294) M.A. Krishtal, Sov. Phys., Dokl., 15, 614 (1970).

(295) D.J. Duquette, p. 12 in ref. (29).

(296) D.J. Duquette, p. 335 in ref. (49).

(297) R.P. gangloff and D.J. Duquette, p. 612 in ref. (233).

(298) D.J. Duquette, Corrosion (NACE) 46, No. 6, 434 (1990).

(299) H.N. Hahn and D.J. Duquette, Acta Metall., 26, 279 (1978).

(300) B.D. Yan, G.C. Farrington, and C. Laird, Acta Metall. 33, 1533 and 1593 (1985).

(301) H. Masuda and D.J. Duquette, Met. Trans., 6A, (1975).

(302) T. Magnin and L. Coudreuse, Mater. Sci. Engng. 72, 125 (1985).

(303) T. Magnin and L. Coudreuse, Acta Metall. 8, 2105 (1987).

(304) D.J. McAdam, Jr. and G.W. Geil, Proc. ASTM, 41, p. 696 (1941).

(305) M.P. Mueller, Corrosion (NACE), 8, 431 (1982).

(306) R.E. Stoltz, and R.M. Pelloux, Metall. Trans., 3, 2433 (1972).

(307) M. Ait Bassidi, thesis D.Sc.A., Ecole Polytechnique de Montréal (1983).

(308) A.K. Vasudevan and S. Suresh, Metall. Trans. 13A, 2271 (1982).

(309) Y. Nakai, K. Tanaka and R.P. Wei, Eng. Frac. Mech. 24, 433 (1986).

(310) R.P. Gangloff, Metall. Trans. A, 16, 953 (1985).

(311) P.K. Liaw, L. Roth, A. Saxena, J.D. Landes, T.R. Leax and N.L. Kilpatrick, Scripta Metall. 17, 611 (1983).

(312) R.N. Parkins and Y. Suzuki, Corrs. Sci. 23, 577 (1983).

(313) A. Boateng, J.A. Begley, and R.W. Staehle, Metall. Trans. A, 14A, 67 (1983).

(314) A.J. McEvily and R.P. Wei, p. 88 in ref. (29).

(315) E.J. Imhof and J.M. Barsom, ASTM STP 536, p. 182 (1973).

(316) R.W. Hertzberg, p. 557 in ref. (13).

(317) H.D. Solomon and L.F. Coffin, ASTM STP 520, p. 112 (1973).

(318) L.A. James and R.L. Knecht, Metall. Trans., 6A, 109 (1975).

(319) R.P. Wei and J.D. Landes, Mater. Res. Stand., 9, 25 (1969).

(320) I.M. Austen and E.F. Walker, p. 334 in ref. (20).

(321) D. Rhodes, J.K. Musuva and J.C. Radon, Eng. Frac. Mech. 15, 407 (1981).

(322) C.A. Stubbington, R.A.E. Report CPM 4, March (1963).

(323) R.J. Selines and R.N.M. Pelloux, Metall. Trans., 3, 2525 (1972).

(324) A. McMinn, Fatigue of Eng. Mat. and Struct. 14, 235 (1981).

(325) M. Ait Bassidi, J. Masounave, J.P. Baïlon, and J.I. Dickson, Defects, Fracture and Fatigue, G.W. Sih and J.W. Provan ed., Martinus Nijhoff, The Hague, p. 359 (1983).

(326) C. Laird, Fatigue Crack Propagation, ASTM STP, 415, p. 131 (1967).

(327) R.J.H. Wanhill, Corrosion, 31, 66 (1975).

(328) R.E. Stoltz and R.N. Pelloux, Corrosion, 29, 13 (1973).

(329) S.P. Lynch, Fatigue 84, C.J. Beevers, ed. EMAS Ltd., Warley, p. 445 (1984).

(330) M. Kaczorowski, C.-S. Lee and W.W. Gerberich, Mater. Sci. Engng., 81, 305 (1986).

(331) J.I. Dickson, Li Shiqiong and J.P. Baïlon, "Microstructural and Fractographic Aspects of Corrosion Fatigue", submitted to Materials Characterization.

(332) J.I. Dickson, Y. Blanchette and J.-P. Baïlon, The Effect of Cathodic Protection on the Propagation of Long and Short Fatigue Cracks, in Cathodic Protection: a + or - in Corrosion Fatigue, O. Vosikovsky and K. Leewis, ed., CANMET, Ottawa, p. 57 (1986).

(333) J.I. Dickson, L. Handfield, S. Lalonde, M. Sahoo and J.-P. Baïlon, Corrosion Cracking, V.S. Goel, ed., ASM, Metals Park, Ohio, p. 279 (1986).

(334) J.I. Dickson, L. Handfield, S. Lalonde, M. Sahoo and J.-P. Baïlon, J. Mater. Engng. 10, 45 (1988).

(335) H.N. Hahn and D.J. Duquette, Metall. Trans. A, 10A, 1453 (1979).

(336) J.I. Dickson, Li Shiqiong and J.-P. Baïlon, to appear in "Corrosion sous contrainte: phénoménologie et mécanismes", Proceedings of a conference at Bombannes, France, September 1990.

(337) J.I. Goldstein et al., Scanning Electron Microscopy and X-Ray Microanalysis, a Text for Biologists, Materials Scientists, and Geologists, Plenum Press, New York and London, (1984).

(338) S.P. Lynch, Metallography, 23, 147 (1989).

(339) D. Broek, Eng. Frac. Mech., 1, 691 (1970).

(340) E.I. Meletis and R.F. Hochmann, J. Testing Eval., 12, 142 (1984).

(341) J.C. Scully, Third Annual Scanning Electron Microscopy Symposium, IIT, Chicago, p. 313 (1970).

(342) F.W. Young, Jr., J. Applied Physics, 32, No. 2, p. 192 (1961).

(343) M. Macecek, A.W. Miller and U.M. Franklin, Praktische Metallugraphie, 10, No. 12, 692 (1973).

(344) L. Illgen, H. Ringfeil and H. Hemschik, Praktische Metallugraphie, 6, 363, June (1969).

(345) M.B. Ives, Localized Corrosion, NACE-3, P.O. Box 1499, Houston, p. 78 (1974).

(346) T. Taoka, E. Furubayashi, and S. Takeuchi, Japan, J. Appl. Phys., 4, 120 (1965).

(347) G.F. Vandervoort, Metallography Principles and Practice, McGraw-Hill Book Company (1984).

(348) Techniques of Metals Research, R.F. Bunshah, ed., vol. 2, part 1, p. 316 (1968).

(349) C.V. Essen, E.M. Schulson and R.H. Donaghay, J. Mater. Sci., 6, No. 3, 213 (1971).

(350) J.L. Nelson and J.A. Beavers, Metall. Trans. A, 10A, 658 (1979).

(351) G. Piazzesi, J. Phys. E., Journal of Scientific Instruments, 6, No. 4, 392 (1973).

(352) R.J. Cooke, and C.J. Beevers, Mater. Sci., Engng., 13, 201 (1974).

(353) K.S. Ravichandran, E.S. Dwarakadasa, and Kishore, Mater. Sci. Engng., 83, L11, (1986).

(354) N. Marchand, M.A.Sc. thesis, Ecole Polytechnique de Montréal (1985).

(355) M.E.L. Boujdaini, M.A.Sc. thesis, Ecole Polytechnique de Montréal (1985).

(356) C.D. Beachem and G.R. Yoder, Metall. Trans., 4, 1145 (1973).

(357) Y. Imashimizu and J. Watanabe, Transaction of the Japan Institute of Metals, 24, No. 1, 1, (1983).

(358) J.D. Meakin, and H.G.F. Wilsdorf, Trans. TMS-AIME, 218, 737 (1960).

(359) E. Horn and U. Lotter, Pract. Met., 22, 397 (1985).

(360) Li Shiqiong, J.I. Dickson, and J.P. Baïlon, in ref. 118, vol. 3, p. 1375.

(361) Li Shiqiong, J.I. Dickson and J.P. Baïlon, "Cracking Crystallography at Threshold in 316 Stainless Steel", Poster in the International Metallography Exhibition, Boston, August, 1986, second place prize for the SEM category.

(362) Li Shiqiong, J.I. Dickson and J.P. Baïlon, "Crystallography of Decohesion During Near-Threshold Fatigue and SCC of FCC Metals", Poster in the International Metallography Exhibition, Monterey, CA, July, 1987, second place prize for the SEM category.

(363) Li Shiqiong, J.I. Dickson and J.P. Baïlon, "Mechanism of Near-Threshold Fatigue Cracking in BCC Metals", Second place prize in the SEM category poster in the International Metallography Exhibition, Virginia, July 1989.

(364) P.A.S. Reed, P. Woollin and J.E. King, in ref. 118, vol. 2, p. 1085.

(365) A.I. Alekseev, Int. J. Fatigue, p. 129 (1981).

(366) O.A. Onyewuyenyi, and J.P. Hirth, Metall. Trans. A, 14, 259 (1983).

(367) H.E. Deve, R.J. Asaro, and N.R. Moody, Scripta Metall., 23, 389 (1989).

(368) Jose Hallen-Lopez, Ph.D. thesis, Ecole Polytechnique de Montréal (1990).

(369) N.A. Neilsen, J. Mater., 5, 794 (1970).

(370) A.J. Russell and D. Tromans, Metall. Trans. A, 10A, 1229 (1979).

(371) J.I. Dickson, A.J. Russell and D. Tromans, Can. Metall. Q, 19, 161 (1980).

(372) M.A. Streicher and I.B. Casale, in ref. 215, p. 305.

(373) A.J. Sedriks, Corrosion, 31, 339 (1975).

(374) D.L. Douglass, G. Thomas and W.R. Roser, Corrosion, 20, 15t (1964).

(375) MT. Hahn and E.N. Pugh, Fractography and Materials Science, ASTM, STP 733, L.N. Gilbertson and R.D. Zipp, ed., p. 413 (1981).

(376) J. Botton, M.A.Sc. thesis, Ecole Polytechnique de Montréal, September (1983).

(377) M.V. Hyatt, Corrosion, 26, No. 11, 487 (1970).

(378) M. Kermani and J.C. Scully, Corrosion Sci., 18, 883 (1978).

(379) E.N. Pugh, J.V. Craig and W.G. Montagne, Trans. of the ASM, 61, 468 (1968).

(380) E.N. Pugh and J.A.S. Green, Metall. Trans., 2, 3129 (1971).

(381) M.B. Hintz, L.J. Nettleton and L.A. Heldt, Metall. Trans. A, 16A, p. 71 (1985).

(382) A.J. McEvily and A.P. Bond, J. Electrochem. Soc., 112, No. 2, 131 (1965).

(383) R.C. Newman, T. Shasrabi and K. Sieradzki, Scripta Metall., 23, 71 (1989).

(384) K. Sieradzki, J.S. Kim, A.T. Cole and R.C. Newman, J. Electrochem. Soc., 134, 1637 (1987).

(385) U. Bertocci, F.I. Thomas and E.N. Pugh, Corrosion, 40, No. 8, 439 (1984).

(386) T.B. Cassagne, W.F. Flanagan and B.D. Lichter, Metall. Trans. A, 19A, No. 2, 281 (1988).

(387) T.B. Cassagne, to appear in "Corrosion sous contrainte: phénomélogogie et mécanismes", Proceedings of a conference at Bombannes, France, September 1990.

(388) E.N. Pugh, Environment-Sensitive Mechanical Behavior, A.R.C. Westwood and N.S. Stoloff, ed. Gordon and Breach, New York, p. 351 (1966).

(389) E.N. Pugh, J.V. Craig and A.J. Sedriks, in ref. 215, p. 118 (1969).

(390) J.I. Dickson, L. Handfield, J.P. Baïlon and M. Sahoo, in ref. 329, vol. 1, p. 191.

(391) J.I. Dickson, J. Hallen-Lopez, L. Handfield, Y. Blanchette and S. Lalonde, D.S.S. Report 64 ss. 23440-5-9054, part I, 1989.

(392) J. Hallen-Lopez, J.I. Dickson and M. Sahoo, Transactions of the American Foundrymen's Society, vol. 99, p. 489 (1989).

(393) A. Couture, M. Sahoo, B. Dogan and J.D. Boyd, Transactions of the American Foundrymen's Society, vol. 95, p. 87 (1987).

(394) J.I. Dickson, L. Handfield, Li Shiqiong and J.P. Baïlon, C.D.T. Report, 24 ST. 23440-5-9054, March 1989.

(395) K.A. Esaklul, A.G. Wright and W.W. Gerberich, p. 299 in ref. 34.

(396) E.R. Fuller Jr., B.R. Lawn and R.M. Thompson, Acta Metall. 28, 1407 (1980).

(397) S.H. Dai and J.C.M. Li, Scripta Metall., 19, 557 (1985).

(398) M. Lii, T. Foecke, X. Chen, W. Zielinski and W.W. Gerberich, Mater. Sci. and Engng., A113, 327 (1989).

(399) W.W. Gerberich and S. Chen, Environment-Induced Cracking of Metals Fundamental Process, NACE, P.O. Box 218340, Houston, p. 167 (1990).

(400) J.D. Fritz, B.W. Parks, H.W. Pickering, Scripta Metall., 22, 1063 (1988).

(401) T.B. Cassagne, W.F. Flanagan and B.C. Lichter, in ref. 233, p. 659 (1987).

(402) U. Bertocci, Embrittlement by the Localized Crack Environment, R.P. Gangloff, ed., Warendale, Pennsylvania, 15086, p. 229 (1984).

(403) U. Bertocci, J. Electrochem. Soc., 136, 1887 (1989).

(404) Hideya Okada, Yuzo Hosoi, and Seizaburo Abe, Corrosion, 26, No. 7, 183 (1970).

(405) M.B. Hintz, W.K. Blanchard, P.K. Brindley, and L.A. Heldt, Metall. Trans. A, 17A, 1081 (1986).

(406) N.J. Petch and P. Stables, Nature, London, 169, 842 (1952).

(407) I. Langmuir and J. Am, Chem. Soc., 38, 2221 (1616), and 40, 1361 (1918).

(408) W.D. Robertson and A.S. Tetelman, in "Strengthening Mechanisms in Solids", ASTM, Metal Park, OH, (1962) p. 217.

(409) M.B. Hintz, Scripta Metall., 19, 1445 (1985).

(410) D. Tromans, Metall. Trans. A, 12A, 1445 (1981).

(411) W.Y. Chu, S.Q. Li, C.M. Hsiao and S.Y. Yu, Corrosion, 37, 514 (1981).

(412) J.A. Smith, M.H. Peterson and B.F. Brown, Corrosion, 26, 539 (1970).

(413) B.F. Brown, C.F. Fujii and E.P. Dahlberg, J. Electro. Soc., 116, No. 2, 218 (1968).

(414) X. Chen, T. Foecke, M. Lii, Y. Katz and W.W. Gerberich, Engng. Frac. Mech., 35, No. 6, 997 (1990).

(415) Shiqiong Li, J.I. Dickson, J.P. Baïlon, and D. Tromans, Mater. Sci. Engng., A119, 59 (1989).

(416) T. Magnin and J. Lepinoux, submitted for the Proceedings of the TMS-AIME R.W. Parkins Symposium on Fundamental Aspects of SCC, Cincinnati, 20-24 Oct. (1991).

ÉCOLE POLYTECHNIQUE DE MONTRÉAL
3 9334 00217844 8